PROCEEDINGS

of the International Conference on

"Microwave and THz Technologies and Applications"

October 2-3, 2014
Aghveran, Armenia

PROCEEDINGS

of the International Conference on

“Microwave and THz Technologies and Applications”

October 2-3, 2014
Aghveran, Armenia

“Gitutiun” Publishing House of the NAS RA
Yerevan 2015

Organized by

Institute of Radiophysics and Electronics NAS RA

Sponsored by

State Committee of Science of Armenia
National Academy of Sciences of Armenia

Organizing Committee

Chairman: Prof. Radik Martirosyan (Armenia)
Co-chairman: Prof. Arsen Hakhoumian (Armenia)

Prof. B.G. Kutuza (IRE RAS, Russia)
Prof. H.P. Roeser (Stuttgart University, Germany)
Prof. K. Lee (Sogang University, South Korea)
Prof. R. Beigang (Kaiserslautern University, Germany)
Prof. R. Minasyan (Sidney University, Australia)
Prof. Yu. Avetisyan (YSU, Armenia)
Dr. Emil Asmaryan (IRPhE, Armenia)

IRPhE'2014 topics

- THz technique and spectroscopy
- Microwave devices and propagation
- Microwave photonics
- Microwave and THz on advanced remote sensing and radar technologies and biomedical applications
- Wireless communications and related information technologies

Preface

The International Conference ***"Microwave and THz Technologies and Applications"*** (IRPhE'2014) was held in Aghveran, Armenia, from October 2 to October 3, 2014. The IRPhE'2014 was directed to the revival of the traditional conferences organized by the Institute of Radiophysics and Electronics, National Academy of Sciences of Armenia, since 1968. In the framework of the Conference four sections were organized: "*THz Technique and Spectroscopy*", "*Remote Sensing and Radar Technologies*", "*Microwave Photonics and Devices*", *and* "*Materials and Electronics*".

UDC 537.86:06.053

ISBN 978-5-8080-1141-0

http://www.irphe.am

CONTENTS

Section 3: Microwave Photonics and Devices

Section 4: Materials and Electronics

Advanced THz-TDS Instrument Applied to Non-destructive Quality Evaluation of Industrial Crystalline Materials

Seizi Nishizawa[1], Takeshi Nagashima[2] and Mitsuo W. Takeda[3]

[1]*FIR FU, University of Fukui, 3-9-1 Bunkyo, Fukui 910-8507, Japan*
[2]*Faculty of Science and Engineering, Setsunan University, Neyagawa 572-8508, Japan*
[3]*Faculty of Science, Shinshu University,3-1-1 Matsumoto 390-8621,Japan*

The coherent terahertz (THz) radiation emitted through the femtosecond pulse laser irradiation on a photoconductive antenna has been effectively utilized for the terahertz time-domain spectroscopy (THz-TDS). A versatile compact THz-TDS instrument was newly developed with an extremely high SNR in the wavenumber region below 170cm^{-1}. For the expansion of spectrum wavenumber coverage up to the IR region, an advanced THz-TDS instrument was developed with the new optics configuration of a composite THz-TDS with Michelson (Matin-Puplett configuration) interferometer (FTIR). Here, an overview of the newly developed THz-TDS instruments with the fundamental optical advantages and further some of the latest results of applications focusing on the THz-TDS non-destructive quality evaluation for industrial interested materials and crystalline polymorphs of active component APIs of OTC pharmaceutical products are described..

1. Introduction

The recent progress in the generation of coherent terahertz (THz) radiation through the femtosecond pulse laser irradiation on a photoconductive antenna has been effectively utilized for the promising new spectrometric technique of the terahertz time-domain spectroscopy (THz-TDS) [1]. The THz-TDS technique [2,3] has the advantage of better signal-to-noise-ratio (SNR) than that of the conventional spectrometric techniques of Raman and FTIR [4], and further makes it possible to measure not only the spectrometric transmission intensities $T(\omega)$ but also the intrinsic phase shifts $\Delta\varphi(\omega)$ of propagating THz radiations through within a sample specimen. The exact measurements of both $T(\omega)$ and $\Delta\varphi(\omega)$ make direct estimation of the real part $\varepsilon'(\omega)$ and the imaginary part $\varepsilon''(\omega)$ of complex dielectric constant $\varepsilon^*(\omega)$ free from the uncertainty caused by the Kramers-Kronig analysis [4]. The intrinsic phase shifts $\Delta\varphi(\omega)$ also enables to make analytical estimation of the dispersion relations for various elementary excitations coupled with the propagating THz radiations. Thus the THz-TDS measurements are effectively applied to the far-infrared spectroscopic investigations of intermolecular vibration modes, crystalline phonon modes, crystalline morphology, photonic dielectric structures and glassy material boson peaks.

The THz-TDS technique has recently been in progress with a wide expansion of fundamental research and industrial investigation applications. A versatile compact THz-TDS instrument has been newly developed with an extremely high SNR in the wavenumber region below 170 cm^{-1}. Further, for the spectrum wavenumber coverage expansion up to the entire IR region, a new instrument of THz-TDS has been developed with the advanced optical configuration which consists of a composite THz-TDS optics and a high throughput Michelson (Matin-Puplett configuration) [4] interferometer (FTIR). These THz-TDS instruments are now being applied to the far-infrared spectrum measurements on dielectric functional materials, polymorphous organic compound, bio-molecules, and crystalline morphology of pharmaceutical reagents. The THz-TDS investigation is also being applied for the non-destructive quality evaluation of industrial products.

Here, an overview of the newly developed instrument performances and some of the latest results of novel applications focusing on the THz-TDS non-destructive qualityevaluation of functional dielectric materials and of crystalline polymorphs in the active components (APIs) of OTC pharmaceutical products are described.

2. Instrumentation Performances

For the Far-infrared spectroscopy, conventionally FTIR technique based on Michelson interferometer has been mainly utilized. A typical FTIR instrument with a high throughput Michelson (Matin-Puplett configuration) interferometer is shown in Fig. 1(a,b,c). THz-TDS technique has recently been in progress with the advantages of higher SNR and more wide dynamic range than that of other techniques (Raman and FTIR).

A compact THz-TDS instrument has been newly developed with the advantages of high SNR in Far-infrared region below 170 cm^{-1} and applied for versatile measurements (transmission, reflection, liquid, gas, ATR, mapping, temperature dependence and etc.) (Fig. 1(d,e,f)) [2]. For the THz-TDS, the sample preparation techniques used here are the same as those used in FTIR and Raman spectroscopy. An absorption spectrum on air was measured and compared with the water vapour absorption spectra offered from the Jet Propulsion Laboratory (JPL). As shown already in the proceedings of the International Conference on "Microwave and THz Technologies and Wireless Communications" (2012) at Yerevan [5], the wavenumbers of the absorption lines agree with the absorption data of JPL and also the spectral resolution is less than 0.02[cm^{-1}] which was confirmed by the water vapour absorption line at 57.22[cm^{-1}] measured at less than 60 Pa. The spectral coverage depends on the femtosecond laser. The THz radiation source spectra measured by the laser (Femtolasers Productions GmbH: Integral Pro) which pulse duration is less than 10 femtosecond is shown in Fig. 1(f). The THz radiation is observed from about 1[cm^{-1}] to 230[cm^{-1}]. Almost all compact type femtosecond lasers are possible to set on the instrument.

Between 230 and 340[cm^{-1}], the THz radiation is absorbed by the GaAs phonon absorption bands of the photoconductive antennas. It is expected that the high frequency limit of THz radiation will become higher than 440[cm^{-1}] by avoiding the absorption of the GaAs substrates. The recent progress in the research applications enables the potential application for the far-infrared measurements on new functional materials. A new instrument of THz-TDS has been developed with the advanced optical configuration which consists of a composite THz-TDS optics and a high throughput Michelson (Matin-Puplett configuration) interferometer. A photographic view of the optical configuration is shown in Fig.2. The instrument is for use in the qualitative analyses of opt electric constants of materials in which the spectrum wavenumber coverage is expanded to the NIR region (Fig. 2(b)).

3. Non-destructive Quality Evaluation

The versatile compact THz-TDS instrument developed with the advantages of wide wavenumber coverage and a high dynamic range has been in progress applied for far-infrared measurements on industrial functional materials, polymorphous organic compounds, bio-molecules, and crystalline morphology of pharmaceutical products, of which THz-TDS investigation is applied to the pharmaceutical industry.

In ferroelectric materials, the dielectric properties in the terahertz (THz) region are of great importance due to the physical and chemical properties of Ferro electricity dominantly originated in this region. The soft optic modes responsible for Ferro electricity appear in the far-infrared region below 100[cm^{-1}]. The measurements of complex dielectric constants at the THz frequencies are very useful. Since ferroelectric soft modes are infrared active and they propagate as polaritons, the polariton dispersion in the far-infrared region gives very important information for both fundamental and technical problems in ferroelectrics. The ferroelectric materials of current interest are mostly perovskite families with oxygen octahedral. The THz-TDS measurements are in focus on the typical perovskite families of current industrial interest, which includes bismuth, titanate $Bi_4T_{i3}O_{12}$ (BIT) (Fig.3), lithium heptagermanate, $Li_2Ge_7O_{15}$ (LGO) (Fig.4) and lithium niobate $LiNbO_3$ (LN) (Fig.5). Their Ferro electricity originates dominantly from the instability of polar soft modes in a ferroelectric transition. So the THz dynamics is very important for the characterization of ferroelectric properties. As one of the great technological achievements in the 1990s, oxide ferroelectric thin films have attracted a great deal of attention for use in non-volatile memories. In which bismuth titanate $Bi_4Ti_3O_{12}$ (BIT) is one of the most important key materials for FeRAM. However, there are still some problems to overcome in order to measure very high-frequency dielectric properties accurately for thin films or for very thin plates. Consequently, an experimental method for determining THz dielectric properties is desired for fundamental and practical research.

As shown in Fig.3(a), the spectral transmission intensity $T(\omega)$ and intrinsic phase shift $\Delta\varphi(\omega)$ of ac-plate of BIT were accurately measured frequency range from 100[cm^{-1}] down to 3[cm^{-1}]. Fig.3(b) shows the frequency dependences of dielectric constant $\varepsilon'(\sigma)$ and loss $\varepsilon''(\sigma)$ derived directly from the measured values of transmission intensity and intrinsic phase shift. For light polarization parallel to the *a*-axis (*E//a*) and *b*-axis (*E//b*), low frequency polariton branches of $A'(x, z)$ and $A''(y)$ symmetries were clearly observed down to 3[cm^{-1}], respectively. In the polariton dispersion, the wavevector $\kappa(\omega)$ is reduced for the observed values of the intrinsic phase shift $\Delta\varphi(\omega)$ through the equation, $\Delta\varphi(\sigma) = d\kappa(\sigma)$ where d is the sample crystal thickness.

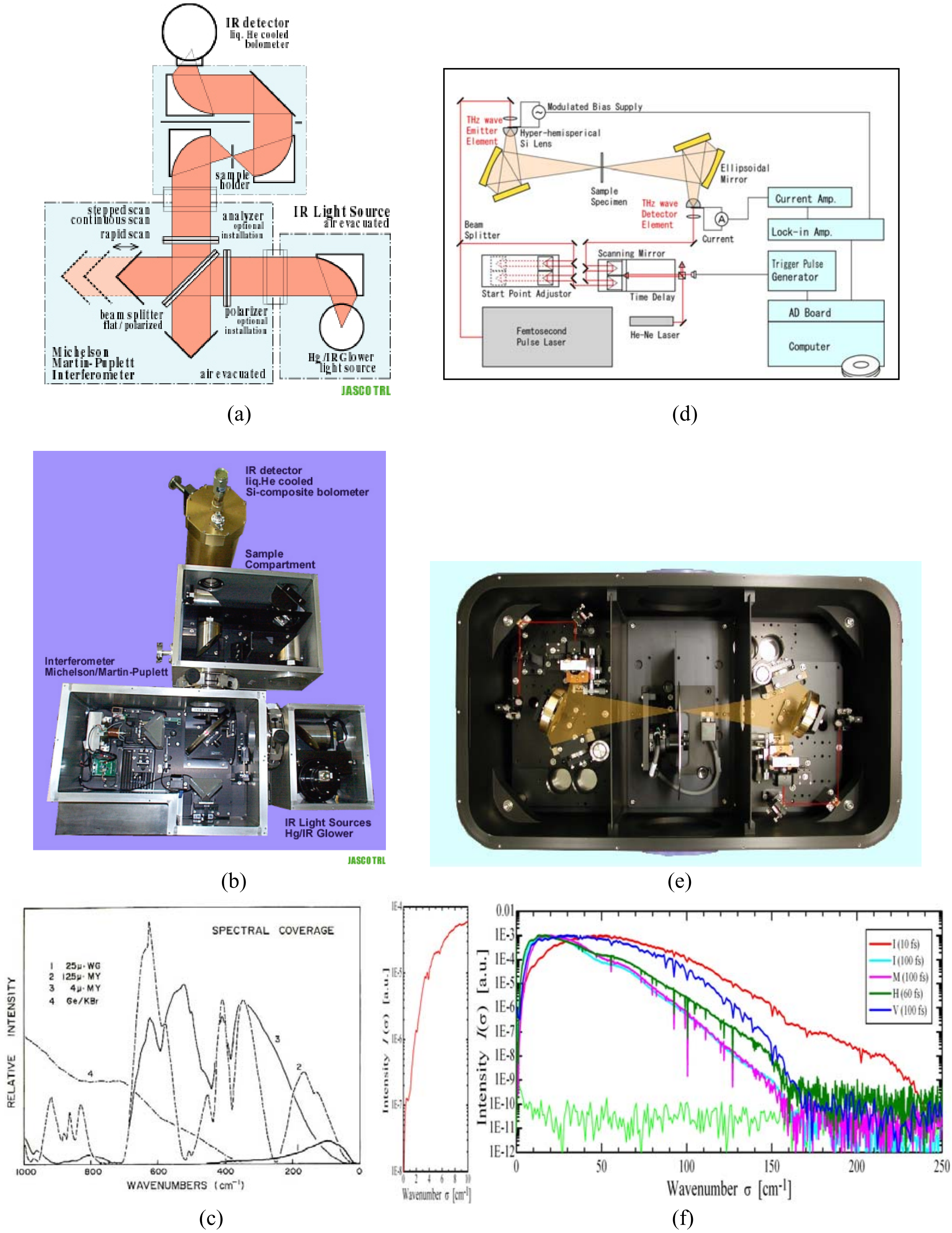

Fig. 1 Spectrometric fundamental properties performed on the far-infrared FTIR spectroscopy and the THz-TDS spectroscopy. The spectrum wavenumber coverage and spectrometric dynamic range of source radiation (a), (b) and (c) are performed on the typical FTIR instrument with a high throughput Michelson (Matin-Puplett configuration) interferometer(JASCO TRL), and other party (d), (e) and (f) are on the newly developed versatile THz-TDS instrument (Aispec model :pulse IRS- 2000) respectively.

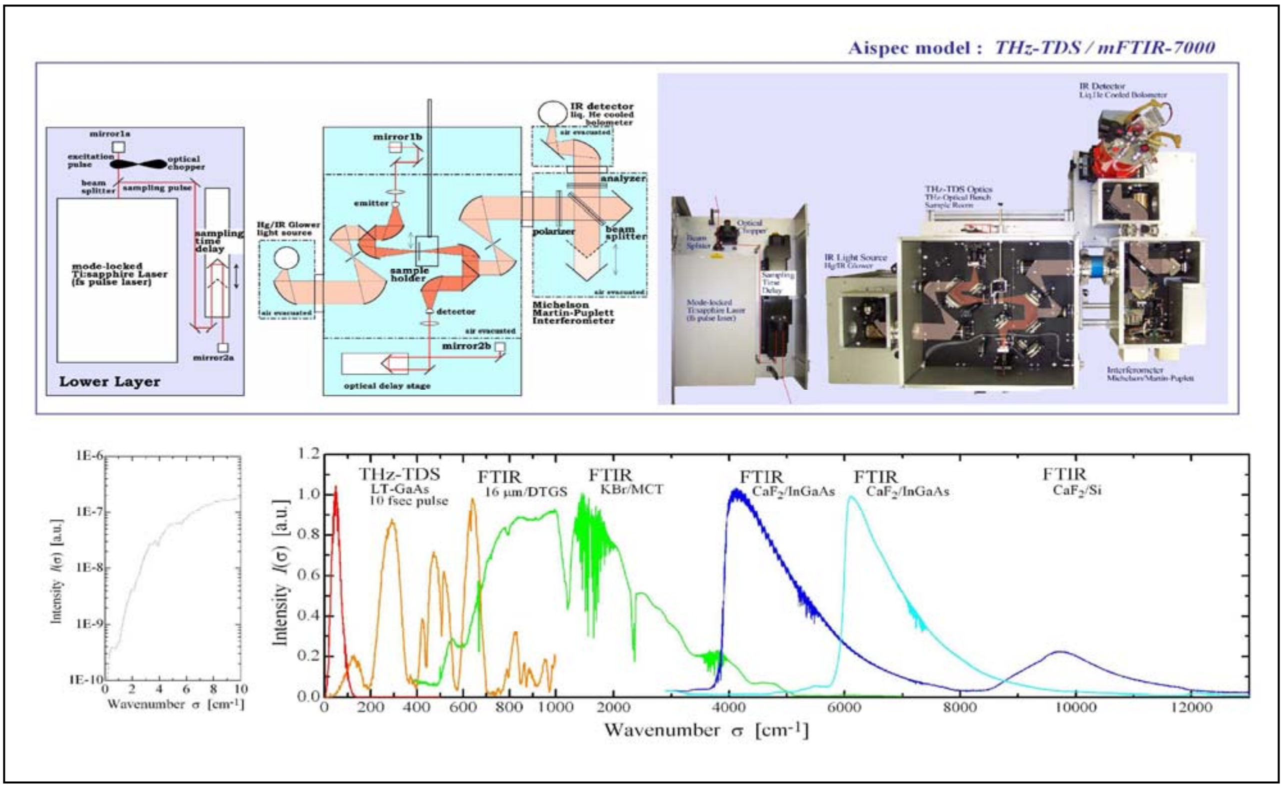

Fig. 2 Advanced optics of the composite THz-TDS com bined wi th a hi gh t hroughput M ichelson (M artin-Puplett configuration) interferometer (FTIR) (Upper) and expansion of the spectrum wavenumber coverage to the NIR region (Lower).

The observed dispersion curves shown in Fig.3(c) by open circles were well reproduced by the phonon-polariton dispersion curves calculated through the Kurosawa formula [6]. The solid curves in Fig.3(c) denote the curve calculated by the Kurosawa formula using mode frequencies of *A'*(*x, z*) symmetry, in which the values of fitting parameters are shown in the table in Fig.3(c). The good agreement concludes that the nonlinear relation reflects the dispersion relation of phonon-polariton. For the polariton coupled to a polar mode with *A'*(*x, z*) symmetry at 28 [cm^{-1}], the nonlinear ω-κ relation of the lowest branch was clearly observed in the frequency range 3-26[cm^{-1}]. The lowest lim it of the static dielectric constants along the *a*- and *b*-axis: ε_a0)=75.99 and $\varepsilon_b(0)$=146.41 were respectively estim ated from the lowest polariton branches [3], whose values showed good agreement with those measured with LCR meter.

The THz-TDS provides inform ation on low-frequency in termolecular vibration m odes, and has a wide range of applications in Pharmaceutical industry including formulation, high throughput screening, and inspection in process. The different form s referred to as “poly morphs” have the sam e chem ical form ula but different crystalline structures that can lead to different phy sical and chem ical properties of the m aterial. The different forms may have different rates of dissolution or bioavailability, and may even effect the stability of the products. The formation of different polymorphs can be controlled during crystallization by the solvent used, the rate of cooling, and the degree of super-saturation of the solu tion. Once in the desired crystalline form the polymorphic state may be changed by incorrect storage or even during tablet preparation. At present, there are no quick and convenient methods for confirming the polymorphic state of products while in storage or during manufacture.

The THz-TDS spectra are sensitive to the difference in the crystalline structure, and thus are applied to search the poly morphs of m edicines. In F ig.6, th e THz-TDS transm ission spectra of some marketed pharmaceutical products are shown with the industrial interest in non-destructive quality evaluation. Fig.6 shows the transmission

spectra measured on the tablets over the counter m edications named G10, GD and G10P identified with the pharmaceutical main active component, namely API famotidine containing the polymorphs of form A, form B and
other forms, and additionally the main additives of lactose and mannite.

A precursory instrument (Fig.7) [7] for the quality control on pharmaceutical products has been newly developed and started trial of practical application with the advantages of high dynamic range, sensitivity, high throughput screening, and high speed inspection in pharmaceutical product line.

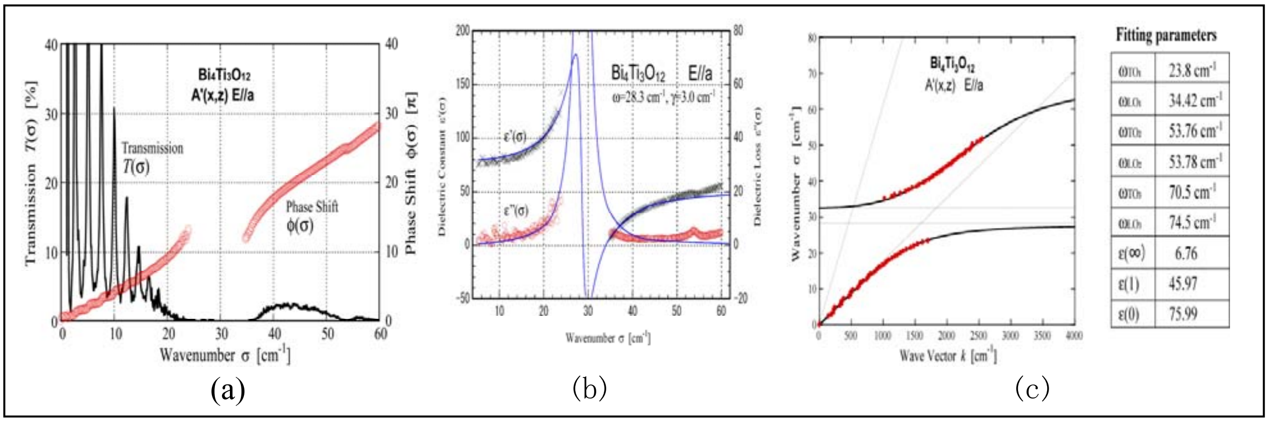

Fig. 3 Far-Infrared phonon-polariton dispersion probed for the ferroelectric bismuth titanate $Bi_4Ti_3O_{12}$ (BIT) crystal by THz-TDS. The transmission T(σ) and the intrinsic phase shift Δφ(σ) measured on the c-plate of high-quality BIT crystal (a), and the complex dielectric constants ε*(σ) { ε'(σ), ε''(σ)} estimated through *T*(σ) and Δφ(σ) of measured transmission spectra in the light polarization along the a-axis (b) are shown. In (b), the solid lines are the calculated curves using the constants of ω_{TO}=28.3[cm^{-1}] and σ=3.0[cm^{-1}] obtained through Raman scattering measurements. It can be found that the estimated values of ε*(σ) through THz-TDS transmission measurements are quite in agreement with the calculated values. The dispersion relations of phonon-polariton are also shown (c), in which the closed circles denote the estimated values through Δφ(σ) and the solid lines denote the calculated curves of phonon-polariton dispersion relation on the basis of the Kurosawa formula[6], and the table in (c) shows the values of fitting parameters for observed polariton.

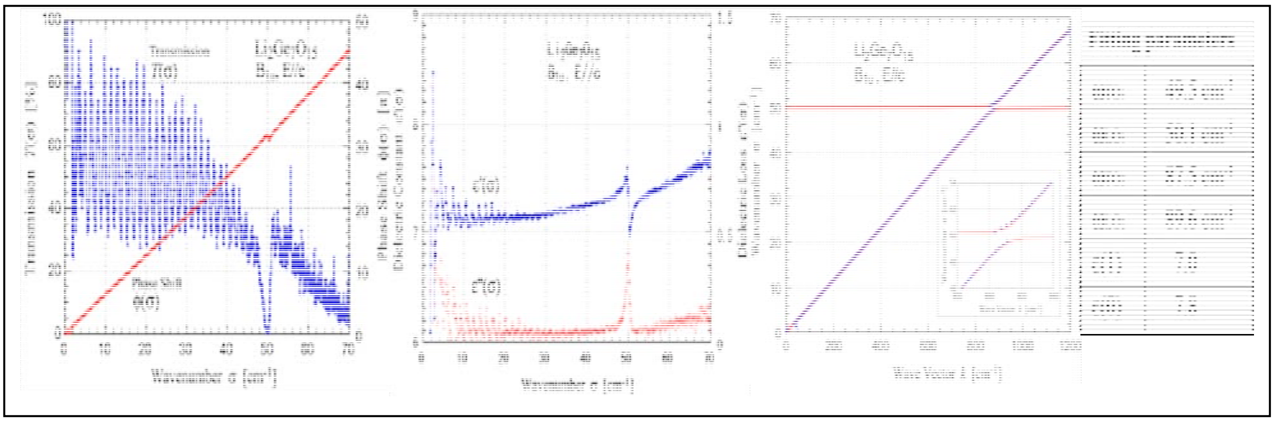

Fig. 4 Complex dielectric constants measured on lithium heptagermanate $Li_2Ge_7O_{15}$ (LGO) crystal for the light polarization parallel to the *c*-axis (Left and Center) and Dispersion relation measured on lithium heptagermanate $Li_2Ge_7O_{15}$ (LGO) crystal for the light polarization parallel to the *c*-axis. (Right). Solid curves denote the calculated curves on the bases of the Kurosawa formula[6]. Closed circles denote the measured dispersion relation for the light polarization parallel to the *c*-axis, and the values of fitting parameters are tabled.

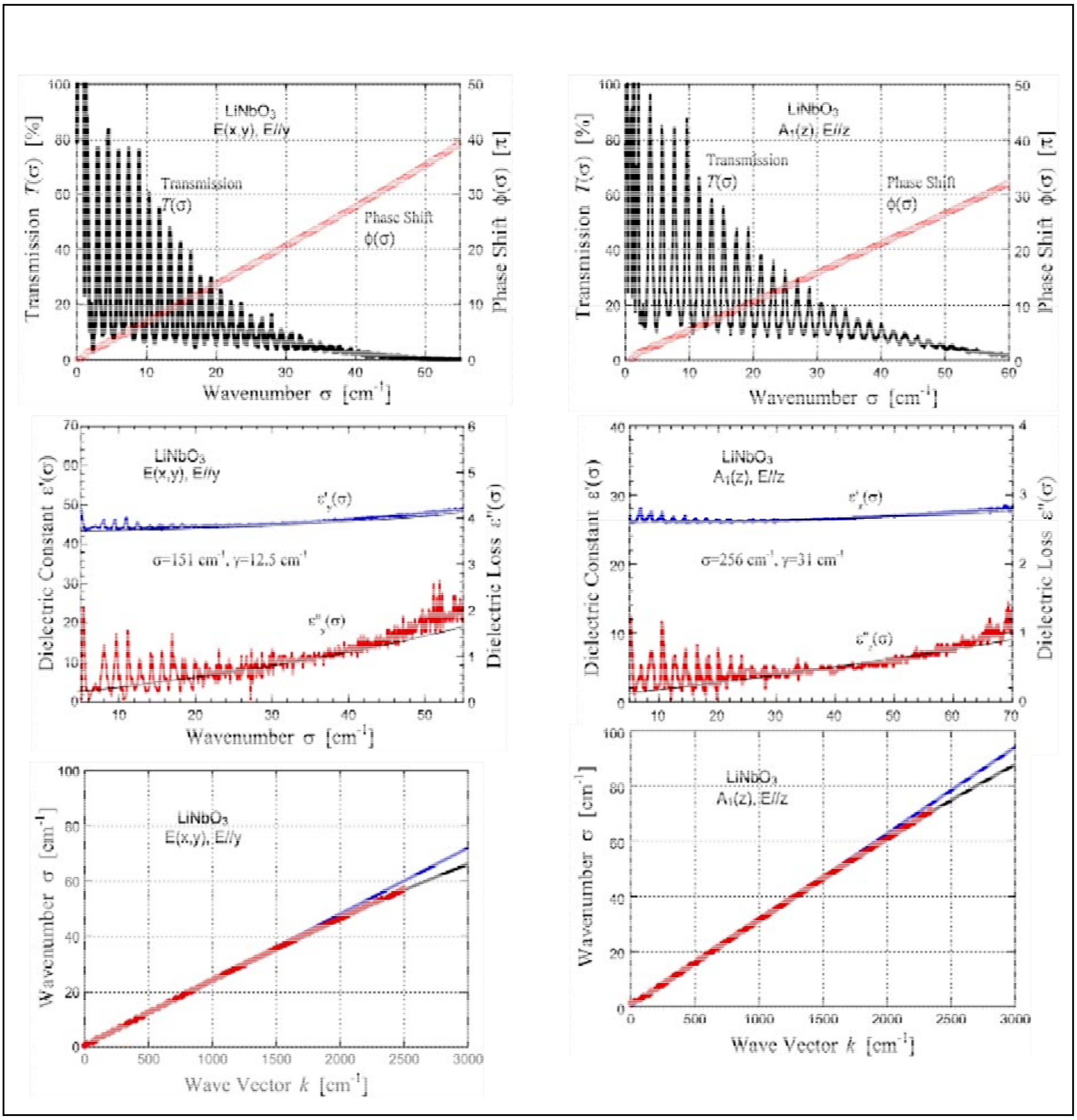

Fig. 5 Transmission intensity and phase shift spectra measured on an *x*-plate of a poled lithium niobate $LiNbO_3$ (LN) for the light polarization parallel to the *y*-axis (*E*//*y*) and the *z*-axis(*E*//*z*); (Upper), Complex dielectric constants measured on an *x*-plate of a poled $LiNbO_3$ (LN) crystal for the light polarization parallel to the *y*-axis and the *z*-axis; (Middle), and Dispersion relations measured on an x-plate of a poled $LiNbO_3$ (LN) crystal for the light polarization parallel to the *z*-axis; (Lower). Solid curves denote the calculated curves on the bases of the Kurosawa formula. The values of fitting parameters are tabled.

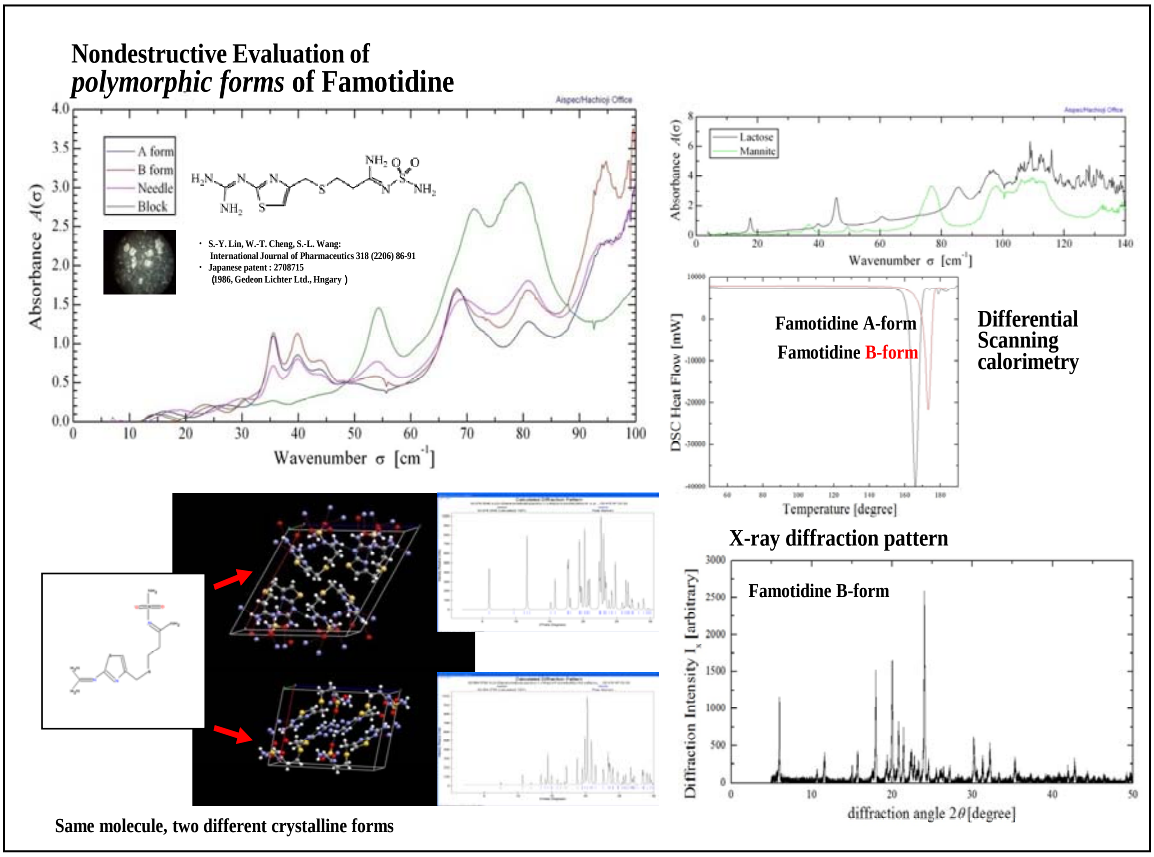

Fig. 6 Polymorphs of Pharmaceutical Active Famotidine
THz-TDS non-destructive polym orphs ch aracterization of pharm aceutical pr oducts. THz-TDS absorption spectral fingerprints obtained by the non-destructive measurements on t he OTC t ablets of st omach m edicine nam ed G10/GD/G10P (a), the transmission API: famotidine containing the different polymorphs of Form A, Form B and others (b), and also additives (c).

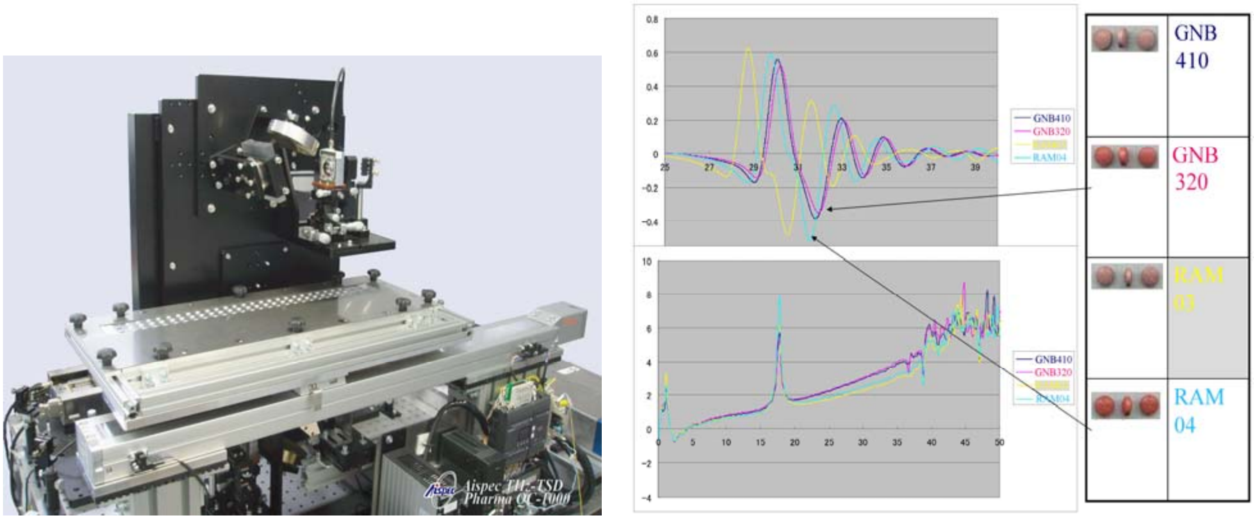

Fig. 7 Ph otographic v iew o f a p recursory THz-TDS p robe [7] for the quality control in the Process Analytical Technology (PAT), with the potential to be extended to at -line and on-line quality control inspection in pharmaceutical product lines (Aispec model: Pharma QC-1000).

4. Summary

The new instruments of THz-TDS have been developed with different optical bench configurations. One is a composite THz-TDS instrument combined with a high throughput Michelson (Martin-Puplett) interferometer applied for research measurements with wide wavenumber coverage from far-infrared to near-infrared. By the THz-TDS instrument, both measurements with THz-TDS and FTIR are possible without moving a sample specimen. Another is a compact THz-TDS instrument with the adaptation of routine quantitative measurements for characterizing industrial products. This compact instrument enables to measure with various sampling optics units inserted in the sample room.

The versatile THz-TDS instruments have applied for accurate quantitative measurements and the spectral intensities $T(\omega)$ and the intrinsic phase shifts $\Delta\varphi(\omega)$ of transmission spectra have carefully been measured on the ferroelectric materials and a glassy material. From the spectral intensities $T(\omega)$ and the intrinsic phase shifts $\Delta\varphi(\omega)$, the complex dielectric constants of the materials were estimated without the uncertainty caused by the Kramers-Kronig analysis in conventional infrared spectroscopy. The dispersion relations of the ferroelectric materials were also derived from the intrinsic phase shifts. The obtained dispersion relations are well reproduced by the phonon-polariton dispersion relations calculated on the basis of Kurosawa's formula [6]. By the THz-TDS instruments, the lowest branch of phonon-polariton dispersion was determined down to the very low frequency of 3cm$^{-1,}$ which could not be attained by other experimental methods. The anisotropy of polariton was also clearly observed simply by rotating the light polarization of the incident THz radiation. The boson peak of a glassy material was also observed by the THz-TDS instruments. Up to now most of properties on boson peaks were discussed only on imaginary parts χ" (δ) of dynamic susceptibility. Therefore, the determination of both the real part and imaginary part of dielectric constant is very important. We believe these observations are the first reported observations of the dispersion relation of phonon-polariton. The novel applications to pharmaceutical products were described. The THz-TDS has a wide range of applications for industrial especially pharmaceutical quality control including formulation, high throughput screening, and inspection in the product process. It is also suggested that THz-TDS has the technological advantage of non-contact measurement on far-infrared dielectric properties, which is usefully applied to both fundamental study of various far-infrared elementary excitations and utilitarian development of electronics devices, and further to quality control of industry products in the near future.

Acknowledgements

This research is partially supported by the Development of Systems and Technology for Advanced and Measurement and Analysis of the Japan Science and Technology (JST). The authors appreciate technical supports and engineering advices by Dr. Toshi Iwamoto with Aispec and Mr. Kikuo Shirawachi with JASCO and further appreciate valuable fundamental advices from Professor Seiji Kojima of Tsukuba University, Dr. Kiyomi Sakai of NICT and Professor Emeritus Mitsuo Tasumi of The University of Tokyo.

References

[1] K. Sakai, K. ed., "Terahertz Optoelectronics", Springer-Verlag Berlin Heidelberg (2005).

[2] S. Nishizawa, T. Iwamoto., K. Shirawachi, and M. W, Takeda, M.Tani and K.Sakai, Special Review issues, Proc.1999, IEEE, 7th Inter. Conf... on Terahertz Electronics, (1999) 308; S. Nishizawa., N. Tsumura, H. Kithara., M. W. Takeda and N. Kojima, Special Review issues, Phys. Med. Bio. 47. (2002) 3771

[3] Kojima, S., Tsumura, N., Takeda, M. W., and Nishizawa, S., Phys. Rev. B67 (2003) 035102; Kojima, S., Takeda, M. W., and Nishizawa, S., J .Molecular Structure 651-653 (2003) 285

[4] Tasumi, M. ed., "Introduction to Experimental Infrared Sppectrosocopy", Johm Wiley, West Sussex (2014)

[5] S. Nishizawa, M. W. Takeda M.Tani, Special issues, Proceedings of the International Conference on "Microwave and THz Technologies and Wireless Communications" Yerevan, Armenia (2012) 5

[6] Kurosawa, T. J. Phys. Soc. Jpn. Volume 16 (1961) 1298.

[7] Nishizawa, S., Suzuki,Y., Iwamoto,T., Takeda, M.W. and Tani, M., Special Review issues, Abstracts, The 6th International Conference on Advanced Vibrational Spectroscopy (ICAVS-11), P901, (2011) 31

THz radiation tapered dielectric antenna partially filling the metal waveguide

A. S. Nikoghosyan[1], H. P. Roeser[2], R. M. Martirosyan[1], H. S. Hakobyan[1], J. M. Chamberlain[3]

[1] *Yerevan State University, Alex Manoogian str. 1, 0025 Yerevan, Armenia*

[2] *Institute of Space Systems, University of Stuttgart, 70569 Stuttgart, Germany*

[3] *University of Durham, Durham DH1 3LE, United Kingdom*

Results of the effective generation of ultra-broadband terahertz (THz) radiation in the band 0.1-2 THz, via optical rectification of femtosecond laser pulses in a nonlinear tapered crystal, are presented. It is shown that by placing the $LiNbO_3$ crystal in free space, and in hollow waveguide, both the phase-matching and time- and spectral-features of the emitted THz field are changed. Several intense spectral regions whose frequency depends on the size of the $LiNbO_3$ crystal are observed. The finite-element method was employed to model and simulate the THz wave propagation in a $LiNbO_3$ tapered crystal in order to analyze experimental results, and to visualize how the form of the crystal influences the distribution of THz radiation both inside and outside the crystal in the near-field zone. It is shown that, during propagation of the THz radiation in the crystal-metallic waveguide system, both the mode structure and phase velocity are changed.

1. Introduction and Background

Tapered dielectric structures are widely used in designing components in millimeter, sub-millimeter (attenuator, phase shifter) and optical devices; and in near-field optical microscopy for concentration of the incident radiation [1]. Tapered waveguides have been proposed to guide and enhance THz radiation into a confined region in [2–5]. The adiabatic compression of tapered parallel-plate waveguides for sensitivity enhancement of waveguide THz time-domain spectroscopy was investigated in [6]. Super-focusing of terahertz waves below λ/250, using plasmonic tapered parallel-plate waveguides, was demonstrated in [7]. A tapered photoconductive THz field probe tip, with subwavelength spatial resolution, was used for imaging in [8]. Tapered dielectric rod antennas of rectangular cross section, in millimeter wave dielectric integrated circuits, were developed in [9]. A metal-dielectric pyramidal tip antenna, with pulsed terahertz radiation or continuous-wave radiation near 80 GHz was used for near-field imaging [10]. A frequency-independent spatial resolution of about 20 μm was obtained, corresponding to λ/200 at 80 GHz, which is only limited by the size of the facet terminating the tip. THz radiation in the tapered $LiNbO_3$ ribbon waveguide and laser-driven $LiNbO_3$ tapered THz antenna placed in free space were studied in [11, 12].

In this paper the experimental results of effective generation of ultra-broadband terahertz radiation, in the band 0.1-2 THz, via optical rectification of femtosecond laser pulses in a $LiNbO_3$ nonlinear crystal, partially filling the metal waveguide, are presented. To avoid THz wave reflections from the output surface of the crystal due to an impedance mismatch with free space, the output surface was cut at an angle. The tapered surface provides the broadband impedance-matching of the crystal with free space: this results in a greater intensity of THz radiation from the crystal compared with its rectangular form [2, 13]. The side ***b*** of a rectangular crystal of dimensions (a, b, L) is reduced linearly from width b to zero while keeping the broad side ***a*** fixed. The semi-angle of the taper is $\alpha=11^0$ ($E_{THz} \sim 1/\alpha$), and the distance between the waveguide aperture and taper aperture is L = 8 mm. To the authors' knowledge, no results have yet been reported concerning simulations and experiment with a tapered nonlinear crystal.

2. THz radiation generation in tapered crystal placed within a hollow waveguide or free space.

Optical excitation of broadband THz pulses was performed with 100 fs pulses from a Ti-Sapphire laser (λ=800 nm) [14]. The linearly polarized THz radiation is generated in TE-like mode (E^{x}_{nm}), due to the largest second-order nonlinear tensor element d_{33}. The temporal waveform of THz radiation from a $LiNbO_3$ crystal located in free space and amplitude spectrum after fast Fourier transformation (FFT) are shown in Fig.1(a, b).

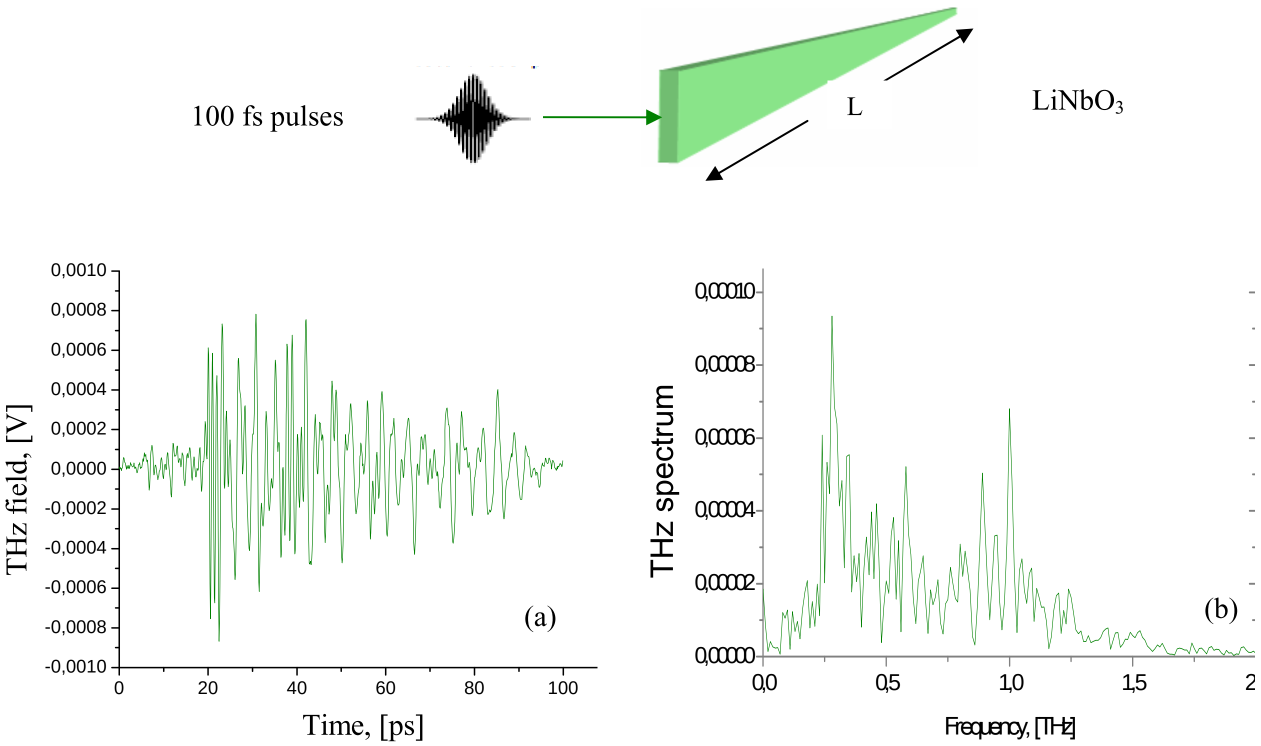

Fig.1. Temporal waveform (a) and (b) amplitude spectrum of the THz pulse generated by optical rectification of 100-fs laser pulses in a $LiNbO_3$ tapered broadband antenna located in free space.

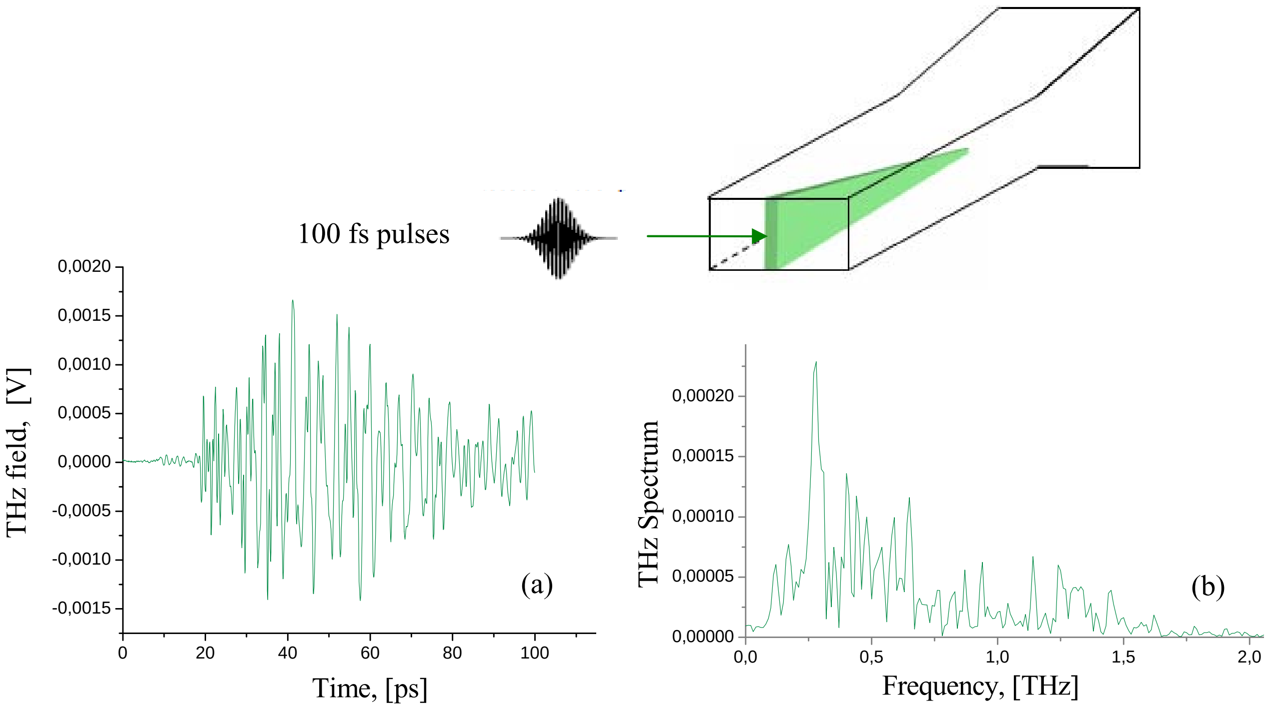

Fig.2. Temporal waveform (a) and (b) amplitude spectrum of the THz pulse from the $LiNbO_3$ tapered broadband antenna within hollow metallic waveguide. The $LiNbO_3$ antenna partially filled the metal waveguide.

Figure 2 shows temporal waveform and the amplitude spectrum of THz radiation when the same tapered $LiNbO_3$ crystal is placed in metal hollow waveguide.

The finite-element method was employed to model and simulate the THz wave propagation in a $LiNbO_3$ tapered crystal in order to analyze experimental results; and to visualize how the form of the crystal influences on the THz radiation both inside and outside the crystal in the near-field zone. The propagation of THz waves in the $LiNbO_3$ waveguide, with frequencies equal to the most intense spectral radiation lines in the THz pulse

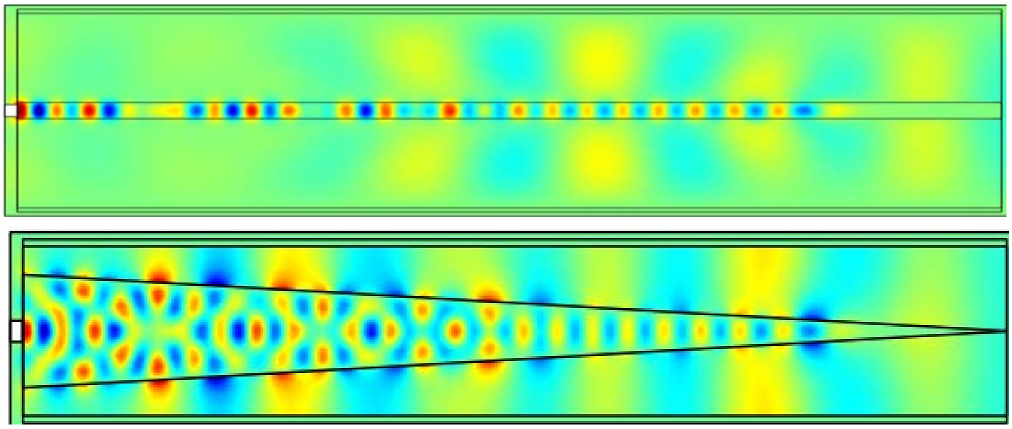

(a)

(b)

Fig.3. The distribution of THz electric field *E*x component with 240 GHz frequency propagating along the *z* axis, L= 8mm: (a) vertical view in (yz) plane; (b) lateral view in (xz) plane**.**

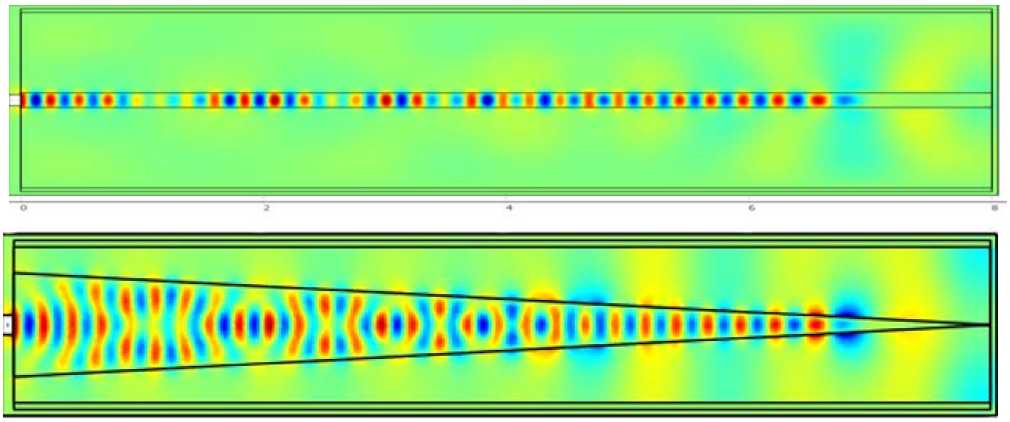

(a)

(b)

Fig.4. The distribution of THz electric field *E*x component with 270 GHz frequency propagating along the *z* axis, L= 8 mm: (a) vertical view in (yz) plane; (b) lateral view in (xz) plane.

spectra (at: 240 GHz, 270 GHz), were studied using the 'COMSOL Multiphysics' program. The distribution of the THz electric field component, propagating along the z axis of the $LiNbO_3$ antenna, at frequencies of 240 GHz and 270 GHz, are given in Fig.3 and Fig.4. Because of the continuously variable height ***b*** of the narrow wall of the waveguide, there is change of the critical frequency and the group velocity of THz wave. The THz wave passes from the multimode regime to single-mode; and the field is concentrated. It is shown that placing the $LiNbO_3$ crystals in free space, and in the hollow waveguide, both the phase-matching, time- and spectral-features of the emitted THz field are changed.

3. Conclusions

The full energy of the THz radiation propagating along straight lines parallel to the z-axis of the tapered crystal has both external (outside of the plate) and internal fields (Fig.3, 4). This type of full-field transmission allows efficient generation of THz radiation in a rectangular metallic waveguide partially filled by nonlinear rectangular crystal if, for given optical and THz frequencies, the collinear phase-matching condition is satisfied. The phase-matching condition can also allow the efficient generation of THz waves at other frequencies, by choosing the appropriate cross- section of the metallic waveguide and the thickness of the $LiNbO_3$ crystal plate [13, 14]. The phase-matching condition is achieved at high frequencies for smaller crystal thickness. The ratio (b/a) of the waveguide affects the propagation loss: for larger ratios, the propagation loss is less. The influence of diffraction on the THz wave propagation in the waveguide also depends on the size and form of the crystal. The tapered crystal antenna eliminates the diffraction of the THz wave which occurs in the crystal of rectangular shape.

Variation of the mode structure during propagation of the THz radiation in the tapered-shaped crystal is accompanied by a change of the phase and group velocities. More wave energy at a frequency of 270 GHz is distributed in the crystal than the energy of 240GHz waves. In the crystal, the low-frequency spectral components of the THz pulse travel less distance than the high-frequency spectral components. They are refracted at the interface between two media and spread in the air between the crystal and the metal waveguide.

Excitation of THz radiation in the tapered nonlinear $LiNbO_3$ antenna using an optical femtosecond laser pulse permits the resolution of problems connected with input/output coupling – mode matching and single mode propagation. Compression of the THz field along the tapered waveguide explains the result, noted experimentally, that the THz radiation (in the range 0.1- 3 THz) from a $LiNbO_3$ crystal, tapered at the end, exceeds the THz radiation obtained from a rectangular crystal by approximately five-ten times [13-15].

The demonstration of the enhanced THz radiation by a tapered $LiNbO_3$ antenna partially filling the metal waveguide opens a range of possibilities for THz spectroscopy of nanostructures or of molecules at low concentrations and near-field imaging [16]. Any nonlinear crystals with selected high non- linear second-order susceptibility, having low absorption coefficients and low dispersion, may also be used as antennas for ultra-high-speed electronic integrated circuits [17].

4. **References**

[1] M.I. Stockman, Phys. Rev. Lett. **93** (2004) 137404.
[2] A.S. Nikoghosyan, Sov. J. Quantum Electron.**18,** No.5 **(**1988) 624**.**
[3] A. Rusina, M. Durach, K.A Nelson and M.I Stockman, Opt. Express. **23** (2008) 18576–89.
[4] S-H. Kim, E.S. Lee Y.B .Ji and T.I .Jeon, Opt. Express. **18 (**2010) 1289–95.
[5] V.B Zon and B.A Zonm, *Phys. Rev.* A **84** (2011) 013816.
[6] J. Zhang and D. Grischkowsky, Appl. Phys. Lett. **86** (2005) 061109.
[7] H. Zhan, R. Mendis and D.M Mittleman, Opt. Express. **18** (2010) 9643–50.
[8] M. Wächter, Nagel M and H. Kurz, Appl. Phys. Lett. **95** (2009) 041112.
[9] S. Kobayashiand, R. Mittra, IEEE Transactions on Antennas and Propagation **30,** No.1 (1982) 54-58.
[10] N. Klein, P. Lahl, and U. Poppe, Journal of Applied Physics. **98**, (2005) 014910.
[11] A.S. Nikoghosyan, H.P. Roeser, R.M. Martirosyan, J.M.Chamberlain H.S.Hakobyan, A. Bohr, D.T. Haslam, J.S. López, and J.. Stepper. (2013). 38 International Conference on IRMMW – THz 2013, Th P3-04.
[12] A.S. Nikoghosyan. (2013). 38th International Conference on IRMMW – THz 2013, Th P3-15.
[13] E.M. Laziev, A.S Nikoghosyan, Proc. SPIE. Mode-Locked Lasers and Ultrafast Phenomena, **1842** (1992) 113, November 30.
[14] A.S Nikoghosyan, P.M. Martirosyan, A.A. Hakhoumian, J.M. Chamberlain, R.A. Dudley and N.N. Zinov'ev, Int. J. Electromagnetic Waves and Electronic Systems. **11**, No.4 (2006) 47-55.
[15] N.N. Zinov`ev, A.S. Nikoghosyan, R.A. Dudley and J.M. Chamberlain, Physical Reviev B, **76** (2007) 1235114–1235114-16.
[16] A.J. Huber, F. Keilmann, J. Wittborn, J. Aizpurua and R. Hillenbrand, Nano Lett**. 8**, No.11 (2008**)** 3766.
[17] J.W. Bowen, S. Hadjiloucas, B.M. Towlson, S.R. Davies, C.E. McIntosh, J.M. Chamberlain, R.E. Miles and R.D. Pollard, Electronics Letters (2006) 20th July.

Broadband THz Generation in LithiumNiobate Crystal by Step-Wise Phase Mask

G.K. Abgaryan, Yu.H. Avetisyan, A.H. Makaryan, V.R. Tadevosyan

Microwave Radiophysics and Telecommunications Dept., Yerevan State University, 1 Alex Manoogian, 0025 Yerevan, Armenia

Recently the narrowband THz radiation has been obtained by using binary phase masks (PM) placed in front of non linear crystal. How ever the u ltrashort (b roadband) TH z pu lses are ne cessary for many applications, such as time-domain spectroscopy, imaging etc.

In this paper a new method for efficient THz-pulses generation by OR in the single-domain lithium niobate crystal is presented. It's based on using the step-wise (SW) phase mask, which provide quasi-linear time delay of femtosecond laser pulses along cross-section of the optical beam.Every crystal layer (along direction of the laser beam propagation) radiate THz-pulses at the Cherenkov angle. Thanks to using of the phase mask these THz-pulses reach exit surface of the crystal simultaneously, thereby providing synchronous broadband radiation.

Theterahertz(THz) band(~ 0.1-10THz) of electromagnetic waveshaslargervariety ofapplications such as high-speed communication, molecular spectroscopy, security imagining, medical diagnosis, and many others [1,2]. However,the applicabilityofterahertzsourcesisstillcriticallydependentonthepoweravailable withcurrent technology, whichhaspromptedmuchresearchin developingcompact table-top THzsources.

The difference-frequency generation and optical rectification (OR) of femtosecond laser pulses are the widely used methods for the generation of narrowband radiation in THz range [3-5]. It was demonstrated [6] that application of wide-aperture beam in transversely patterned PPLN crystal leads to THz generation with $\Delta f \approx 17$ GHz bandwidth. The fs-laser beam propagates collinear to PPLN domain wall. THz-wave is generated in the direction determined by Cherenkov radiation angleθ_{ch}=acos(n_g / n_{THz}), where$n_g = c/u$is the group index, u- group velocity of the laser pulse, c- light velocity and n_{THz} is the refractive index at generated frequency. The periodical domain-inverted structure in the PPLN crystal serves to obtain a constructive interference of THz fields radiated by separate PPLN's domains. In the result will be obtained quasi-monochromatic THz radiation with a center frequency of F- (THz), determined by the spatial period Λ of the PPLN crystal.The main drawback of this method is that the periodical domain inverting technique is applicable only to the ferroelectric material, such as LiNbO3.Furthermore, generation frequency is predetermined by the spatial period of the domain-inverted structure and therefore it cannot be modified after the sample fabrication. To overcome this problem a scheme proposed where a virtual quasi-phase-matching structure in single-domain LiNbO3 crystal is formed by the crystal illumination through a phase mask or shadow mask.

Recently the narrowband THz radiation has been obtained by using binary phase masks (PM) placed in front of nonlinear crystal as seen in the Fig.1 [7].

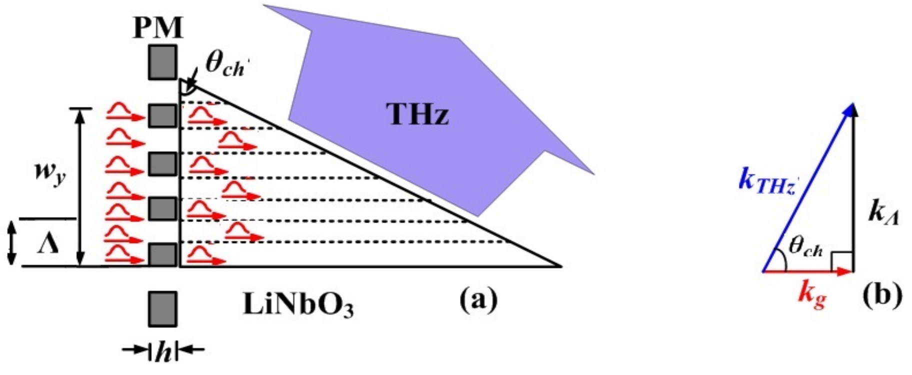

Fig. 1. (a) Schematic view for THz-wave generation in $LiNbO_3$ crystal with using a phase mask, (b) wave vector diagram.

Using this method, an eff ective phase matching for ge neration of THz radiati on in t he dir ection of the

Cherenkov angle can be obtained. TH z pulses em itted from different lay ers reach the edge of the cry stal alternately, yielding narrowband THz radiation.

However, the broadband THz pulses are nec essary for m any applications, such as ti me-domain spectroscopy, imaging and etc.

To obtain of broadband terahertz radiation is necessary that the THz pulses emitted from each layer of the crystal reached the exit su rface of the crystal simultaneously. This is equivalent to scenario i n which, TH z pulses radiated from each layer of crystal reaches to next layer at the same time as optical pulse. To provide this condition it is necessary to have slope am plitude front of optical beam . This would be achieved if the optical beam could be passed through the prismatic form phase mask, as shown in Fig. 3.

From quasi-phase-matching condition it is necessary that:

$$\frac{l_1}{c}n_m + \frac{l_2}{c}n_{op} = \frac{l_1}{c} + \frac{l_3}{c}n_{THz}, \qquad (1)$$

where $l_1 = AO = CD$, $l_2 = ON$, $l_3 = DN$, n_{op} is refractiv e index of cry stal for optical pulse, n_{THz} is refractive index of cry stal for THz waves and n_m is refractive index of m ask's medium for optical pulse.

From (1) follows that to obtain the desired slope of amplitude frontthe angle α must be equal to:

$$\alpha = \mathrm{arctg}\frac{n_{THz} - n_{op}\cos\theta_{Ch}}{(n_m - 1)\sin\theta_{Ch}}. \qquad (2)$$

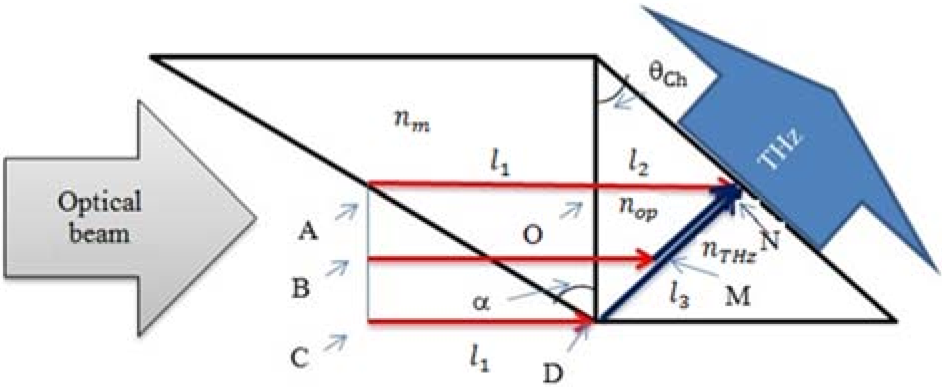

Fig. 2.Vector view of structure for generating broadband THz pulses.

Unfortunately, cannot be used a prism to obtain this structure, because of therefraction of optical beam.

To overcome this pr oblem we present a new method for efficient THz-pulses generation by OR in t he single-domain lithium niobate cry stal. It' s based on using the step-wise (SW) phase mask(Fig. 3), which provide quasi-linear ti me delay of femtosecond laser pulses along cross-section of the opti cal beam.Every crystal layers (along direction of the la ser beam propagation) radiate THz-pul ses at the Ch erenkov angle. Due to using of step-wise phase m askit is possible to have structure where these THz-pulses rea ch exit surface of the crystal simultaneously.

In Fig. 4 is shown position of laser pulses in the successive different of time moments into different layers of the phase mask and the nonlinear cry stal, necessary to obtain of sim ultaneous em ission of THz pulses from the output surface of the crystal.

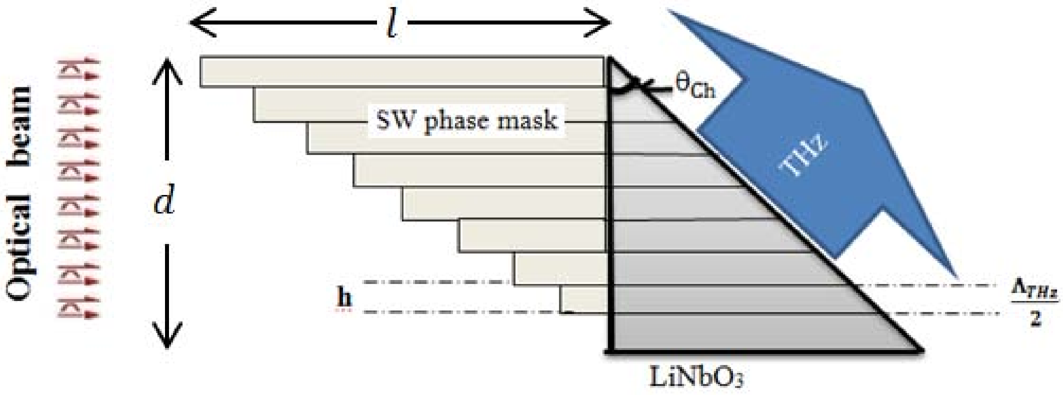

Fig. 3. Step-wise phase mask in front of crystal.

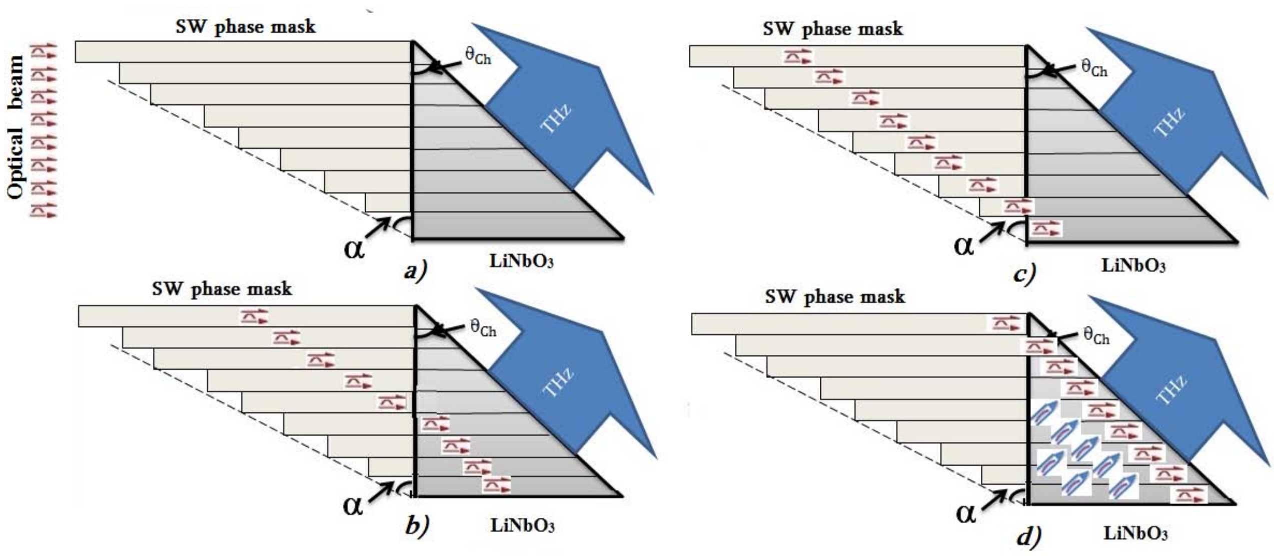

Fig. 4.The position of optical puls in different time. (a) The position of optical pulses in input of SW phase mask. (b) The formation of slope front of optical beam. (c) Deformation of aplitude front in nonliner crystal.(d) Position of pulses near exit surface.

To ensure the propagation of the laser beam in a mask without deflection, step size of the mask must be much larger than the wavelength of the laser radiation. However, the size of step cannot be larger approximately the half length of THz wave.It is necessary for phase-matching from different layers of crystal [7].In addition, to the laser pulse propagation on SW phase mask with low distortion before entering the nonlinear crystal, the mask length $l$is important. Using the expression (2) for the angle α, it is not difficult to determine mask length by its certain thickness $d$and refractive index$n_m$of its material.

$$l = d \cdot \mathrm{tg}\alpha = d \cdot \frac{n_{THz} - n_{op}\cos\theta_{\mathrm{Ch}}}{(n_m - 1)\sin\theta_{\mathrm{Ch}}} \quad (3)$$

Taking into account losses of THz radi ation i n a nonlinear crystal, there is no sense to use laser beams with transverse dimensions greater than 1 / β (β - loss coefficient), and therefore it is reasonable to limit the size *d* of the nonlinear crystal.When using crystalline quartz as a material of the mask and *d* = 1 mm we are getting for the mask len gth *l*≈ 8 mm.The length of mask can decrease by using a material with a high refractive index.

In order to avoid diffraction the layers of mask necessary to separate from each other using mirrors.

Conclusion

A new method for efficient THz-pulses generation by OR in the single- domain lithium niobate crystal was presented.It's based on using the step-wise phase mask, which provide quasi-linear time delay of femtosecond laser pulses along cross-section of the optical beam. Every crystal layers (along direction of the laser beam propagation) radiate THz-pulses at the Cherenkov angle. Due to using of the SW phase mask these THz-pulses reach exit surface of the crystal simultaneously, thus providing broadband THz radiation from the surface of the crystal.

References

1. J. Federici and L. Moeller, “Review of terahertz and subterahertz wireless communications,” J. Appl. Phys., **107**(11), (2010) 111101.
2. S. Yoshida, K. Suizu, E. Kato, Y. Nakagomi, Y. Ogawa, and K. Kawase, “A high-sensitivity terahertz sensing method using a metallic mesh with unique transmission properties,” J. Mol. Spectrosc. **256**(1), (2009) 146–151.
3. G. Kh. Kitaeva, “Terahertz generation by means of optical lasers,” Laser Phys. Lett. **5**(8), (2008) 559–576.
4. M. Tonouchi, “Cutting-edge terahertz technology,” Nat. Photonics **1**(2), (2007) 97–105.
5. Y.-S. Lee, *Principles of Terahertz Science and Technology* (Springer, 2009).
6. C. Zhang, Yu. Avetisyan, A. Glosser, I. Kawayama, H. Murakami, M. Tonouchi, “Bandwidth tunable THz wave generation in large-area periodically poled lithium niobate”, OPTICS EXPRESS **20** (8), (2012) 5784-5790.
7. Yu. Avetisyan, M.Tonouchi, "Terahertz generation in quasi-phase- matching structure formen by a phase mask", Optics Letters, Vol.**37**, No. 19, (2012) pp. 4155-4157.

THz emission from optically pumped GaP layer within 1D microcavity: numerical modelling by the method of single expression

H.V. Baghdasaryan[1], T.M. Knyazyan[1], T.T. Hovhannisyan[1], A.A. Hakhoumian[2], M. Marciniak[3,4]

[1] *State Engineering University of Armenia, Fiber Optics Communication Laboratory, 105 Terian str., Yerevan 0009, Armenia*
[2] *Institute of Radiophysics & Electronics, Armenian National Academy of Sciences Alikhanian brs. 1, Ashtarak 0203, Armenia*
[3] *National Institute of Telecommunications, Department of Transmission and Optical Technologies, 1 Szachowa Street, 04-894 Warsaw, Poland*
4 Kielce University of Technology, Faculty of Electrical Engineering, Automatics and Computer Science, Al. Tysiaclecia Panstwa Polskiego 7, 25-314 Kielce, Poland

Electromagnetic modelling of THz wave emission from GaP layer imbedded in a Fabry-Perot micro-resonator formed by DBR mirrors is performed. The frequency-domain modelling is carried out by the method of single expression. The modelling permits to reveal favourable structures for DBR mirrors, where layers adjacent to GaP layer have higher permittivities. By proper choose of DBR mirrors it is possible to attain an essential enhancement of THz radiation from optically pumped GaP layer.

1. Introduction

The terahertz (THz) band of electromagnetic (EM) waves is under high interest during last decades since a lot of new phenomena in matter – EM wave interaction in this range have been observed [1,2]. THz waves find applications in wireless communication, biological imaging systems, medical spectroscopy, security services, etc [1-5]. There are some possibilities to excite THz waves [1,2,6-8]. Our interest is directed to THz wave emission technique using non-linear optical effect in semiconductors via THz wave rectification [9,10]. THz waves are generated by using difference frequency generation via excitation of phonon-polaritons in semiconductor layer at high power optical wave incidence [11,12]. Insertion of a semiconductor layer in a Fabry-Perot micro-resonator permits to enhance THz wave emission [13,14]. It is important to note that Fabry-Perot micro-resonators considered in [13,14] consist only of one type of DBR mirrors, namely, DBRs where layers adjacent to non-linear semiconductor layer have a lower permittivity. However, as it was indicated before the best DBR mirror characteristics can be achieved by having outermost layers of high permittivity [15]. Then, it is expected to achieve an enhancement of THz wave emission by using DBRs having high permittivity layers outermost.

In the current work THz wave emission from semiconductor layer of GaP within the 1D Fabry-Perot microcavity formed by DBRs is numerically analysed by the method of single expression (MSE) [15-19]. GaP layer is pumped by an external optical radiation. DBRs consist of SiO_2/air quarter-wavelength bilayers. An influence of permittivity of outermost layers of DBRs operating in THz range on emission from semiconductor layer is investigated.

2. Method of single expression [15-19]

Here the backbone of the MSE for wave normal incidence on a multilayer structure is presented. From Maxwell's equations in 1D case the following Helmholtz equation can be obtained for linearly polarized complex electric field component $\dot{E}_x(z)$:

$$\frac{d^2\dot{E}_x(z)}{dz^2} + k_0^2\tilde{\varepsilon}(z)\,\dot{E}_x(z) = 0, \tag{1}$$

where $k_0 = \omega / c$ is the free space propagation constant, $\tilde{\varepsilon}(z) = \varepsilon'(z) + j\varepsilon''(z)$ is the complex permittivity of a medium. The essence of the MSE is presentation of a general solution of Helmholtz equation for electric field component $\dot{E}_x(z)$ in the special form of a single expression:

$$\dot{E}_x(z) = U(z)\cdot\exp\left(-jS(z)\right) , \tag{2}$$

instead of the traditional presentation as a sum of counter-propagating waves. Here U(z) and S(z) are real quantities describing the resulting electric field amplitude and phase, respectively. Time dependence $\exp\left(j\omega t\right)$ is assumed but suppressed throughout the analysis. Solution in the form (2) prevails upon the traditional approach of counter-propagating waves and is more general because it is not relied on the superposition principle. This form of solution describes all possible distributions in space of electric field amplitude, corresponding to propagating or evanescent waves in a medium of negative permittivity. It means that no preliminary assumptions concerning the Helmholtz equation's solution in different media are needed in the MSE. This gives advantages in investigation of wave interaction with any longitudinally non-uniform linear and intensity dependent non-linear media with the same ease and exactness.

Based on expression (2) the Helmholtz equation (1) is reformulated to the set of first order differential equations regarding the electric field amplitude $U(z)$, its spatial derivative $Y(z)$ and a quantity $P(z)$ - proportional to the power flow density (Poynting vector) in a medium:

$$\begin{cases} \dfrac{dU(z)}{d(k_0 z)} = Y(z) \\ \dfrac{dY(z)}{d(k_0 z)} = \dfrac{P^2(z)}{U^3(z)} - \varepsilon'(z)\cdot U(z) \\ \dfrac{dP(z)}{d(k_0 z)} = \varepsilon''(z)\cdot U^2(z) \end{cases} , \tag{3}$$

where $P(z) = U^2(z)\dfrac{dS(z)}{d(k_0 z)}$. The sign of $\varepsilon'(z)$ can take either positive or negative describing relevant electromagnetic features of dielectric or metal (plasma), correspondingly. The sign of $\varepsilon''(z)$ indicates loss or gain in a medium.

The set of differential equations (3) is integrated numerically starting from the non-illuminated side of a multilayer structure, where only one outgoing travelling wave is supposed. Initial values for integration are obtained from the boundary conditions of electrodynamics at the non-illuminated side of the structure. Numerical integration of the set (3) goes step by step towards the illuminated side of the structure taking into account an actual value of structure's permittivity for the given coordinate at each step of integration. In the process of integration any variable of the set (3) is possible to record in order to have full information regarding distributions of electric field amplitude, its derivative and power flow density inside and outside of a structure. At the borders between constituting layers of a multilayer structure ordinary boundary conditions of electrodynamics bring to the continuity of $U(z)$, $Y(z)$ and $P(z)$. From the boundary conditions of electrodynamics at the illuminated side of the structure the amplitude of incident field E_{inc} and power reflection coefficient R are restored at the end of calculation. The power transmission coefficient is obtained as the ratio of transmitted power to the incident one.

2. Numerical analysis of THz Fabry-Perot micro-resonator with GaP spacer

For electromagnetic modelling the structure presented in Fig.1 has been considered.

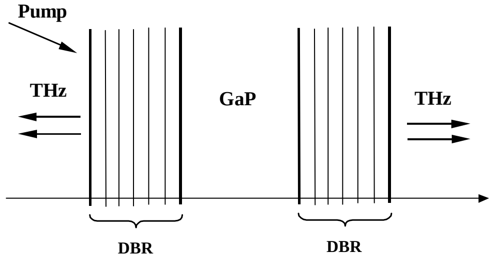

Fig.1 Fabry-Perot structure under modelling

The considered structure is created by DBRs from odd or even number of alternating layers of high (H) and low (L) permittivities. Modelling has been done for THz frequency range as: $\Delta f = 0.25 - 1.25$ THz or at wavelengths: $\Delta\lambda_0 = 240\ \mu\text{m} - 1200\ \mu\text{m}$. DBR's layer of high permittivity is taken from SiO_2 ($\varepsilon_{SiO_2} = 4.4944$ at the central wavelength $\lambda_{0centr} = 620\ \mu\text{m}$ [20]) and has the thickness $d_{SiO_2} = \dfrac{\lambda_{0centr}}{4\sqrt{\varepsilon_{SiO_2}}}$ = 73.1132 μm. Layer of low permittivity is an air with $\varepsilon = 1$ and the thickness $d_{air} = \dfrac{\lambda_{0centr}}{4} = 155\ \mu\text{m}$. Permittivity of non-linear semiconductor GaP at the central wavelength $\lambda_{0centr} = 620\ \mu\text{m}$ is $\varepsilon_{GaP} = 11.02$ [21]. Thickness of GaP layer is chosen as $d_{GaP} = 100\ \mu\text{m}$, which is approximately the half-wavelength.

It is important to choose proper structure of DBRs with high Q-factor providing THz field localization in active semiconductor layer favourable for its emission. The favourable DBR structure is one starting and ending by layers of high permittivity [15]. In this case the higher reflection coefficient is possible to attain at reduced number of alternating quarter-wavelength layers.

Numerical modelling has been done for the structure with two types of DBRs: with layers of low permittivity adjacent to GaP layer [structure $(HL)^m$-GaP-$(LH)^m$] and high permittivity [structure $(LH)^m$-GaP-$(HL)^m$]. Here layers of high and low permittivity are indicated by letters H and L, m is the number of bilayers in DBR, which in our case is four. The considered structures are presented in Fig. 2 where at both sides of the structure is the free space.

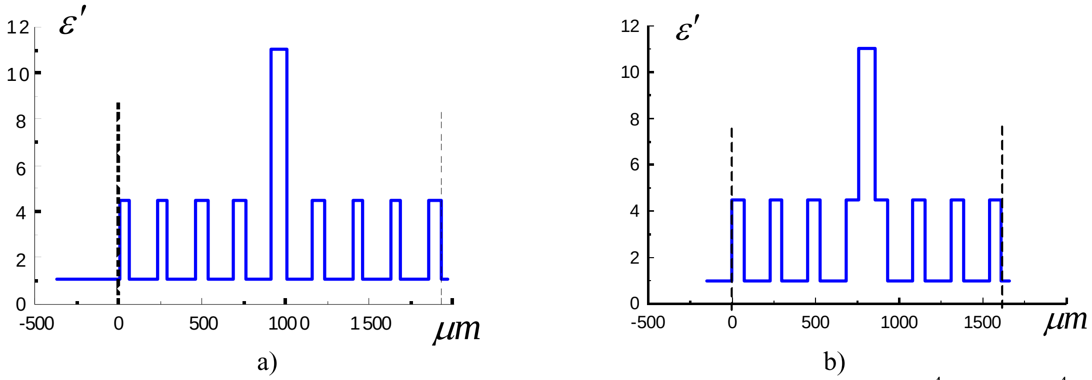

Fig. 2. Distribution of permittivities in two types of Fabry-Perot structures: a) structure $(HL)^4$-GaP-$(LH)^4$ where adjacent to GaP layers of DBRs have low permittivity and b) structure $(LH)^4$-GaP-$(HL)^4$ where adjacent to GaP layers of DBRs have high permittivity

The relevant transmission spectra for both types of the structures are presented in Fig. 3.

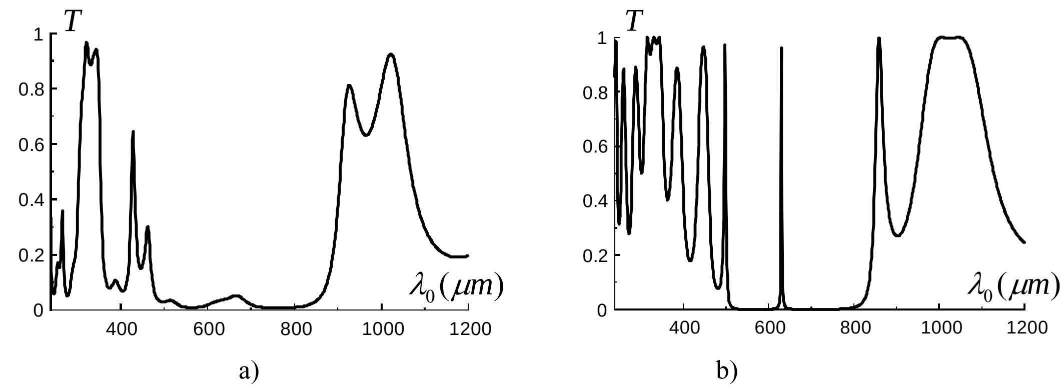

Fig. 3. Transmission spectra of Fabry-Perot micro-resonators: a) for the structure $(HL)^4$-GaP-$(LH)^4$ and b) for the structure $(LH)^4$-GaP-$(HL)^4$. Forbidden range of wavelengths is connected to the forbidden region of DBRs

In the spectrum presented in Fig. 3b it is clearly visible the narrow transmission peak located within the forbidden range, that is the well known Fabry-Perot resonant peak stipulated by half-wavelength GaP spacer located between two highly reflective DBR mirrors. In the spectrum presented in Fig. 3a the peak in the middle of forbidden range is very small that can be explained by low reflection coefficient of DBRs starting and ending by layers of low permittivity.

External optical pump brings to THz waves excitation in a non-linear semiconductor GaP layer. In electromagnetic modelling generation of THz waves in a non-linear semiconductor GaP layer can be described by the positive value of imaginary part of its permittivity. To model THz waves generation different positive values for imaginary part of GaP's permittivity have been applied.

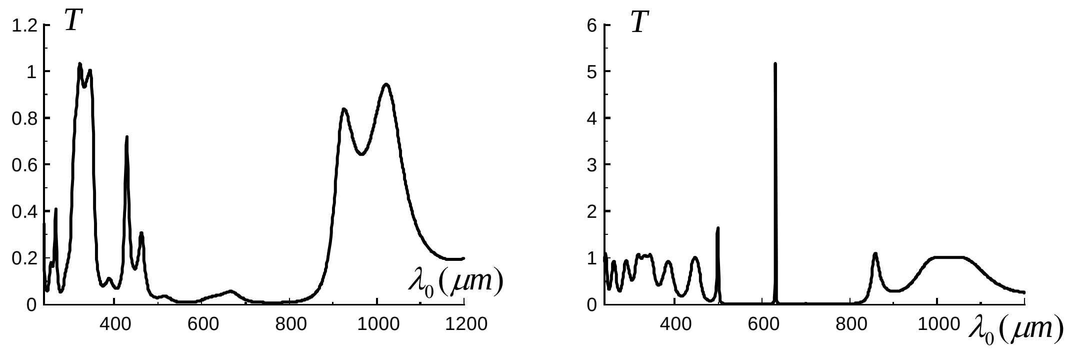

a) b)

Fig. 4. Transmission spectra of Fabry-Perot micro-resonators when GaP is pumped by external optical radiation: a) the structure $(HL)^4$-GaP-$(LH)^4$ and b) the structure $(LH)^4$-GaP-$(HL)^4$. In both structures imaginary part of GaP permittivity is taken as $\varepsilon''_{GaP} = 0.07$

As it follows from Fig. 4 for the same value of positive imaginary part of GaP permittivity there is clear indication of strong enhancement of transmitted wave for the structure where adjacent layers of DBRs are of high permittivity (Fig. 4b). Modest transmission enhancement is observed for unfavourable structure (Fig. 4a). To understand the physics of this difference it is useful to observe the electric field distribution within the structures. In Fig. 5 relevant field distributions of THz wave for both structures at the central wavelength are presented.

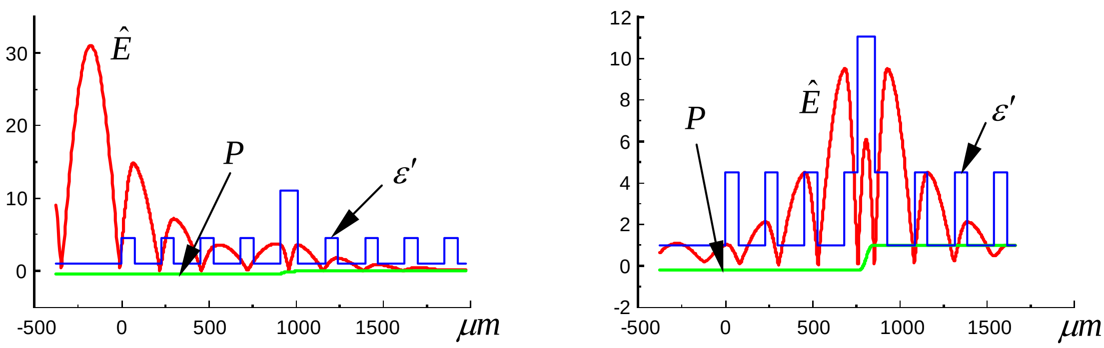

a) b)

Fig. 5. Distributions of electric field amplitude $\hat{E}$ and power flow density P within the Fabry–Perot structures at central wavelengths, where transmission peaks are observed in Fig. 4

As it follows from Fig. 5, in favourable structure (Fig. 5b) DBR mirrors create resonant field distribution with local maximum in GaP layer. The last is responsible for efficient THz wave emission. Power flow density has positive value in the right part of the structure and negative – in the left side of the structure. This is a real indication on emission out of the structure. In the structure, where GaP is covered by layers of DBRs of low permittivity adjoined to GaP (Fig. 5a) THz field distribution has its local minimum in GaP and for that reason a small change of power flow is indicated in Fig. 4.

3. Conclusion

Performed electromagnetic analysis permits to indicate the favourable Fabry-Perot micro-resonator structure for rectification of THz waves at optical pumping of non-linear semiconductor layer, serving as micro-resonator's spacer. In favourable DBR-GaP-DBR structure layers adjacent to GaP should be of high permittivity. Thus, to have highly reflective DBR mirrors in Fabry-Perot micro-resonator it is important to locate DBRs' layers of high permittivity just adjoining to spacer.

Distributions of electric field amplitude and power flow obtained by electromagnetic modelling permit to explain optical characteristics of Fabry-Perot structures with different DBR mirrors depending on the starting layers adjoining to the spacer.

Though the electromagnetic analysis has been done for specific materials of DBRs and spacer, the same analysis possible to perform for any optically active materials by advanced method of single expression.

4. Acknowledgements

This work was supported by State Committee Science MES RA, in the frame of the research project № SCS 13-2J204. H.V. Baghdasaryan, T.M. Knyazyan, T.T. Hovhannisyan and M. Marciniak are thankful to COST TU1208 members for fruitful discussions.

5. References

[1] M. Perenzoni, D. J. Paul, Physics and Applications of Terahertz Radiation (Springer, London, 2013).

[2] A. Rostami, H. Rasooli, H. Baghban, Terahertz Technology: Fundamentals and Applications (Springer, 2011).

[3] J.F. Federici, B. Schulkin, F. Huang, D. Gary, R. Barat, F. Oliveira, D. Zimdars, THz imaging and sensing for security applications — explosives, weapons and drugs, Semicond. Sci. Technol. **20** (2005) S266–S280.

[4] M.J. Fitch, R. Osiander, Terahertz Waves for Communications and Sensing, Johns Hopkins APL Technical Digest **25** (2004) 348-355.

[5] B. Ferguson, Xi-Cheng Zhang, Materials for terahertz science and Technology, Nature materials **1**, (2002) 26-33.

[6] D. Dragoman, M. Dragoman, Terahertz fields and applications (Review), Progress in Quantum Electronics **28** (2004) 1–66.

[7] Yu.H. Avetisyan, A.A. Hakhoumian, H.K. Melikyan, V.R. Tatevosyan, H. Ito, Y.Sasaki, A new scheme of THz-wave difference-frequency generation in highly-absorbing cubic nonlinear crystal, CLEO 2005, CWM4.

[8] A.S. Nikoghosyan, E.M. Laziev, R.M. Martirosyan, A.A. Hakhoumian, J.M. Chamberlain, R.A. Dudley, N.N. Zinov'ev, Terahertz Generation In Waveguide Partially Loaded With Nonlinear Crystal, ICONO 2005, Proc. of SPIE **6257** (2006) 62570O-1.

[9] K.Sakai, ed., Terahertz Optoelectronics (Springer, 2005).

[10] M. Hangyo, T. Nagashima, S. Nashima, Spectroscopy by pulsed terahertz radiation, Meas. Sci. Techn., **13** (2002) 1727-1738.

[11] T. Tanabe, K. Suto, J. Nishizawa, , K. Saito , and T. Kimura, Frequency-tunable terahertz wave generation via excitation of phonon-polaritons in GaP," J. Phys. D, Appl. Phys., **36 (**2003) 953–957.

[12] K. Suto, T. Sasaki, T. Tanabe, K. Saito, J. Nishizawa, and M. Ito, GaP THz wave generator and THz spectrometer using Cr:Forsterite lasers, Rev. Sci. Instrum., **76** (2005) 123109 1.

[13] H. Shirai, K. Ishii, H. Miyagawa, Sh. Koshiba, S. Nakanishi, N. Tsurumachi, Efficient terahertz emission, detection, and ultrafast switching using one-dimensional photonic crystal microcavity, J. Opt. Soc. Am. B, **31 (**2014), 1393-1401.

[14] H. Shirai, E. Kishimoto, T. Kokuhata, H. Miyagawa, Sh. Koshiba, Sh. Nakanishi, H. Itoh, M. Hangyo, T. G. Kim, N. Tsurumachi, Enhancement and suppression of terahertz emission by a Fabry–Perot cavity structure with a nonlinear optical crystal, Applied Optics **48** (2009), 6934-6939.

[15] H.V. Baghdasaryan, T.M. Knyazyan, T.H. Baghdasaryan, B. Witzigmann, and F. Roemer, Absorption loss influence on optical characteristics of multilayer distributed Bragg reflector: wavelength-scale analysis by the method of single expression, Opto−Electronics Review, **18** (2010). 438–445.

[16] H.V. Baghdasaryan, Method of backward calculation, in the book: *Photonic Devices for Telecommunications: how to model and measure*/ Editor G. Guekos (Springer-Verlag, 1999) 56-65.

[17] H.V. Baghdasaryan, T.M. Knyazyan. Problem of plane EM wave self-action in multilayer structure: An exact solution, Optical and Quantum Electronics, **31** (1999)1059-1072.
[18] H.V. Baghdasaryan and T.M. Knyazyan, Modelling of strongly nonlinear sinusoidal Bragg gratings by the Method of Single Expression, Optical and Quantum Electronics, 32 (2000) 869-883.
[19] H.V. Baghdasaryan, Basics of the Method of Single Expression: New Approach for Solving Boundary Problems in Classical Electrodynamics (Chartaraget, Yerevan, 2013).
[20] E.V. Loewenstein, D.R. Smith, R.L. Morgan, Optical Constants of Far Infrared Materials.2: Crystalline Solids, Applied Optics, **12** (1973) 398-406.
[21] I.D. Vugmeyster, J.F. Whitaker, R. Merlin, GaP based terahertz time-domain spectrometer optimized for the 5-8 THz range, Appl. Phys. Lett., **101** (2012) 181101-1 -181101-4.

Method of determination the femtosecond fiber laser pulse central wavelength phase offset in respect to the envelope

A.A. Hakhoumian, G.D. Hovhannisyan

Institute of Radiophysics and Electronics, Alikhanian Brothers str. 1, 0203 Ashtarak, Armenia

The method of determination of carrier–envelope phase shift for a femtosecond fiber laser pulse in the infra-red range (λ_0=1.98 μm) is offered. It is shown that the proposed method can be used for phase synchronization of femtosecond fiber lasers. The method is based on difference frequency radiation generation by mutually orthogonally linearly polarized pulses, which interacted with periodically polled GaSe crystal. It's considered the difference frequency radiation generation in the 8μm-12μm range by laser pulses with 30fs durations at 1.98μm central wavelength and with 100MV/m electrical field amplitudes.

1. Introduction

For transfer of high stability of optical standards in a radio range femtosecond lasers with passive synchronization are used, and the first optical hours of new generation were realized in [1, 2] by means of the Ti:Sp–femtosecond laser (λ=0.8 μm). The radiation of such lasers consists of "comb" equidistantly spectral components with frequencies of $f_m = m \cdot f_{rep} + f_0$, m $\sim 10^6$–an integer, f_{rep}–repetition frequency of pulses, f_0–shift of a comb respect to zero frequency. Frequencies of f_{rep} and f_0 lie in a radio range. On base of this relation, it is possible to establish direct phase-coherent coupling between optical and radio ranges by control of two parameters of a comb of f_{rep} and f_0 [2]. If frequency of the optical reference standard oscillator f_{st} less than a width of a "comb", the scheme of optical hours can be simplified essentially, by elimination the f_0 due to "comb" spectral range transformation in a nonlinear crystal [3, 4,5]. In this work a method of determination of carrier–envelope phase shift for an femtosecond fiber laser pulse is proposed. It is considered the pulses with central wavelength λ_0=1.98 μm. It is shown that the proposed method can be used for phase synchronization of two fiber lasers when frequency of beating between lasers is equal to frequency of the reference oscillator. The offered method is based on generation of radiation at difference frequency (DF) by mutually orthogonal and linearly polarized laser pulses, which interacted with periodically polled GaSe crystal. It is considered generation of DF radiation in 8μm–12μm range by the pulses with 30fs duration at 1.98 μm central wavelengths and 100 MV/m electrical field amplitudes.

2. Mathematical description of few cycle mutually orthogonal and linearly polarized pulses interaction with the periodically polled GaSe crystal

Let us consider a case where linearly polarized laser pulses with plain wavefronts and mutually orthogonal planes of polarization E_x and E_y are propagating along the *z*-axis, coinciding with the optical Z ([001]) axis, in an anisotropic crystal of periodically polled GaSe (fig. 1).

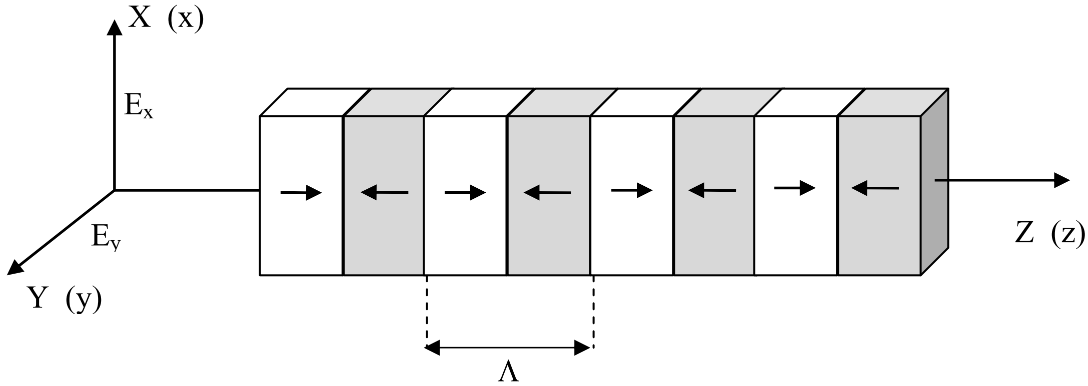

Figure 1. Periodically polled GaSe crystal structure.

As seen from fig. 1 E_x pulse is polarized along a crystal X axis ([100]) and E_y– along Y ([010]). So the E_x and E_y pulses correspond to waves with ordinary polarization. The corresponding wave equations may be represented in the form

$$\frac{\partial^2 E_{x,(y)}}{\partial z^2} - \frac{1}{c^2}\frac{\partial^2 E_{x,(y)}}{\partial t^2} = \frac{4\pi}{c^2}\frac{\partial^2 P_{L,x,(L,y)}}{\partial t^2} + \frac{4\pi}{c^2}\frac{\partial^2 P_{NL,x,(NL,y)}}{\partial t^2} \qquad (1)$$

where $P_{L,x}$ and $P_{L,y}$ are, respectively, linear and nonlinear parts of the medium polarization, P_{NLxz} and $P_{NL,y}$ are, respectively, nonlinear parts of the medium polarization. The linear response of the medium to the *x*- and *y*-polarizations is determined by the expressions

$$P_{Lx,Ly}(\omega) = \varepsilon_0 \chi_o^{(1)}(\omega) E_{x,y}(\omega) \qquad (2)$$

where ε0 is the vacuum dielectric constant and $\chi_o^{(1)}(\omega)$ is the linear susceptibility of the medium for ordinary polarized wave. According to [6] the linear susceptibility of GaSe for ordinary polarized wave can in the spectral range 0.622 μm–20μm at T=293K temperature be presented as

$$\chi_x^{(1)}(\omega) = \chi_y^{(1)}(\omega) = \chi_o^{(1)}(\omega) = n_o^2(\omega) - 1 = a_0 + \frac{b_0\omega^2}{(2\pi c)^2 - c_0\cdot\omega^2} - d_0\frac{(2\pi c)^2}{\omega^2} \qquad (3)$$

where $a_o = 6.4437$, $b_o = 0.3757, c_o = 0.1260$, $d_o = 0.00154$. In the chosen geometry the nonlinear polarization of the medium caused by quadratic susceptibility may in the quasistatic approximation be written as

$$P_{xNL}(t) = -2\cdot\varepsilon_0\cdot d_{22}\cdot E_x(t)\cdot E_y(t) \quad (4a), \qquad P_{yNL}(t) = -\varepsilon_0\cdot d_{22}\cdot E_x^2(t) + \varepsilon_0\cdot d_{22}\cdot E_y^2(t) \quad (4b),$$

where $d_{22} = 54$ pm/V is the coefficient of nonlinear susceptibility of GaSe crystal. It's considered the case when spectra of both laser and difference frequency radiation lie below the electronic resonance frequencies, but above ionic resonance frequencies of the medium. Under these conditions the refractive index in (3) is represented as a Taylor series [7, 8]. In periodic domain structures the periodic change in sign of quadratic susceptibility occurs at interfaces between domains, which produce conditions for constructive interference of signal and idle waves in bulk crystals with arbitrary dispersion characteristics. The nonlinear susceptibility may in this case be written as [7]

$$d_{22}(z) = d_{22}\sum_{m=0}^{M}\frac{\sin(2\pi z[2m+1]/\Lambda)}{(2m+1)}\frac{\sin[\pi(m+1)/M]}{\pi(m+1)/M} \qquad (5)$$

where Λ is the period of the domain structure, m = 0, 1, 2, M, and M is the number of terms in the sum (5). Obviously, the nonlinear part of medium polarization will also be a periodic function of the z-coordinate. The value of the period should be determined by the energy and momentum conservation laws

$$\frac{1}{\lambda_p} = \frac{1}{\lambda_s} + \frac{1}{\lambda_{IR}}, \frac{n_o(\lambda_p)}{\lambda_p} = \frac{n_o(\lambda_s)}{\lambda_s} + \frac{n_o(\lambda_{IR})}{\lambda_{IR}} + \frac{1}{\Lambda} \qquad (6)$$

with λ_p and λ_s being, respectively, the short and the long wavelengths, within the spectral band of the few-cycle laser pulse, whose interaction in quadratically nonlinear medium may lead to difference frequency (λ_{IR}) generation. In the periodic domain structures the quasi-phase matching is realized for all pairs λ_p and λ_s spectral components satisfying the condition (6). In particular, for a laser pulse with Gaussian time profile, duration τ_0 = 30fs, central wavelength λ_0 = 1.98 μm, and the spectrum width $\Delta\nu = \sqrt{2\ln 2}/\pi\tau_0$ = 24.99 THz (Δλ= 329 nanometers), spectral components from 1.813μm to 2.144μm are within the spectral bandwidth. In fig. 2 (a) is shown dependence of the period Λ vs. wavelength of DF radiation for a case when short and long-wavelength spectral a component's are λ_p= λ_o–0.82Δλ = 1.71μ m and λ_s = λ_o + 0.03 Δλ = 1.99μ m respectively. In fig. 2 (b) is shown dependence of the period Λ vs. wavelength of DF radiation for a case when short and long-wavelength spectral a component's are λ_p = λ_o–0.82Δλ = 1.71μm and λ_s = λ_o + 0.58Δλ = 2.17μm respectively.

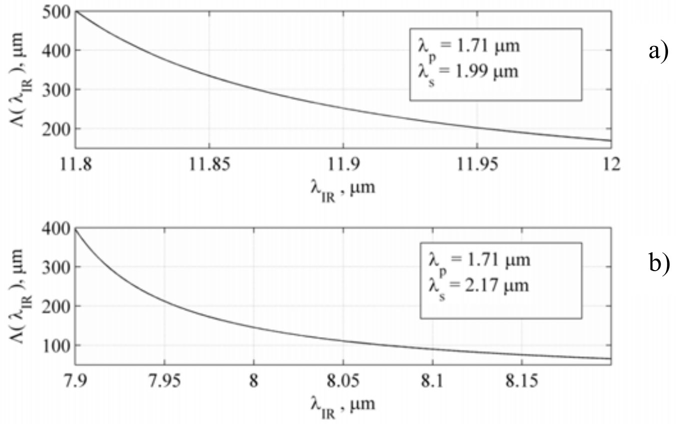

Figure 2. Dependence of the period Λ vs. wavelength of DF radiation for a case when short and long-wavelength spectral a component's are $\lambda_p = \lambda_o - 0.82\Delta\lambda = 1.71\mu m$ and $\lambda_s = \lambda_o + 0.03\Delta\lambda = 1.99\mu m$ respectively–2(a), and when short and long-wavelength spectral a component's are $\lambda_p = \lambda_o - 0.82\Delta\lambda = 1.71\mu m$ and $\lambda_s = \lambda_o + 0.58\Delta\lambda = 2.17\mu m$ respectively 2(b).

The numerical integration of the equations (1) in the approximation of unidirectional waves were realized by the method of lines [8, 9]. For numerical integration of the system of equations (1) we choose the boundary conditions

$$\Phi_x(\xi=0,\eta)=\Phi_{x0}\exp\left(-\eta^2/\tau_p^2\right)\cos(\eta),\quad \Phi_y(\xi=0,\eta)=\Phi_{y0}\exp\left(-\eta^2/\tau_p^2\right)\cos(\eta-\delta\varphi) \tag{7}$$

where $2\tau_p$ = 30fs, (λ_0 = 1.98 µm) and $\Phi_{y0} = \Phi_{x0} = \Phi_0$ are the normalized initial values of the amplitudes of *y*- and *x*- polarized pulses respectively , $\delta\varphi$– phase difference between the interacted pulses. The maximum values of initial values of amplitudes are equal to 100 MV/m. For numerical simulation we choose the period of the regular domain structure Λ = 304µm and the length of nonlinear crystal $11\cdot\Lambda$ = 3.344mm. According to fig. 2 at Λ = 304µm it take place the quasi-phase matched generation of DF radiation at 12 µm and at Λ = 152µm take place the quasi-phase matched generation of DF radiation at 8µm . The relative error in computation was chosen to be 10^{-6}.

3. Computation Results and Discussion

Here we describe the results of numerical integration of system of the (1) equations for the different values of phase difference between the interacted pulses by the method of lines. For the study of dependences of spectral distributions of the mutually orthogonal and linearly -polarized DF radiation pulses at the crystal exit on phase difference $\delta\varphi$ during numerical integration the spectral filtration of electric fields of *x*- and *y*- polarized radiation pulses by means of the low pass filter was carried out. The transmission function of used low pass filter can be presented as

$$H(f)=1/\left(1+(f/f_c)^4\right) \tag{8}$$

where f_c = 85.71THz low pass filter cut frequency, which correspond to the wavelength $\lambda_{of\,c} = c/f_c$ = 3.5µm. According to (4 a), (7) for *x*- and *y*- polarized interacted pulses with equal amplitudes the spectrum of medium nonlinear polarization at $\delta\varphi = 0$ can be presented as $\tilde{P}_{xNL}(\omega)\propto\tilde{F}(\omega)+\tilde{F}(\omega-2\omega_0)$, $\tilde{P}_{yNL}(\omega)=0$ and at $\delta\varphi=\pi/2$ as $\tilde{P}_{xNL}(\omega)\propto\tilde{F}(\omega-2\omega_0)$, $\tilde{P}_{yNL}(\omega)\propto\tilde{F}(\omega-2\omega_0)$, where $\tilde{F}(\omega)$– initial pulse (7) envelope Fourier transformation. So, after spectral filtration at $\delta\varphi$= 0 the spectrum of generated in the medium *x*-polarized pulse, will be concentrated near *dc* and the spectrum of generated in the medium y- polarized pulse will tend to zero. At $\delta\varphi=\pi/2$ the spectrums of *x*- and *y*- polarized pulses will be zero. On fig. 3 temporal profiles of *x*- and *y*- polarized interacted pulses on the exit of periodically polled GaSe crystal with the period equal to 304µm and number of periods equal to 11 are shown at $\delta\varphi$= 0, $\delta\varphi$= 30° and $\delta\varphi$= 60°.

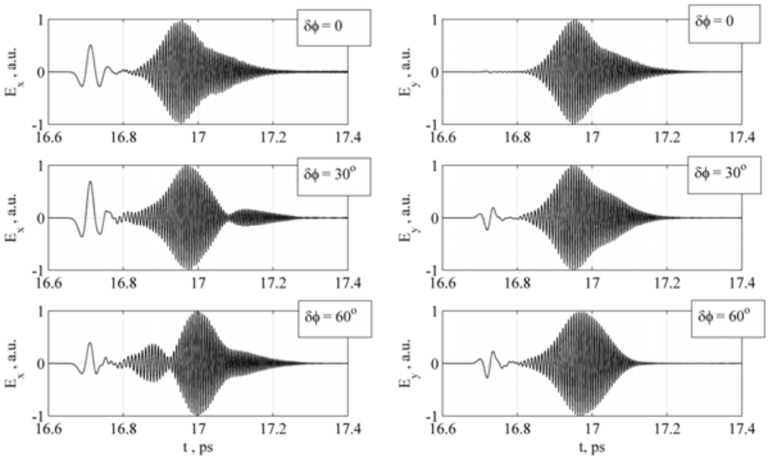

Figure 3. Temporal profiles of *x*- and *y*- polarized interacted pulses on the exit of periodically polled GaSe crystal structure with the period equal to 304μm and number of periods equal to 11 are shown at δφ= 0, δφ= 30^o and δφ= 60^o respectively.

According to simulation results and as seen from fig. 3 the maximum of absolute value of electric field of *y*-polarized DF radiation pulse at δφ = 0 forms 0.03-th part from a pump pulse maximum, at δφ= 30^o–the 0.21th part from a maximum and at δφ= 60^o–0.23-th parts and when δφ changing from 0 to 60 ^{o} the maximum of absolute value of electric field of *x*- polarized DF radiation pulse decrease from the 0.5th part of a maximum to the 0.4th part. In the fig. 4 are shown dependences of normalized spectral densities of *x*- and *y*- polarized pulses at the crystal exit from wavelength (fig. 4a, 4b, 4c) at the phase differences' δφ = 0, δφ = 30^o and δφ = 60^o. In fig. 4 also shown dependences of normalized spectral densities of *x*- and *y*- polarized pulses at the crystal exit from wavelength after spectral filtration in the 4μm -18μm spectral range (fig. 4d, 4e, 4f).

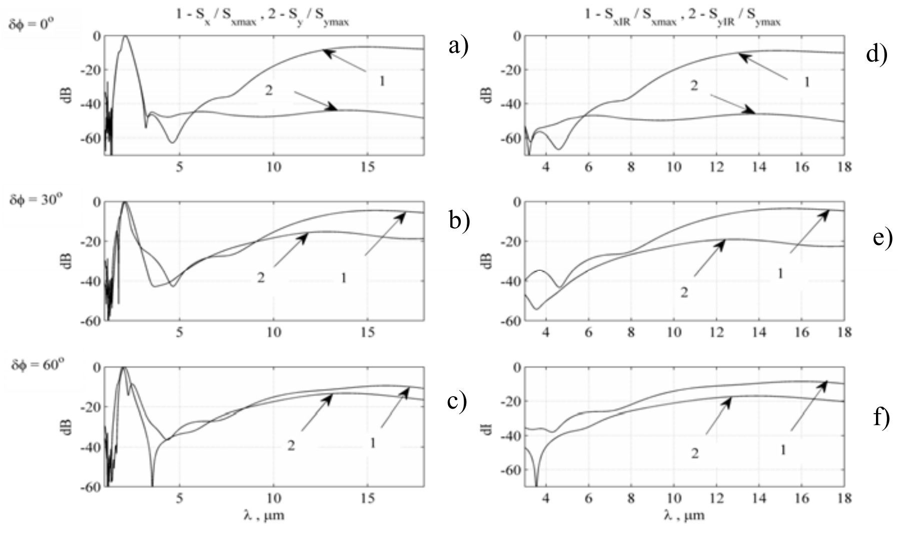

Figure 4. Dependencies of normalized spectral densities of *x*- and *y*- polarized pulses at the crystal exit from wavelength (4a, 4b, 4c) at the phase differences' δφ = 0, δφ= 30^o and δφ= 60^o. Dependencies of normalized spectral densities of *x*- and *y*- polarized pulses at the crystal exit from wavelength after spectral filtration in the 4μm-18μm spectral range (4d, 4e, 4f).

As seen from figure the amplitude of *x*- polarized pulse is more than amplitude of *y*- polarized pulse and, particularly, when phase difference increase from 0^o to 60^o the difference between pulses spectrum levels in decibels at 12μm wavelength decrease from -34dB to -9dB. The 12μm wavelength of DF radiation corresponds to that wavelength at which take place the quasi-phase matched interaction. In fig. 5 are shown dependencies of spectral densities of *x*- and *y*- polarized DF radiation pulses at low pass filter exit normalized to the maximum of *x*- and *y*- polarized radiations taken before radiation spectral filtration – S_{xIR}/S_{xmax} and S_{yIR}/S_{ymax}. As seen from fig. 5 when the phase difference between interacted pulses vary from -45° to 0° and from 0° to 45° between phase difference and normalized spectral densities of *x*- and *y*- polarized pulses appears a relationship.

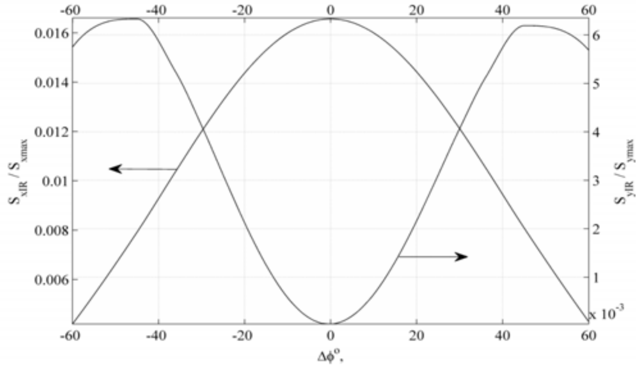

Figure 5. Dependencies of spectral densities of *x*- and *y*- polarized DF radiation pulses at low pass filter exit normalized to the maximum of *x* and *y* polarized radiations taken before spectral radiation – S_{xIR}/S_{xmax} and S_{yIR}/S_{ymax}.

According to fig.5 the efficiency of DF radiation generation for *x*- polarized wave reaches $16.3\cdot10^{-3}$ and $6.12\cdot10^{-3}$ for *y*- polarized wave. In fig. 6 is shown dependence of the wavelength Λ_{xIR} (Λ_{yIR}) corresponding to the maximum of the spectral density of *x*- (*y*-) polarized DF radiation vs. phase difference between interacted initial pulses. According to fig. 6 when $|\delta\varphi|$ vary from 0° to 45° DF central wavelength Λ_{xIR} vary from 15.1μm to 16μm.

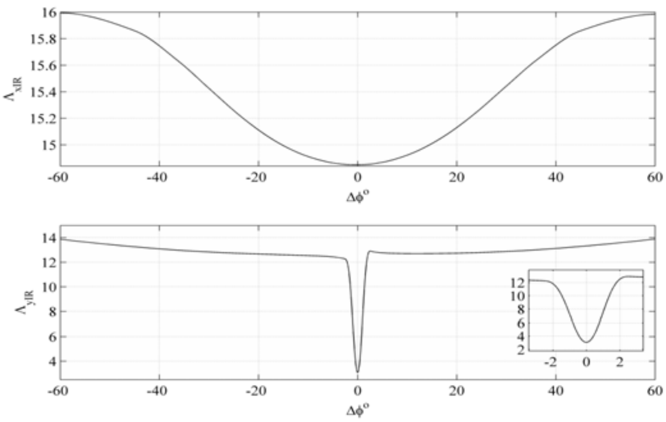

Figure 6. Dependence of the wavelength Λ_{xIR} (Λ_{yIR}) corresponding to the maximum of the spectral

In other words, there is a relationship between Λ_{xIR} and phase difference when the latest vary from -45° to 0° and from 0° to 45°. When $\delta\varphi$ vary from 0° to 2° the Λ_{yIR} vary from 3.093μm to 12.56μm and when $\delta\varphi$ vary from -2° to 0° the Λ_{yIR} vary from 11.84μm to 3.093μm. When $|\delta\varphi|$ vary from 2° to 60° Λ_{yIR} increase and become equal to 13.88 μm. So, by "mixing" of *x*- polarized DF radiation pulse in the spectral range 15.1 μm – 16 μm with the radiation of single-frequency quantum-cascade laser based on a bound-to-continuum transition working at room -temperature at 16μm [10] it's possible to establish a direct phase-coherent relationship between the laser central frequency and DF radiation frequency where the beat frequency will be located in the radiofrequency range and will be proportional to the initial pump pulse phase difference. The proposed method, particularly, can be used for the phase synchronization of two femtosecond fiber lasers one of which is frequency stabilized [11, 12]. As seen from abovementioned, when $|\delta\varphi|\leq2°$ for establishment of direct phase-coherent relationship between frequencies of the synchronized laser and reference stabilized laser, by using the *y*- polarized DF radiation, as the reference source will necessary use a tunable source with 3μm – 16μm tuning range. In fig. 7 presented dependencies of *x*- and *y*- polarized radiations spectral densities S_x / S_{xmax} and S_y / S_{ymax} , normalized to the maximum values, taken at the input of low pass filter from the phase difference. As seen from the figure and as follows from the simulation results when the phase difference vary from - 45 ° to 45 ° there is established the unique relationship between spectral densities of radiations and the phase difference. Wherein, for negative phase differences normalized spectral density for *y*- polarized radiation is more than the spectral density for *x*- polarized radiation and for positive phase differences vice versa.

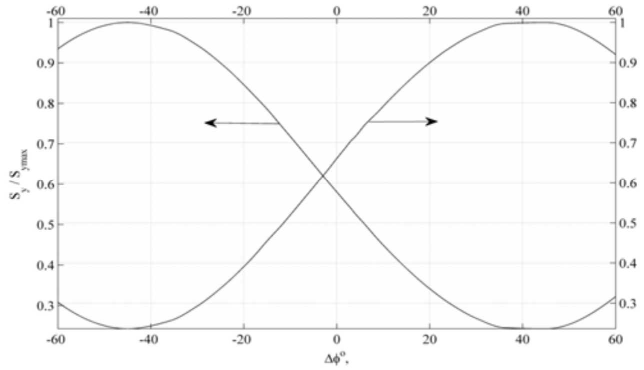

Figure 7. Dependencies of *x*- and *y*- polarized radiations spectral densities S_x / S_{xmax} and S_y / S_{ymax} , normalized to the maximum values, taken at the input of low pass filter from the phase difference.

So, the additional registration of the ratio of spectral densities of *x*- and *y*- polarized radiations before filtration process will allow to get the unique relationship between spectral densities of radiations and the phase difference up to sign in all range of phase difference variation from -45° to 45°.

4. Conclusion

In this work is shown that by DF radiation generation due to nonlinear interaction of mutually orthogonal and linearly polarized pump pulses with periodically polled GaSe crystal it's obtained the direct phase-coherent relationship between the carrier–envelope phase shift of the synchronized pump pulse and the DF radiation frequency. The proposed method, particularly, can be used for the phase synchronization of two femtosecond fiber lasers one of which is frequency stabilized.

5. Reference

[1] M.A. Gubin, A.S. Shelkovnikov, E.V. Kovalchuk, D.D. Krylova, et. all., in Proc. 1999 Joint Meeting EFTF/IEEE IFCS, Besancon, France, (1999), 710.

[2] Leo Hollberg, Chris W. Oates, E. Anne Curtis, Eugene N. Ivanov, Scott A. Diddams, Thomas Udem, Hugh G. Robinson, James C. Bergquist, Robert J. Rafac, Wayne M. Itano, Robert E. Drullinger, David J. Wineland, IEEE Journalof QE, 37, 12, (2001), 1502.

[3] M. Zimmerman, C. Gohle, R. Holzwarth, T. Udem, T.W. Hansch, Opt. Lett., 29, 310 (2004), 310.

[4] S. Foreman, A. Marian, J. Ye, E. Petrukhin, M. Gubin, O. Mucke, F. Wong, E. Ippen, F. Kaertner, Opt. Lett., 30, 570 (2005), 570.

[5] B.R. Washbum, S.A. Diddams, N.R. Newbury, J.W. Nicholson, M.F. Yan, C.G. Jorgensen, Opt. Lett., 29, 3, (2004), 250.

[6] David N. Nikogosyan, Nonlinear Optical Crystals: A Complete Survey, Springer, (2005), 108.

[7] A.A. Hakhoumian,, G.D. Hohvannisyan, NAN of Armenia, Physicist, 49, 2, (2014), 99.

[8] D.L. Hovhannisyan, V.O. Chaltykyan, G.D. Hovhannisyan, A.S. Martirosyan, K.A. Hovhannisyan, NAN of Armenia, Physicist, 46, 2, (2011), 91.

[9] W.E. Schiesser, G.W. Griffiths, A Compendium of Partial Differential Equation Models, Method of Lines Analysis with Matlab. Cambridge University Press, New York, (2009).

[10] M. Rochat, D. Hofstetter, M. Beck, J. Faist, Appl. Phys. Lett. 79, (2001), 4271.

[11] I.I.Korel, V.I.Denisov, B. N. Nyushkov, V. S. Pivtsov, Proceedings of MIPT, 6, 1, (2014), 7.

[12] M.A.Gubin, A.N.Kireev, A.V.Konyashchenko, P.G.Kryukov, A.V.Tausenev, D.A.Tyurikov,

Mobile VHF radar

M.V. Markosyan, V.H.Avetisyan, A.A.Hovhannisyan, A.A.Manukyan, M.A.Mosesov, A.K.Aharonyan, A.I.Petrosyan, G.Z.Sughyan, A.Y.Saryan, R.M.Petrosyan, E.A.Harutyunyan, K.A.Ghazaryan
Yerevan Telecommunication Research Institute,Armenia
mark@yetri.am

Operation of the radar in up-to-day conditions requires improving its performance characteristics. On the other hand, modern capability of detection and destruction of the radars require strongly the increasing of its mobility, which is determined by the radar folding time from operation mode to transport state and vice versa. For VHF radars, which are objects with bulky antenna system, at first place there is a need to develop the antenna system, the design of which is mainly determined by the above mentioned characteristics. The designing of antenna system is divided in two areas: radio technical and design-engineering. The purpose of this work is the representation of researches and solutions directed to improve the radio-technical parameters of the VHF radar antenna system and its mobility by reducing the transition time of radar from the transport state to operational readiness and back.

Antenna array radiating elements

Mentioned above two areas are closely linked with each other, since the choice of antenna array radiators and its excitation system (in terms of its shape and dimensions) largely determines the choice of design and engineering solutions for the optimal layout of whole antenna system to the transport state. The problem of increasing of radar mobility [1] connects initially with the choice of array radiating elements. However, its choice is determined by the directional properties of the antenna array, its directional pattern (DP), gain (G), side lobe levels (SLL) etc.

From the comparative analysis of different radiators of antenna array, calculation and simulation results (using the software package FEKO 5.5) it was revealed that the most acceptable values has circular antenna, developed and designed in the likeness of a micro-strip antenna proposed in [2]. The parameters were as follows: the relative frequency broadband is about 20 ... 25%,VSWR $\leq$ 1,6, G $\approx$ 8,5 ... 9 dB at the reflector size 1,2 m $\times$ 1,2 m and a longitudinal dimension 0 2 m along the axis of radiation. The general view and operation construction of circular antenna with linear horizontal polarization are shown in fig. 1.For reducing of weight and windage of antenna its reflector and a metal disc are made as a metallic grids and circular radiator is perforated. The weight of the antenna is about 6.5 kg. For improvement of antenna ground-based measurements and minimization of errors at determination of antenna pattern and gain (corresponding to conditions of free space) from ground-based measurements in conditions of specular reflections from the Earth the problem of reception in that conditions was researched theoretically [3].

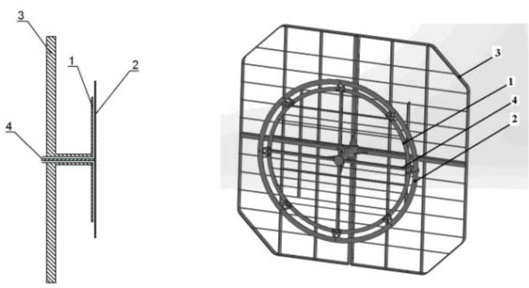

a) b)

Fig. 1. Circular antenna (a) and general view (b): 1 –metal disc, 2 –circular antenna, 3 - reflector, 4 –feeding coaxial cable

In the result, the equivalent model of two-beam reception with virtual receiving antennas was proposed. On this basis the methodology for determination of required parameters from measurements with the help of two identical antennas method was developed [4]. The optimal configuration of arranging of two identical circular antennas was selected and measurements for determination of required DP and G have been carried out [5].

Antenna array

The antenna array made mockup contains 24 circular radiators in two line arrows of radiators with 12 pieces in each row. The dimensions of the mockup are: horizontal - 17.7 m, vertical - 3.6 m. The excitation of radiators in each row is in-phase. The relative smallness of the radiator longitudinal size (0.2 m) along the radiation axis has been used for it folding of antenna array to the transport state. Phase excitation of upper row radiators relatively to lower row radiators is shifted on 90^0. The excitation amplitudes of both rows are the same, but in each row the amplitude distribution changes from the central radiator to the edge radiator by the Dolph-Chebyshev law for providing of low SLL of the array. The strip design dividers of low power level (Wilkinson dividers) and high power level dividers on coaxial circular bridge have been developed for implementation of the calculated amplitude distribution.

Preliminary measurements of DP and G of antenna array mockup in reception mode have been carried out by the on-site measurement method on the airfield territory. A helicopter МИ8-МТВwas used as the aircraft. For reducing the measurement errors, caused by the influence of frame and propeller of helicopter on DP of measuring radiating half- wave vibrator, the special device has been proposed which was mounted on the bottom of the helicopter[6].The realized device is a new radiating system "vibrator-box." The box has a special design and includes an electromagnetic energy absorber. Relatively low weight of box and pointed at the ends of its shape practically no effect on the aerodynamic characteristics of the helicopter. The photo of made mockup of array, mounted on the flying field for the measurements is shown on fig. 2.

The measurement method, which differs by cheapness of measurement process, has been developed and employed for determination of the array parameters [7]. The method is based on a special program of vertical and horizontal flights of the helicopter.

At the measurements of the elevation DP the binding of coordinates (altitude above ground and the horizontal distance from the array) of helicopter during flights with samples of relevant signal registrations, carried out by the ground measurement equipment ,has been implemented by the synchronization of operation of GPS navigators of the helicopter and the operator of the ground measurement equipment.

Azimuth (horizontal) DP in the direction of maximum of elevation DP lobes was measured by rotating of the array on 360^0 around its vertical axis at the hung position of the helicopter. The measurement samples were taken over a discrete 0.5^0 given by n-coder of rotation drive. Measurement results of DP by the elevation and azimuth planes are shown on fig. 3 and 4.

Fig. 2. Antenna array mockup on flying field

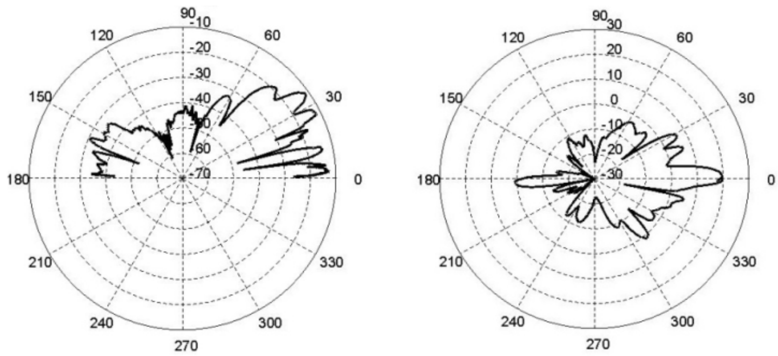

a) b)

Fig. 3. a) Elevation DP measured at horizontal flights (angle sector$1^0 ... 179^0$);
b) Azimuth DP measured in direction of the first lobe maximum of elevation DP at hung helicopter

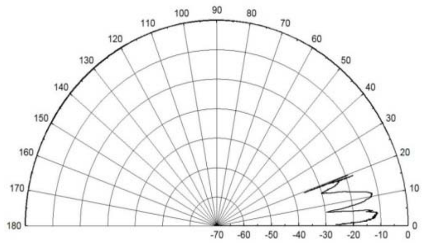

Fig 4. Vertical (elevation) DP in angle sector 0... 20^0, measured at vertical flight of helicopter

Operating antenna system.

Antenna system of radar includes:

- antenna array;
- antenna–mast equipment;
- energy supply and automatic control subsystem

The whole antenna system is mounted on a three-axis platform of container of standard trailer. The photo of the antenna system in operation mode on the carrier support of the container is shown on fig.5, and the photo of the antenna system in the folded state is shown on fig. 6.

Adjustable by height supports of platform create enough arms, providing sustainable and stable state of the antenna system at the presence of weight and wind loads during operation. The horizontalizing of the platform is provided by special hardware and software subsystem of supports regulation by height. At transport state the radar antenna system is in container having a length of 13,62m, width 2,55m and 2,48m height. Since the horizontal size of the antenna array is 17,7m [8], the total horizontal frame is in the form of two composite folding frames with length 8,8m each, that is enough for arrangement of array in folded state along the length of the container.

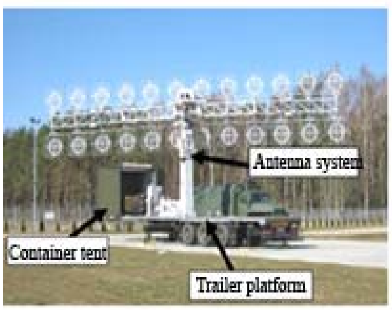

Fig. 5. Antenna system on platform Fig. 6. Antenna system in folded state

Design of array

The main units of the array are the central section and two folding frames of array radiators. Frames are fixed to the sides of the central section by the pin hinges. These main units are shown on fig. 7.

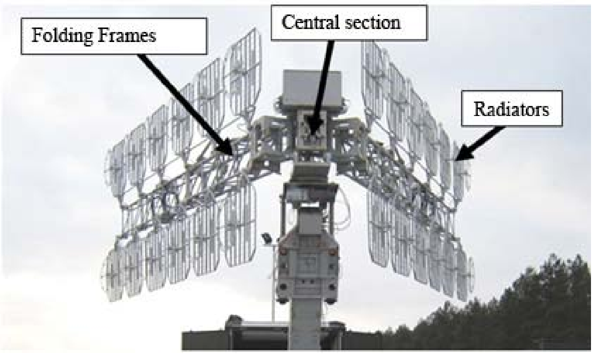

Fig. 7. Antenna array

Antenna-mast equipment.

The main units of antenna-mast equipment are shown on fig.8.

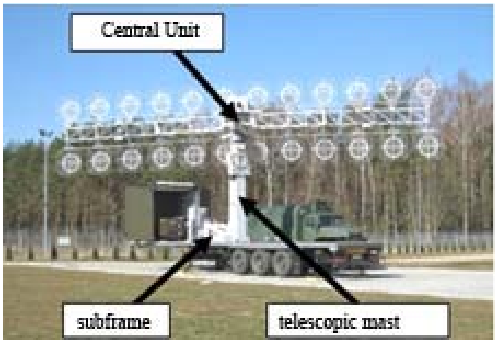

Fig. 8. Main units of antenna-mast equipment

That are a base-subframe, telescopic mast, two corresponding actuator for mounting the telescopic mast from transport horizontal state to operating vertical state and vice versa, and the central unit, which is under the central section of the array. The drive of sliding inner tube of telescopic mast provides arrangement of array symmetry center on heights from 6.5m to 9.7m with 0.8m discrete.

Energy supply and automatic control subsystem

It contains two diesel generator of autonomous power (operating and standby) and a lower electro-cabinet for control and check, placed on the platform of the container. This subsystem contains also the upper electro-cabinet for control and check mounted on the upper part of the array central section (fig. 9). The control structure provides two modes - automatic mode by the "one button" principle and the manual mode, allows automatic control of each mechanism.

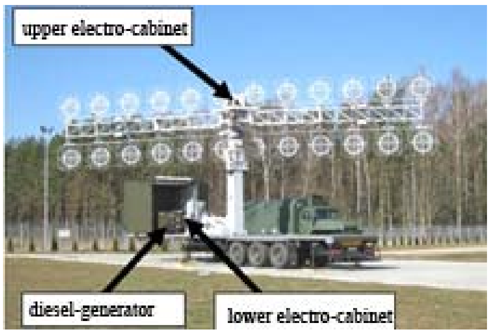

Fig. 9. The main units of energy supply and automatic control

Stages of automatic folding and unfolding of antenna system

The automatic unfolding of the ante nna sy stem c onsists of 6-consecutive s tages with its final following states:

- first stage - tent of trailer container is stacked and the supports of container platform is at operating position;
- second stage - telescopic mast of antenna system is raised and it has an angle of 60° relative to the horizon;
- third stage – array radiators are unfolded to the operating vertical position;
- four stage – array frames are unfolded to the operating position and are fixed;
- five stage - telescopic mast is raised to the working vertical position;
- fix stage - the array is raised to the desired height and azimuth rotation of array is started;

Stages of automatic folding are carried out in inverse order.

Total amount of time of unfolding (folding) is 15min.

Abstract of the antenna system structural design

The modeling and calculations were made for all main constructions with the goal of selection of materials and to deter mine the robustness and stiffness under real operating conditions - weight loads, loads at transportation and wind loads at wind speeds up to 40m / s, at t he thickness of the icing to 10mm and the azimuth rotation of the array with speed 6 rpm /s. The calculations were made by the progra m Solid Works 2012, Solid Works Flow Simulation CO-ADAPCO STAR -CCM +.

The required powers of electromechanical actuators and its support points have been determined during the simulation of whole system. Designed and manufactured actuators are supplied by the ball-screw assemblies, servo m otors, feedback sensors, tem perature sensors a nd brakes. The actuators have high efficiency a nd provide high-precision motions with control program [9].

As a result , realized radar has bett er performance characteristics, the possibilit y of its use at the reduced number of staff and significantly increased mobility which is most essentially.

References

[1] Մ.Վ. Մարկոսյան ՀՕՊ-ի զորքերի տարաշարժունության մեծացման տեսանկյունից արդիական ռադարների ստեղծման որոշ հարցեր // Հանդես «Հայկականբանակ».– 2013.- 1-2 (75-76).- էջ 45-49:

[2] Արտոնագիր № 2508Ա, ՀՀ: Միկրոշերտային անտենա / Ա.Սահակյան, Մ.Մարկոսյան, Ա.Հովհաննիսյան: - Առաջնության թվ. 18.01.2011: Հրապարակման թվ. 25.04.2011:

[3] В.Г. Аветисян. Эквивалентная модель двухлучевого приема при зеркальном отражении от Земли // Вестник ГИУА. Серия "Информационные технологии, электроника, радиотехника".– 2013. Вып.16 , №2.- с.82-92.

[4] V.H. Avetisyan, A.A .Sargsyan. On the measurements of UHF antenna parameters by two antennas technique // Proc. Intern. Conf. on Microwave and THz Technologies and Wireless Communication. - Yerevan, Armenia, October 16-17, 2012.- pp.149-155.

[5] M.V. Markosyan, V.H. Avetisyan, A.A. Hovhannisyan, A.K. Aharonyan et al. The measurements of parameters of UHF antenna array radiators // Proc. Intern. Conf. on Microwave and THz Technologies and Wireless Communication.-Yerevan, Armenia, October 16-17, 2012. - pp. 156-161.

[6] Արտոնագիր № 2803Ա, ՀՀ: Շրջաթիռ եղանակով վերգետնյա անտենայի պարամետրերի չափման սարք / Մ.Մարկոսյան, Վ.Ավետիսյան, Ա.Հովհաննիսյան, Ա.Ահարոնյան, Ա.Սարգսյան: - Առաջնության թվ. 23.05.2013: Հրապարակման թվ. 29.01.2014:

[7] Արտոնագիր № 2814Ա, ՀՀ: Ուղղաթիռի միջոցով վերգետնյա անտենայի ուղղորդվածության դիագրամի չափման եղանակ / Մ. Մարկոսյան, Վ. Ավետիսյան, Ա. Նիկողոսյան,Ա. Սարգսյան: - Առաջնության թվ. 23.05.2013: Հրապարակման թվ. 25.02.2014:

[8] М.В. Маркосян, В.Г. Аветисян, А.А. Оганесян, А.К. Агаронян, А.И. Петросян, Г.З. Сугян. Модернизация антенной системы радиолокационной станции диапазона метровых волн // Известия НАН и ГИУ Армении, серия технических наук, т. 67,2, 2014, с.173-182

[9] И.А. Биргер и др. Расчет на прочность деталей машин: Справочник / И.А.Биргер, Б.Ф.Шорр, Г.Б. Иосилевич.-4-е изд., перераб. и доп - М.: Машиностроение,1993.-640 с.

Civil engineering applications of Ground Penetrating Radar: research activities in COST Action TU1208

Hovik Baghdasaryan[1], Marian Marciniak[2,3], Lara Pajewski[4]

[1] *State Engineering University of Armenia, Yerevan, Armenia*
[2] *National Institute of Telecommunications, Warsaw, Poland,*
[3] *Kielce University of Technology, Kielce, Poland*
[4] *"Roma Tre" University, Department of Engineering, Rome, Italy*

Ground Penetrating Radar (GPR) is a non-destructive imaging technique that can be effectively used for advanced inspection of composite structures and for diagnostics affecting the whole life-cycle of civil engineering works. GPR provides high-resolution images of the investigated structures through wide-band electromagnetic waves. It is possible to identify four main areas that have to be addressed in order to promote a wider use of this technology in civil engineering: a) design of innovative systems; b) development of data-processing algorithms and analysis tools, for the interpretation of experimental data; c) integration of GPR with other non-destructive methods; d) development of guidelines and training of end users. The COST Action TU1208 "Civil Engineering Applications of Ground Penetrating Radar" is running since 2013 and this paper will present its main activities and objectives, as well as the results achieved until now.

1. Introduction

Ground Penetrating Radar (GPR) is a safe, advanced, non-destructive and non-invasive sensing technique that can be successfully employed for sub-surface investigation, inspection of natural or manmade complex structures, and diagnostics affecting the whole life-cycle of civil engineering works [1-3]. In particular, it can be effectively used for the surveying of roads, bridges, tunnels, railways, dams, the detection of underground cavities, and the inspection of modern and historical buildings. It can also be used to map the buried utilities in a region, enabling rapid installation of a new plant with minimum disruption and damage to the existing one; gas, water, sewage, electricity, telephone, and cable utilities can be localised. Furthermore, with GPR it is possible to perform detailed inspection of reinforced concrete, to locate steel reinforcing bars and pre/post-tensioned stressing ducts. Quality control of pre-cast concrete structures, such as deck beams, can be carried out. Deterioration and delamination on bridge decks can be mapped; zones of termite attack or fungal decay in wooden bridge beams can be found. An analysis of geological structures can be made with GPR, for the mapping of soil, rock or fill layers, in geotechnical investigations and for foundation design.

GPR provides high-resolution images of the investigated structures through wide-band electromagnetic waves. Penetration and resolution depend primarily on the transmitting frequency of the equipment, the antenna characteristics, the electrical properties of the ground or surveyed material, and the contrasting electrical properties of the targets with respect to the surrounding medium. The centre frequency of GPR antennas typically ranges from 25 MHz to 4 GHz. Generally, there is a direct relationship between the chosen frequency and the resolution that can be obtained; conversely, there is an inverse relationship between frequency and penetration depth. High frequencies can therefore be used to detect small and shallow targets, whereas low frequencies allow the sensing of larger and deeper targets. GPR works best in dry ground environments, but can also give good results in wet, saturated materials; it does not work well in saline conditions, in high-conductivity media and through dense clays limiting the signal penetration.

Different approaches can be employed in the processing of collected GPR data, aiming at transforming radar data into user-usable images of the subsurface. The procedures depend on the site and equipment characteristics, how data were collected and the aims of the survey. The classical strategy usually includes band-pass filtering to remove unwanted high or low frequency noise, stacking to improve the signal-to-noise ratio, moving-average filtering to smooth out jitter between wave fronts, background-noise removal to remove clutter bands parallel to the air-soil interface, de-convolution filtering to remove multiple echoes or signal ringing, and the application of a migration algorithm to focus the diffractions from buried objects to their true positions. By means of gain adjustment algorithms, signal strengths in different regions are often balanced and corrections are applied for variations in surface topographic elevation.

Once data have been processed, they still have to be analysed. This is a challenging problem, since interpretation of GPR radargrams is typically non-intuitive and considerable expertise is needed. In the presence of a complex scenario, accurate electromagnetic-modelling software is a fundamental tool for the validation of data interpretation. It can be employed for the characterisation of scenarios, as a preliminary step that precedes a survey, or to gain ‘a posteriori’ a better understanding of measured data. Moreover, it can help to identify signatures generated by uncommon or composite targets. A forward electromagnetic solver can be used to perform repeated evaluations of the scattered field due to known targets, in combination with optimization techniques, in order to estimate – through comparison with measured data – the physics and geometry of the region investigated by the GPR.

It is possible to identify four main areas, in GPR field, that have to be addressed in order to promote the use of this technology in the civil engineering. These are: a) design of novel systems; b) development of electromagnetic modelling, imaging, inversion and data-processing tools for the interpretation of GPR results; c) integrate GPR with other non-destructive testing (NDT) methods; d) contribute to the development of new standards and guidelines and to training of end users, that will help to increase the awareness of operators.

In this framework, the COST (European COoperation in Science and Technology) Action TU1208 "Civil Engineering Applications of Ground Penetrating Radar" is carrying out its activities. The main objective of the Action is to exchange and increase scientific-technical knowledge and experience of GPR techniques in civil engineering, whilst promoting a more effective use of this safe and non-destructive technique. The Action involves 27 COST Countries (Austria, Belgium, Croatia, Czech Republic, Denmark, Estonia, Finland, France, former Yugoslav Republic of Macedonia, Germany, Greece, Ireland, Latvia, Malta, Netherlands, Norway, Poland, Portugal, Romania, Serbia, Slovakia, Slovenia, Spain, Switzerland, Turkey, United Kingdom), a COST Cooperating State (Israel), 3 COST Near Neighbour Countries (Armenia, Egypt, Ukraine), and 4 COST International Partner Countries (Australia, Hong Kong Special Administrative Region of the People's Republic of China, Rwanda, U.S.A.). University researchers, software developers, civil and electronic engineers, archaeologists, geophysics experts, non-destructive testing equipment designers and producers, end users from private companies and stakeholders from public agencies, are participating to the Action.

In Section 2, COST and the Action TU1208 are presented. The Action’s ongoing activities are resumed, as well as the results achieved by now within the four Working Groups composing the scientific pattern of the Action. Information concerning the meetings, workshop and conferences organised by the Action is provided.

In Section 3 importance and interest of Armenian group to cooperate with European colleagues under COST 1208 Action umbrella is presented.

In Appendix, the list of Universities, research centres, private companies and public agencies currently participating to the COST Action TU1208 is reported.

2. COST and the Action TU1208 “Civil Engineering Applications of Ground Penetrating Radar”

COST is the longest-running European (EU) framework supporting cooperation among scientists and researchers across Europe; founded in 1971, it has been confirmed in Horizon 2020. It contributes to reducing the fragmentation in EU research investments, building the European Research Area (ERA) and opening it to cooperation worldwide. It also aims at constituting a “bridge” towards the scientific communities of emerging countries, increasing the mobility of researchers across Europe, and fostering the establishment of excellence in various key scientific domains. Gender balance, early-stage researchers and inclusiveness are strategic priorities of COST.

COST does not fund research itself, but provides support for activities carried out within Actions: these are bottom-up science and technology networks, centred around nationally funded research projects, with a four-year duration and a minimum participation of five COST Countries. The Actions are active through a range of networking tools, such as meetings, workshops, conferences, training schools, short-term scientific missions, and dissemination activities; they are open to researchers and experts from universities, public and private research institutions, non-governmental organisations, industry, and small and medium-sized enterprises.

COST Actions are funded within nine key science and technology fields: biomedicine and molecular biosciences; food and agriculture; forests, their products and services; materials, physics and nanosciences; chemistry and molecular sciences and technologies; earth system science and environmental management; information and communication technologies; transport and urban development; individuals, societies, cultures and health. In addition, Trans-Domain Actions deal with broad, multidisciplinary topics and Targeted Networks target specific policy strategies.

For more information on COST, please visit www.cost.eu.

The COST Action TU1208 is running in the "Transport and Urban Development" COST domain; it was launched in April 2013 and will end in April 2017. The scientific structure of the Action includes four Working Groups (WGs). The WG1 focuses on the design of novel GPR instrumentation (more details are given in Subsection 2.1). The WG2 deals with the development of guidelines for the surveying of transport infrastructures and buildings, and for the sensing of underground utilities and voids (see Subsection 2.2). The WG3 studies electromagnetic forward and inverse methods for the solution of near-field scattering problems by buried structures and data-processing techniques (further information can be found in Subsection 2.3). The WG4 is concerned with applications of GPR outside from the civil-engineering field and integration of GPR with other NDT technologies (see Subsection 2.4).

Several events were organised by the Action, during the first 18 months of its lifetime. A kick-off meeting was held, to launch the activities (Brussels, Belgium, April 2013). The first general meeting was mainly devoted to address the state of the art, advancement, ongoing studies and open problems, in the topics of interest for the Action (Rome, Italy, July 2013) [4, 5]. A workshop on finite-difference time-domain (FDTD) modelling was held, along with WG 2 and 3 meetings (Nantes, France, February 2014) [6]. A second general meeting was organised jointly with the European Geosciences Union General Assembly, to present and discuss the results achieved during the first year of the Action (Vienna, Austria, April-May 2014) [7]. A Working Group Meeting focusing on the organisation of dissemination and training initiatives took place (Barcelona, Spain, May 2014). In June-July 2014, the Action co-organised with the Université Catholique de Louvain the 15th International Conference on Ground Penetrating Radar (GPR 2014), held in Brussels, Belgium [3].

The Action TU1208 is also active in offering Training Schools (TSs) [8] for PhD Students and early-stage researchers. A TS on "Microwave Imaging and Diagnostics: Theory, Techniques, Applications" was co-organised with the COST Action TD1301 "Development of a European-based Collaborative Network to Accelerate Technological, Clinical and Commercialisation Progress in the Area of Medical Microwave Imaging" and the European School of Antennas (Madonna di Campiglio, Italy, March 2014). A TS on "Future Radar Systems: Radar 2020" was co-organised with the European School of Antennas and the European Microwave Association (Karlsruhe, Germany, May 2014), it covered the state of the art and new trends on radar technologies. Finally, a Training School on "Civil Engineering Applications of GPR" was held in the University of Pisa (Pisa, Italy, September 2014), covering topics as GPR basics and history, how to conduct a survey, the main applications of GPR in civil engineering, design of GPR systems, radar interferometry, electromagnetic techniques for the modelling of GPR scenarios, imaging and inversion techniques for the interpretation of GPR data.

In Subsection 2.5, the next meetings and training activities are announced.

The COST Action TU1208 is constantly promoting its activities in prestigious international conferences related to the Ground Penetrating Radar [9]-[13].

It is still possible to join the Action TU1208, in order to contribute to its scientific activities and participate to its events; interested researchers and experts are welcome to take contact with the Authors of this paper. Information on the Action can be found at www.cost.eu/COST_Actions/tud/Actions/TU1208 and www.GPRadar.eu.

2.1. Novel GPR instrumentation

The **WG1 of the COST Action TU1208** focuses on the development of innovative GPR equipment dedicated for civil engineering applications. It includes three Projects. Project 1.1 deals with the "Design, realisation and optimisation of innovative GPR equipment for the monitoring of critical transport infrastructures and buildings, and for the sensing of underground utilities and voids." Project 1.2 is concerned with the "Development and definition of advanced testing, calibration and stability procedures and protocols, for GPR equipment." Project 1.3 focuses on the "Design, modelling and optimisation of GPR antennas."

During the first year of the Action, the Members coordinated between themselves to address the state of the art and open problems in the scientific fields identified by these Projects [4, 14]. In carrying out this review work, the WG1 benefited from the contribution of Dr. David J. Daniels, participating to the First

General Meeting as an external expert and giving a plenary talk on GPR design challenges; he also prepared for the Action a special paper that is included in [4], resuming the characteristics of GPR systems, with particular reference to the various modulation techniques, highlighting the issues related to the design of GPR antennas, suggesting what improvements in subsystems - such as antennas, receivers and transmitters - are needed to increase overall GPR performance, and giving ideas for further research and developments. The WG also benefited from the contribution of Dr. Erica Utsi, participating to the First General Meeting as an external expert and sharing with the Members her wide experience on GPR technology and methodology. The synergy with WG2 and WG4 was useful for a deep understanding of the problems, merits and limits of available GPR equipment, as well as to discuss how to quantify the reliability of GPR results.

An innovative reconfigurable ground-coupled stepped-frequency GPR is being studied and optimised by the Members; it was designed in Italy and is equipped with two bow-tie antennas with a series of switches along their arms, so that their size can be varied. The system was tested in several sites, both indoor and outdoor, in comparison with a commercial ground-coupled pulsed system [3, 4, 7]. Subsequently, within a Short-Term Scientific Mission (STSM), the prototype device was sent to Norway and compared with commercial ground-coupled stepped-frequency radar [15]. These experimental activities were fundamental to gain a deepen knowledge of the reconfigurable GPR prototype and to plan its improvement.

Another innovative system being designed within the Action and proposed by Italian Members, will allow investigating the mechanical properties of pavement, in addition to its geometrical and electromagnetic properties [3, 4].

Cooperation with the COST Action IC1102 "Versatile, Integrated, and Signal-aware Technologies for Antennas (VISTA)" has been established, concerning the design of GPR antennas.

At least two more WG1 activities need to be mentioned, as they are very interesting and promising. The first one, coordinated by Italy and involving Members and external experts from Germany, United Kingdom, Japan and United States, is the development of a protocol providing recommendations for the safety of people and instruments in near surface geophysical prospecting, with a particular focus to the use of GPR.

The second initiative is called GPR4Everyone, it was proposed by Italy and consists in creating a virtual store of GPR equipment at the disposal of Members from inclusiveness Countries: some Institutes have GPR systems and complementary NDT equipment no longer used, while there are Institutes who cannot afford to buy a GPR; thus, the idea is to cense the unused equipment and make it available to be given for free to researchers from less research-intensive countries, as a small step to counterbalance research communities' unequal access to funding and resources distribution.

2.2. GPR surveying of pavements, bridges, tunnels, and buildings; underground utility and void sensing

The **WG2 of the COST Action TU1208** deals with the development of guidelines and protocols for the surveying, through the use of a GPR system, of transport infrastructure and buildings, as well as for the sensing of utilities and voids. It includes five Projects. Project 2.1 focuses on outlining "Innovative inspection procedures for effective GPR surveying of critical transport infrastructures (pavements, bridges and tunnels)." Project 2.2 is concerned with the development of "Innovative inspection procedures for effective GPR surveying of buildings." Project 2.3 deals with identifying "Innovative inspection procedures for effective GPR sensing and mapping of underground utilities and voids, with a focus to urban areas." Project 2.4 focuses on the development of "Innovative procedures for effective GPR inspection of construction materials and structures." The WG2 also includes Project 2.5 on the "Determination, by using GPR, of the volumetric water content in structures, sub-structures, foundations and soil," this is a topic of great interest in civil engineering, as water infiltration is often a relevant cause of degradation of structures, such as roads of bridges, and of rebar corrosion.

During the first year of the Action, information was collected and shared about state-of-the-art, ongoing studies, problems and future research needs, in the topics covered by the five above-mentioned Projects [4, 14, 16]. In carrying out this review work, the WG2 benefited from the contribution of Dr. Janne Poikajarvi who participated to the WG Meeting in Nantes as an external expert and presented the Mara Nord Project, recently carried out in Finland, Sweden and Norway, aiming at demonstrating the potential of GPR in road-condition measurement and rehabilitation planning, and at creating and harmonising Scandinavian recommendations; he prepared for the Action a special paper as well, that is included in [6], where the achieved results are presented and how the project was carried out is explained step by step.

Based on the experience and knowledge gained from the in-depth review work carried out by WG2, several case studies were conducted; they were presented during the Second General Meeting and the GPR 2014 conference [3, 7] and are not resumed here for brevity reasons. Furthermore, the extension of GPR application to railways track ballast assessment was demonstrated [17].

The Action identified some reference test-sites, for an advanced comparison of available inspection procedures to be carried out in the next years of activity (taking advantages of the interaction with WG4), as well as to test GPR equipment (interacting with WG 1), electromagnetic simulators, and data-processing algorithms (thanks to the cooperation with WG3). In particular, the Action chose the IFSTTAR geophysical test site and the accelerated pavement testing (APT) facility. The geophysical test site is an open-air laboratory including a large and deep area, filled with various materials arranged in horisontal compacted slices, separated by vertical interfaces and water-tighted in surface; several objects as pipes, polystyrene hollows, boulders and masonry are embedded in the field [6]. The full-scale APT facility is an outdoor circular carousel dedicated to full-scale pavement experiments, consisting of a central tower and four long arms equipped with wheels, running on a circular test track [6].

Another interesting and promising WG2 initiative that has to be mentioned is the development of a Catalogue of European test sites and laboratories for the testing of GPR equipment, methodology and procedures that is being coordinated by France and Italy. The catalogue will represent a useful tool for the GPR community and it will contribute to identifying new cooperation possibilities among research groups, to clarifying which are the missing testing facilities in the various European regions, and to addressing current or future research needs.

2.3. Electromagnetic methods for near-field scattering problems by buried structures; data-processing techniques

The **WG3 of the COST Action TU1208** focuses on the development of accurate, versatile and fast electromagnetic scattering methods for the characterisation of GPR scenarios and on the improvement of inversion, imaging and data-processing algorithms for the elaboration of GPR data collected during civil engineering surveys. It includes four Projects. Project 3.1 deals with the development of advanced "Electromagnetic modelling for GPR applications." Project 3.2 is concerned with the development of advanced "Inversion and imaging techniques for GPR applications." The topic of Project 3.3 is the "Development of intrinsic models for describing near-field antenna effects, including antenna-medium coupling, for improved radar data processing using full-wave inversion." The Project 3.4 focuses on the "Development of advanced GPR data-processing algorithms."

During the first year of the Action, information was collected and shared about state-of-the-art of the available electromagnetic-scattering, imaging and inversion data-processing methods [4, 14]. In carrying out this review work, the Members of Project 3.1 could benefit from the special workshop on FDTD organized in Nantes [6]. The Members of Project 3.4 could benefit from the contribution of Prof. Andreas Tzanis, who participated to the WG Meeting in Nantes as an external expert and presented the well-known matGPR software that he developed, providing a broad and functional range of tools for the analysis of GPR data; he also prepared for the Action a special paper giving an overview on GPR data processing, suggesting open issues and possible future developments in this area, that is included in [6].

Reference test scenarios were defined by the WG3 Members, in cooperation with WG2, to test the modelling/inversion/imaging/data-processing techniques during the next years of activity [7, 8].

For what concerns electromagnetic-scattering methods, particular attention is being paid to the FDTD technique and the spectral domain Cylindrical-Wave Approach (CWA). In the FDTD technique, the Maxwell's equations are solved through space and time discretization; GprMax is a freeware and versatile FDTD simulator, very well-known in the GPR community. This tool is being further tested and improved by WG3 Members. In particular, the possibility to adopt a more realistic representation of the soil/material hosting the sought structures and of the GPR antennas is being introduced in the software; moreover, input/output procedures to ease the definition of scenarios and the visualisation of numerical results were developed [3, 7]. Part of this work was carried out during two STSMs involving Members from Italy and United Kingdom [8].

In the CWA, the field scattered by subsurface two-dimensional targets with arbitrary cross-section is expressed as a sum of cylindrical waves; use is made of the plane-wave spectrum of such waves to take into account the interaction of the scattered field with the interfaces between different materials that constitute the medium hosting the sought targets. The method was extended to deal with through-the-wall scenarios [18].

Advancements of inversion/imaging/data-processing algorithms achieved by Action Members were presented during the Second General Meeting and the GPR 2014 conference [3, 7], as well as in [19, 20]. They are not resumed here for brevity reasons.

2.4. Different applications of GPR and other NDT technologies in civil engineering

The **WG4 of the COST Action TU1208** focuses on applications of GPR outside from the civil engineering field. It also deals with the integration of GPR with other NDT techniques, in order to improve the potential of the combined methods. Among such techniques there are ultrasonic testing, radiographic testing, methods employing surface waves, approaches involving the using of an open coaxial probe combined with a vector network analyser, liquid-penetrate testing, magnetic-particle testing, acoustic-emission testing, eddy-current testing, self-potential methods and DC methods; the coupling of GPR with infrared thermography or with Falling Weight Deflectometer (FWD) and its Light version (LFWD) is promising, too. In civil engineering, several methods that are commonly used in solid-earth geophysics have their counterparts in non-destructive testing. In fact, the most used construction materials are mineral aggregates, such as concrete (mineral aggregates, cement, additives) or asphalt (mineral aggregates, bitumen, additives), and also soils and rocks are mineral aggregates; thus, it is possible to effectively use earth-monitoring methods for civil engineering applications, of course the scale of structures and infrastructures is much smaller rather than the one of the earth and an adaption of the methods is recommended and required.

The WG4 includes six Projects. Project 4.1 deals with the "Application of GPR and other non-destructive testing methods in archaeological prospecting and cultural heritage diagnostics." Project 4.2 is concerned with the innovative "Application of GPR to the localisation and vital signs detection of buried and trapped people." Project 4.3 focuses on the "Application of GPR in association with other non-destructive testing methods in surveying of transport infrastructures." Project 4.4 regards "Applications of GPR in association with other non-destructive testing methods in building assessment and in geological/geotechnical tasks." Project 4.5 is about the "Development of other advanced electric and electromagnetic methods for the characterisation of construction materials and structures." Project 4.6 focuses on the "Application of GPR in association with other non-destructive testing methods in the management and protection of water resources." During the first year of the Action, information was collected and shared about state-of-the-art, ongoing studies, problems and future research needs, in the topics covered by these Projects [4, 7, 14, 21].

Based on the experience and knowledge gained from the in-depth review work carried out by WG4, several new case studies were conducted, mainly relevant to archaeological prospecting; some of them were carried out through STSMs in Greece and Austria, involving Members from Spain and Belgium [8]. The results of these studies were presented during the Second General Meeting and the GPR 2014 conference [3, 7], as well as in [22, 23]; they are not resumed here for brevity reasons.

Within the WG4 activities, the cooperation with the COST Action TU1206 "Sub-Urban - A European network to improve understanding and use of the ground beneath our cities" has to be mentioned. This Action focuses on highlighting the importance of the ground beneath cities, which is often under-recognised and overlooked, with the main aim of transforming the relationship between experts who develop urban subsurface knowledge and those who can benefit most from it – as urban decision makers, practitioners as well as the wider research community.

2.5. Next events and training activities

The Third General Meeting of the COST Action TU1208 is going to be held in London, United Kingdom, on March 4-6, 2015. It will include a half-day training for PhD Students and early-stage researchers, the Management Committee meeting, and the meetings of the four WGs. Special sessions will take place, focusing on the condition assessment of transport infrastructure and the mapping of urban subsoil with GPR: the main challenges of these tasks will be discussed, the view-points of stakeholders, private and academic GPR end-users will be presented and compared, with the aim of making a significant step forward in the development of GPR European guidelines and protocols.

The Action is organising a Session on "Civil Engineering Applications of Ground Penetrating Radar," within the 2015 EGU General Assembly, to be held in Vienna, Austria, on April 12-17, 2015.

Furthermore, the Action is co-organising, jointly with the European School of Antennas and the European Association on Antennas and Propagation, a Training School on "Ultra-Wide Band Antennas, Technologies and Applications," to be held in the Karlsruhe Institute of Technology, in Karlsruhe, Germany, on April 20-24, 2015. The course will present an insight into the design, evaluation and measurement procedures for ultra wideband (UWB) antennas, as well as the characteristics of the UWB radio channel. The theoretical lectures will be complemented with laboratory tutorials on antenna design, experimental techniques including measurements in anechoic chamber, detection of hidden objects and wave propagation simulations.

Finally, the Action is organising a workshop on "Advanced GPR surveys using multichannel antenna arrays," to be held in May 2015, in the archaeological site of Carnuntum, Austria. The scope of the workshop is to inform about the potential of multichannel GPR systems, to educate on exact data positioning using motorized array GPR systems in combination with GPS and robotic total stations, and to familiarize the participants with common systems and workflows in regard to data acquisition, processing and efficient interpretation. Carnuntum was a Roman army camp on the Danube in the Noricum province and after the 1st century the capital of the Pannonia Superior province, with 50,000 people; its remains are situated in Lower Austria, halfway between Vienna and Bratislava, and the "Archaeological Park Carnuntum" extends over an area of 10 km² near today's villages Petronell-Carnuntum and Bad Deutsch-Altenburg. The whole area is being mapped with GPR by the Ludwig Boltzmann Institute for Archaeological Prospection and Virtual Archaeology.

3. GPR activities in Armenia and Participation to TU1208

In July 2013 Fiber Optics Communication Laboratory at State Engineering University of Armenia joined the COST 1208 Action as a representative from COST Near Neighbour Countries. In the end of April 2014 it was the first COST TU1208 meeting where participated Armenian group [24]. The following information has been presented on this meeting.

Armenia is a country located in a very complicated region from geophysical point of view. It is situated on a cross of several tectonic plates and a lot of dormant volcanoes. The main danger is earthquakes and the last big disaster was in 1988 in the northwest part of contemporary Armenia. As a consequence, the main direction of geophysical research is directed towards monitoring and data analysis of seismic activity. National Academy of Sciences of Armenia is conducting these activities in the Institute of Geological Sciences and in the Institute of Geophysics and Engineering Seismology.

Research in the field of ground penetrating radars is considered in Armenia as an advanced and perspective complement to the already exploiting research tools. The previous achievements of Armenia in the fields of radiophysics, antenna measurements, laser physics and existing relevant research would permit to initiate new promising area of research in the direction of theory and experiments of ground penetrating radars.

One of the key problems in the operation of ground penetrating radars is correct analysis of peculiarities of electromagnetic wave interaction with different layers of the earth. For this, the well-known methods of electromagnetic boundary problem solutions are applied. In addition to the existing methods our research group of Fiber Optics Communication Laboratory at the State Engineering University of Armenia declares its interest in exploring the possibilities of new non-traditional method of boundary problems solution for electromagnetic wave interaction with the ground. This new method for solving boundary problems of electrodynamics is called the method of single expression (MSE) [25-27]. The distinctive feature of this method is denial from the presentation of wave equation's solution in the form of counter-propagating waves, i.e. denial from the superposition principal application. This permits to solve linear and nonlinear (field intensity-dependent) problems with the same exactness, without any approximations. It is favourable also since in solution of boundary problems in the MSE there is no necessity in applying absorbing boundary conditions at the model edges by terminating the computational domain. In the MSE the computational process starts from the rear side of any multilayer structure that ensures the uniqueness of problem solution without application of any artificial absorbing boundary conditions.

Previous success of the MSE application in optical domain gives us confidence in successful extension of this method's use for solution of different problems related to electromagnetic wave interaction with the layers of the earth and buried objects in the ground.

Armenian group involved mainly in COST TU1208 activities carrying out in WG3, where other methods of electromagnetic modelling are in use by European colleagues. It is expected to perform comparison of the MSE with other existing modelling methods in frame of COST cooperation.

4. Acknowledgement

The Authors sincerely thank COST for funding the Action TU1208, supporting this work.

5. References

[1] Nondestructive Testing and Evaluation, SI on Civil Engineering Applications of Ground Penetrating Radar, L. Pajewski, A. Benedetto, Guest Eds., **27** (Taylor and Francis, 2012).
[2] Journal of Applied Geophysics, SI on Ground Penetrating Radar for Nondestructive Evaluation of Pavements, Bridges and Subsurface Infrastructures, L. Pajewski, A. Benedetto, A. Loizos, E. Slob, Guest Eds., **97** (Elsevier, 2013).
[3] Proc. 15th Internat. Conference on Ground Penetrating Radar - GPR2014, S. Lambot, A. Giannopoulos, L. Pajewski, F. De André, E. Slob, C. Craeye, Eds., IEEE Conf. Number **35163** (IEEE, 2014).
[4] Proc. First Action's General Meeting (Rome, Italy, 22-24 July 2013), 1st edition, COST Action TU1208, L. Pajewski, A. Benedetto, Eds., ISBN **978-88-548-6191-6** (Aracne, 2013).
[5] Booklet of Participants and Institutions, 1st edition, COST Action TU1208, L. Pajewski, A. Benedetto, Eds., ISBN **978-88-548-6192-3** (Aracne, 2013).
[6] Proc. 2013 Working Group Progress Meeting (Nantes, France, 24-25 February 2014), COST Action TU1208, L. Pajewski, X. Derobert, Eds., ISBN **978-88-548-7223-3** (Aracne, 2014).
[7] Proc. Second Action's General Meeting (Vienna, Austria, 30 April-2 May 2014), COST Action TU1208, L. Pajewski, A. Benedetto, Eds., ISBN **978-88-548-7224-0** (Aracne, 2014).
[8] Short Term Scientific Missions and Training Schools – Year 1, COST Action TU1208, L. Pajewski, M. Marciniak, Eds., ISBN **978-88-548-7225-7** (Aracne, 2014).
[9] L. Pajewski, A. Benedetto, A. Loizos, E. Slob, F. Tosti, "Civil Engineering Applications of Ground Penetrating Radar: Research Perspectives in COST Action TU1208," Geophysical Research Abstracts, 2013 EGU General Assembly (2013) EGU2013-13941.
[10] L. Pajewski, A. Benedetto, G. Schettini, F. Soldovieri, "Applications of GPR in archaeological prospecting and cultural heritage diagnostics: Research Perspectives in COST Action TU1208," Geophysical Research Abstracts, 2013 EGU General Assembly (2013) EGU2013-14010.
[11] L. Pajewski, A. Benedetto, X. Dérobert, A. Giannopoulos, A. Loizos, G. Manacorda, M. Marciniak, C. Plati, G. Schettini, I. Trinks, "Applications of Ground Penetrating Radar in Civil Engineering – COST Action TU1208," Proc. 7th International Workshop on Advanced Ground Penetrating Radar, ISBN **978-1-4799-0937-7** (IEEE, 2013).
[12] L. Pajewski and A. Benedetto, "Advanced Ground Penetrating Radar: open issues and new research opportunities in Europe," Proc. 10th European Radar Conference, 2013 European Microwave Week (IEEE, 2013), 1847.
[13] L. Pajewski, A. Benedetto, A. Loizos, E. Slob, and F. Tosti, "COST Action TU1208 "Civil Engineering Applications of Ground Penetrating Radar:" first-year activities and results," 2014 EGU General Assembly (2014) EGU2014-16933.
[14] Civil Engineering Applications of Ground Penetrating Radar, A. Benedetto, L. Pajewski, Eds., ISBN **978-3-319-04812-3** (Springer, 2015).
[15] L. Matera, "Tests, comparisons and plans of improvements for an innovative reconfigurable stepped-frequency GPR," COST STSM Report TU1208-010614-045484 (2014).
[16] A. Benedetto, "State of the Art of GPR Applications and New Trends in Transportation Infrastructures," Future Trends in Civil Engineering, A. Ceric, S. Lakusic, Eds., ISBN **978-953-6272-65-5** (2014).
[17] S. Fontul, F. De Chiara, E. Fortunato, A. Lopes, "Evaluation of ballast condition using Ground Penetrating Radar," The Ninth Intl. Conf. on Engineering Computational Technology (2014).
[18] F. Frezza, L. Pajewski, C. Ponti, G. Schettini, "Through-wall electromagnetic scattering by N conducting cylinders," J. Opt. Soc. Am. A, **30**(8) (2013).
[19] S. Meschino, L. Pajewski and G. Schettini, "A SAP-DoA Method for the Localization of Two Buried Objects," International J. Antennas and Propagation, **2013** (2013) Article ID 702176.

[20] M. Salucci, L. Tenuti, C. Nardin, M. Carlin, F. Viani, G. Oliveri, A. Massa, "GPR survey through a multi-resolution deterministic approach," Proc. IEEE Antennas and Propagation Society International Symposium (IEEE, 2014).

[21] L. Crocco and V. Ferrara, "A Review on Ground Penetrating Radar Technology for the Detection of Buried or Trapped Victims," Proc. 2nd International Workshop on Collaborations in Emergency Response and Disaster Management (2014).

[22] V. Pérez-Gracia, J. O. Caselles, J. Clapés, G. Martinez, R. Osorio, "Non-destructive analysis in cultural heritage buildings: Evaluating the Mallorca cathedral supporting structures," Elsevier Non Destructive Testing and Evaluation International **59** (2013) 40.

[23] M. Solla, S. Lagüela, H. González-Jorge, P. Arias, "Approach to identify cracking in asphalt pavement using GPR and infrared thermographic methods: Preliminary findings," Elsevier Non Destructive Testing and Evaluation International **62** (2014) 55.

[24] H. Baghdasaryan, T. Knyazyan, T. Hovhannisyan, Research perspectives in the field of ground penetrating radars in Armenia, General Assembly 2014 of the European Geosciences Union, Research Abstracts Vol. 16, EGU2014-8891, (2014).

[25] H.V. Baghdasaryan, T.M. Knyazyan, "Problem of Plane EM Wave Self-action in Multilayer Structure: an Exact Solution", Optical and Quantum Electronics, **31** (1999), 1059.

[26] H.V. Baghdasaryan, T.M. Knyazyan, "Modelling of strongly nonlinear sinusoidal Bragg gratings by the Method of Single Expression", Optical and Quantum Electronics, **32** (2000), 869.

[27] H.V. Baghdasaryan, "Basics of the Method of Single Expression: New Approach for Solving Boundary Problems in Classical Electrodynamics" (Yerevan, Chartaraget, 2013), ISBN **978-9939-55-972-8**.

Appendix - Universities, research institutes, private companies and public agencies, participating to the COST Action TU1208.

COST Countries

AUSTRIA: Ludwig Boltzmann Institute for Archaeological Prospection and Virtual Archaeology, Vienna; Zentralanstalt für Meteorologie und Geodynamik, Vienna. **BELGIUM**: Université Catholique de Louvain, Louvain-la-Neuve; Belgian Road Research Centre, Brussels; Ghent University, Ghent; University of Liège, Liège; Vrije Universiteit, Brussels. **CROATIA**: University of Zagreb, Zagreb; University of Split, Split. **CZECH REPUBLIC**: Transport Research Centre, Brno; Arcadis Geotechnika, Prague; Inset, LtD, Prague; Brno University of Technology, Brno; Czech Technical University in Prague, Prague. **DENMARK**: Ramboll Denmark, Department of Geophysics and Geohydrology, Copenhagen. **ESTONIA**: Institute of Ecology, Tallinn. **FINLAND**: Aalto University, Espoo, Helsinki; Geological Survey of Finland, Espoo, Helsinki. The **FORMER YUGOSLAV REPUBLIC of MACEDONIA**: Ss. Cyril and Methodius University, Skopje. **FRANCE**: Institut Français des Sciences et Technologies des Transports, de l'Aménagement et des Réseaux (IFSTTAR), Bouguenais Cedex; Alyotech Technologies, Nantes; Université Bordeaux, Bordeaux; Centres d'Etudes Techniques de l'Equipement (CETE), Angers – Blois – Les Ponts de Cé; Clermont-Ferrand University - Blaise Pascal Institute, Clermont-Ferrand cedex; École supérieure d'électricité (SUPELEC), Gif sur Yvette; Institut Fresnel, Marseille; Institut National des Sciences Appliquées (INSA), Toulouse; Strasbourg University, Strasbourg; University of Nantes, Nantes; University Nice Sophia Antipolis, Sophia Antipolis; Laboratoire d'Etudes et de Recherches sur les Matériaux (LERM), Arles Cedex. **GERMANY**: Federal Institute for Material Research and Testing (BAM), Berlin; DMT GmbH & Co. KG, Exploration & Geosurvey, Hamburg; Karlsruhe Institute of Technology (KIT), Karlsruhe; Institute of Bio and Geosciences, Forschungszentrum Jülich, Jülich; Technische Universität Ilmenau, Ilmenau; Ruhr-Universität Bochum, Bochum; Fraunhofer Institute for High Frequency Physics and Radar Techniques, Wachtberg. **GREECE**: National Technical University of Athens, Athens; Aristotle University of Thessaloniki, Thessaloniki; Geoservice, Athens; Technical University of Crete, Crete; Geoterra, Athens. **IRELAND**: National Transport Authority, Dublin. **ITALY**: "Roma Tre" University, Rome; ELEDIA Research Center, Trento; IDS Ingegneria dei Sistemi SpA, Pisa; Consiglio Nazionale delle Ricerche (CNR), Istituto per i Beni Archeologici e Monumentali (IBAM), Lecce and Potenza; Consiglio Nazionale delle Ricerche (CNR), Istituto per il Rilevamento Elettromagnetico dell'Ambiente (IREA), Naples; "La Sapienza" University, Rome; Seconda Università di Napoli, Napoli; Università Mediterranea di Reggio Calabria, Reggio Calabria; University of Genoa, Genoa; INFN & University of Naples “Federico II”, Naples; Provincia di Roma, Rome; Provincia di Rieti, Rieti; University of Napoli "Parthenope”; Politecnico di Torino, Torino; Università di Firenze, Firenze; Università di Perugia, Perugia; Università di Catania, Catania. **LATVIA**: Transport and Telecommunication Institute, Riga. **MALTA**: University of Malta, Msida. **NETHERLAND**: Technical University of Delft, Delft. **NORWAY**: Norwegian University of Science and Technology, Trondheim; SINTEF, Trondheim; 3d-Radar AS, Trondheim. **POLAND**: National Institute of Telecommunications, Warsaw; Road and Bridge Research Institute, Warsaw; University of Science and Technology - Akademia Górniczo-Hutnicza im. Stanisława Staszica, Kraków; Kielce University of Technology, Kielce. **PORTUGAL**: Escola Superior de Tecnologia e Gestão, Instituto Politécnico de Leiria, Leiria; University of Minho, Guimarães; National Laboratory for Civil Engineering (LNEC), Lisbon. **ROMANIA**: Ion Mincu University of Architecture and Urbanism, Bucharest; National Institute of R&D for Optoelectronics (INOE 2000). **SERBIA**: Faculty of Technical Science, Novi Sad. **SLOVAKIA**: Technical University of Kosice, Kosice. **SLOVENIA**: University of Ljubljana, Ljubljana. **SPAIN**: Geofisica Consultores, Madrid; Universidade de Vigo, Pontevedra; Universidad Politécnica de Catalunya, Barcelona; Polytechnic University of Valencia, Valencia; Public University of Navarra, Pamplona. **SWITZERLAND**: Hochschule Rapperswil, Rapperswil; Scuola Universitaria Professionale della Svizzera Italiana, Lugano-Manno; Smartec, Lugano-Manno; Meet Electronic Engineering, Coldrerio. **TURKEY**: Ankara University, Ankara; Suleyman Demirel University, Isparta. **UNITED KINGDOM**: The University of Edinburgh, Edinburgh; The University of Greenwich, Chatham Maritime; Atlas Geophysical Limited, Powys; British Geological Survey, Edinburgh; Edinburgh Napier University, Edinburgh; GM RADAR Solutions, London; Infrastructure Services - Mouchel, Glasgow; Queen Mary University of London, London; The University of Nottingham, Nottingham; Keele University, Keele; TRL Ltd – Infrastructure Division, Wokingham. **ISRAEL** (COST Cooperating State): Holon Institute of Technology (HIT).

COST “Near Neighbour Countries”

ARMENIA: State Engineering University of Armenia, Yerevan. **EGYPT**: National Research Institute of Astronomy and Geophysics (NRIAG). **UKRAINE**: Usikov Institute for Radiophysics and Electronics of the National Academy of Sciences of Ukraine.

COST “International Partner Countries”

AUSTRALIA: Department of Transport and Main Roads. **RWANDA**: National University of Rwanda. **HONG KONG**: The Hong Kong Polytechnic University, Hong Kong. **UNITED STATES OF AMERICA**: University of Mississippi, Oxford, Mississippi; University of New Mexico, Albuquerque, New Mexico; University of Texas, Austin, Texas; Washington State Department of Transportation, Olympia, Washington.

A metod and an autonomous and automate operating hail preventing sonic cannon

A. Arakelyan[1,2], A. Hambaryan[2]

[1]*Institute of Radiophysics and Electronics, Alikhanian Brothers str. 1, 0203, Ashtarak, Armenia*
[2]*ECOSERV Remote Observation Centre Co. Ltd., 2 G. Njdeh str., #24, 0006, Yerevan, Armenia*

In this paper a new method of anti-hail protection and an autonomous and automate operating hail preventing sonic cannon (generator) will be discussed. As well as the results of radiometric measurements of clear air and hail clouds brightness temperatures will be presented, measured at various frequencies and polarizations. The results have been obtained during the measurements carried out in Armenia from the measuring complex built under the frameworks of ISTC Projects A-872 and A-1524. The measurements were carried out at vertical and horizontal polarizations, at various angles of sensing by C-, Ku-, and Ka-band combined scatterometric-radiometric systems developed and built by ECOSERV Remote Observation Centre Co.Ltd. In this paper a method of anti-hail protection, structural and operational features of the autonomous and automate operating hail preventing sonic cannon will be considered and discussed.

1. Introduction

Each year hail and shower cause great and severe damage to agriculture and human properties and to minimize or to prevent economic disruption and downturn in agriculture various kind of anti-hail protection methods and stations are used to reduce the material damage in size.

At present several anti-hail protection methods and stations are known in the art. It is known an anti-hail protection method with an active effect on hail clouds by shells or rockets which spread reagents or aerosol in clouds [1,2].

It is known as well an anti-hail protection method with an active effect (impact) on hail clouds by significant (powerful) shock waves directed upwardly to the sky [3,4]. It is believed that the succession of shock waves transports positive ions from ground level to cloud level which disrupt formation of hail nuclei.

This method of anti-hail protection is fulfilled by the following way. Supersonic and significant shock waves is generated by sequential (serial) detonating an explosive mixture of combustible gas (combustible fuel) and air in a combustion chamber (in an enclosed body) of a hail preventing sonic generator (an anti-hail shock wave generator) and is directed upwardly to the sky. By selecting material and quantity of the combustible fuel, number and duration of detonations it is possible to provide significant shock waves and to effect on the hail clouds up to 10km of altitude, changing hail cloud structure, preventing further development of hail and transforming hail to (into) rain, to wet snow or to small ice drops. As the fuel or combustible gas may be used acetylene gas, a mixture of propane-butane gases or other gas or liquid fuel with high energy capabilities [3,4].

Usually, for hail detection powerful Weather Doppler radar is used, operating at short centimeter or millimeter band of waves. These radars cost several hundred thousand or million USD, have serious disadvantages and cannot solve the problem totally.

Therefore a reason is appeared to develop and to produce new kind of detector-identifiers, which will cost cheaper and have additional advantages.

Clouds brightness temperature is a function of many parameters, in which air and particles temperature, fraction type (water or ice) and particles size are the principal variables. The changes of clouds radio brightness temperatures, related with the changes of dielectric properties of particles and their temperatures, depend on frequencies and polarizations of observation. Therefore, by a microwave radiometers it is possible to make precise and high probable detection and classification of hail clouds

Radiometric observation may not miss the stage of transformation of water vapour and drops of water to hail as well, because water and ice dielectric constants are very differ and such formations' brightness temperatures will sufficiently vary one from the other.

In this paper a new method of anti-hail protection and an autonomous and automate operating hail preventing sonic cannon (generator) will be discussed As well as the results of radiometric measurements of clear air and hail clouds brightness temperatures will be presented, measured at various frequencies and polarizations.

The results have been obtained during the measurements carried out in Armenia from the measuring complex built under the framework of ISTC Projects A-872 and A-1524. The measurements were carried out at vertical and horizontal polarizations, under various angles of sensing by C-, Ku-, and Ka-band combined scatterometric-radiometric systems (ArtAr-5.6, ArtAr-15, and ArtAr-37) developed and built by ECOSERV Remote Observation Centre Co.Ltd., under the framework of the above Projects [5-8].

In the paper structural and operational features of the autonomous and automate operating hail preventing sonic cannon, utilized measuring systems and the whole measuring complex will be considered and discussed as well.

2. A new method and corresponding device for anti-hail protection

The results of experimental researches, carried out in the framework of ISTC Project A-1524 [5-8] and partially are presented in Fig.1 have shown, that the radiothermal contrasts from hail clouds may reach up to 50-100K in dependence of the frequency band. These results have suggested that radiometric measurements may be successfully used for hail detection and hail clouds classification. On the basis of these results a new method and corresponding device for hail detection and prevention have been developed as an invention.

The method and the autonomous and automate operating hail preventing sonic cannon has already patented in Armenia by ECOSER Remote Observation Centre Co.Ltd [9]. A PCT Application (PCT/AM2012/000001) was submitted to WIPO (World Intellectual Property Organization) and a Report of the International Searching Authority on a patentability of this invention was received [10].

In Fig.2 a block diagram of the autonomous and automate operating hail preventing sonic cannon is presented.

Preferred modes of operation of the autonomous and automate operating hail preventing sonic cannon are described with reference to Fig 1. After initial starting (running) of the ant-hail protection system, that is after opening mechanical valve and switching on power supply, which begins feed control means, ignition means and detector-warner (detector-alerter), the anti-hail protection system continues its operation automatically. The control means opens solenoid valve and sets hail preventing sonic generator in a waiting mode of operation. Flow of the combustible gas through open solenoid valve and pressure regulator (pressure reducer) comes to the input of closed fuel injector. Up-directed antenna observes the sky, receives continually signals of sky proper radiothermal emission and transfers them to the input of radiometric receiver. Radiometric receiver processes received signals and outputs to the input of controlling compensation circuit a signal corresponding to a sum of powers of signals of external emissions and internal noises. The compensation circuit outputs its signals to the input of controlling multi-channel thresholder. In the controlling multi-channel thresholder the signals is compared with N various threshold levels. The warning device processes jointly received signals, generates a warning (alert) signal and outputs generated warning signal to the input of the control means.The control means sets the operation mode of hail preventing sonic generator in accordance with the received warning signal, such as a switching-on mode, a waiting mode, an operating mode and a turning-off mode, and sets operation parameters, such as power (the combustible fuel quantity) and duration of detonations, number (frequency) of detonations and a detonation window.

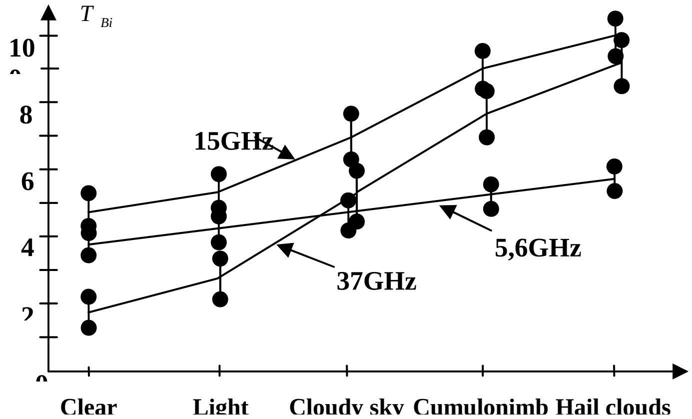

Fig 1. Radiothermal contrasts from various types of clouds at various frequencies and at vertical polarization of sensing

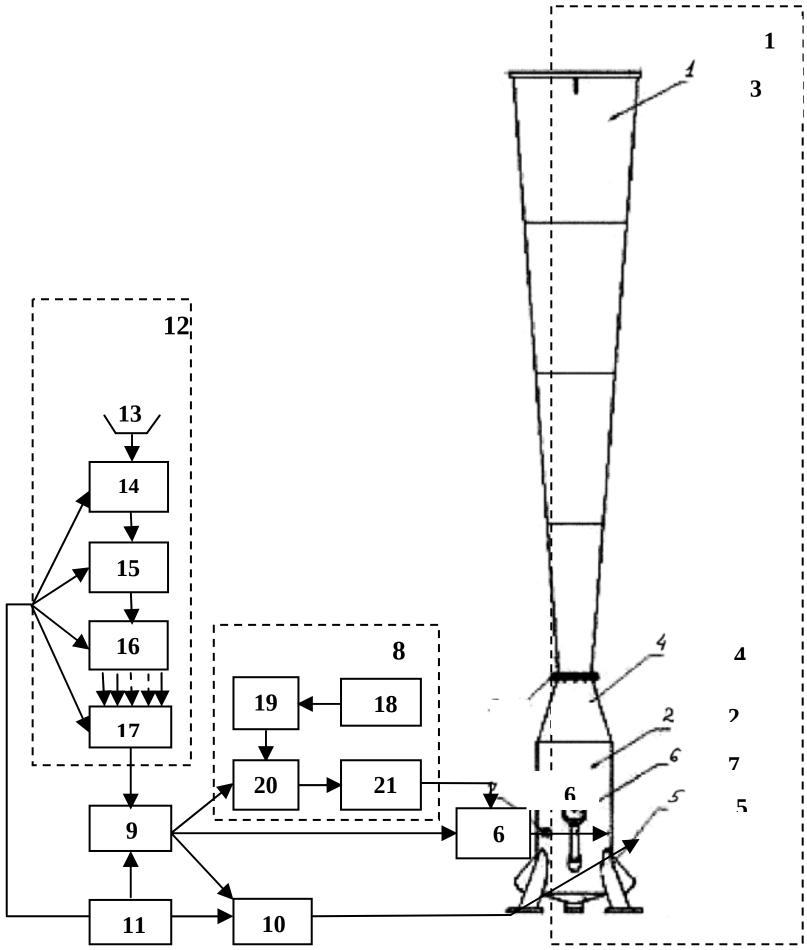

Fig.1 A block diagram of the autonomous and automate operating hail preventing sonic cannon
1- a hail preventing sonic generator, 2- a cylindrical combustion chamber, 3– a conical barrel, 4- a neck, 5 air inlet ports, 6- a fuel injector, 7- an igniter, 8- a fuel supply system, 9- a control means, 10- an ignition means, 11- a power supply, 12- a detector-warner (detector-alerter), 13- an antenna, 14- a radiometric receiver, 15- a controlling compensation circuit, 16- a controlling multi-channel thresholder, 17- a warning device, 18- a combustible fuel reservoir, 19- a mechanical valve, 20- a solenoid valve, 21 a pressure regulator

The control means keeps hail preventing sonic generator in a waiting mode of operation if received warning signal has the value "0". When the control means receives a warning signal with the value "1" or more it sets the operating mode of operation, sets operation parameters of hail preventing sonic generator in accordance with the value of the received warning signal, creates command (control) signals and runs hail preventing sonic generator. When the hail preventing sonic generator is operated, the control means causes combustible fuel to be released through fuel injector into combustion chamber, until sufficient combustible gas for a full explosion resulting in a significant shock wave is present in combustion chamber. Mixing of the combustible fuel (combustible gas) with air in the combustion chamber is automatic and rapid. A short time after the solenoid valve of fuel injector is closed the control means triggers spark gap coil of the ignition means to create a high voltage pulse resulting in a spark across the electrodes of igniter. As the gas in combustion chamber rapidly combusts, a shock wave results which is directed by conical barrel. The momentum of the combustion gases is directed upwardly, and once the combustion gases have fully expanded, the upward momentum of the gases causes a negative pressure to be created in the combustion chamber which results in flaps of air inlet ports being drawn open so that fresh air may be drawn from ambient through air inlet ports to fill combustion chamber.

It is important to select a fuel and ignition system which can operate even when rain water (ice, snow) passes through the conical barrel into combustion chamber. It is important to select the parameters of combustible fuel, the combustion chamber volume to upper orifice size as well as the conical barrel dimensions in order that a good shock wave is generated and sufficient aspiration through air inlet ports takes place in order to bring in sufficient fresh air for the next combustion.

When the control means receives the warning signal with the upper-range (maximum) of value, then the control means sets the turning-off mode of operation, switches off hail preventing sonic generator and interrupts detonations, that is stops fuel injection and ignition. Control means switches on hail preventing sonic generator and resets for hail preventing sonic generator the waiting mode of operation when it receives from warning device next (next in turn) signal with the value "0" only.

The detector-warner may be mounted at any distance (close, near, not so far, far) away from hail preventing sonic generator **.** The antenna may be directed to the sky under any elevation (vertical) and azimuth angles. Preferable elevation angle is from the interval 0-30 ^{0} from the vertical. When the detector-warner is mounted close to the hail preventing sonic generator then more preferable interval for radiometric observation is 0-10^0 from the vertical. Preferable azimuth direction for radiometric observation is the sector North West-North-North East, since it allows practically exclude the sun direct influence on antenna at any time and at any season. For the detector-warner any kind of antenna may be used, with any beamwidth. Preferable antenna beamwidth is 10-20 ^{0} at 3dB level. Radiometric receiver **(16)** may operate at any allowed central radio frequency from L to W-band of microwave (L, S, C, X, Ku, K, Ka, W), at any interference (noise) free bandwidth of receiving (reception) and at any polarization of sensing. Preferable bands for operation are X, Ku, K and Ka. For the detector-warner any type radiometric receiver may be used. For the radiometric receiver preferred integration time is 1-5 second and preferred sensitivity is 01-05K in dependence on frequency band.

When the detector-warner is mounted far (away) from hail preventing sonic generator then it is preferable to control the hail preventing sonic generator remotely and transfer warning (alert) signals generated by the warning device to control means by means of cell phone, by radio aids (by radio technical devices), by means of radio communication, by means of telephone communication, or by other technical means of communication.

Detail descriptions of structural, technical, operational and application features of hail preventing sonic generator **(9)** are presented in [9,10].

The hail preventing sonic generator's impact area is limited in a size and usually is about 500-600m in a radius over the generator [3]. Therefore, the hail preventing sonic generator is mounted near protected agricultural fields and lands.

3. References

[1] Russian Patent, RU 2083999, G01S 13/95, 1997

[2] Russian Patent, RU 1839961, A01G 15/00, 2006

[3] U.S. Patent, US 5381955, E01H13/00, 1995

[4] Armenian patent, Patent AM 2505, E01H 13/00, 2011

[5] A.K.Arakelyan, I.K.Hakobyan., A.A.Arakelyan, A.K.Hambaryan, M.L.Grigoryan, V.V.Karyan, M.R.Manukyan, G.G.Hovhannisyan, N.G.Poghosyan and T.N.Poghosyan, "Dual-Channel, Polarimetric, Combined Scatterometer-Radiometer at 5.6GHz", Electromagnetic Waves and Electronic Systems, Vol.11, No.2, 2007, pp.41-47. (In Russian).

[6] A.K.Arakelyan, I.K.Hakobyan., A.A.Arakelyan, A.K.Hambaryan, M.L.Grigoryan, V.V.Karyan, M.R.Manukyan, G.G.Hovhannisyan, N.G.Poghosyan and S.F.Clifford, "Ku-Band, Short Pulse, Dual-Polarization, Combined Scatterometer-Radiometer", Progress in Contemporary (Present-Day) Radio Electronics, No.12, 2007, pp. 41-50. (In Russian).

[7] A.K.Arakelyan, A.K.Hambaryan V.V.Karyan, G.G.Hovhannisyan, M.L.Grigoryan, I.K.Hakobyan, M.R.Manukyan, A.A.Arakelyan and G.G.Muradyan "K_u-band, combined scatterometer-radiometer system and the results of preliminary polarimetric measurements of snow, bare and vegetated soil, waved water surface microwave reflection and emission", Radar Sensor technology XIII, edited by Kenneth I. Ranney, Armin W. Doerry, Proc. of SPIE, vol.7308, 2009, pp. 730816-1-730816-12.

[8] A.K.Hambaryan, A.K.Arakelyan, A.A.Arakelyan, S.A.Darbinyan, M.L.Grigoryan, I.K.Hakobyan, V.V.Karyan, M.R.Manukyan, G.G.Muradyan and G.G.Hovhannisyan, "C-band, polarimetric, combined radar-radiometer system and the results of measurement of waved water surface microwave reflective and emissive characteristics angular dependences", Ocean Sensing and Monitoring, edited by Weillin (Will) Hou, Proc. of SPIE, vol.7317, 2009, pp. 7317OM-1-7317OM-11.
[9] Armenian patent # 2746 A.
[10] PCT/AM2012/000001 application number, International Publication Number WO 2013/078485 A1.

Acknowledgement

Authors express their gr atitude to the Internationa l Science and Technology Center of M oscow (ISTC), since the experi mental si te and ArtAr-5.6, ArtAr-1 5 and ArtAr-37 com bined scattero metric-radiometeric systems were developed and built due to the financial maintenance provided by ISTC through the Project A-872 and A-1524.

The Results of C-, Ku-, and Ka-band multi-frequency radiometric measurements of clear air and clouds brightness (antenna) temperatures

A.K. Hambaryan[1], A.K.Arakelyan[1,2], A.A.Arakelyan[1]

[1]*ECOSERV Remote Observation Centre Co. Ltd., 2 G. Njdeh str., #24, 0006, Yerevan, Armenia*
[2] *Institute of Radiophysics and Electronics, Alikhanian Brothers str. 1, 0203, Ashtarak, Armenia*

In this paper the results of multi-frequency (at 5.6GHz, 15GHz and 37GHZ) and polarization measurements of clear air and clouds brightness (antenna) temperatures are presented, measured under various observation angles. The results have been obtained during the measurements carried out in Armenia from the measuring complex built under the framework of ISTC Projects A-872 and A-1524. The measurements were carried out at vertical and horizontal polarizations, under various angles of sensing by C-, Ku-, and Ka-band combined scatterometric-radiometric systems (ArtAr-5.6, ArtAr-15, and ArtAr-37) developed and built by ECOSERV Remote Observation Centre Co.Ltd. under the frameworks of the above Projects. In the paper structural and operational features of the utilized system and the whole measuring complex will be considered and discussed as well.

1. Introduction

Hail and shower cause great and severe damage to agriculture and human properties. To reduce material damage in size it is necessary to have many stations of anti-hail protection equipped by hail clouds detector-classifiers. Usually, for hail detection powerful Weather Doppler radar is used, operating at short centimeter or millimeter band of waves. These radars cost several hundred thousand USD, have serious disadvantages and cannot solve the problem totally. Therefore a reason is appeared to develop and to produce new kind of detector-identifiers, which will cost cheaper and have additional advantages.

Clouds brightness temperature is a function of many parameters, in which air and particles temperature, fraction type (water or ice) and particles size are the principal variables. The changes of clouds radio brightness temperatures, related with the changes of dielectric properties of particles and their temperatures, depend on frequencies and polarizations of observation. Therefore, by synergetic application of data of multi-frequency and multi-polarization microwave radiometric observations it is possible to detect and to recognize type of the clouds, its water content and the stage of transformation of water vapour and drops of water to hail (to ice). Radiometric observation may not miss the stage of transformation of water vapour and drops of water to hail, because water and ice dielectric constants are very differ and such formations' brightness temperatures will sufficiently vary one from the other. So, for precise and high probable detection and classification of hail clouds, for real time scale recording of hailing time, for upcoming hail storm's start time prediction, for retrieval of hail-stones' probable sizes, for assessment of expected quantity of hail precipitation it is necessary to develop multi-frequency and multi-polarization microwave radiometric system to carry out clear sky and clouds sustainable monitoring. Before that, it is necessary to specify appropriate frequencies and polarization for solution of hail clouds detection, classification and precipitation parameters and quantities assessment by multi-frequency and multi-polarization microwave radiometric system.

In this paper the results of multi-frequency (at 5.6GHz, 15GHz and 37GHZ) and polarization measurements of clear air and clouds brightness (antenna) temperatures are presented, measured under various observation angles. The results have been obtained during the measurements carried out in Armenia from the measuring complex built under the frameworks of ISTC Projects A-872 and A-1524. The measurements were carried out at vertical and horizontal polarizations, under various angles of sensing by C-, Ku-, and Ka-band combined scatterometric-radiometric systems (ArtAr-5.6, ArtAr-15, and ArtAr -37) developed and built by ECOSERV Remote Observation Centre Co.Ltd. under the frameworks of the above Projects. In the paper structural and operational features of the utilized system and the whole measuring complex will be considered and discussed as well [1-4].

2. Measuring facilities and microwave devices

The measurements were carried out in ECOSERV Remote Observation Centre's experimental site, equipped by indoor and outdoor measuring platforms, scanners, an indoor calibration room and facilities (See Fig.1) [1-5]. The calibration facilities of the indoor calibration room are used for microwave devices external calibration purposes, by sky and by indoor ABB layer. Besides of calibration needs this indoor measuring complex is used for researches of clouds and precipitations microwave features.

Fig.1 The experimental site of the ECOSERV ROC Co.Ltd.and the indoor calibration room with the scanner and CSRS

For these measurements C-, Ku-, and Ka-band radiometers of ArtAr-5.6, ArtAr-15, and ArtAr-37 combined scatterometric-radiometric systems (CSRS) were used [6-10]. The main technical characteristics of utilized ArtAr-5.6, ArtAr-15, and ArtAr-37 systems' radiometers are presented in the Table below.

	ArtAr-5.6	*ArtAr-15*	***ArtAr-37***
Central frequency	5,6GHz	15GHz	37GHz
Antenna and beamwidth	Parabolic 5.2^0	Parabolic 5.6^0	Horn 7^0
Radiometer receiver's bandwidth	~0.5GHz	~0.5GHz	~1GHz
Radiometer channel's sensitivity at 1s	~0.1K	~0.2K	~0.3K

Detail descriptions of utilized CSRS and the whole experimental site and facilities are possible to find as well in http://www.ecoservroc.com. The principal advantages of these unique measuring complex are the capability to perform, multi-frequency, spatio-temporally combined angular and polarization measurements of soil, snow, ice, water surface, clear air, clouds and precipitation microwave, active-passive characteristics, under controlled and far field conditions of sensing. Except of the above mentioned external calibration facilities radiometric channels of all utilized CSRS have internal calibration modules, comprising thermo stabilized noise input generators and thermo stabilized, controlled microwave input keys. These keys in their switched off operational mode are used as internal calibration levels (starting points) for estimation of measured data, such as water surface, external calibration ABB layers and sky brightness temperatures. The noise generators feed the systems' inputs by specified calibration noise signals of 18K of level, for instance, which are necessary for estimation of observed surfaces and sky brightness temperatures fluctuations.

The measurements of clear air (sky) and clouds brightness temperatures were carried out by two ways. The first way includes direct measurements of sky brightness temperatures from indoor calibration room or from outside located (outdoor) platform. Outdoor platform allowed carry out measurements of sky brightness temperature under various azimuth angles as well.

The second way includes measurements of changes of smooth water surface brightness temperature due to appearance of clouds and precipitation. Scatterometric measurements by a scatterometers of utilized ArtAr-5.6, ArtAr-15, and ArtAr-37 CSRS were used to estimate perturbation level of pool water surface, for correction clouds and precipitation contribution in water surface brightness temperature.

3. The results of measurements

Before and after all series of measurements of sky brightness temperature (antenna temperatures or more exact apparent temperatures) from indoor platform the measurements of indoor ABB layer's brightness temperature (antenna temperatures or more exact apparent temperatures) were carried out. Measurements of sky brightness temperature from indoor platform were carried out consequently under elevation angles 10^0 and 30^0 from nadir at both vertical and horizontal (cross) polarizations of observation. Before and after all series of measurements of sky brightness temperature from out door platform the measurements of noise temperatures of ArtAr-5.6, ArtAr-15, and ArtAr-37 CSRS radiometric channels' controlled microwave input keys at their switched off operational modes were carried out, to get starting points for estimation the absolute values of sky brightness temperatures at various frequencies and polarizations.

Before all series of measurements of pool water surface microwave reflective and emissive characteristics, preliminary measurements of indoor ABB layer's and clear sky brightness temperatures at observation angles 10^0 and 30^0 from nadir were performed. After that, the CSRSs were set on the mobile buggy and measurements of smooth pool water surfaces were carried out at each angle of incidence from 80^0 to 0^0, by a step of 10^0. The measurements were carried out at "v" and "h" polarizations for radiometric observations and at "vv" and "vh" or "hh" and "hv" polarizations for scatterometric observations, under various conditions of water t_w and air t_a temperatures. During each series of measurement, at the beginning and at the end of the series, an internal calibration noise signals were switched on and were used for calibration of data obtained by radiometric channels of observation. For scatterometric channels calibration internal calibration signals of a level of $\sim 10^{-11}$W were used, estimated to the receivers inputs. These calibration signals allowed approximately estimate absolute values of water surface radar backscattering coefficients and brightness temperatures. Remote control of each CSRS was performed by its personal computer set in the work laboratory built just near the platforms. During measurements the output signals of scatterometric and radiometric receivers were recorded by personal computers as a file. After each series of measurements the saved files have been reproduced on the computer monitor as chart records and were used for further processing and estimation of the observed surface radar backscattering coefficients and brightness (antenna) temperatures at various polarizations and frequencies.

The absolute values of water surface or sky brightness temperatures were estimated from the following equation:

$$T_{Bi} = T_i^K - \frac{U_i^K - U_i^S}{\Delta U_i^{cal}},$$

where, $T_{Bi} = \chi \cdot (273 + t_K)$ is a brightness temperature of the matched load, t_K is a physical temperature of the matched load in centigrade, the coefficient of emission of the matched load χ was estimated and was taken equal to 0.99. U_i^K, U_i^S and ΔU_i^{cal} are outputs of the radiometer receiver, corresponding to the matched load, water surface or sky and the increment of the radiometric output's due to internal calibration noise signal's switching, respectively. The accuracy of estimation of the absolute value of water surface and sky brightness (antenna) temperatures is about 8-15K, in accordance with the frequency. The accuracy of relative measurements of angular changes of water surface and sky brightness (antenna) temperatures is better than 0.1-0.5K, for C-Ka-band, respectively.

In Fig.2 measured values of clear sky, lightely clouded and cloudy sky brightness temperatures are presented, measured at 37GHZ from indoor calibration room. The results of such measurements at 15GHz are presented in Fig.3.

In Fig.4 the results of direct measurements and corresponding estimations of clear air and various kind of cloudy sky brightness (antenna) temperatures measured simultaneously at 5.6GHz, 15GHz and 37GHz are presented. In accordance with the results of Fig.4 the radiothermal contrasts between clear air sky and cloudy sky brightness temperatures may reach up to 30-40K at 37GHz and ~15-20K at 15GHz. For hail clouds the contrasts may reach 50-100K in dependence of the frequency of sensing.

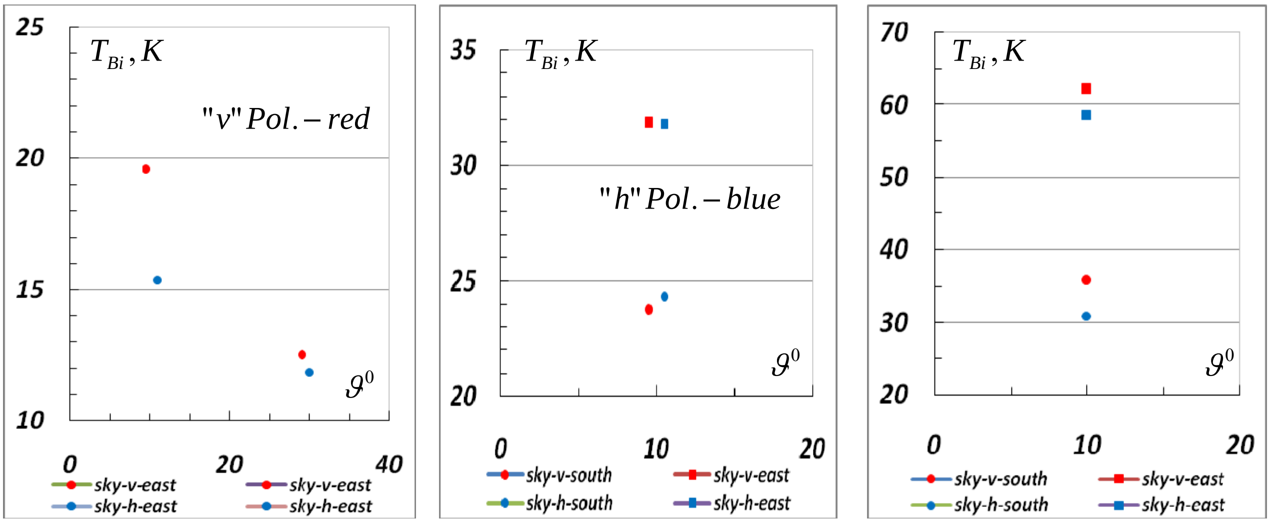

Clear sky Lightely clouded sky Cloudy sky

Fig.2 The measured values of clear sky, lightely clouded and cloudy sky brightness temperatures at 37GHz

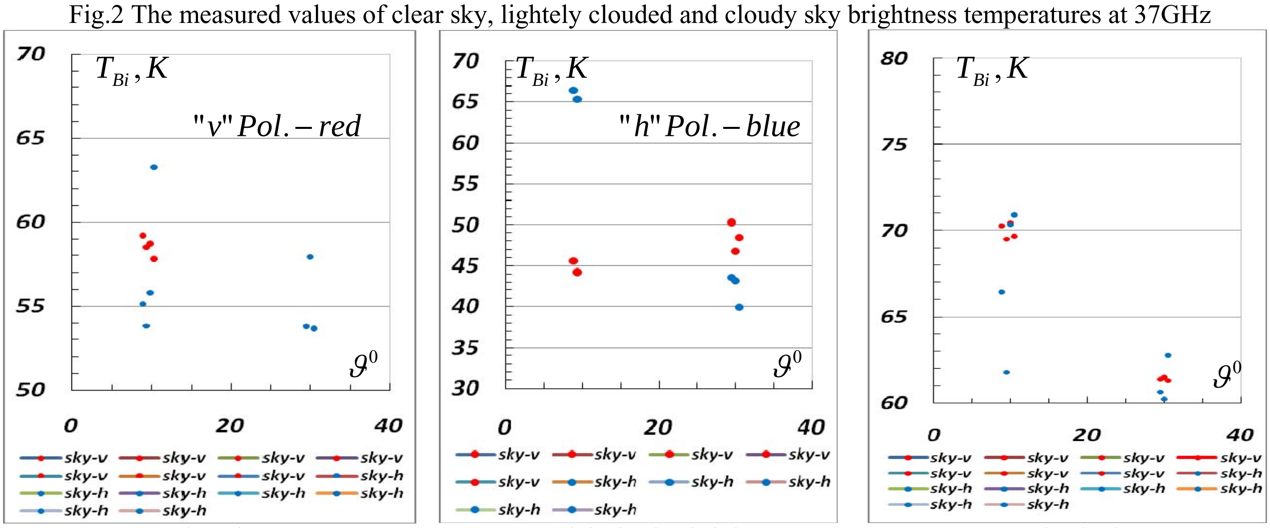

Clear sky Lightely clouded sky Cloudy sky

Fig.3 The measured values of clear sky, lightely clouded and cloudy sky brightness temperatures at 15GHz

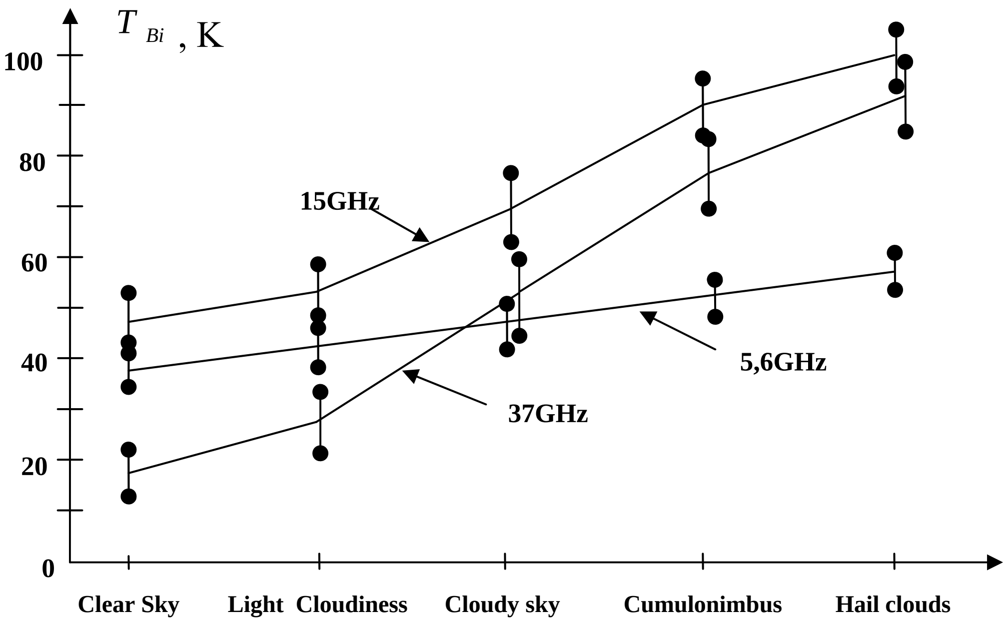

Fig.4 The measured and estimated values of clear sky and cloudinesses brightness (antenna temperatures at 5.6GHz, 15GHz and 37GHz

6. References

[1] A.K.Arakelyan, I.K.Hakobyan., A.A.Arakelyan, A.K.Hambaryan, M.L.Grigoryan, V.V.Karyan, M.R.Manukyan, G.G.Hovhannisyan, N.G.Poghosyan and T.N.Poghosyan, "Dual-Channel, Polarimetric, Combined Scatterometer-Radiometer at 5.6GHz", Electromagnetic Waves and Electronic Systems, Vol.11, No.2, 2007, pp.41-47. (In Russian).

[2] A.K.Arakelyan, I.K.Hakobyan., A.A.Arakelyan, A.K.Hambaryan, M.L.Grigoryan, V.V.Karyan, M.R.Manukyan, G.G.Hovhannisyan, N.G.Poghosyan and S.F.Clifford, "Ku-Band, Short Pulse, Dual-Polarization, Combined Scatterometer-Radiometer", Progress in Contemporary (Present-Day) Radio Electronics, No.12, 2007, pp. 41-50. (In Russian).

[3] A.K.Arakelyan, A.K.Hambaryan V.V.Karyan, G.G.Hovhannisyan, M.L.Grigoryan, I.K.Hakobyan, M.R.Manukyan, A.A.Arakelyan and G.G.Muradyan "K_u-band, combined scatterometer-radiometer system and the results of preliminary polarimetric measurements of snow, bare and vegetated soil, waved water surface microwave reflection and emission", Radar Sensor technology XIII, edited by Kenneth I. Ranney, Armin W. Doerry, Proc. of SPIE, vol.7308, 2009, pp. 730816-1-730816-12.

[4] A.K.Hambaryan, A.K.Arakelyan, A.A.Arakelyan, S.A.Darbinyan, M.L.Grigoryan, I.K.Hakobyan, V.V.Karyan, M.R.Manukyan, G.G.Muradyan and G.G.Hovhannisyan, "C-band, polarimetric, combined radar-radiometer system and the results of measurement of waved water surface microwave reflective and emissive characteristics angular dependences", Ocean Sensing and Monitoring, edited by Weillin (Will) Hou, Proc. of SPIE, vol.7317, 2009, pp. 7317OM-1-7317OM-11.

On the Method of Distant Infrared Monitoring of Gas Main Pipelines

R.S. Asatryan[1], H.S. Karayan[2], N.R. Khachatryan[1]

[1]*National Institute of Metrology, Komitas ave. 49/4, 0051, Yerevan, Armenia*

[2]*Yervan State University,1 A.Manoogian str.,0025, Yerevan, Armenia*

The development results of a new method of aerial (on a helicopter or airplane) infrared (IR) scanning of gas main pipelines and detecting gas leaks is described. IR scanning of pipelines was performed in the wavelength range 8–12 μm by a helicopter flying along the routes of pipelines. In the paper there is presented the description of the IR radiometer as well as the measurement method of point and extended thermal sources wavelength range of 2.5 to 5.5 and 8-12 microns.

1. Introduction

The environment monitoring, investigation and control of ecological conditions attract a great attention of the mankind, especially at the present stage of development of industry, energetic and urban building.

Optoelectronic systems and devices designed for application in ecological studies and in arising extremely situations are always in the center of the scientists' and engineers' attention.

The main artificial source of atmospheric gaseous pollution is leakage of natural gas, in which the methane content is 95%. However, the problem is aggravated by the fact that gas main pipelines (GMPs) run through sparsely inhibited and hard to reach territories, where testing is especially impeded.

It is obvious that the development of a state of the art remote and efficient method for ecological monitoring of GMPs is especially pressing. In this situation, the only practical method is remote testing from an aircraft (e.g., a helicopter) flying along the pipeline route at heights of up to 1000 m.

The objective of this study is the description of a universal IR spectroradiometer (SR) we developed and demonstration that one possible field of its application is the airborne IR monitoring of GMPs.

Therefore, the development and creation of infrared devices and systems of thermal monitoring of environment is a rather important problem.

2. Brief Technical Description of a Measuring System

Structurally the measuring complex consists of two basic units: an optico-mechanical unit of the IR radiometer and an electronic control unit joined to a personal computer. It is designed to measure spectral radiance and radiation temperature (or its drops) of point and extended sources of infrared radiation under laboratory and field conditions [1-3]. To automate data acquisition and processing the spectroradiometer is joined to a personal computer via a series port RS 232. Optical scheme of the optico-mechanical unit (OMU) is shown in Fig.1.

- Input mirror objective of Cassegrain type;
- A telescope for operative pointing to an object under test, equipped with a sighting grid visible through an eyepiece on the OMU back panel;
- Parallax free sight for accurate pointing the spectroradiometer to an area to be measured. The sight has a sighting grid with a cross and a circle which defines visual field boundaries of the device;
- Projection objectives which serve for refocusing the radiation from a field diaphragm to the plane with light filters and to a sensing site of the photodetector. They represent pairs of spherical mirrors the application of which enables to avoid achromatic aberrations;

- A block of removable ring wedge variable light filters which provide a total working spectral range of 0.4 to 14μm;
- A photodetector which structurally represents a removable block with a photodetector placed inside it in accordance with the spectral range, a preamplifier, and an adjusting

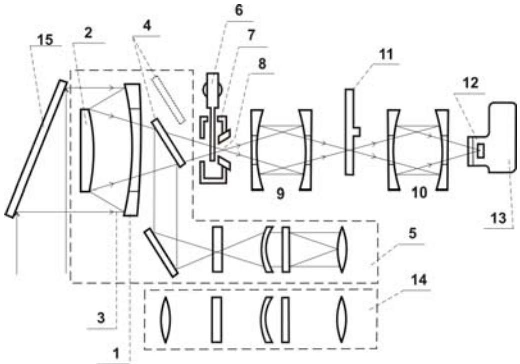

Figure 1. Optical scheme of OMU.1-Primary mirror of the objective; 2- secondary mirror of the objective; 3- radiation from an object; 4- removable plane mirror; 5- a sight; 6- a modulator; 7- a reference cavity; 8- a field diaphragm; 9,10- projection objective; 11- a disk with interferential light filters; 12- a sensing site of the photodetector; 13- a thermos for liquid nitrogen; 14- a telescope; 15- a deflection mirror.

Full working spectral range of the device is covered with the help of three sets of removable light filters and photodetectors in the sub bands of 0.4 to 1.1 μm, 2.5 to 5.5 μm, and 8 to 14 μm. Main technical parameters of the device are given in the Table.

№	Parameter Name	Value
1.	Input objective diameter	180 mm
2.	Focal distance mechanism.	200 mm
3.	Distances to be focused	from 5m to ∞
4.	Working spectral range I sub band (spectral resolution of 10 %) II sub band (spectral resolution of 3 %) III sub band (spectral resolution of 8 %)	from 0,4 to 14 μ m from 0,4 to 1,1 μ m from 2,5 to 5,5 μ m from 7,9 to 13,5 μ m
5.	Photodetectors : I sub band II sub band III sub band	 Si – photodiode InSb – photoresist CdHgTe – photoresist
6.	Field of vision	3 mrad
7.	Noise equivalent difference of the radiation temperatures (at 295^o K)	0,05 K
8.	Continuous work time	8 hours
9.	Time of preparation to work	15 min
10.	Dimensional size of spectroradiometer: OMU ECU	 415x278x254 mm 500x420x210 mm
11.	Weight: OMU ECU	 not more than 12 kg not more than 15 kg
12.	Climatic conditions of operation: Ambient temperature Atmospheric pressure Air relative humidity	 from –35^o to +45^o from 84 to 107 kPa (from 630 to 800 mm Hg) up to 98% at 35^{o}C

13.	Supply voltage frequency	(220 ± 22) V (50 ± 1)Hz
14.	Power consumed	not more than 200W

During operation the OMU, by means of the wedge guide, is placed on a rotary mechanism which is fastened to the horizontal platform of a specially prepared tripod

The electronic control unit (ECU) is structurally of on-top variant. All indication and control elements are mounted on the front panel of the ECU.

Under laboratory conditions the ECU is placed on the table, and under field conditions it can be mounted in a helicopter with the help of dampers. External appearance of the units is shown in Fg.2.

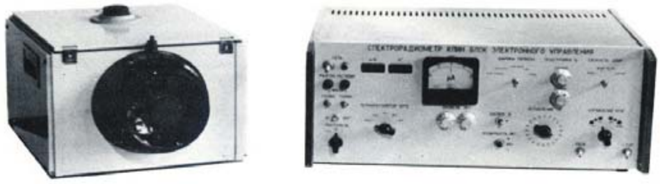

(A) (Б)

Figure 2. External appearance of the radiometer A)OMU, Б) ECU.

In brief, the operation principle of the spectroradiometer consists in the following: Inside the OMU the radiation flow from the object under test is collected by means of an optical system (see Fig.1) and focused onto a sensing site of the photodetector. Further, a preamplifier amplifies an electric signal and transmits it to the ECU. In the ECU the electronic schemes amplify, demodulate and filter the signal from the photodetector output, and as a result of this there appears a signal at the output the amplitude of which is a measure of the radiation temperature of the object. Knowing the value of the collected radiation power (through the data of preliminarily conducted energetic calibration of the device), spectral filter features of the system and amplification degree, the output signal can be exactly transformed into an absolute measurement of radiation temperatures of the objects under test.

Let's notice some advantages of the IR radiometer developed by us [4] compared to the existing close analogs. To widen functional capabilities in the sphere of spectral investigations of thermal objects, besides wideband interferential light filters for spectrum parts of 0.4 to 1.1,2.5 to 5.5., and 8 to14 μm, the device is also provided with ring reflective light filters. To eliminate chromatic aberrations the device optical scheme includes two pairs (see Fig.1) of mirror projection objectives in the focuses of which there are placed light filters and the receiving site of photodetectors.

The IR radiometer is mounted in the helicopter and, with the help of a deflecting plane mirror, by its field of vision scans (through the bottom hatch, along the helicopter motion routing) terrestrial surface.

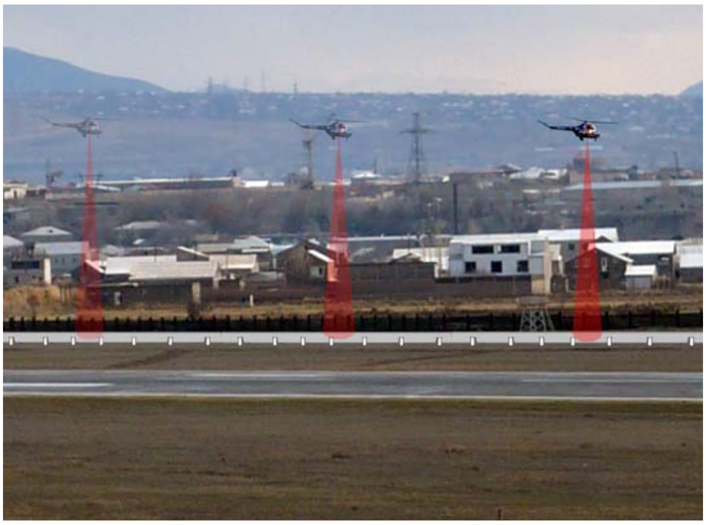

Figure 3. Helicopter IR scanning of GMPs.

The IR radiometer scans the Earth's surface along the GMPs routes within its field of view through the bottom hatch. If there are macroscopic gas leaks in this region, the radiation temperature (in the wavelength region 8–14 μm) drops significantly [5] and is recorded by the ECU.

At helicopter flight altitudes of 200 and 150 m, the radiometer fields of view on the ground encompass surfaces with radius of ~6 and ~2.5 m, respectively, see fig. 3.

With the helicopter speed of 150-200 km/hr the time of one measurement cycle is 0.1 sec.

3. Measurement Technique of IR Flows From Extended and Point Thermal Sources

Before carrying out quantitative measurements of IR radiation emitted by an unknown source, it is necessary to fulfill energetic calibration of the spectroradiometer, the aim of which is the measurement of the device response to the known standard source (usually a black body with known temperature). By definition, the device calibration means obtaining an electrical signal at the output, which corresponds to a radiation flow unit incident into the radiometer inlet. The calibration is expressed by some function k(λ) called spectral calibration characteristic of the device, which includes combined effect of optical elements and electronic amplification of the whole system. k(λ) is expressed in V/radiation unit, with standard level of amplification degree. An output signal of the device is proportional to the difference between the IR radiation flows coming to the photodetector from an external source and from the internal modulated reference black body. In calibrating the radiation from the calibration black body (with known temperature) entirely fills the device field of vision. An output signal S(λ) is expressed by the following ratio:

$$S(\lambda) = k(\lambda)\cdot\{r(\lambda,T)\cdot\tau(\lambda,l) - r(\lambda,T_0) + r(\lambda,T_B)[1-\tau(\lambda,l)]\} \quad (1)$$

where $r(\lambda,T)$ is Plunk function at the temperature T and the wavelength λ;

T – temperature of the calibration black body;

$\tau(\lambda,l)$ – atmospheric transparency over the path l between the calibration source and device;

T_0 – temperature of the internal reference black body;

T_B – temperature of the air during the experiment.

In the windows of the atmosphere transparency (e.g. for the wavelength range of 2.5 to 5.5 μm), where the transmission is high, $\tau(\lambda,l)$ may be taken as 1, if the calibration is carried out from the distance "l" equal to several meters. Therefore in this approximation for $S(\lambda)$ we can write:

$$S(\lambda)=k(\lambda)\cdot[r(\lambda,T)-r(\lambda,T_0)] \quad (2)$$

with the amplification coefficient equal to 1. And in measuring with the amplification coefficient different from 1 the $S(\lambda)$ value decreases by the same factor. The Plunk function value is calculated according to the ratio:

$$r(\lambda,T)=\frac{c_1}{\lambda^5}[\exp(c_2/\lambda T)-1]^{-1}$$

where

$c_1=3{,}74-10^4$ W μ m^4/cm^2

$c_2=1{,}438\cdot10^4$ μ m deg

The objects studied the radiation flow of which completely fills the device field of vision are extent in these measurements. In this case radiance spectral density (W (λ,T) W/cm^2 μ m) of the object is measured. The ratio (1) may be rewrite as:

$$S(\lambda)=k(\lambda)\{W(\lambda,T)\cdot\tau(\lambda,l)-r(\lambda,T_0)+r(\lambda,T_B)[1-\tau(\lambda,l)]\}\cdot\beta \quad (3)$$

where $W(\lambda,T)$ is the radiance spectral density of the object studied, β is an amplification coefficient of the whole system, and the rest symbols remain previous. The atmosphere transparency $\tau(\lambda,l)$ is either measured simultaneously, or calculated with the help of data from literature [5,6]. From the ratio (3) we can get for $W(\lambda,T)$:

$$W(\lambda,T)=\frac{S(\lambda)/k(\lambda)\beta+r(\lambda,T_0)-r(\lambda,T_B)\cdot[1-\tau(\lambda,l)]}{r(\lambda,l)} \quad (4)$$

Usually the radiation of point sources does not fill the visual field of the device. If the area A of a radiating object is known we can measure its spectral radiance according to the above-stated technique, that is

$$W_p(\lambda,T)=W(\lambda,T)\cdot\omega\cdot\frac{l^2}{A} \quad (5)$$

Where ω is a solid angle of the spectroradiometer visual field, W(λ,T) is a total spectral radiance measured according to (4); l is the distance from the object under test to the spectroradiometer. While measuring point sources spectral contrast of a radiation source is also of interest, when the background radiance is comparable to the object radiation. In this case it is necessary to separate the background signal $S_\Phi(\lambda)$ from the signal "source+background" S(λ). For the spectral radiation contrast of the source we can get the ratio:

$$W(\lambda)=\frac{\Delta S(\lambda)\cdot\omega\cdot l^2}{\beta\cdot k(\lambda)\cdot\tau(\lambda,l)A} \quad (6)$$

Where $\Delta S(\lambda)=S(\lambda)-S_\Phi(\lambda)$

If A is unknown we may define the contrast of the spectral luminous intensity of the source (in W/strad.μm):

$$I(\lambda)=W(\lambda)\cdot A=\frac{\Delta S(\lambda)}{\beta\cdot k(\lambda)\cdot\tau(\lambda,l)}\cdot\omega\cdot l^2 \quad (7)$$

Calculation of the radiation temperatures of the objects under test is carried out in accordance with specially developed algorithms and programs.

4. Conclusion

Application of the given method of remote ecological monitoring of vast forest spaces and extended gas pipelines will undoubtedly bring to the considerable technical-economical effectiveness and will also have a great importance in the problem of monitoring atmospheric pollution from natural – gas emissions.

5. References

[1] R.S. Asatryan, Optoel ectronic Methods and Mean s of Intesting Ph ysico-Ecological Parameters of Atmosphere and Thermal Objects, Ne ws of NAS RA, Techn. Sciences, Vol. LX, No. 2 , (200 7), 30 7(in Russian). [2] R.S. Asatryan , S.R. Asatryan , et al., Infrared Scan ning Complex for Preventing Large-Scale Fires, Ecological Sy stems and Devices, No. 1,(2008) 17(in Russian). [3] R. S. Asatryan et al. Universal Infrared Spectral Radio meter. Intern. Journal of IR and MM Wav es, vol. 24, N o. 6..(2003), 1035. [4] R.S. Asatryan, H. G . Gevorg yan et al. The Spectroradiom eter, Patent of Ra, No.1678 A2, Appl. No. P20050042, 11.04.2005.(in Armenian). [5] B. V.Shilin and I. A. Molodchi nin, Kontr ol' sostoy aniya okruzhayushchei sredy tepl ovoi (Monitoring of Environment by IR Aerial Survey), Moscow: Nedra, 1992. [6] P. Kruz , aeros"emkoi (Mo nitoring of E nvironment by IR Aerial Survey), M oscow: Nedra, 1992. 464p.(in Russian). [7] A.V. Pavlov , Optoelectronic Devices, M. Energia, 1974, 360p(in Russian).

Optical-Electronic Equipments of Ecological Dedication

R.S. Asatryan[1], H.S. Karayan[2], N.R. Khachatryan[1]

[1] *National Institute of Metrology, Komitas ave. 49/4, 0051, Yerevan, Armenia*
[2] *Yerevan State University, str. A. Manoogyan 1, 0025, Yerevan, Armenia*

The creation of optoelectronic devices and systems with the best metrological parameters that enable the operational analysis of basic physical and environmental parameters, and distant monitoring of the atmosphere and air infrared environmental control of vast forest spaces (for detection of fires in the early stages of their development) and pipelines of natural gas is a very important task. The present work is devoted to presenting the results of research and development work on the development and manufacturing of optical-electronic instruments for environmental purposes to explore the basic physical and ecological parameters of the atmosphere, as well as monitoring forest spaces and main gas pipelines.

1. Introduction

Currently sharply increased interest in environmental issues, which is primarily due to the ever-increasing contamination of the environment.

According to the latest data on the study of atmospheric pollution in industrial developed countries [1-4], the main sources of pollution are industrial and energy facilities and transport, which accounted for over 80% of the total amount of pollution. The major components of air pollution are gaseous compounds of carbon, nitrogen and sulfur, as well as solid and liquid aerosol formation, which are of particular concern for the normal functioning of humans and other biological objects [5-6].

Significant contamination of air space and its devastating effects on human health, climate and vegetation is also due to macroscopic leaks (or sometimes emissions) of natural gas pipelines and extensive fires, particularly forest areas.

Therefore, the creation of optoelectronic devices and systems with the best metrological parameters that enable the operational analysis of basic physical and environmental parameters, and distant monitoring of the atmosphere and air infrared environmental control of vast forest spaces (for detection of fires in the early stages of their development) and pipelines of natural gas is a very important task.

The present work is devoted to presenting the results of research and development work on the development and manufacturing of optical-electronic instruments for environmental purposes to explore the basic physical and ecological parameters of the atmosphere, as well as monitoring forest spaces and main gas pipelines.

2. Optical-Electronic Measuring System for Atmospheric Transparency

Measuring complex called "The Field Optical-meteorological post-Machine (FOMPA)" [7], designed for continuous measurement of meteorological optical range, or the extinction of the atmosphere in the wavelength range from 0.35 to 1.1 microns, and the automatic processing of the results of the spectral transparency of the atmosphere in the range of from 1 to 14 microns.

Complex "FOMPA" is composed of two units: Optical-mechanical (OMU) and electronic control unit (ECU).

Optical scheme OMU is shown in Figure 1.

Optoelectronic d evice pa th i s formed o f three c hannels, measuring, con trolling and o f the backg round. Unlike remote (OMU) unit, which operates directly in the atmosphere, ECU and recording of the complex may be in the room or in the back of the auto laboratory for the distance control the operation of the equipment.

When full-scale measurements in the atmosphere calculation of the attenuation of the atmosphere $\alpha(t_i)$ and meteorological visibility range $S_M(t_i)$ at any given time (t_i) in absolute units is based on measurements of the measuring signal $U_1(t_i)$, background $U_2(t_i)$ and control $U_3(t_i)$ channels, according to the relations:

$$\alpha(t_i) = A \cdot \left(U_3^0 / U_3(t_i)\right)\left(U_1(t_i) - U_2(t_i)\right); \tag{1}$$

$$S_M(t_i) = 3.91/\alpha(t_i) \tag{2}$$

on wave length $\lambda = 0.55\ \mu m$.

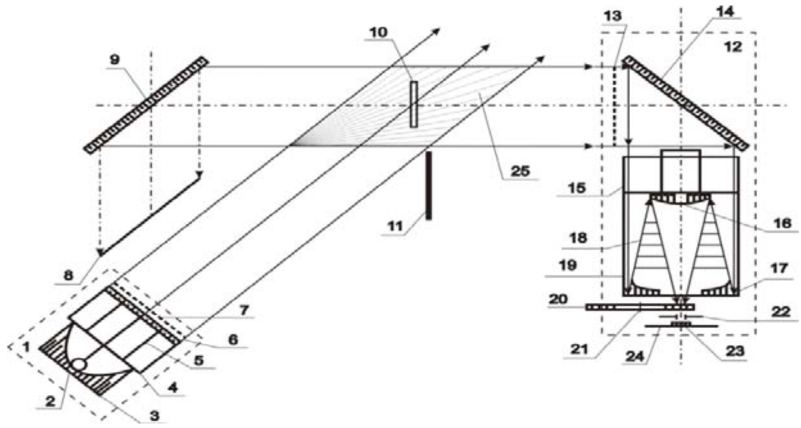

Figure 1. Optical Scheme of OMU Measurer of Spectral Transparency of the Atmosphere: 1-illuminating; 2-lamp ISSH-100-5; 3-parabolic mirror; 4,15-cellular hood; 5,11-screen; 6.23-protective glass; 7.13-iris aperture; 8-absorber of light; 9-mirror "Black"; 10-control lens; 12-photometer; 14-flat mirror; 16.17-mirror objectives; 18-round lens hood; 19-cylinder lens hood; 20-filter; 21-rotation axis; 22-aperture; 24-plane of FEU; 25-working volume of device.

A significant advantage of the above developed by us optical-electronic complex “FOMPA” compared to the currently operating (especially in the aviation services) similar devices [8] is the ability to provide for periodic monitoring sensitivity of apparatus in the time operating instructions manual and all measurements against the “black” mirrors which provides a high sensitivity reception system.

3. The Metrological Characteristics of Equipment “FOMPA”

Metrological certification of equipment “FOMPA” conducted according to the specially developed program of metrological certification (A EL2.766.000PMA) [9]. When certification apparatus defined metrological characteristics indicated in Table 1.

Experimental studies of the metrological characteristics of the equipment “FOMPA” held in the chamber for an optical calibration, the description of which is presented in [10]. The list of all products used in the certification of the equipment, with its precision classes presented in [9].

Certification shall be subject to the sensitivity of the equipment, “FOMPA” to the value of the attenuation coefficient of the atmosphere. It is determined by recording the electrical signal output apparatus for measuring the attenuation in a clean atmosphere.

Table 1: Metrological Parameters of theEquipment "FOMPA"

The Name of the Metrological Characteristics and Units of Measuring	**Nom. Values**	**Permissible Declinations**
The sensitivity of instruments in the four wavelengths to the value of the attenuation coefficient of the atmosphere, [Km^{-1}/mV]	A_1 (0.35) A_2 (0.55) A_3 (0.70) A_4 (1.10)	± 15% ± 15% ± 15% ± 15%
The ratio of the sensitivity of the equipment for measurements in clean air and carbon gas	2.61	± 0.03
The rms value of relative error in the measurement of the instrument attenuation coefficient of the atmosphere, no more than		± 15%

Electrical output devices "FOMPA" is linearly related to the attenuation coefficient of the atmosphere and the dependence of $U = f[\alpha(\lambda)]$ can be normalized as the main metrological characteristics of the equipment.

The main metrological parameters in equation (1) are the sensitivity of the equipment A (0.55).

The basic error of the measurement sensitivity of the outfit consists of errors of measuring circuits and errors in the determination of the coefficients. Additional hardware error associated with the impact of destabilizing factors such as changes in the ambient atmosphere, changing the supply voltage, vibration loads, etc.

Chimneys control exposed the threshold sensitivity of A (0.55) of the device, which is the measurement error of ± 15% (signal / noise ratio of 2.8).

When the ambient temperature changes from 273 to 313 K (0^0 to 40 ^{0}C) the additional error of the output signal does not exceed 20% of the basic error.

4. Universal Infrared Spectral Radiometer "USR-A"

For the purpose of spectral and radiometric studies of atmospheric and thermal objects parameters in the wavelength range from 0.4 to 14 microns, we have developed and manufactured a universal spectral radiometer "USR-A", a detailed description and principle of operation is presented in [11,12].

"USR-A" is designed to measure the spectral density of the brightness and radiation temperature (or drops) of point and extended sources of infrared radiation in the laboratory and field conditions, as well as for remote spectral analysis of hot gas facilities.

Structurally spectroradiometer made up of two parts: optical-mechanical (OMU) and the electronic control unit (ECU). The electrical connection between the units is by means of cables. Full spectral range of the instrument is covered by three sets of interchangeable filters and photo detectors sub bands: from 0.4 to 1.1 microns from 2.5 to 5.5 microns and from 8 to 14 microns. Optical scheme OMU is shown in Figure 2.

An Electronic Control Unit Constructively Desktop Performance: all organs and display controls are located on the front of the ECU. We note some of the benefits we developed IR spectroradiometer "USR-A" as compared to the existing close analogues (see for example [13]). To extend the functionality of spectral studies of thermal objects, except for the broadband interference filters for spectral regions from 0.4 to 1.1, from 2.5 to 5.5 and from 8 to 14 mm, the device is also provided with the ring tunable optical filters [14].

In order to eliminate chromatic aberrations in the optical system of the device includes two pairs (Fig. 2) Mirror projection lenses, in the focus of which are installed filters and photo detectors tipple.

At the end of this se ction, we no te t hat aft er s ome de sign im provements in t he optical system spectroradiometer "U SR-A" (a dding the inp ut deflecting mirror) in [20] described in d etail the method o f air environmental control of forest spaces and gas main pipelines.

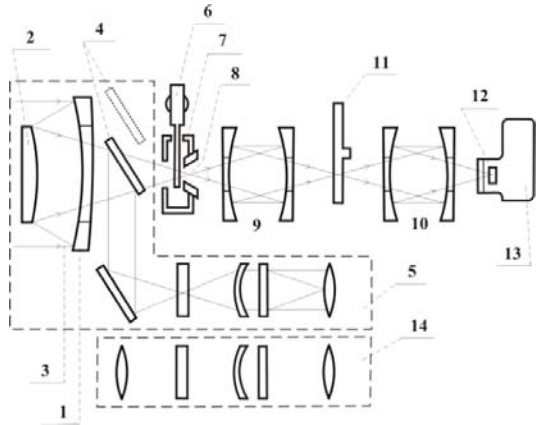

Figure 2. OMB Opti cal Sch eme: 1-Primary mirror lens; 2 -secondary mirror lens; 3-r adiation from the object; 4-r etractable flat mirror; 5-sight ; 6- modulator; 7 -bearing cavi ty; 8-field stop; 9 ,10-projection len s; 11-disk inte rference fil ters; 12-sensitive area of the photo detector; 13-dewar of liquid nitrogen; 14-visual tube.

5. The Metrological Characteristics of a Universal Spectroradiometer "USR-A”

Metrological ce rtification was conducted in a ccordance with th e universal spectrora diometer spe cially designed p rogram o f metrological certifica tion (AEL2 .807.007PMA, [15]). In metrological eva luation determined device characteristics shown in Table 2. In carrying out metrological certification spectroradiometer “USR-A” t o a pply the necessa ry instru mentation a nd e quipment refe rred to in [1 5]. In the sa me pap er the conditions and procedure for certification are presented. Measurements to determine the difference between the radiation temperature equivalents to noise $\Delta T_{eq.N}$, performed with the setup diagram of which is shown in [15].

Value of noise equivalent temperature difference $\Delta T_{eq.N}$ determined by the formula:

$\Delta T_{eq.N} = \dfrac{U_N}{K_{\Delta T}}$, was found to be 0.05 within ± 10%.

To determine the basic error of measurement of radiation temperature difference Spectroradiometer, on the installation of certification established blackbody temperature in the range of 288 to 298 and in increments of 1^0 K, five times the output signals of the device checked.

The standard deviation of the measurements was determined by the formula: $S_{U_{sr}} = \sqrt{\dfrac{\sum_{i=1}^{n}(U_{sri} - U_{sr})}{n(n-1)}}$.

Reduced error in the measurement of the difference between the spectroradiometer radiation temperatures was within ± 15%.

Table 2: Metrological Parameters of the Equipment “USR-A”

The Name of the Metrological Characteristics and Units of Measuring	**Nom. Values**	**Permissible Declinations**	**Comment**
Working spectral ranges, μm : I channel II channel III channel	 0.40-1.1 2.50-5.50 7.90-13.5	 ± 10% ± 10% ± 10%	Provided with filters
Field of view, mrad, no more than: I channel II channel III channel	 3 3 3	 ± 10% ± 10% ± 10%	
The d ifference in noise-equivalent radiation te mperatures, $\Delta T_{eq.N}$, K , no more than: II channel III channel	 0.05 0.05	 ± 10% ± 10%	
Summary reduced measurement error o f the temperature diff erence b etween the radiation ran ge of 0.5 to 20^0 at th e lever 293 ± 5^0 K, no more than: II channel III channel		 ± 15% ± 15%	

6. Multi-Channel Aerosol Spectrometer

Developed m ultichannel aero sol spectrometer “Masnik-A” [16], is the optical-electronic auto matic device for measuring the concentration and si ze d istribution of liqu id an d solid aer osol formations of na tural and artificially origin in the laboratory and field conditions.

Structurally, t he spectrometer consists of two units: t he e lectronic-optical s ensor (EOS) an d the un it o f reference and control (URS), connected by a cable.

The principle of the device is based on measuring the intensity of the radiation scattered by aerosol particles. Optical scheme of EOS is shown in Figure 3.

The op tical system o f the illuminator a nd t he ph oto detector (F igure 3) a re used for the formation o f the optical counting volume (item 11 in Fig. 3) of the sensor. It is a glowing cube with a discrete change in its size, which is achieved by replac ing t he field d iaphragms, wh ich are depo sited on flat bo nding surfaces o f condensers.

Prior to the actual measurements in the atmosphere of the optical calibration of the spectrometer is carried out according to standard polystyrene latex particles [17].

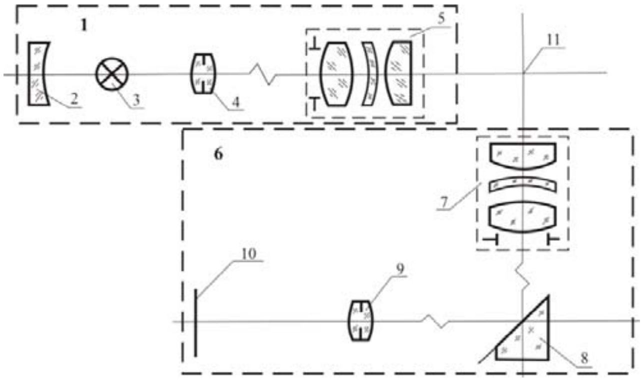

Figure 3. Optical Scheme of the Spectrometer "Masnik-A":1-illuminating; 2-spherical mirror; 3-lamp lighting; 4,9 - condenser with integrated field diaphragm; 5,7-projection lenses; 6-photometer; 8-mirror flat; 10-sensitive area of the photo detector; 11-space of work volume.

At the end of this section should be noted that the advantage of the developed by us aerosol spectrometer, compared with the currently operating appliances similar to [18], is the ability to change (operation unit) orifice size field illuminator and a photometer which in turn leads to a change the geometric dimensions of the working volume (or countable volume, see Figure 3) of the device, which can significantly extend the range of the measured aerosol number concentration of particles from the surrounding area, as well as the design concept of the spectrometer "Masnik-A" in the two blocks, the operation of which ensures the safety of the service operator from possible harmful effects of ambient aerosol.

7. The Metrological Characteristics of a Multi-Channel Aerosol Spectrometer “MASNIK-A”

Metrological certification of multi-channel aerosol spectrometer "Masnik-A" was carried out according to a specially developed program AEL2.851.002PMA [19]. For certification identified metrological characteristics of the instrument are presented in Table. 3.

Table 3 : Metrological Parameters of the Equipment “Masnik-A”

The Name of the Metrological Characteristics and Units of Measuring	Permissible Declinations
The relative error in the reproducibility of the calibration of the instrument at the reference desk of monodisperse aerosol particles, no more than	± 15%
The relative error in the measurement aerosol particles sizes in the range from 0.4 to 40 μm, no more than	± 20%

A list of all assets, conditions and procedures, as well as a description of the measuring system for calibration certification set forth in [19].

The relative error in the reproducibility of the calibration of the instrument is determined by the formula:

$$\delta_g = \frac{d_u - d_0}{d_0} \cdot 100\% \tag{10}$$

where d_0 - nominal size of aerosol particles used reference, du - measured values of particles in micron. The deviation of the reproducibility of the calibration of the instrument was within ± 15%.

To assess the relative accuracy of measurement of dimensions of the aerosol particles, all operations were carried out as set out in [19] and a particle size of 0.5 microns.

According to the formula (3) is defined relative error of measuring the size of aerosol particles, which proved to be within ± 20%.

When the ambient temperature changes from -40 to 40 ^{0}C additional error measure the size of aerosol particles does not exceed 20% of the relative error of measurement.

It should be noted that the above optical-electronic systems, we designed three patents for inventions.

Conclusion

The developed optical-electronic systems offer the possibility of remote sensing of physical and environmental parameters of the atmosphere and IR sources, as well as the aerosol component in the environment.

The experimental results of the metrological characteristics developed devices confirm the high accuracy of the measurements.

The developed method of infrared air monitoring can be widely used for remote environmental monitoring forest spaces and natural gas main pipelines.

Mobile version of the complex created instruments can be used successfully for the rapid assessment of physical and ecological state of the atmosphere, as well as for the distant researches of thermal objects.

References

[1] S.M. Musaelyan,The Problems of Clean Air. - Yerevan: Armenia, 1985 – 225 p. [2] A.G. Bannikov, A.K. Rustamov, The Nature Conservancy. 2nd ed., Rev. and add. - M. Agropromizdat, 1985 – 287 p. [3] O.S. Owen, Protection of Natural Resources / Transl. from English. - Moscow: Kolos, 1977– 416 p. [4] Y.T. Feldman,Hygienic Evaluation of Motor Vehicles as a Source of Air Pollution. - M., - 1975, – 187 p. [5] Laser Monitoring of Air Pollution: SO_2, NO_2, Ozone, Benzene, Toluene and Aerosols.- ELIGHT, Laser systems, GmbH, Berlin. - 2000. [6] A.A. Popov, S.V. Kachin, Computerized Analytical Systems for Environmental Monitoring.- Devices and control systems. -1994 - № 9 –p. 15-17. [7] R.S. Asatryan, S.R. Asatryan, G. Gevorgyan and others, Optical-Automatic Meteorological Office. - PTE. -2003 - № 4 –p. 125-126. [8] Guide to practice observing the runway visual range and sending messages about it, The International Civil Aviation Organization. Forward-scatter Meters. - Doc. 9328 - AN/908.- Ed. the second. - 2000 – p. 49-53. [9] R.S. Asatryan,Development and Manufacture of Optical and Meteorological Field Post-Machine ("FOMPA")- Report R & D (final) n / I-A-1376, № 0928-DSP, Yerevan.-1987-113 p. [10] R.S. Asatryan, S.R. Asatryan, Gevorgyan G.and others, Set the Meter Calibration Optical Transparency of the Atmospheree. - PTE.-2004 - № 6-p. 132-133. [11] R.S. Asatryan, R.A. Epremian, H. G. Gevorkyan and others, Universal Infrared Spectral Radiometer. - Intern. Journal of IR and MM Waves.-2003-V.24, № 6–p. 1035-1046. [12] R.S. Asatryan, Yu,A. Abrahamyan, H.G. Gevorkyan and others,IR Spectral Method of Monitoring the Industrial Gas Ejections in Atmospere. - Dubai Intern. Confer. on Atmospheric Pollution: 21-24 febr. 2004 - Dubai, UAE-2004.-Proceed. – p. 134-139. [13] Dual Channel Radiometer- Patent Internationally U. S. Pat. 3476914.-1998. [14] Ring Price filter for Tunable Optical Spectral Range from 1.8 to 5.6 Microns- OST-5683-84. [15] R.S. Asatryan, Development and Manufacturing of Infrared Spectroradiometer "Wedge". – Report R & D (final) p/ya- A-1376: № 4115-DSP, Erevan.-1987–143 p. [16] R.S. Asatryan, S.R. Asatryan, L.A. Vardumyan. and others, The Multi-Channel Aerosol Spectrometer. - PTE.-2004 - № 4 –p. 166-167. [17] R.S. Asatryan, V.I. Sidorenko, The

Optical Aerosol Spectrometer Calibration. - Proc. Reports. III Republic. Teach-tech. Conf. "New advances in instrumentation."-Yerevan-1987–p. 29. [18] V.P. Shmargunov, V.V. Polkin, Counter Aerosol Particles on the Basis of A3-5. - PTE.-2007- № 2.-p. 165. [19] R.S. Asatryan, Design and Manufacture of Aerosol Spectrometer "Alternative". -Report R&D (final) p/ya- A-1376: № 1228-CPD, Yerevan.-1986–128 p. [20] S.R. Asatryan, Method of Air Environmental Control Forest Spaces and Gas Pipelines. – Herald MANEB.-2011.-v.16.-: № 5.-MY. 2–p. 60-64.

Pedestrian detection using higher order statistics (HOS) or polyspectral analyses.

A.A. Hakhoumian**, E.R. Sivolenko**

Institute of Radiophysics& Electronics, Armenian National Academy of Sciences , Armenia

The analysis of the signal using the power spectrum and autocorrelation function is insufficient. We do not have complete information about such signals, because of the loss of the phase information in the power spectrum and autocorrelation function. In that case it is very important using higher order statistics (HOS). The subject of higher order statistics (HOS) has received much attention in recent years. We are using higher order statistics for pedestrian detection. The pedestrian detection is modeled as amplitude modulation.

Introduction.

Cumulants and its Fourier transform, known as higher order statistics, become very important. As we know second order statistics (i.e. autocorrelation, power spectrum and etc.) are phase blind. Using of Higher order statistics gives opportunities to find phase information. In generally, HOS or polyspectral analyses are used in signal processing frameworks for several reasons, as for additive Gaussian noise suppression (white or colored), information about the signal phase, detection and characterization of non-linearity, detection of Gaussian deviations and etc.

Below mentioned advantages are used in this paper for two experiments: mixer output signal detection and pedestrian detection. The pedestrian has center of gravity and his hands are moving concerning that center. Pedestrian hands are moving opposite sides, so we have two mathematical pendulums with opposite phases but with the same frequencies. This means that we have Doppler shift to different sides. Namely by first approximation we have amplitude modulation: pedestrian gravity center is moving with velocity V_1 and has ω_1 Doppler shift, hands are moving to opposite sides with velocity V_2 and have ω_2 Doppler shift but with opposite phases. In this case we have a carrier frequency and side frequencies with opposite phases like in amplitude modulation. The pedestrian detection example is modeled by using above described approximation.

In case of mixer output signal detection bispectral analysis was used for showing the main advantages of HOS.

Bispectrum processing.

Cumulants have the same meaning as moments. The moments of a random process are derived from the characteristic function $\Phi_x(\omega)$, and the cumulant generating function $C_x(\omega)$ is defined as the logarithm of the characteristic function as

$$C_x(\omega) = ln\Phi_x(\omega) = lnE[\exp(j\omega x)] \qquad (1)$$

It is very simple to show Gaussian noise suppression using higher order statistics.

$$\psi_x(\omega) = j\omega a - \frac{\sigma^2\omega^2}{2} \qquad (2)$$

Equation (2) is Gaussian noise cumulant function. Now using a Taylor series we have

$$\psi_x(\omega) = j\omega C_1 + \frac{(j\omega)^2}{2!}C_2 + \frac{(j\omega)^3}{3!}C_3 + \ldots \qquad (3)$$

Comparing equation (2) and (3) we have the following results: $C_1 = a$; $C_2 = \sigma^2$; $n > 3, C_n = 0$.

Gaussian noise cumulants show the main reason of HOS using. The main advantages of using HOS are that starting from 3rd cumulant all Gaussian noise cumulants equal to zero. It means that we have Gaussian noise suppression.

Gaussian noise suppression was done using bispectral estimation. Now the *(k-1)* - dimensional Fourier transform of the k^{th} order cumulant is the k^{th} order spectrum of a signal *x(m)* and defined as

$$C_x(\omega_1,..,\omega_{k-1}) = \frac{1}{(2\pi)^{k-1}} * \sum_{\tau_1=-\infty}^{\infty} \dots \sum_{\tau_{k-1}=-\infty}^{\infty} c_x(\tau_1,..,\tau_{k-1}) e^{-j(\omega_1\tau_1+\omega_{k-1}\tau_{k-1})} \qquad (5)$$

The bispectrum is set as

$$C_x(\omega_1,\omega_2) == \frac{1}{(2\pi)^2} \sum_{\tau_1=-\infty}^{\infty} \sum_{\tau_2=-\infty}^{\infty} c_x(\tau_1,\tau_2) e^{-j(\omega_1\tau_1+\omega_2\tau_2)} \qquad (6)$$

where$c_x(\tau_1,\tau_2) = E\{x(m)x(m+\tau_1)x(m+\tau_2)\}$ is 3rd order cumulant.

The detection of mixer output signal.

The first example shows Gaussian noise suppression in mixer output. In this example we have two signals and Gaussian noise.

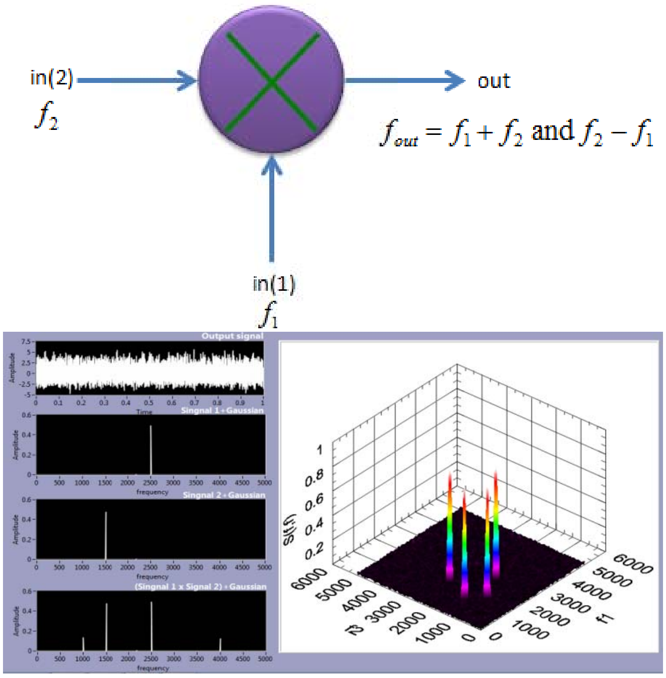

Fig. 1. Mixer output signal without Gaussian noise.

We have two signals on figure 1 without Gaussian noise: On the last graph we have all signals components. Also we have all signal components on the bispectrum indicator.

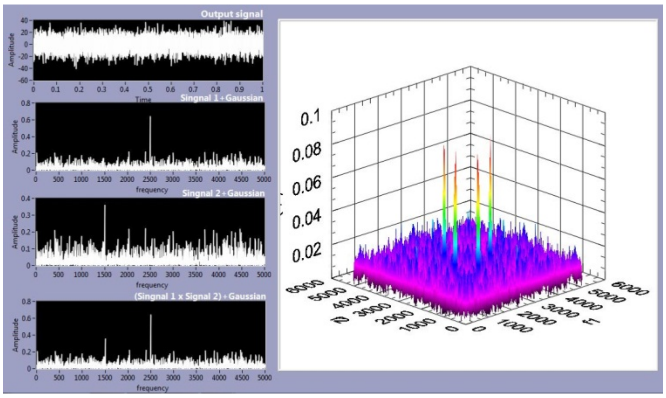

Fig. 2. Mixer output signal with Gaussian noise

On the last graph of figure 2 we have only input signals without useful components. But we have all signal components on bispectrum indicator as it is shown on figure 2. As it is shown from the example we can suppress Gaussian noise using HOS.

Pedestrian detection using higher order statistics.

In this example the pedestrian movement is modeling. We compare pedestrian movement with mathematical pendulumoscillation. It is means that we have graph like amplitude modulation in power spectrum. So pedestrian is moving with velocity V, his hands are moving forward and backward like mathematical pendulum with velocity V_1 i.e. we have three frequencies picks in power spectrum

- moving pedestrian ω_1
- forward moving hand ω_2
- backward moving hand $-\omega_2$

On figure 3 is illustrated pedestrian detection without Gaussian noise.

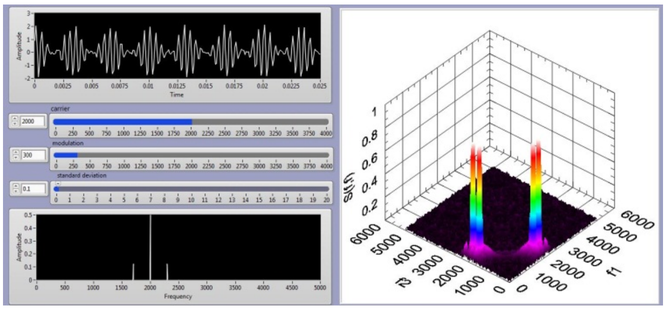

Fig. 3. Pedestrian detection without Gaussian noise

We have amplitude modulation on power spectrum i.e. useful picks and we have the same picks on bispectrum graph as it is shown on figure 3.

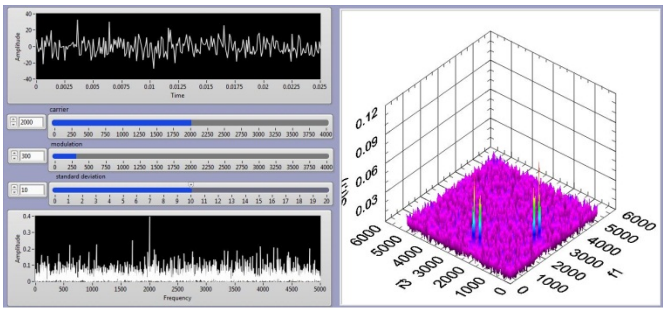

fig. 4. Pedestrian detection in case of Gaussian noise

As it is shown on figure 4 we have signal like a noise on power spectrum graph without useful picks. But on bispectrum graph we have useful picks again as on figure 3. Figure 4 shows that we can suppress Gaussian noise and find useful picks using higher order statistics. The result is shown on figure 5.

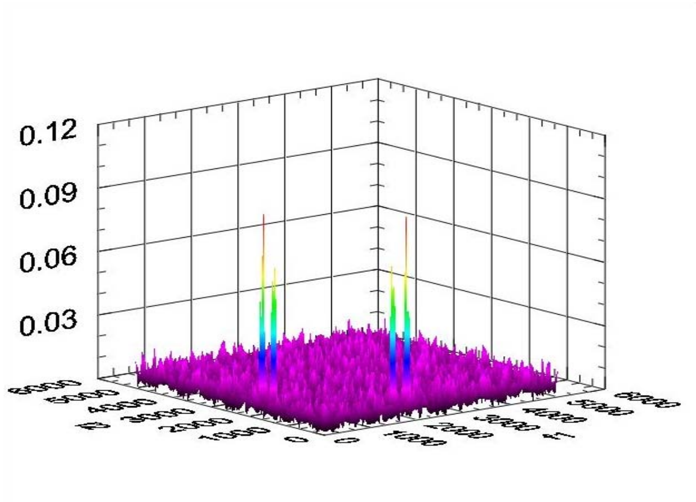

Fig.5. Gaussian noise suppression

Figure 5 shows the main point of using higher order statistics. We have more than four times higher picks from noise level.

Conclusions.

In this paper mixer output signal detection has been used in order to simulate Gaussian noise suppression. In particular, pedestrian detection using higher order statistics has been examined. The most important points of HOS are given and it has been shown that they can provide information which second order statistics cannot. Finally, a new detection method was presented which early results are very promising.

References.

[1]. ChenganGuo, Zeng-GuangHou and ZhingangZeng "Advanced in Neural Networks" part 1, Dallan, China 2013 by Springer

[2]. Saeed V. Vaseghi "Advanced digital signal processing and noise reduction" second edition, 2000 UK by John Wiley & Sons, Ltd

[3]. M.A.A. Shoukat Choudhury, Sirish L. Shah, Nina F. Thornhill "Diagnosis of process nonlinearities and Valve stiction" p 17-41. 2008 by Springer

Experimental investigation of “plasmonic black hole” phenomena

H.Haroyan
Yerevan State University, Alex Manoogian 1, 0025, Yerevan, Armenia, hharoyan@ysu.am

A plasmonic structure consisted of touching spherical and plane metallic surfaces have been experimentally investigated. Because of the spherical shape a circularly symmetric radially decreasing effective refractive index is produced, which is a necessary requirement for imitating a black hole. The trapping and steering features of such structure have been demonstrated which had been theoretically predicted. Experimental investigations have been realized by using experimental setup based on simultaneously usage of two scanning near-field optical microscope (SNOM) probe measurements; first one was used to land a gold microsphere (the diameter of sphere was 50 µm) on plane metallic surface, and the second one to obtain the field distribution and scanned region image. To estimate the contact region the roughness of both surfaces has been also measured.

1. Introduction

Numerousoptical black hole models have been devised to enable investigation of blackhole phenomena within laboratory conditions. A lot of attempts to replicate the behavior of black holes by implementing optical analogues have been taken by scientists.Narimanov and Kildishev [1, 2] considered an inhomogeneousmedium that resulted to a Hamiltonian guiding electromagnetic radiation towards ahighly absorptive central core. Functional designs of this model was later proposedand implemented by Cheng et al. [3] and Lu et al. [4] for transverse electric (TE) andtransverse magnetic (TM) electromagnetic waves respectively. Similarly, Jiang et al .[5] presented a design that operates for propagating surface plasmon-polaritons (SPP) along a graphene sheet . Numerical simulations showed that a graded index photoniccrystals can also be used to realize this black hole model [6]. In 2009, Genov etal. [7] came up with a photonic black hole model that exploits the invariance ofMaxwell's equation with coordinate transformation to design a medium that satisfiesthe Schwarzschild metric. Numerical simulations have shown that Genov's model doesindeed behave like a black hole and can possibly be implemented using metamaterials[7]. Nerkararyan et al. developed another unique approach where they utilizechange in the effective refractive index by bringing a metal sphere in contact witha second metallic surface [8]. Surface plasmon-polaritons (SPPs) propagating alongthe gap between metallic surfaces encounter a spatially varying refractive index in thevicinity of the contact point. SPPs are then trapped or deflected by this refractiveindex distribution.

This work is focused on the plasmonic black hole model proposed by Nerkararyan etal. Compared to other models, this plasmonic black hole model has the advantage ofonly requiring homogeneous materials. We aim to implement this model experimentallyand demonstrate the predicted SPPs trapping and path deflection. An experimentalsetup is based on a scanning near-feld optical microscope (SNOM), which holds (insteadof a sharp tip) a gold coated microsphere, and approaches it on a planar metallicsurface.

2. Theory

The plasmonic black hole model proposed by Nerkararyan et al. consists of a metalsphere in contact with a second metallic surface: planar or spherical (Fig. 1).

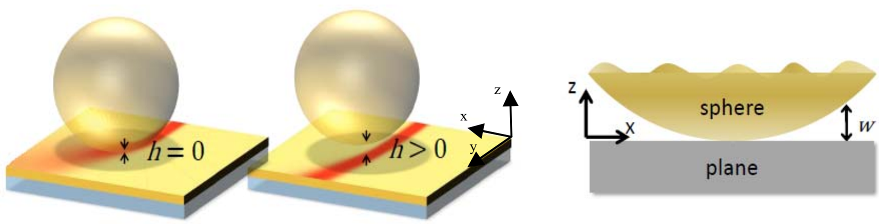

Fig.1. Schematic view of plasmonic black hole based on spherical metallic surface placed above the planar metallic layer.

A circularly symmetric radially decreasing effective refractive index is produced by bringing a metal sphere in contact with a second metallic surface. Surface plasmon-polaritons (SPPs) propagating along the gap between metallic surfaces encounter a spatially varying refractive index in the vicinity of the contact point. SPPs are then trapped or deflected due to refractive index distribution.

In the immediate vicinity of the point of contact (except at the contact point itself),the only allowed plasmonic modes are those with a transverse electric field component along z axis (Fig. 1) [8]. Due to the cylindrical symmetry this plasmonic black hole, it is more convenient to solve these modes using the cylindrical form of Helmholtz equation

$$\frac{\partial^2 E_z}{\partial \rho^2} + \frac{1}{\rho}\frac{\partial E_z}{\partial \rho} + \frac{1}{\rho^2}\frac{\partial^2 E_z}{\partial z^2} + \varepsilon_{d,m} k_0^2 E_z = 0, \tag{1}$$

where k_0 is the wave number, and ε_m and ε_d are the permittivities of the metal anddielectric, respectively.

By employing the effective index methodsome key parameters such as critical launch distance b_r can be calculatednecessary for experimental investigations [8].

$$b_{cr} = \sqrt{\frac{4rR}{k_0\sqrt{\varepsilon_d}}}, \tag{2}$$

where

$$r = \sqrt{\frac{\varepsilon_d(\varepsilon_d - \varepsilon_m)}{-\varepsilon_m}} \tag{3}$$

R is the radius of the metal sphere.

3. Experiment

To realize experiment should be taken into account following features and consideration. It should be kept in mind that the effective permittivityis directly dependent on the spacing between the two surfaces significant scratches orunevenness will surely affect the resulting permittivity distribution. Not to mentionthat such roughness on the surface may cause the plasmons to scatter or coupledout into free space.Furthermore, the sphere must be held in position as steadily aspossible since instability will surely influence the observation of black hole behaviorand possibly damaging the surfaces. For these reasons, simply placing a metal sphereon top of metallic plane would not serve. In our measurements, we used scanningnear-fieldoptical microscope (SNOM) probes to land a gold microsphere on a planemetallic surface.Experimental investigations have been performed by the set up schematically shown in Fig.2. The free space beam mildly focused on a grating via low NA objective placed below the sample. Manipulations of the plasmonic black hole and mapping of the SPP have been performed in double scanning near-field optical microscope (SNOM) setup [9, 10]. One of the tuning-fork curried the gold sphere and second one the metal-coated aperture based fiber tip. The tip scanned the sample surface to map the SPP.

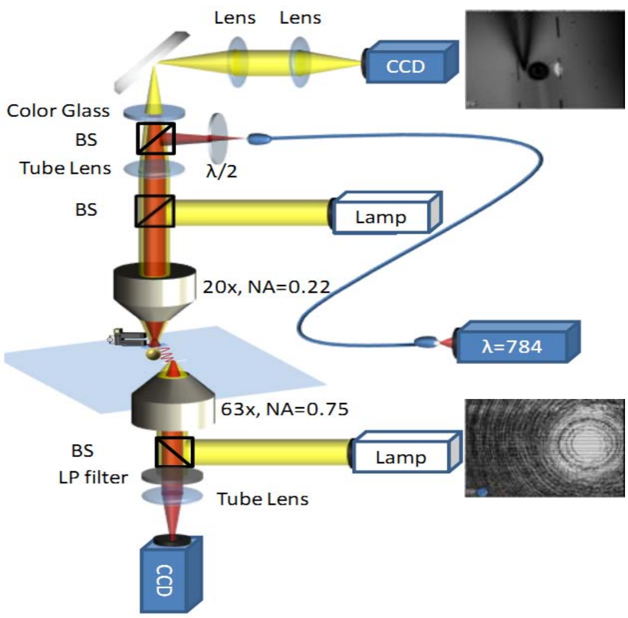

Fig.2. Schematic view of the experimental setup.

The SPP excitation on the metallic planar layer has been realized by a grating, milled in the metal layer (Fig.3).The free space beam mildly focused on a grating via low NA objective placed below the sample. One of the tuning-fork curried the gold sphere and second one the metal-coated aperture based fiber tip. The tip scanned the sample surface to map the SPP. In Fig.3.the scanned SPP map of flat silver surface without gold sphere is presented.

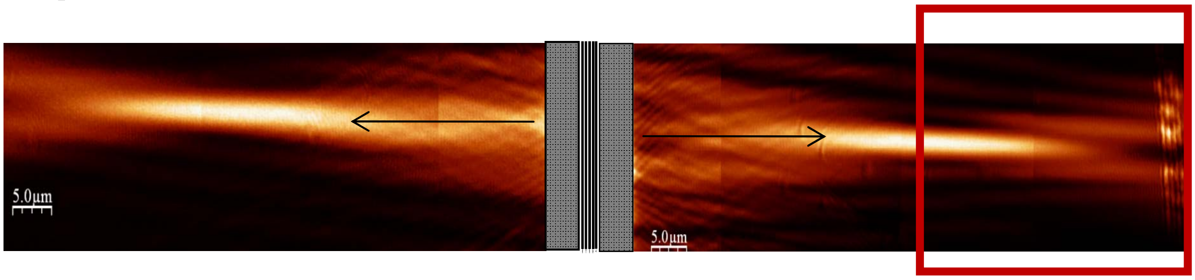

Fig.3. Quasi-collimated plasmonic beam propagation in both directions from excitation grating

The focusing and steering features of black hole structure have been demonstrated by SNOM measurements (see Fig.4). The gold sphere has been landed by using first one of the tuning-forkat the most collimated region of SPP (in the center of the left side of the red frame in Fig.3).The width of collimated branch is about 3.5μm. After this, by using second tuning fork the scanning of the sample surface to map the SPP has been realized. The scanned region represented in Fig.4 is corresponding to the framed region in Fig.3.

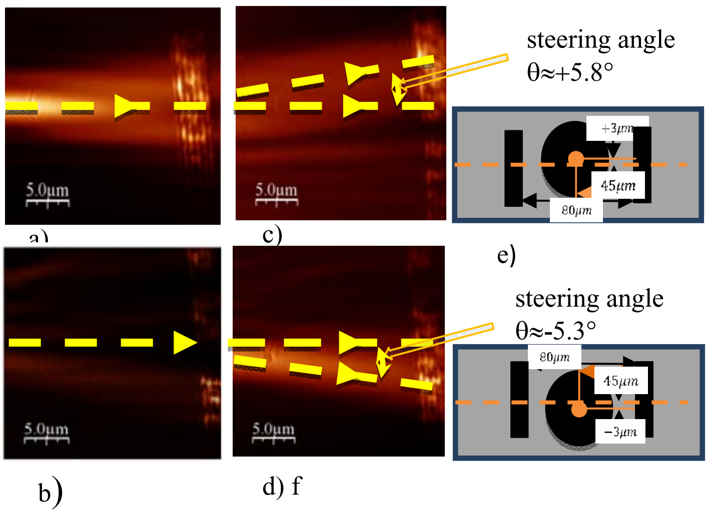

Fig.4. a) SNOM image of plasmonic beam without metal sphere; b) SNOM image of plasmonic beam trapped by plasmonic black hole (the output intensity of plasmonic beam decreased about 32 times); c) and d) steering of plasmonic beam for different relative positions presented in e) and f) correspondingly.

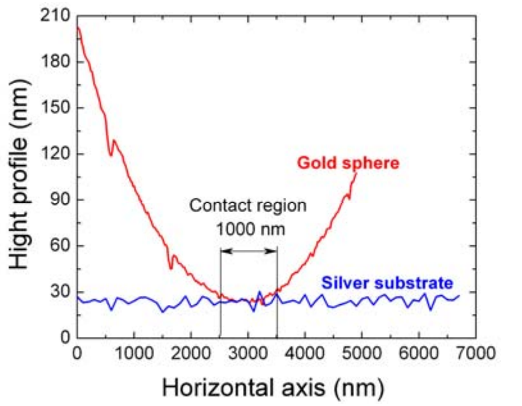

Fig.5. Measurement of gold sphere and flat silver surfaces roughnesses and contact region estimation.

As it can be seen from Fig.4(b), if the beam distance b from contact region is smaller than critical distance ($|b| \leq b_{cr}$, see eq. (2)), the GSPwaves are trapped. Otherwise ($|b| > b_{cr}$) the system steering features prevail (see Fig.4(c,d)).

To estimate the contact region the roughness of gold sphere and silver substrate surfaces has been also measured by using atomic-force microscope (AFM). Measurements show that the contact region is about 1μm (see. Fig.5).

3. Conclusion

A plasmonic structure consisted of touching spherical and plane metallic surfaces have been experimentally investigated. Because of the spherical shape a circularly symmetric radially decreasing effective refractive index is produced, which is a necessary requirement for imitating a black hole. The trapping and steering features of such structure have been demonstrated which had been theoretically predicted. Experimental investigations have been realized by using experimental set up based on simultaneously usage of two scanning near-field optical microscope (SNOM) probe measurements; first one was used to land a gold microsphere (the radius of sphere equal to 25 μm) on plane metallic surface, and the second one to obtain the field distribution and scanned region image. To estimate the contact region the roughness of both surfaces has been also measured.

4. References

[1] E. E. Narimanov and A. V. Kildishev, Applied Physics Letters 95 (2009)041106.
[2] A. V. Kildishev, L. J. Prokopeva, and E. E Narimanov, Optics Express 18 (2010)16646.
[3] Q. Cheng, T. J. Cui, W. X. Jiang, and B. G. Cai, New Journal of Physics12 (2010)063006.
[4] W. Lu, J. Jin, Zh. Lin, and H. Chen, Journal of Applied Physics 108 (2010)064517.
[5] Yu. Jiang,W. B. Lu, H. Ju Xu, Zh. G. Dong, Physics Letters A 376 (2012)2739.
[6] H.Wang and L. Chen, Journal of Applied Physics 109 (2011)103104.
[7] DA.Genov, Sh. Zhang, and X. Zhang, Nature Physics, 5 (2009) 687.
[8] Kh. V. Nerkararyan, S. K. Nerkararyan, and S. I. Bozhevolnyi, Optics Letters 36 (2011) 4311.
[9] A.Minovich,A. E. Klein, N.Janunts, Th.Pertsch, D. N. Neshev, and Yu. S. Kivshar, Physical Review Letters, 107 (2011) 116802.
[10] M. Sison, Investigation of Plasmonic Black Holes, MS thesis, (2013).

The changes of the cellular indicators of leucopoiesis in animals irradiated by millimeter waves under hypomotile conditions

V. Kalantaryan[1] , R. Martirosyan[1], Ts. Adamyan[2], E. Gevorgyan[2] and H.Badalyan[3]

[1]Department of Microvawe Radiophysics and Telecommunication, Yerevan State University,Alex Manoogian str.1,Yerevan 0025,Armenia

[2]Department of Human and Animals Phisiology,Yerevan State University,Alex Manoogian str.1,Yerevan 0025,Armenia

[3]Department of general physics, Yerevan State University,Alex Manoogian str.1,Yerevan 0025,Armenia

We study the nature of the changes of the morpho-functional indicators of leukopoiesis in hypokinesia dynamics on the background of multiple impact of the millimeter electromagnetic waves. It is shown that the preliminary radiation increases the potential capacity of the regulatory systems of leukopoiesis, activates the proliferative and maturation processes of the stem cells, and boosts the adaptive compensatory mechanisms thus resulting in preventing of the negative impact of hypokinesis.The obtained data allow us to assume that the millimeter waves are means of non-medicational treatment under stress rectifying the changes of the morpho-functional indicators.

1.Introduction

At the present time, a dramatic change in the human life style has led to restriction of motive activity and to a sedentary lifestyle. Today, the computer technology is evolving into different fields of human activity and is becoming indispensable for work and the learning process. Relative non- motile stages create a stress reaction, the tension of regulatory mechanisms, the movements in the immune system and the reduction of the reserve capacity of the organisms. These processes are responsible for the development of pathologic processes in the organisms. The results of experimental investigations show that in the case of hypokinesia, the concentration of lysozyme, the amount of complimentary lymphocytes and immunoglobulins are decreased. In addition, it was observed that the functional activity of neutrophils is decreased as well. As a consequence of this the resistance of the organism against various infections and diseases decreases. Therefore, it is important to find means that under the hypomotile conditions will help either to prevent and correct such deviations. The clinical and experimental data of numerous investigations have shown that the electromagnetic waves are considered to be a new , highly efficient method for the treatment of various diseases. They have anti-stress effect on neuroendocrine and immune systems, as well as on the peripheral regulatory structures [1-7]. The anti-stress effect of the millimeter wave electromagnetic radiation (EMR) has been studied in [8-9] by Temuryants et al.It has been shown that the millimeter waves increase the functional activity of leucocytes, particularly neutrophils and lymphocytes. Thus they can increase the physiological protection and the level of resistance of an organism. There is high interest to study the changes in morphological indicators of the blood under hypomotile conditions, because the blood system is connected to the all working systems of the body.Therefore, the aim of the present work is to study the changes of morphological indicators in the blood of animals that have been pretreated by the millimeter waves under the condition of hypokinesia.

2.Materials and methods

Experiments were carried out on rabbits of the same weight (2.5-3 kg) and under the same care and nutrition survey conditions. 10 rabbits have been taken and two experimental setups have been used to achieve our goals. In the first setup, the changes in morphological indicators of eucopoiesis were studied under dynamics of hypokinesia. In the second setup, before hypokinesia the animals were treated during 20 days by EMR. In order to restrict the movements of the animals, they were placed in a special wooden box for 20 days, 22 hours for each day. 2 hours were used to take blood samples and for the feed. For the irradiation treatments, the G4-141 generator (Russian made) was used with the frequency 42.2 GHz. The exposure time was 30 minutes per day during 20 days. A whole-body EMR exposure of rabbits was conducted in the far-field zone of antenna (50 cm). The intensity of the power of the influence was less than 10 $\mu W/cm^2$.

3.Results and discussion

The investigations have shown that in the initial period (5-10 days),the hypomotility causes distributional leukocytosis. The number of leukocytes was increased by about 28% ($p < 0,001$) compared to the initial stage. In the leukocytes formula lymphocytosis, neutrophilis, basophilia, monocytosis and eosinophilia were observed (Table 1). These changes are results of the activation of blood distributional _eucopoie mechanisms. The increase of the numbers of granulocytes and lymphocyte is apparently due to their quick export to the peripheral blood, by the stressor mobilization of granulocytes of bone marrow reserve and spleen, and of lymphocytes of thymus gland.Under the stress the latter provide the cell composition of the peripheral blood. During the mentioned period, in myelogram we have observed a moderate reduction of the number of young neutrophils and the increase in the number of lymphocyte. The maturation index of neutrophils was 0,6. On the 15th day under hypomotile conditions, the total amount of leucocytes droped by 15% as compared to the data for 10th day, but it was higher by 123 % ($p < 0,001$) from the initial level. The absolute number of lymphocytes was 97%. The high level of matured neutrophilis, eosinophilis, basophilis and monocytosis were maintained. On the 20th day of the investigation, the number of leucocytes returned to the initial level (102%). In the leucocyte formula a reduction of the absolute number of lymphocytes was observed (86% ($p < 0,001$)). The numbers of eosinophilis and monocytosis dropped compared to the results of previous days and have been maintained on normal level. The number of mature neutrophilis and basophilis was maintained at high level, 127% ($p < 0,001$), 204% ($p < 0,001$), respectively.

Table 1: The changes of peripheral white blood indicators under hypomotile dynamics

Indicators	Initial data	The days of investigation					
		5 10		15	20	25	30
Numbers of leukocytes	8400± 270	10800± 245	11600± 381	10400± 305	8600± 221	7600±1 99	7425±1 89

in 1mm^3 blood		p<0.001	p<0.001	p<0.001		p<0,05	p<0,01
Band neutrophil	42±6	54±1.8 p<0.001	29±2 p<0.001	26±1.9 p<0.001	22±1.6 p<0.001	38±2.1 p<0,01	38±2.1 p<0,01
Segmented neutrophils	2772±121	4698 ±146 p<0.001	4147±123 p<0.001	4550±142 p<0.001	3526±136	2622±129	2450±126 p<0.01
Eosinophilis	168±7	162±10	232±14 p<0,001	208±11 p<0.001	172±10	152±9 p<0.01	148±9 p<0.01
Basophilis	84±5	162±9 p<0.001	203±14 p<0.001	208±13 p<0.001	172±9 p<0.001	152±7 p<0,001	148±7 p<0,001
Monocytes	546±10	756±17 p<0.001	725±16 p<0.001	728±16 p<0.01	580±12	456 ±10 p<0.001	481±11 p<0.001
Lymphocytes	4788±156	4968 ±112	6264±205 p<0.001	4680 ±114	4128±111 p<0.001	4180±113 p<0.001	4158±112 p<0.001

According to the literature data, the hypomotility, as a stress factor, reduces the organism resistance, the amount of lysozyme, compliments and induces movements in the immune system. Analyzing the literature data and the data obtained in our work we conclude that under the initial stage of the hypomotility influence the body mobilizes its recovery and defense mechanisms, which provide the vital activities at the expense of the us of the functional reserves, but the long-term impact induces the strain in regulatory mechanisms and the reduction of reserve capacities of the organism.Therefore, in the next series of experiments, for the rectification of the negative effects of hypokinesia the animals have been pretreated by the millimeter waves during 20 days. From the analyzis of the obtained results it follows that after the 20 days irradiation the standards of the morphological indicators of _eucopoiesis have been increased and, on that background, the significant changes in the indicators of _eucopoiesis have not been observed (Table 2).

Table 2: The changes of peripheral white blood indicators in irradiated animals under hypomotile dynamics

Indicators	Initial data	On 20th day of irradiation	The days of investigation			
			5	10	15	20
Numbers of leukocytes in 1mm^3 blood	7800±210	9200±222	10200±262 p<0.05	10000±338	9160±236	9200±235
Band neutrophil	78±3	115±6	127±6 p<0.02	100±4	114±4	115±4
Segmented neutrophils	2574±150	3036±148	4080±165 p<0.001	3300 ±139 p<0.05	3114±141	2898±125
0.Eosinophilis	156±10	161±6	178±7 p<0,02	175±7 p<0.02	160±6	184±8 p<0.02
Basophilis	78±6	92±4	152±5 p<0.001	150±5 p<0.001	138±6 p<0.001	161±8 p<0,001
Monocytes	546±9	644±13	663±15	700±16 p<0.001	595±16 p<0.05	690±17 p<0.05
Lymphocytes	4368±180	5152±260	4998±221	5600±224	5038±220 p<0.01	5152±222

According to our data, the EMR pre-treatments of animals elevate the potential of regulatory systems and prevent the negative effect of hypomotility on blood system, resulting in the disappearance of the changes in indicators of leukopoiesis. Thus, under stress condition the millimeter waves are able to alter the function of immune system, which is one of the main mechanisms for the correction of the state of the organism. It was shown that under hypomotile condition the functional activity of the neutrophils and lymphocyte is decreased, and on the contrary, in neutroohils the activity of hydrophilic enzymes is elevated, which can promote the development of the processes of cytolysis, and, consequently, the tissue damages. Such different by directed recoveries suppress the natural defense forces in body's cells.Under the influence of the millimeter waves in the neutrophils and lymphocytes the activity of succinate dehydrogenase is increased, which is an evidence of the energetic level of these cells. It is known that the fertile cells participate to the regulation of the adaptive processes at cellular level and have a significant influence on the properties of the neutrophils. Under hypomotile condition, the degranulation level of the fertile cells is increased. Under the combined effect of the millimeter waves and hypokinesia, the degranulation level of the fertile cells is decreased, that is why they are considered as regulators.

Thus, on the base of our results and the literature data we conclude that the millimeter waves elevate the functional state of the blood cells, the functional potential of the leukocytes, preparing the cells to resist against other agents.

References

1. S. Minasyan, G. Grigoryan, S.Saakyan, A. Akhumyan, V. Kalantaryan. Effects of the Action of Microwave-Frequency Electromagnetic Radiation on the Spike Activity of Neurons in the Supraoptic Nucleus of the Hypothalamus in Rats.*Neuroscience and Behavioral Physiology (USA),* 2007, vol.37, N 2, pp.175-180.
2. H.Tadevosyan, V. Kalantaryan, A. Trchounian. Extremely High Frequency Electromagnetic Radiation Enforces Bacterial Effects of Inhibitors and Antiobiotics. *Cell Biochemestry & Biophysics* 2008, 51(2-3), 97-103,July
3. V. Kalantaryan, P. Vardevanyan, Y. Babayan, E. Gevorgyan, S. Hakobyan, A. Antonyan. Influence of low intensity coherent electromagnetic millimeter radiation (EMR) on aqua solution of DNA. *Progress In Electromagnetics Research Letters* 2010,vol.13,p.1-9
4. H.Torgomyan, V. Kalantaryan, A. Trchounian. Low Intensity Electromagnetic Irradiation with 70.6 and 73 GHz Frequencies Affects Escherichia coli Growth and Changes Water Properties. *Cell Biochemestry & Biophysics* 2011, 60(3),p.275-281.
5. V. Kalantaryan, R. Martirosyan, L. Nersesyan, A.Aharonyan, I. Danielyan,H. Stepanyan, J. Gharibyan, N. Khudaverdyan Effect on tumoral cells of low intensity electromagnetic waves. *Progress In Electromagnetics Research Letters* 2011,vol.20,p.98-105 .
6. H. Torgomyan, V. Ohanyan, S. Blbulyan, V. Kalantaryan, A. Trchounian. Electromagnetic irradiation of Enterococcus hirae at low-intensity 51.8- and 53.0-GHz frequencies: changes in bacterial cell membrane properties and enhanced antibiotics effects. *FEMS Microbiology Letters* 2012, Apr.,329(2),131-137
7. V. Kalantaryan, R. Martirosyan, Y.Babayan, L. Nersesyan, H. Stepanyan Preliminary Results of Influence of Nonionizing Electromagnetic Radiation on Tumor and Healthy DNA and Role of Water American Journal of Medical and Biological Research. 2014, 2(1), 18-25
8. Temuryants, N.A. and E. N. Chuyan, "Effect of microwaves of nonthermal intensity on the development of hypokinetic stress in rats with different individual characteristics". *Millimeter waves in biology and medicine*,Vol.1, 22 –32,1992.
9. Temuryants, N.A., E.N. Chuyan, E.N. Tumanyants, et al, "Dependence of the anti-stress action of electromagnetic radiation of millimeter range from impact localization in rats with different typological features", *Millimeter waves in biology and medicine*,Vol.2, 51-58,1993.

Исследование характеристик радиотелескопа РТ-13 ИПА РАН

Р. М. Мартиросян, А. Г. Гулян, Г. А. Пирумян, С. А. Саркисян, Г. С. Аветисян

Институт Радиофизики и Электроники НАН РА.

В статье приведены результаты фокусировки и измерений характеристик радиотелескопа РТ-13 ИПА РАН на пункте назначения, в диапазонах S, X, Ka. по эталонному космическому радиоисточнику “Кассиопея - А”, по разработанной в ИРФЭ программой/методикой. для высокоточного и оперативного обеспечения системы **ГЛОНАСС** данными о координатах полюса и Всемирном времени и для связи с международной **РСДБ-**сетью и другими международными службами.

1.Введение.

Глобальная навигационная спутниковая система (ГЛОНАСС) разработана по заказу Министерства обороны СССР/РФ, в рамках федеральной целевой программы «Поддержание, развитие и использование системы ГЛОНАСС на 2012-2020 годы» и является одной из двух функционирующих на сегодня систем глобальной спутниковой навигации. **ГЛОНАСС** предназначена для оперативного навигационно-временного обеспечения неограниченного числа пользователей наземного, морского, воздушного и космического базирования. Доступ к гражданским сигналам **ГЛОНАСС** в любой точке земного шара, предоставляется российским и иностранным потребителям на безвозмездной основе и без ограничений.

Основой системы должны являться 24 спутника, движущихся над поверхностью Земли в трёх орбитальных плоскостях с наклоном орбитальных плоскостей 64,8° и высотой 191 00 км. Принцип измерения аналогичен американской системе навигации **NAVSTAR GPS**. Основное отличие от системы **GPS** в том, что спутники **ГЛОНАСС** в своём орбитальном движении не имеют резонанса (синхронности) с вращением Земли, что обеспечивает им большую стабильность. Таким образом, группировка КА ГЛОНАСС не требует дополнительных корректировок в течение всего срока активного существования. Целью выполнения работы является разработка программы/методики для фокусировки и исследования характеристик радиотелескопа **РТ-13 ИПА РАН** а так же проведение измерений на пунктах назначений.

Объектом исследования является построенный по двухзеркальной схеме с кольцевым первичным фокусом трехдиапазонный радиотелескоп **РТ-13 ИПА РАН**, на котором установлена радиоастрономическая приемная система **(РПС)** с криостатируемым трехдиапазонным облучателем и малошумящими усилителями **(МШУ).** Рабочие диапазоны частот радиотелескопов: **S – (2,2 – 2,6) ГГц, X – (7,0 – 9,5) ГГц и Ka – (28 – 34)ГГц.**

1. Программа и методика определения оптимального положения контррефлектора (фокусировка)

Оптимальное положение контррефлектора радиотелескопа (фокусировка) и величины смещения фазовых центров облучателя в S, X и Ka-диапазонах волн относительно оптимального положения контррефлектора ($\Delta x=\Delta y=\Delta z=0$) определялись на программе слежения космического радиоисточника, путем выбора положения контррефлектора, обеспечивающего соответствие формы ДН расчетной (достижением максимального приращения выходного сигнала). Фокусировка проводилась при угле места 45°. Исследование характеристик радиотелескопа проводились после его фокусировки. В таб.1 приведены поправки от отсчетного (Δx=Δy=Δz=0) положения контррефлектора.

Таб.1.

№	Название характеристик	Ед. изм.	Величина
1.	Смещение от отсчетного (Δx=Δy=Δz=0) положения контррефлектора	мм	
2.	Δx_s	мм 3	
3.	Δy_s	мм -2	
4.	Δz_s	мм 2	
5.	Δx_x	мм -1	
6.	Δy_x	мм 3	
7.	Δz_x	мм 2	
8.	Δx_k	мм 0	
9.	Δy_k	мм 2	
10.	Δz_k	мм 1	
11.	$\Delta\overline{x}$	мм 0,7	
12.	$\Delta\overline{y}$	мм 1	
13.	$\Delta\overline{z}$	мм 1,7	

2.Программа исследования характеристик радиотелескопа РТ-13 ИПА РАН

Измерения проводились в обсерватории ИПА РАН «Бадары» при слабой облачности и средней температуре -20 ^{0}С, в период с 26.11. 2014 по 06. 12.2014 г.г. по эталонному радиоисточнику “Кассиопея - А” со следующими характеристиками:

- прямое восхождение $\alpha_{1950,0} = 23^h\,21^m\,10^s{,}2$
- склонение $\delta_{1950,0} = 58^0\,32'\,40''{,}5$ (1)

Значения экваториальных координат для данной эпохи М вычисляются по формулам [1]:

$$\alpha_{2014} = \alpha_{1950,0} + (2014-1950)\times 2^s{,}70$$

$$\delta_{2014} = \delta_{1950,0} + (2014-1950)\times 19''{,}761 \qquad (2)$$

значения плотности потока для данной эпохи вычисляются по формулам[2]:

$$\log F_{1980,0} = 5{,}745 - 0{,}770\log f \qquad (3)$$

$$F_{2014} = F_{1980,0}[1-(0{,}0097-0{,}0003\log f)]^{2014-1980}$$

где f-частота в гигагерцах.В таб.2 представлены значения плотностей потоков на работчих частотных диапазонов.

Таб.2.

Диапазон S		X_1	X_2	X_3 Ka	$_1$ Ka	$_2$ Ka	$_3$
ГГц 2,4		7,0	8,25	9,5	28,0	31,0	34,0
$F_{2014} 10^{-26}$ вт/м^2	950 430		380	340	150	141	128

3. Определение шумовой температуры антенны по всему угловому разрезу с шагом Δh=10°.

3.1. Записываем выходной уровень при отключенном приемнике (РПС).

3.2 Включаем РПС и записываем выходной уровень $T_{ША}$.

3.3. Включаем ГШ, и записываем выходной уровень $T_{ША}+ T_{ГШ}$.
3.4. По показанием 3.1, 3.2 и 3.3 определяем $T_{ША}$.
3.5. П.п. 3.1-3.4 выполняем в S, X, Ka-диапазонах (Таб. 3).

Таб. 3

Диапазон S								
h(грд)	80°	70°	60°	50°	40°	30°	20°	10°
$T_{ША}$(K°)	67	79	92	107	122	137	147	157

Диапазон X								
h(грд)	80°	70°	60°	50°	40°	30°	20°	10°
$T_{ША}$(K°)	63	78	98	123	143	163	173	183

Диапазон Ka								
h(грд)	80°	70°	60°	50°	40°	30°	20°	10°
$T_{ША}$(K°)	196	204	216	218	231	241	256	273

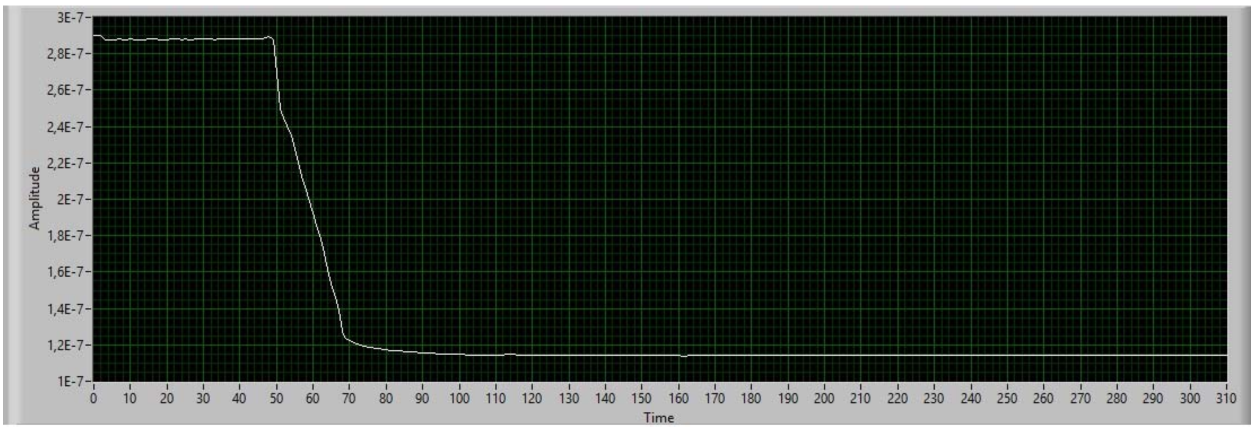

Рис.1. Разрез атмосферы в диапазоне X

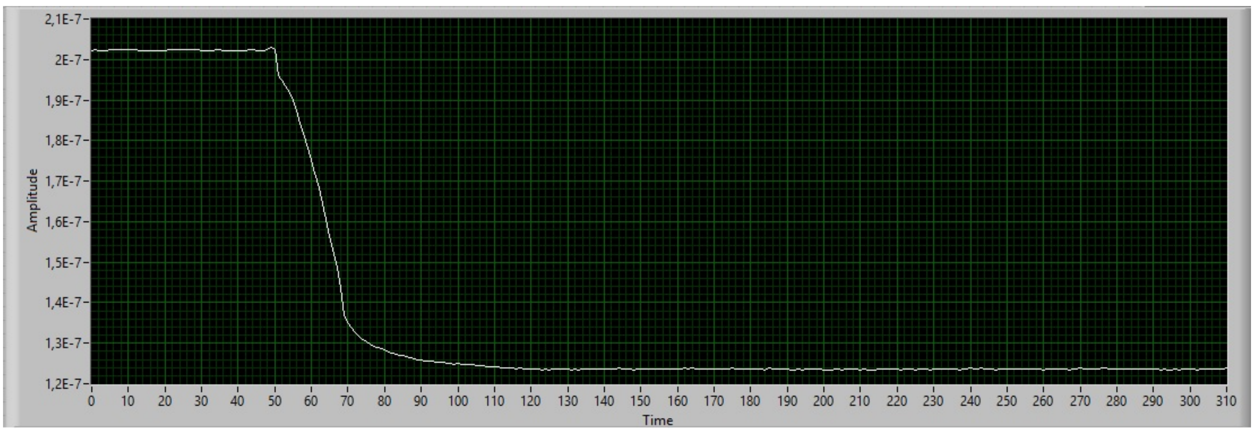

Рис.2. Разрез атмосферы в диапазоне Ka.

4. Измерение смещений электрической оси антенны от геометрической по всему угловому разрезу с шагом Δh=10°.

4.1.Выставляем антенну на программу слежения источника “Кассиопея А” с нулевыми поправками по углу и по азимуту.

4.2. С изменением программных величин азимута и угла места добиваемся максимального приращения выходного сигнала источника.

4.3. П.п. 4.1-4.2. выполняем в S, X, Ка-диапазонах (Таб. 4).

Таб.4

диапазон S	диапазон X	диапазон Ka
Δh_S= 30'	Δh_X= 26'	Δh_{Ka}= 20'
ΔA_S= -14'	ΔA_X= -10'	ΔA_{Ka}= -15'

5. Измерений ширин диаграмм направленности антенны, их зависимость от угла места (Δh=10°) в S, X, Ka диапазонах.

5.1. Радиотелескоп установить на программу слежения траектории источника “Кассиопея А” и с учетом поправок ΔA, Δh и рефракции, достичь максимального уровня выходного сигнала.

5.2. Остановить движение антенны по азимуту и определить временной отрезок между значениями выходных сигналов $T_{ист.макс.}$ и 0,5 $T_{ист.макс}$ в единицах времени ($\Delta t_{0,5}$) и найти половину ширины кривой прохождения по формуле:

$$\varphi_{0,5\,изм} = 15 * \Delta t_{0,5} * \cos\delta_m.$$

Ширину диаграммы направленности в азимутальной плоскости вычислить по формуле

$$\varphi_{0,5} = 2\sqrt{\varphi^2_{0,5\,изм} - 2(\ln 2)R^2}$$

5.3. С учетом п.4.1., остановить движение антенны по угломестной координате и определить временной отрезок между значениями выходных сигналов $T_{ист.макс.}$ и 0,5 $T_{ист.макс}$ в единицах времени ($\Delta t_{0,5}$) и найти половину ширины кривой прохождения по формуле:

$$\theta_{0,5\,изм} = \Delta t_{0,5}\ 15\cos\delta_m.$$

Ширину диаграммы направленности в угломестной плоскости вычислить по формуле:

$$\theta_{0,5} = 2\sqrt{\varphi^2_{0,5\,изм} - 2(\ln 2)R^2}\,,\quad \text{где}$$

$\delta_m = \delta_{1950,0} + (M - 1950) \times 19'',761 = 58^0\,53'\,40''$

$R = 2'15''$ - радиус диска радиоисточника “ Кассиопея - А”.

5.4. П.п. 5.1-5.3. выполняем в S, X, Ка-диапазонах (Таб. 5).

Таб.5

Диапазон S								
h 80	° 70	° 60	° 50	° 40	° 30	° 20	° 10	°
$\theta_{0,5}$	31'50" 32'	00" 32'	05" 32'	15" 32'	20" 32'	25" 32'	25" 32'	30"
$\varphi_{0,5}$	31'20" 31'	25" 31'	32" 31'	36" 31'	40" 31'	50" 31'	55" 32'	00"

Диапазон X								
h 80	° 70	° 60	° 50	° 40	° 30	° 20	° 10	°
$\theta_{0,5}$	9'04" 7'42" 6'41"	9'08" 7'44" 6'47"	9'10" 7'50" 6'52"	9'12" 7'54" 6'55"	9'15" 7'58" 7'00"	9'25" 8'00" 7'05"	9'26" 8'04" 7'10"	9'28" 8'10" 7'15"
$\varphi_{0,5}$	9'03" 7'35" 6'37"	9'08" 7'39" 6'40"	9'12" 7'43" 6'43"	9'15" 7'48" 6'47"	9'20" 7'51" 6'50"	9'24" 7'55" 6'55"	9'28" 7'58" 6'58"	9'30" 8'00" 7'00"

Диапазон Ka								
h 80	° 70	° 60	° 50	° 40	° 30	° 20	° 10	°
$\theta_{0,5}$	2'17" 2'03" 1'52"	2'19" 2'05" 1'53"	2'20" 2'08" 1'55"	2'23" 2'11" 1'58"	2'25" 2'14" 2'00"	2'28" 2'17" 2'03"	2'30" 2'03" 2'05"	2'30" 2'20" 2'08"
$\varphi_{0,5}$	2'16" 2'03" 1'45"	2'18" 2'05" 1'46"	2'19" 2'08" 1'47"	2'22" 2'11" 1'50"	2'24" 2'14" 1'52"	2'25" 2'16" 1'54"	2'27" 2'17" 1'56"	2'28" 2'18" 1'58"

6. Измерение эффективной площади антенны.

6.1. Включить РПС, выбрать требуемый частотный диапазон и направить на “холодное” небо, близ возможно высокой угломестной координаты траектории радиоисточника.

6.2. Включить ГШК и измерять величину выходного сигнала АС ($T_{\text{ГШК.}}$).

6.3. Выйти на программу радиоисточника с учетом поправок контррефлектора, ΔA, Δh и измерить величину выходного сигнала АС ($T_{\text{ист.}}$).

6.5. Эффективная площадь вводится следующей формулой[3]:

$$A_{\text{эфф.}} = g\,\frac{2KT_{ист.}}{F}, \quad \text{где}$$

$A_{\text{эфф.}}$- эффективная площадь антенны,

$K=1{,}38.10^{-23}$ Дж/град –постоянная Больцмана,

F - спектральная плотность потока излучения радиоисточника (Вт/м^2 Гц).

g -безразмерная величина, которая учитывает соизмеримость угловых размеров источника и ширины диаграммы направленности антенны и вычисляется из выражения.

$$g=\left\{\left[1-\frac{1}{2}\left(\frac{R}{0{,}6\theta_{0,5}}\right)^2+\frac{1}{6}\left(\frac{R}{0{,}6\theta_{0,5}}\right)^4\right]\left[1-\frac{1}{2}\left(\frac{R}{0{,}6\varphi_{0,5}}\right)^2+\frac{1}{6}\left(\frac{R}{0{,}6\varphi_{0,5}}\right)^4\right]\right\}^{\frac{1}{2}}$$

6.6. Выполнить п.п. 6.1.-6.5. для убывающей угломестной координаты с шагом $\Delta h=10^{o}$.

6.7. Произвести операции по п.п. 5.1.-5.6. на диапазонах “X” и ”Ka”:

По результатам измерений параметров указанных в п.п. 5.1.-5.7. по формулам

$$КИП=A_{\text{эфф.}}/A_{\text{геом.}}, \qquad SEFD= 2KT_{сист}/A_{эфф}$$

определить зависимость коэффициента использования поверхности (КИП) и эквивалентной плотности потока приемной системы (SEFD) от угла места (Таб. 6).

Таб.6

Диапазон S								
h 80	° 70	° 60	° 50	° 40	° 30	° 20	° 10	°
$A_{эфф.}$	90	89 87		87 86	85	84		84
КИП	0,68	0,67 0,65		0,65 0,65	0,64	0,63		0,63
SEFD	1983 2371		2844 3305	3767	4294	4680		4998

Диапазон X								
h 80	° 70	° 60	° 50	° 40	° 30	° 20	° 10	°
$A_{эфф.}$	86	85 85		84 83	82	81		80
КИП	0,70	0,69 0,69		0,67 0,67	0,66	0,66		0,65
SEFD	1940 2262		2842 3673	4270	4941	5244		5632

Диапазон Ka								
h 80	° 70	° 60	° 50	° 40	° 30	° 20	° 10	°
$A_{эфф.}$	68	67 66		66 65	63		61	60
КИП	0,51	0,5 0,5		0,5 0,49		0,47	0,46	0,45
SEFD	7686 8160		8640 8720	9429	10255		11130	12044

7. Измерения уровней ближних боковых лепестков

7.1**.** Радиотелескоп с учетом всеми поправками установить на программу слежения траектории радиоисточника с временным опережением не менее шестикратной ширины главного лепестка, обеспечивающий прохождение источника через главный и ближайшие боковые лепестки диаграммы направленности.

7.2. Остановить АС по обеим координатам и измерять величину выходного сигнала АС ($T_{ш.сист.}$).

7.3. Для калибровки АС, включить ГШК и измерять величину выходного сигнала АС ($T_{гкш.}$).

7.4. При прохождении радиоисточника через боковые лепестки диаграммы направленности, при необходимости, с учетом динамического диапазона АС выбираем необходимое усиление и измерять величины выходных сигналов АС ($T_{бок.\ макс.л}$,$T_{бок.\ макс.п.}$).

7.5. По выходным значениям $T_{бок.\ макс.л.}$,$T_{бок.\ макс.п.}$ и $T_{ист.\ макс.}$ (Рис.3) определяем уровни боковых лепестков.

7.6. Произвести операции по п.п 7.1.- 7.6. для частотных диапазонов “X” и “Ka” (Таб. 7).

Таб.7

Диапазон S								
h 80	° 70	° 60	° 50	° 40	° 30	° 20	° 10	°
Бок.л.	25 24		23,5	23	22,5	22 22		21
Бок.п.	19 18,8		18,5	18	17,4	17 16,5		16

Диапазон X								
h 80	° 70	° 60	° 50	° 40	° 30	° 20	° 10	°
Бок.л.	24 23	22,5		22 21,5		21	20 19	
Бок.п.	17,5	17,3	17	16,5	16,1	15,7	15,2	15

Диапазон Ka								
h 80	° 70	° 60	° 50	° 40	° 30	° 20	° 10	°
Бок.л.	21	20,5	20	20	19 18,5		18 17	
Бок.п.	16	16,7	16,2	16	15,5 15		14,5 14	

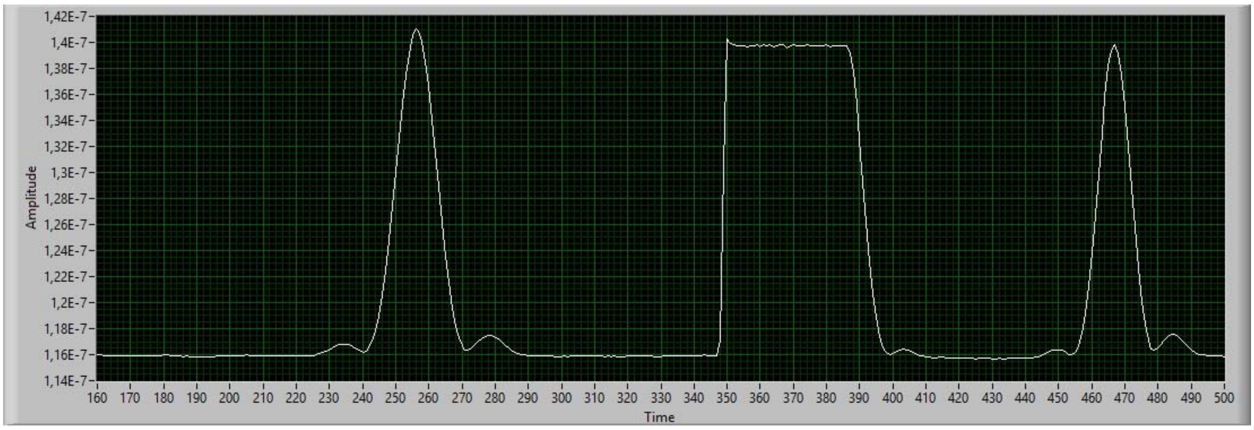

Рис.3. Сканирование источника "Кассиопея-А"

9. Выводы

- Значения измеренных характеристик РТ-13 в основном соответствуют ожидаемым.
- Параметры РТ-13 измерялись в дневное время суток и при температурах окружающей среды -20^{0}С и ниже. С целью уменьшения воздействия солнечного излучения, желательно измерения повторить при умеренных температурах и в ночное время суток.

Литература

1. Астрономический ежегодник (постоянная часть).
2. J. W. Baars, R. Genzel, I. I. K. Payting- Toth, A. Witzel. Astrophys., 1977, v.61, p. 99.
3. Цейтлин Х. М. Антенная техника в радиоастрономии. М., " Сов. радио", 1976.

Microwave Photonic Processing of High-Speed Microwave Signals

Invited Paper

R. A. Minasian, *Fellow, IEEE, Fellow OSA*

School of Electrical and Information Engineering,
University of Sydney, NSW, Sydney, 2006, Australia

Microwave photonic techniques are attractive for processing high bandwidth signals, overcoming inherent electronic limitations. These processors provide new capabilities for realising high time-bandwidth operation and high-resolution performance. In-fibre signal processors are inherently compatible with fibre optic microwave systems that can integrate with wireless antennas, and can provide connectivity with in-built signal conditioning. Recent new methods in wideband signal processors including ultra-wideband phase shifters for phased array beamforming; widely tunable single passband filters; switchable microwave photonic filters; wideband photonic mixers; high-resolution multiple frequency microwave photonic measurement systems; and photonic RF memory structures; are presented.

1. Introduction

Photonic signal processing, using photonic approaches to condition microwave signals, is attractive due to the inherent advantages of high time-bandwidth product and immunity to electromagnetic interference (EMI) [1-3]. It opens up new possibilities for overcoming the inherent bottlenecks caused by limitations in conventional electrical signal processors [1]. In-fibre signal processors are directly compatible with fibre optic microwave systems, and can provide connectivity with in-built signal conditioning. These new techniques transcend the limitations of existing electronic methods, and enable new structures to be realised, which not only can process high-speed signals but which can also realise adaptive operation.

A key benefit of using optical techniques for wideband electromagnetic systems is that the entire RF/mm-wave spectrum constitutes only a small fraction of the carrier optical frequency, thus offering the fundamental advantage of very little frequency-dependent loss and dispersion across entire microwave bands of interest. Photonic signal processing leverages the advantages of the optical domain, which can then benefit from the wide bandwidth, low loss, and natural immunity to electromagnetic interference that photonics offers. Photonic signal processing also enables dynamic reconfiguration of the processor characteristics over multi-GHz bandwidths, which is a difficult task for electrical microwave approaches. This offers the ability to realise functions in microwave systems that are either very complex or, perhaps not even possible in the RF domain.

Recent new methods in wideband signal processors are presented including ultra-wideband phase shifters for phased array beam forming; widely tunable single passband filters; switchable microwave photonic filters; wideband photonic mixers; high-resolution multiple frequency microwave photonic measurement systems; and photonic RF memory structures that can realise a long reconfigurable storage time with wide instantaneous bandwidth.

2. Wideband phase shifters for phased array beamforming

Optically controlled beamforming techniques for phased array antennas are of significant interest due to the advantages that photonics can offer. These include a wide operating bandwidth, remote antenna feeding, and immunity to electromagnetic interference. Programmable phase shifters are required for beam forming; however it is difficult to realize phase shifters that can operate over a very wide microwave frequency range.

Techniques based on microwave photonics can offer a solution to this limitation. A phase shifter structure based on the use of spatial light modulators is shown in Fig. 1 [4]. The use of spatial light modulators is attractive for this purpose because of their versatile and powerful optical signal processing capabilities. Phase shifting is achieved by adjusting the relative optical phase of the carrier and the sideband within the full 0 ° to 360 ° range by means of a two-dimensional (2D) diffraction-based Fourier-domain optical processor (FD-OP) comprising an array of liquid crystal on silicon (LCoS) pixels [5], and this phase shift is directly translated to the RF signal after detection. Multiple wideband phase shifters are realised within the single structure by processing the WDM wavelengths simultaneously. The LCoS pixels enable dynamic wavelength routing to the output ports, and optical to RF signal conversion with direct phase and amplitude translation control. The diffraction grating disperses and images different spectral components of the input modulated light onto a different portion of the LCoS horizontally while overlapping a large number of vertical pixels. Then specially calculated phase modulation patterns are applied to impress optical phase differences between the respective optical carrier and the sideband for each WDM channel, which are directly translated to the RF signal after detection. This beam forming network is highly flexible and reconfigurable since it is software programmable. Also, since the microwave phase shifters in the array are independent and have quasi-continuous phase control from 0 to 2 π, arbitrary scanning beam angles can be realised.

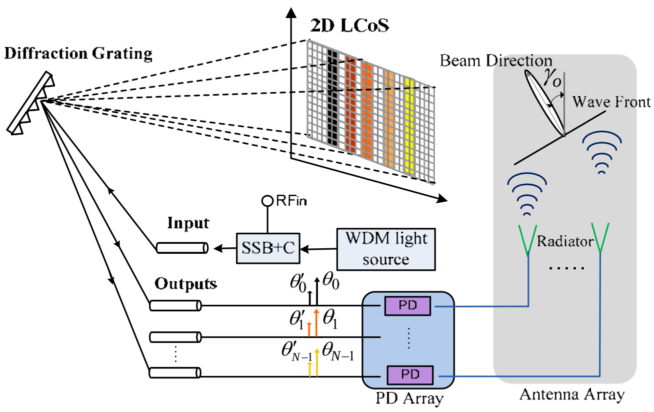

Fig. 1. Topology of the photonic controlled beamforming network and its operation.

The measured response for a single microwave photonic phase shifter is shown in Fig. 2 [6]. Different RF phase shifts are obtained by software programming of the spatial light modulators to control the relative phase of the carrier and the sideband. Fig. 2 demonstrates that the phase shift achieved for the microwave signal covers the full −180° to +180° range, and that the phase shift is frequency independent over the range of 14 GHz to 20 GHz.

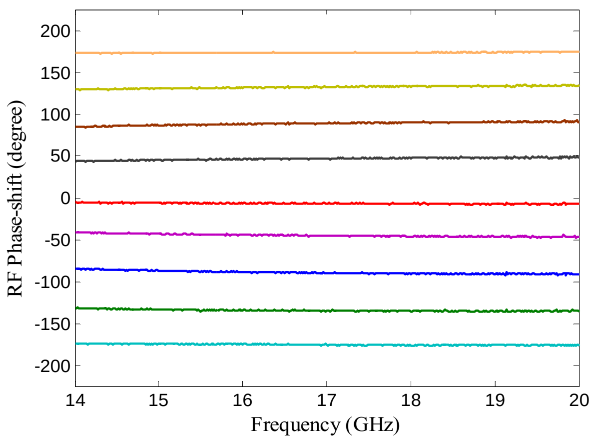

Fig. 2. Measured RF phase shift response of the optical RF phase shifter.

Multiple phase shifters can be realized within a single structure by processing the WDM wavelengths simultaneously. Experimental results are shown in Fig. 3, which demonstrate four independent microwave phase shifters that operate simultaneously over a 10-20 GHz frequency range. Fig. 3(a) shows a set of four phase shifters to obtain a scanning angle of 20 ° (with half wavelength radiating element spacing). Fig. 3(b)-

(d) shows the flexibility of the structure for tuning the beam direction for scanning angles of -20°, 40° and -40°, which was achieved by programming the RF phase shifters. This approach can enable scalability to larger phased arrays due to the parallel processing capability of the concept.

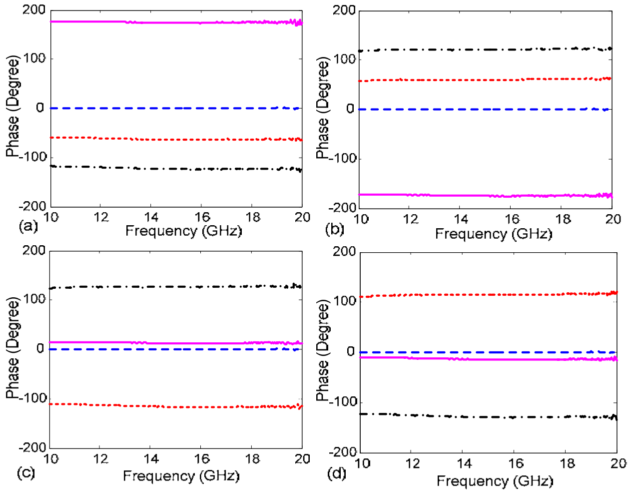

Fig. 3. Measured phase shifts corresponding to the scanning angle of (a) 20 °, (b) -20 °, (c) 40 °, (d) -40 ° (phase shifter 1 ; 2 , 3 , 4).

Fig. 4 shows the array factors for a linear 4-element phased array antenna optical beamforming feeder at 18 GHz, with measured phase controllers set for scanning angle (a) 20° (b) 40° (c) -20° (d) -40°

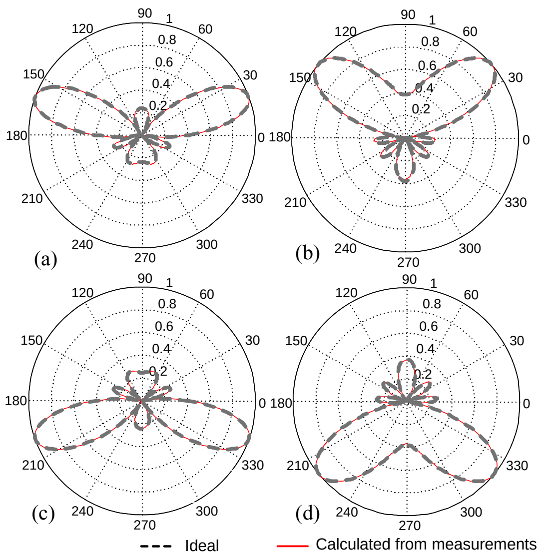

Fig. 4. Beamsteering for 4-element phased array antenna at 18 GHz

A different structure for a microwave photonic phase shifter that can achieve a full 360 ° phase shift with very little RF signal amplitude variation, and which can operate over a very wide frequency range is shown in Fig. 5. It is based on controlling the amplitude and phase of the optical carrier and the two RF modulation sidebands via the DC bias voltages to a dual-parallel Mach-Zehnder modulator (DPMZM) [7]. The two RF modulation sidebands, which have different amplitudes and phases, beat with the optical carrier at the photodetector to generate the output phase shifted RF signal. The amplitude and RF phase of this output RF signal depends on the amplitude and phase of the optical carrier as well as the differing amplitudes and phases of the two RF modulation sidebands. The two RF modulation sidebands that have different amplitudes and phase are set through the use of a DPMZM for the modulator unit. The DC bias voltages control the amplitude of the optical carrier and the sidebands. The structure is simple, only requiring a single laser, a single DPMZM modulator unit that is commercially available, and a single photodetector. It has the advantage of having a very convenient control of the RF phase shift which is set by adjusting DC voltages.

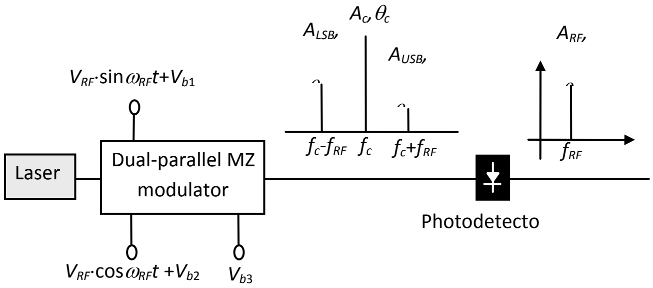

Fig. 5. Microwave photonic RF phase shifter showing the optical and RF spectrums.

Fig. 5 shows the dissimilar sidebands generated by the DPMZM when driven by a single frequency RF signal, and the output RF signal with a phase shift of θ_{RF} after photodetection. The idea is based on designing the amplitudes (A_c, A_{LSB} and A_{USB}) and the phases (θ_c, θ_{LSB} and θ_{USB}) of the optical carrier and the two RF modulation sidebands by controlling the modulator bias voltages (V_{b1}, V_{b2} and V_{b3}), so that the output RF signal phase θ_{RF} can be shifted between 0 ° and 360° while the output RF signal amplitude A_{RF} remains unchanged.

The measured phase and amplitude response of the phase shifter over a wide frequency range from 2 GHz to 16 GHz for different modulator bias voltages, are shown in Fig. 6. This demonstrates a flat phase response performance over a wideband 8:1 frequency range. The phase ripple standard deviation is less than 2° for all the measured phase responses in Fig. 6(a). Furthermore, Fig. 6(b) shows that there are less than 3 dB changes in the RF signal amplitude over the entire broadband frequency range during the 0° to 360° phase shift operation, which is one of the flattest responses reported for a wideband RF phase shifter.

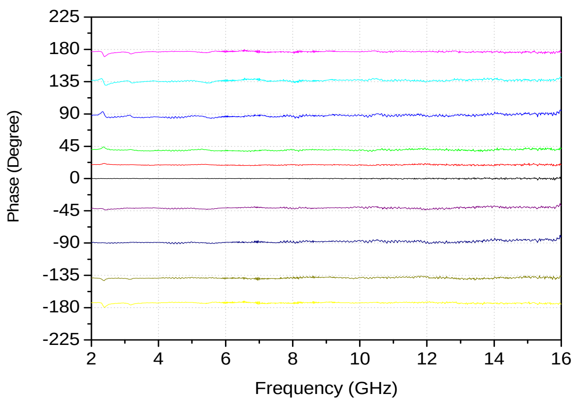

(a)

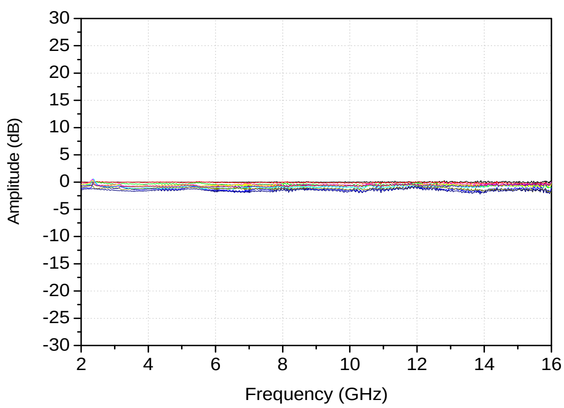

(b)

Fig. 6. Measured (a) phase and (b) amplitude responses of the photonic RF phase shifter.

3. Ultra-wide continuously tunable single passband filters

Microwave filters having high passband selectivity and wide continuous tunability are required in many applications. The use of the stimulated Brillouin scattering principle (SBS) is an attractive approach for implementing high-resolution, high Q-factor microwave photonic filters. A tunable single-passband microwave photonic filter structure using the SBS principle is shown in Fig. 7 [8]. The Brillouin gain and loss spectra are shown in Fig. 7(b).

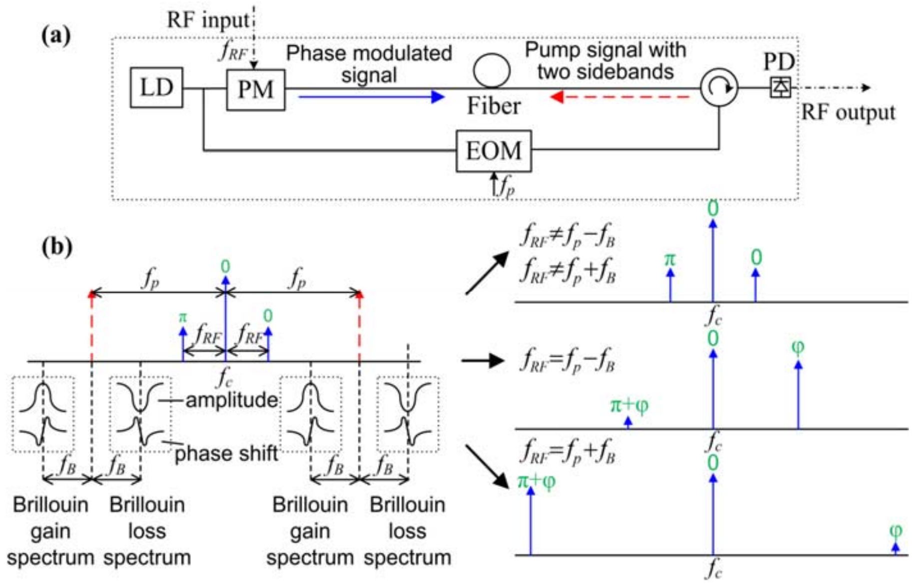

Fig. 7. Tunable single-passband microwave photonic filter structure using the SBS principle

Fig. 8(a) shows the measured response of the SBS-based microwave photonic filter operating at a centre frequency of 10 GHz. The filter exhibits an extremely high resolution: -3 dB bandwidth of 21.25 MHz, an excellent shape factor: -20 dB bandwidth of 170 MHz, and a high out-of-band rejection of 35 dB. Fig. 8(b) shows the measured results showing the continuous tuning range of the single-passband bandpass filter tuned from 1-20 GHz together, which exhibits. The filter exhibits an extremely high Q of around 1000 and a high resolution with a -3 dB bandwidth of only 16 MHz, and a -20 dB bandwidth of 130 MHz, together with a high out-of-band rejection of 35 dB. The filter realises single passband shape-invariant tuning over the entire 1-20 GHz tuning range.

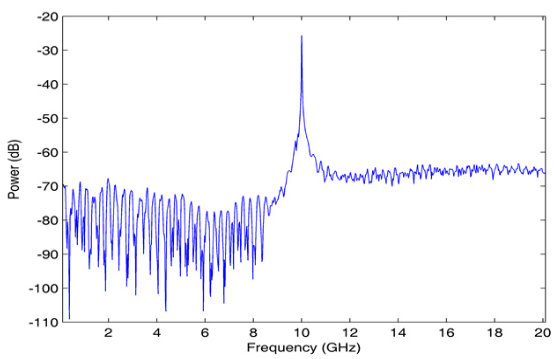

(a)

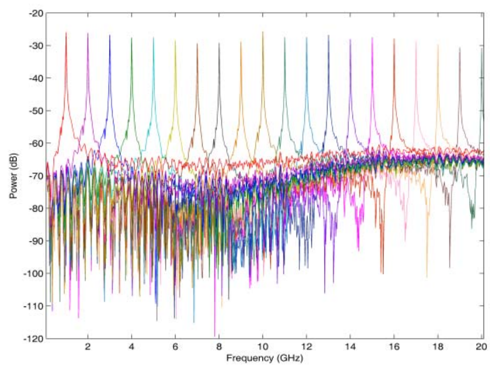

(b)

Fig. 8. (a) Measured frequency response of the microwave photonic filter operating at a centre frequency of 10 GHz. (b) Measured frequency response for the continuously tunable single-passband microwave photonic filter.

4. **Programmable switchable microwave photonic filters**

Multi-function applications require the ability to switch the different filtering functions e.g. between a bandpass filter and a notch filter to provide both channel selection and channel rejection. A structure that enables the realisation of a switchable microwave photonic filter that can be switched between a bandpass filter and a stopband notch filter response, using simple and rapid control is shown in Fig. 9 [9]. It is based on a SBS technique in conjunction with a dual drive Mach-Zehnder modulator (DDMZM) that processes the sidebands of the RF modulated signal. Switching of the filter function is simply and conveniently obtained by changing the DC bias to the DDMZM. In addition, the centre frequency of the switchable filter can be tuned over a wide frequency range.

The pump light is modulated at RF frequency f_p by a low-biased intensity modulator (IM) in the lower branch which generates a double-sideband suppressed-carrier signal, and which is used to tune the filter frequency by changing the positions of the SBS gain and loss. The filter switching function is achieved by changing the DC bias voltage V_{DC} of the DDMZM to control the relative phase differences between the carrier and the sidebands. The SBS process occurs in the fibre between the RF modulated signal and the pump signal. Each sideband of the pump signal introduces both SBS gain and SBS loss spectra at frequency f_B away from the sideband, where f_B is the Brillouin frequency shift.

In order to realise bandpass filtering, the bias is selected so that the DDMZM operates as a phase modulator. Only the RF signal with the frequency of $f_{RF} = f_p - f_B$ undergoes the SBS effect which consequently breaks the amplitude equality between the sidebands since the lower sideband of the RF modulated signal is significantly attenuated while the upper sideband is amplified, as shown in the right-hand side of Fig. 9(b), and this creates a bandpass response. In order to realise notch filtering, we select the bias so that the phase difference between the upper sideband and the carrier is $\pi/4$ while the phase difference between the lower sideband and carrier is $3\pi/4$, and in addition there is a large amplitude imbalance between the sidebands, as shown in Fig. 9(b). Hence, an RF signal is obtained at the photodetector output at all frequencies except when the input RF frequency is $f_{RF} = f_p - f_B$, and the amplitudes of the two sidebands are equalised by properly choosing the SBS pump power, as shown in the right-hand side of Fig. 10(b), when the beatings between the carrier and the two sidebands are out-of-phase and fully cancel, thus creating a notch. Consequently, a switchable microwave photonic filter at the centre frequency of $f_p - f_B$ is realised, in which the switching function is easily accomplished by changing the DC bias of the DDMZM. The frequency where the switched filtering occurs can also be tuned by changing the drive frequency f_p.

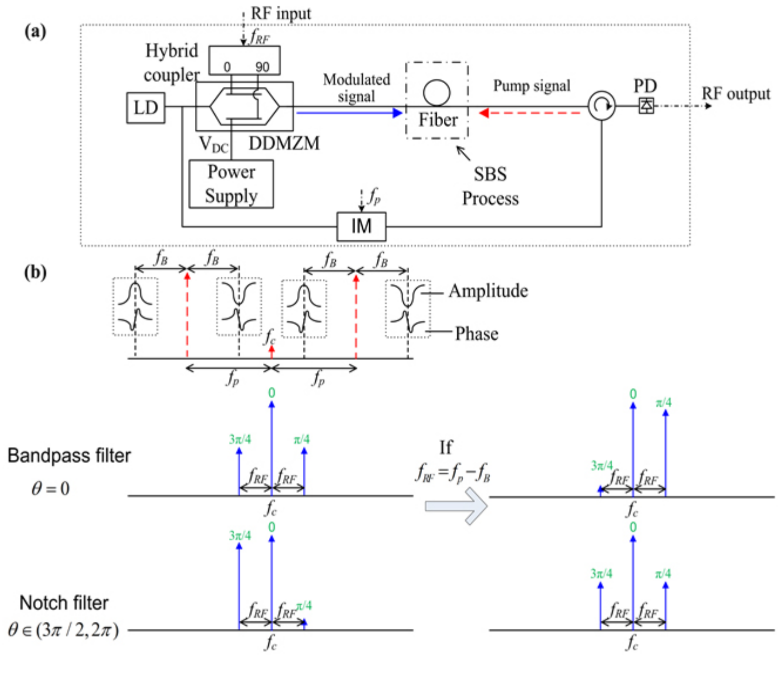

Fig. 9. Operational principle of the switchable filter (a) structure; (b) spectra.

Experimental results are shown in Figs. 10(a) and 10(b) which demonstrate the ability of this structure to switch between a high-resolution bandpass filter and a high-resolution notch filter at each frequency, with Q values around 400 to 500, and the ability to operate over a wide frequency range from 2-20 GHz. Tuning of the filter was obtained by changing the pump frequency f_p. Switching between high-resolution bandpass and notch filtering with 3-dB widths of 30-40 MHz, at all frequencies from 2-20 GHz with shape-invariant response is demonstrated.

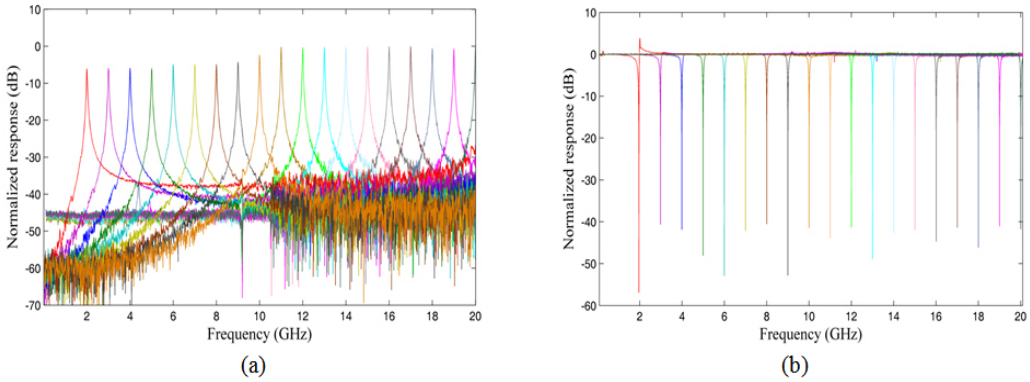

Fig. 10. Measured normalised frequency response of the switched tunable filter between (a) bandpass response; and (b) notch response.

5. Photonic mixers

Microwave frequency conversion is a key function that is essential in many optical-wireless system applications. Advanced communication and radar systems need to operate over multiple passbands simultaneously. Photonic microwave mixers bring advantages of extremely wide bandwidth of operation, near infinite isolation between the RF and the LO ports, and EMI immunity, which are unique and fundamental features of photonics. They are also attractive for enabling the processing of microwave and RF signals directly within the optical fibre transport system.

Fig. 11 shows an example of a fibre optic antenna remoting configuration using optical frequency downconversion for the receive mode operation.

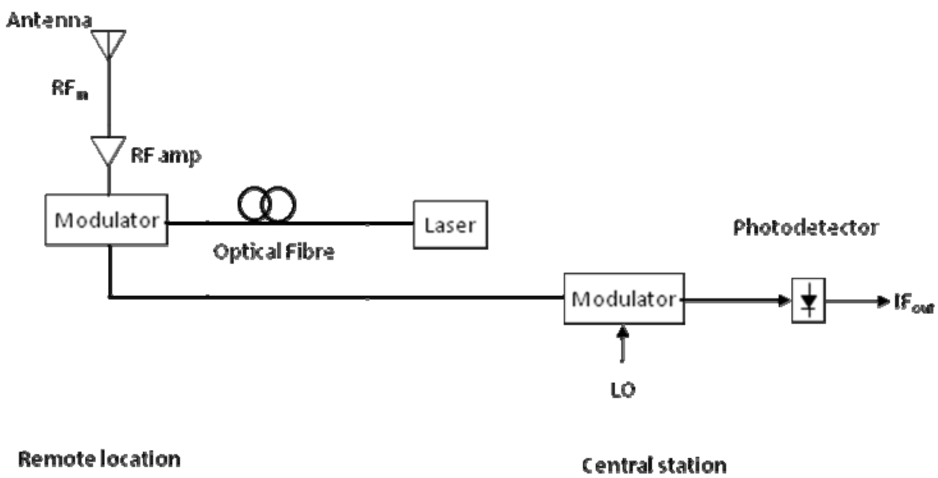

Fig. 11. Fibre optic antenna remoting configuration using microwave photonic frequency downconversion for the receive mode operation.

Note that the remote antenna subsystem, which may need to operate in unfavourable environments, comprises a minimum of hardware. It simply uses a modulator to impress the RF signal onto an optical carrier and transports it to the central station from the remote location using optical fibre. The central station, which operates in a well-regulated controlled environment, comprises most of the system including the laser source, the LO modulator, the photodetector, and the processing electronics. This ability to transport signals to and from remote locations and to minimize the hardware needed at the remote location is a key advantage of microwave photonic mixing. It eliminates the principal limitations of conventional electronic microwave receiver approaches that require multiple-stage down-converting mixers which require the generation of multiple associated LO oscillators that have problems with size, weight, power requirements, reduced dynamic range due to multiple stage downconversion, and the important deficiency of limited mixer port-to-port isolation. These issues exacerbate as wider bandwidth systems are needed. Microwave photonic mixing offers a unique solution for some of the most demanding, wideband antenna receiver applications. It enables a single-stage direct frequency conversion to IF frequencies with excellent port-to-port isolation. Achieving high LO-RF isolation is difficult in conventional electronic mixers, though it is extremely important in surveillance, radar, and defence systems. The important advantage of microwave photonic mixers is that the LO-RF isolation is inherently nearly infinite because there is no leakage path from the optical carrier to the RF electrodes on the modulator. In addition, microwave photonic downconversion also enables low frequency photodetectors to be used, which have enhanced efficiency and higher power handling capabilities.

Several defence applications require the ability to process microwave signals in systems that are spatially distributed. For instance, electronic support systems require a spatial distribution of antennas for direction finding [10]. These need to process microwave signals extending to millimeter wave frequencies, with high dynamic range capabilities, while also being low noise, robust, and spatially distributed. A long baseline technique is necessary for high accuracy, which requires the antennas to be placed at locations that are far apart. On aircraft platforms, typical configurations have antenna sensors located at the extremities of the airframe to provide good long-baseline antenna coverage for greater accuracy in direction finding over broader bandwidths.

Fig. 12 shows a simple photonic mixer comprising a series of optical phase modulators and a fibre Bragg grating FBG. The FBG blocks the optical carrier frequency , which then enables the IF to be produced by the beating between the RF sidebands and LO sidebands only at the photodetector following amplification by the erbium doped optical amplifier EDFA. This has advantages of the ability to operate over a very wide frequency range, and also enables the RF and LO to be at separate ports which enables antenna remoting.

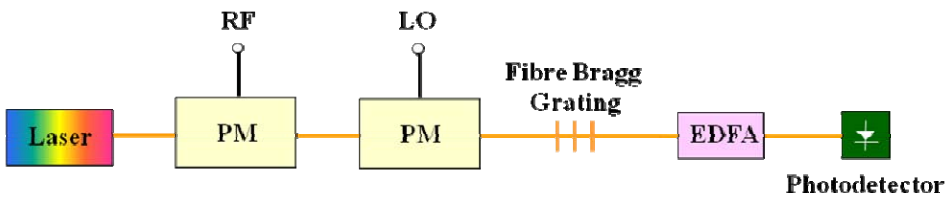

Fig. 12. Dual series photonic mixer structure.

The problem of processing multiple remote sensors /antennas simultaneously can be solved using microwave photonic mixers by invoking WDM techniques. Fig. 13 presents the concept for achieving multiple channel microwave photonic mixing using a single LO. The remote antennas are at disparate locations, and WDM is used to combine the multiple channels and apply frequency downconversion simultaneously to all the channels by passing the multiplexed signals to a modulator driven by the LO signal, before being demultiplexed and detected. This produces *N* downconverted IF outputs for each of the *N* channels. Microwave photonic frequency conversion can exploit the wavelength domain which enables a reduction in the component count (with advantageous size, weight complexity and reliability implications), as well as allowing the use of a common local oscillator to be applied to all channels. An important feature of this approach is that it enables minimal and simple hardware to be used at the remote antenna locations, i.e. just an optical modulator and an RF amplifier, whereas the rest of the system is located and distributed from the central station.

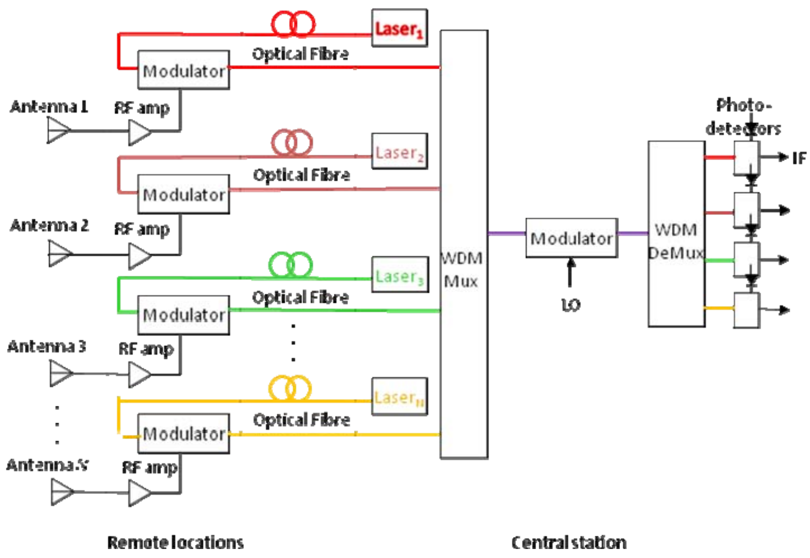

Fig. 13. Multiple channel microwave photonic frequency downconversion for *N* remote antennas in different locations, using a single LO at the central station.

6. Microwave frequency measurement

The ability to perform frequency measurement (FM) on an unknown microwave signal over several decades of RF bandwidth with high resolution is an important requirement for defence and radar warning system applications. This is essential in order identify the frequency of the intercepted microwave signal so that it can then be used to cue and reduce the search parameters of other specialised receivers [11]. With future defence systems being driven to higher frequencies and larger bandwidths, the challenge has been to realise a frequency measurement technique that can operate over an ultra-wide frequency range from sub-gigahertz to millimeter-wave frequencies, together with high resolution, and near real-time response.

Conventional electronic FM techniques are limited in their bandwidth of operation, and can suffer from electromagnetic interference (EMI). Microwave photonic systems can provide exceptionally high bandwidth of operation as well as EMI immunity to enable a solution to these problems. FM systems utilising microwave photonic technique can generally be divided into three categories i.e. frequency-to-power mapping, frequency-to-space mapping, and frequency-to-time mapping.

A new FM structure that can realise multiple-frequency measurement, while simultaneously achieving a high resolution and a wide measurement range is shown in Fig. 14 [12].

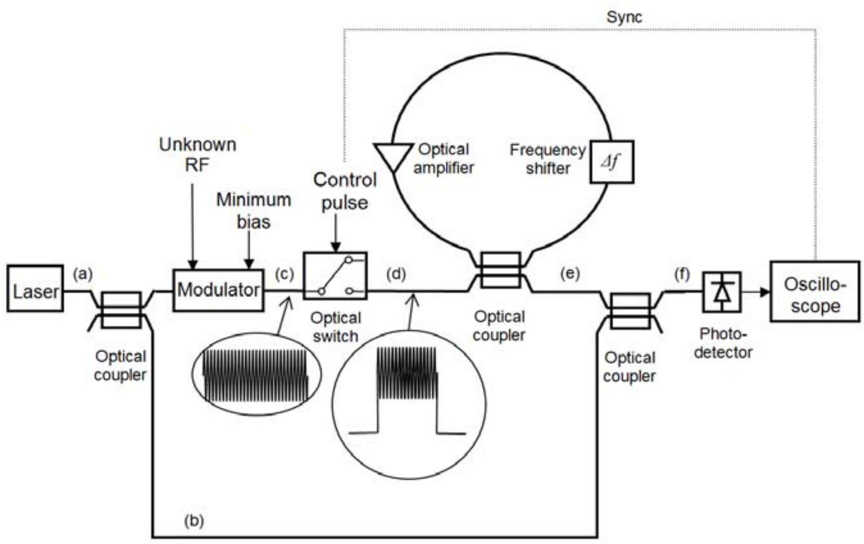

Fig. 14. Structure of the frequency measurement technique based on the FS-RDL structure.

The concept is based on successively frequency-shifting (using a recirculating loop) a modulation sideband of the optical signal until it is brought close to the reference carrier frequency, and then combining and detecting them through a narrowband filter. This approach requires only simple pulse detection and simple counting of the number of recirculations until an output signal is detected, from which the frequencies inherent in the unknown input microwave signal can be measured over a wide frequency range and with high resolution.

Light from a laser is split into two branches by an optical coupler. In the upper branch it is modulated by the unknown microwave signal through a null-biased electro-optic modulator (EOM). The carrier suppressed double sideband (CSDSB) modulated optical signal is then time-gated by an optical switch which is controlled by an electrical square pulse and injected into a frequency shifting recirculating delay line (FS-RDL) loop. The loop comprises an optical frequency shifter and an optical amplifier. The optical frequency shifter imposes a frequency shift Δf on the light after each circulation, while the optical amplifier is used to compensate for the system loss to obtain a large number of circulations. The output of the loop is combined with the unmodulated laser light that is carried in the lower branch, and is then detected by a low-speed photodetector (PD). The photo-detected current is then observed using a low-bandwidth oscilloscope.

The operation principle of the photonic FM technique based on a FS-RDL structure is explained in Fig. 15.

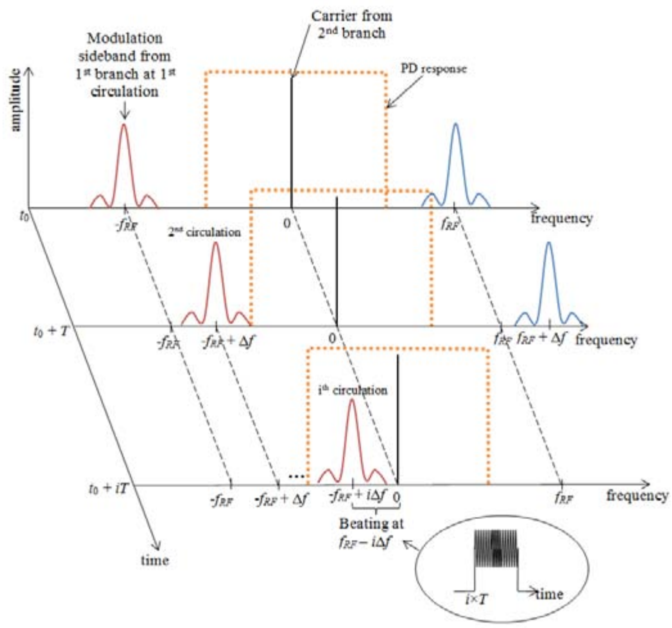

Fig. 15. Principle of operation of the frequency measurement technique based on FS-RDL structure.

At the upper branch, after the optical switch, there are two sinc-shape spectra corresponding to the time-gated CSDSB optical signal. This signal is launched into the FS-RDL loop, in which, after each circulation, the lower sideband will be frequency shifted toward the carrier wavelength while the upper sideband will be shifted away from the carrier wavelength. At the output optical coupler, these frequency-shifted replicas of the CSDSB optical signal are combined with the unshifted carrier from the lower branch. The sidebands and the carrier will beat at the PD to produce beatings at the frequencies corresponding to the differences between the frequency-shifted modulated sidebands and the unshifted optical carrier. These beatings result in RF pulses at different carrier frequencies, determined by the difference between the original carrier frequency and the frequency-shifted modulated sidebands frequencies. If the PD is designed to have a narrow bandwidth of less than half of the frequency shift i.e. $\Delta f/2$ so that all beatings with high frequency RF pulses will be filtered out, this leaves only one beating with a low frequency RF pulse to pass when the sideband is shifted close enough to the carrier, and there will be only one RF pulse displayed on the oscilloscope. Since the loop unit delay time is known, we can determine how many circulations have occurred in order for the frequency-shifted modulated sideband to produce such beating, by observing the time position of the RF pulse on the oscilloscope. The number of circulations, in turn, can be used to calculate how much frequency shift the sideband has experienced in order to move close to the unshifted carrier. Thus, the total amount of frequency shift required for the sideband to move close to the carrier gives an estimation of the relative position of the sideband to the carrier, or in other words, the RF frequency of the modulating microwave signal. The estimated microwave frequency is given by

$$f_{RF} = n_0 \times \Delta f \qquad (1)$$

where n_0 is the number of circulations it takes for the modulation sideband to be frequency shifted close to the carrier so that the condition $(n_0\Delta f - f_{RF}) < \Delta f/2$ is satisfied.

Thanks to its frequency-to-time mapping nature, this photonic FM system has the capability to measure multiple frequencies. Also it can be noted that since the resolution and error performance of the FS-RDL based FM system only depends on the frequency shift value introduced by the optical frequency shifter, it remains constant over the entire wide frequency range.

Fig. 16 shows the measured output results on the oscilloscope for a single input microwave signal as its frequency was changed between 10 MHz to 20 GHz. By measuring the time delay of the RF pulse, the estimation of the microwave frequency can be worked out using (1). As expected, the time position of the observed RF pulse changes as the frequency of the microwave signal changed. It can be seen that the estimation error stayed within 250 MHz, which was the frequency shift amount. Fig. 16(a) summarises the signal frequency to time mapping from inputs ranging from 0.1 to 20 GHz. Excellent agreement between the measurement and the simulation result can be seen. The measurement error as a function of the input frequency is shown in Fig. 16(b). It can be noted that the errors stayed within ± 125 MHz, and did not change when the RF frequency was increased. In other words, the frequency measurement resolution was the same for the whole measurement range.

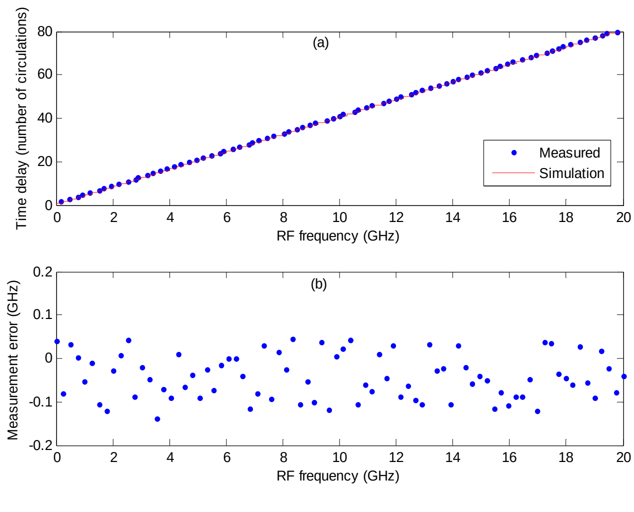

Fig. 16. (a) Measured and simulated RF frequencies versus the time delay of the RF pulse observed on the oscilloscope. (b) Measurement errors for the microwave signals at different RF frequencies.

Fig. 17 shows the measured output results on the oscilloscope for a two simultaneous input microwave signals injected into the EOM. It can be observed on the oscilloscope that there were two RF pulses and their time positions were dependent on the input frequency of the two microwave signals. Fig. 17 shows the display of the oscilloscope with different sets of input frequencies. Again, using (1), the frequencies of the input signals can be worked out and the estimation errors were less than 250 MHz.

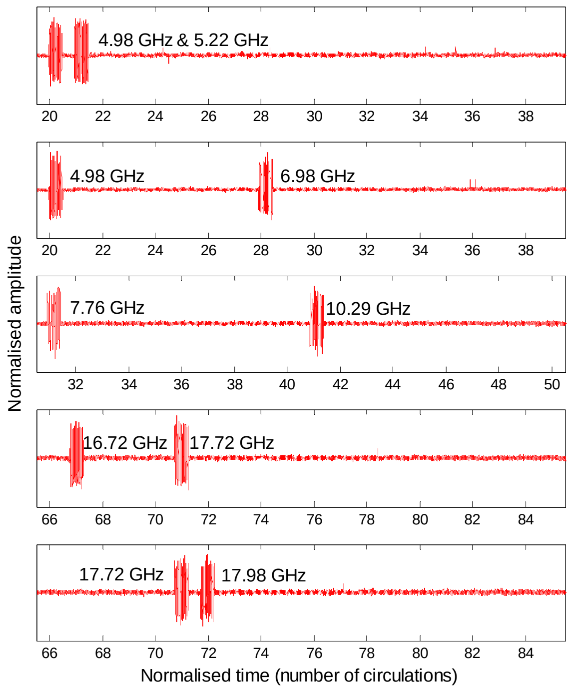

Fig. 17. Measured photocurrent waveform on the oscilloscope after the PD when two RF tones are applied to the EOM.

Measurements have shown that more than 400 circulations can be achieved. This is equivalent to a measurement range of more than 100 GHz when using a 250 MHz optical frequency shifter, while also providing the capability to detect multiple-frequency signals.

7. Photonic RF memory

The realisation of high-fidelity RF memory structures has been a difficult and long-standing problem. Many applications in radar and defence require reconfigurable high-fidelity storage of received radar pulses. An RF memory is an essential component for electronic countermeasure (ECM) applications such as range gate pull-off/pull-in. In such applications, an RF memory is used to store and retransmit one or more replicas of the threat radar RF pulse. However, the storage of complex-waveform microwave radar pulses with the required high fidelity is particularly difficult using electronic approaches due to A/D conversion resolution limitations at microwave frequencies. Electronic digital RF memory (DRFM) is currently the only effective solution for coherent RF signal storage. However, this suffers from the important limitations that it cannot simultaneously achieve both a wide instantaneous bandwidth (IBW) and a high dynamic range performance. This is because of the inherent use of the quantisation process, which generates unwanted spurious terms. Moreover, wide IBW operation capability is required for RF memory jammers.

Photonic approaches can provide a solution to these problems. This is because optical waveguides are one of the best delay line media for microwave and millimetre wave modulated signals, and the unique, high time-bandwidth product capabilities of photonic signal processing offer the possibility of overcoming the inherent bottlenecks caused by limited sampling speeds in conventional electrical signal processors [13].

Photonic RF memory (PRFM) structures can be designed to have a wide dynamic range so that time-coincident multiple signals, each at different RF frequencies, can be stored and retransmitted. However to date, their storage time capabilities have been severely limited by the potential onset of lasing. The lasing problem occurs because the conventional single-wavelength recirculating structure [14] is equivalent to a ring laser structure, and to realise multiple recirculations the operating loop gain must be close to unity. This corresponds to the onset of lasing, causing potential instability and limiting the number of recirculations and the delay time attainable in practice.

Fig. 18 shows the structure of a new PRFM that can realise a long storage time, wide IBW and high dynamic range [15]. The concept is based on the use of an optical frequency shifter inside a recirculating delay line loop to overcome the lasing problem and to enable multiple recirculations and long storage time to be realised. Modulated light from a laser is injected into a frequency shifting recirculating delay line (FS-RDL). The loop contains an optical frequency shifter and an optical amplifier. Each recirculation imposes a frequency shift Δf on the light. Consequently it prevents the significant problem of oscillation or lasing in the cavity of conventional single-wavelength loops that operate with a closed-loop gain close to unity, because here all the spectral components are continuously shifted and they cannot resonate. This permits a large number of recirculations to be obtained without pulse power degradation. The optical amplifier is used to compensate for the system loss to obtain a large number of circulations for long storage time. Optical switches are used at the input to switch the pulse into the loop, and at the output to switch out the selected RF pulse after the desired storage time for subsequent detection by a photodetector.

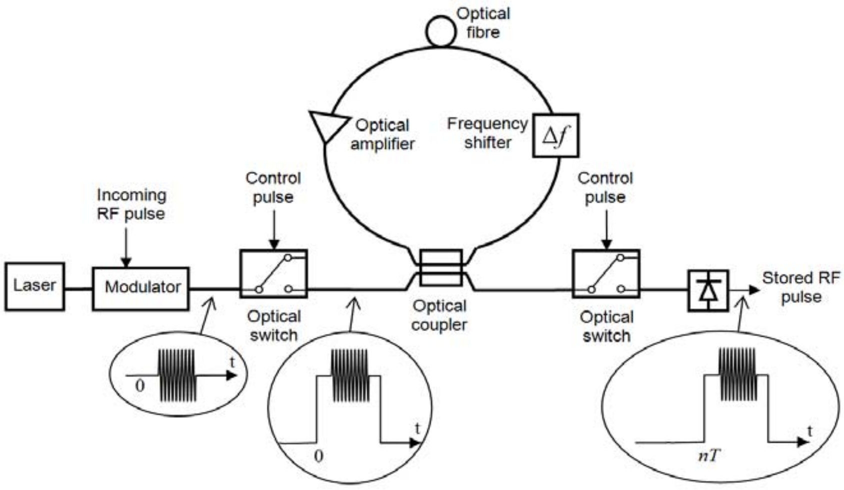

Fig. 18. Structure of the PRFM utilising the frequency shifting loop.

Fig. 19 shows the measured input RF pulse after the input optical switch as injected into the loop.

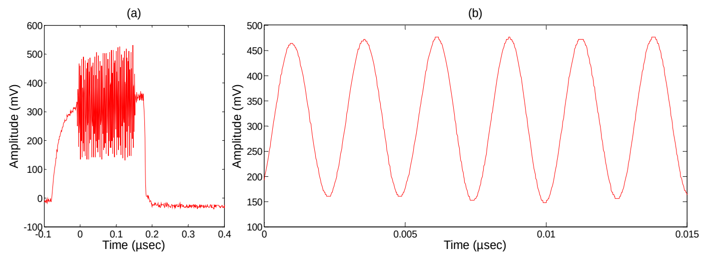

Fig. 19. Measured waveform of the input RF pulse injected into the FS-RDL loop. (a) Time scale = 0.1 μs/div, and (b) time scale = 5 ns/div. The RF pulse width was 200 ns and the RF pulse repetition interval was 500 μs.

After 150 μs, which was equivalent to 100 circulations, the RF pulse was switched out from the FS-RDL loop and passed to the photodetector. Fig. 20 shows the waveform of the RF pulse measured using the oscilloscope after the storage. It can be seen that the stored RF signal waveform is similar to the one that was injected into the FS-RDL loop, which shows high signal fidelity even after 100 circulations.

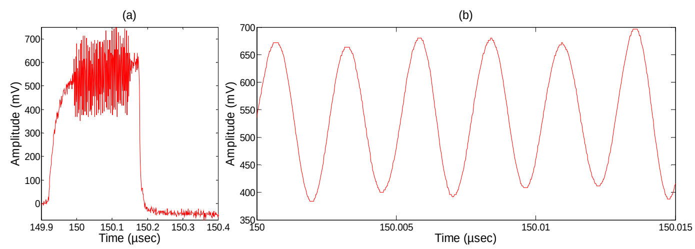

Fig. 20. Measured waveform of the stored RF pulse after 100 circulations in the FS-RDL loop. (a) Time scale = 0.1 μs/div, and (b) time scale = 5 ns/div.

Fig. 21 shows the measured results for a 5 GHz input RF pulse. A frequency shift of 750 MHz was used in the FS-RDL. The output was displayed on a spectrum analyser whose centre frequency was set to the RF pulse signal frequency and the frequency span was set to 0 Hz. Fig. 21 displays the time domain display on the spectrum analyser before and after the output optical switch. It can be seen from Fig. 21(a) that the FS-RDL can store an RF pulse carrying a 5 GHz RF signal with less than 10 dB change in the pulse amplitude for 320 µs, corresponding to 215 circulations. Fig. 21(b) and 21(c) shows the output RF pulse after being stored for 150 µs and 280 µs, which correspond to 100 and 186 circulations respectively.

To the best of our knowledge, this is the first structure that realises a photonic RF memory with long measured storage time.

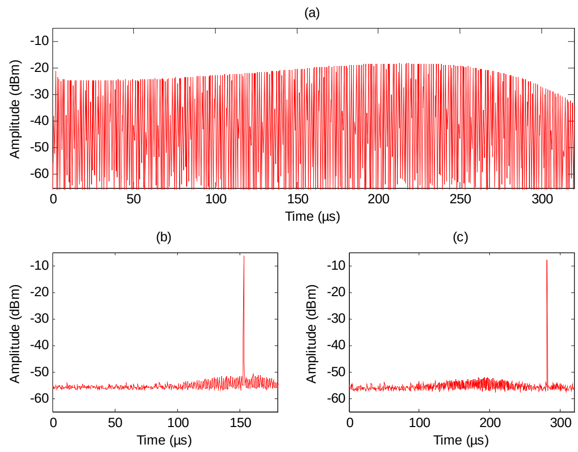

Fig. 21. Measured results for a 5 GHz RF input pulse (a) the output of the FS-RDL loop before the output optical switch, and (b) the selected RF pulse at 150 µs and (c) 280 µs.

8. Conclusion

Photonic signal processing offers the advantages of high time-bandwidth product capabilities to overcome inherent electronic limitations. A key benefit for wideband systems is that the entire RF/mm-wave spectrum constitutes only a small fraction of the carrier optical frequency. Microwave photonic structures provide attractive features for RF pre-processing with EMI immunity for fibre-fed systems, and enable in-fibre processors with connectivity and in-built signal conditioning. Recent new methods in wideband signal processors including ultra-wideband phase shifters for phased array beamforming; widely tunable single passband filters; switchable microwave photonic filters; wideband photonic mixers; high-resolution multiple frequency microwave photonic measurement systems; and photonic RF memory structures that can realise a long reconfigurable storage time with wide instantaneous bandwidth, have been presented. These processors provide new capabilities for the realisation of high-performance and high-resolution signal processing.

Acknowledgement

This work was supported by the Australian Research Council. Thanks are extended to E.H.W Chan, T.X. Huang and W. Zhang for their valuable contributions to this work.

References

[1] R. A. Minasian, “Photonic signal processing of microwave signals", IEEE Trans. Microwave Theory Tech., vol. 54, pp. 832-846, 2006.

[2] J. Capmany, B. Ortega, and D. Pastor, "A tutorial on microwave photonic filters," J. Lightwave Technol., vol. 24, pp. 201-229, 2006.

[3] J. P. Yao, "Microwave photonics," J. Lightwave Technol., vol. 27, pp. 314-335, 2009.

[4] X. Yi, T. X. H. Huang, and R. A. Minasian, “Photonic beamforming based on programmable phase shifters with amplitude and phase control,” IEEE Photon. Technol. Lett., **23**, 1286-1288 (2011).

[5] M. A. F. Roelens, S. Frisken, J. A. Bolger, D. Abakoumov, G. Baxter, S. Poole, and B. J. Eggleton, "Dispersion trimming in a reconfigurable wavelength selective switch," J. Lightwave Technol., **26**, 73-78 (2008).
[6] X. Yi, T.X. Huang, and R. A. Minasian, "Tunable and reconfigurable photonic signal processor with programmable all-optical complex coefficients", IEEE Trans. Microwave Theory Tech., vol. 58, pp. 3088 - 3093, 2010.
[7] E.H.W Chan, W. Zhang and R. A. Minasian, "Photonic RF phase shifter based on optical carrier and RF modulation sidebands amplitude and phase control", IEEE Journal of Lightwave Technology, Vol. 30, pp. 3672-3678, 2012.
[8] W. Zhang and R. A. Minasian, "Widely tunable single-passband microwave photonic filter based on stimulated Brillouin scattering," IEEE Photon. Technol. Lett. **23**, 1775-1777 (2011).
[9] W. Zhang and R. A. Minasian, "Switchable and tunable microwave photonic Brillouin-based filter," IEEE Photonics Journal**,** **4**, 1443-1455 (2012).
[10] M. E. Manka, "Microwave photonics electronic warfare technologies for Australian defence," IEEE International Topical Meeting on Microwave Photonics (MWP 2008) 2008.
[11] L. V. T. Nguyen and D. B. Hunter, "A photonic technique for microwave frequency measurement", IEEE Photon. Technol. Lett., vol. 18, no. 10, pp. 1188–1190, 2006.
[12] T.A. Nguyen, E.H.W Chan and R.A. Minasian, "Photonic multiple frequency measurement using a frequency shifting recirculating delay line structure", IEEE J. Lightwave Technology, vol. 32, Issue 20, pp. 3831-3838 (2014).
[13] R.A. Minasian, E.H.W. Chan and X. Yi, "Microwave photonic signal processing", Optics Express, vol. 21, No. 19, pp. 22918-22936, (2013).
[14] L. V. T. Nguyen, "Photonic radio frequency memory – design issues and possible solutions," Defence Science and Technology Organisation, (2003).
[15] T.A. Nguyen, E.H.W Chan and R.A. Minasian, " Photonic radio frequency memory using frequency shifting recirculating delay line structure", IEEE J. Lightwave Technology, vol. 32, No. 1, pp. 99 - 106, (2014).

Features of application of spherical harmonics method in near field antenna measurements in the presence of external radiation

M. Ivanyan[1], N. Khachatryan[1], E. Tagvoryan[1]

[1]*National Institute of Metrology, Komitas ave. 49/4, 0015 Yerevan, Armenia*

The paper analyzes various modifications of spherical harmonic methods as applied to the theory of definition antenna far-field characteristics using near field measurement. The most common method is based on the measured data of antenna radiation field electrical component. It is also possible simultaneous use of the electric and magnetic ones. The first case requires half the number of measurements compared with the last one, but distort the reconstructed far field in the presence of external source of the radiation. Last method avoids exposure to external radiation on the probe, however, in addition to twice the amount of necessary input data, it requires a mutual agree calibration of electric and magnetic probes. This paper shows that the combination of above recovery algorithms eliminates the effect of external stray fields on the measuring probe, allowing, at the same time, limited to measuring only the electric field on a spherical surface surrounding the antenna.

1. Introduction

Vector spherical harmonics [1] method is a method of determining the far-field antenna characteristics [2,3]. Its feature - the measurement of antenna near field on a spherical scanning surface embracing antenna, followed by restoring the far fields using mathematical processing of the measured data.

Here we propose a modified algorithm for the mathematical processing of the measured antenna electric field components allows to exclude the impact of stray field external sources which is fixed measuring probe, on the final result of mathematical processing of the measured data.

2. Vector spherical harmonics. Scope

Electric and magnetic vector spherical harmonics of the four kinds are the solutions of the homogeneous Maxwell equations in free space in a spherical coordinate system r,ϑ,φ. Harmonics of each of the four genera together form a countable set of solutions and form a complete set of orthogonal functions. Arbitrary field, which distributed in the part of a space in which there are no charges and radiation sources may be represented by one of the kind or their superposition. In particular, if the currents $\vec{I}_1$ occupy a limited volume of the space, their field outside a sphere S_0 $(r = r_0)$ is represented as an expansion in a complex vector spherical harmonics of the third kind $\vec{E}_N(\vec{r})$, $\vec{H}_N(\vec{r})$ (with time dependence $e^{-j\omega t}$):

$$\vec{E}(\vec{r}) = \sum_N d_N \vec{E}_N(\vec{r}),\ \vec{H}(\vec{r}) = \sum_N d_N \vec{H}_N(\vec{r}). \tag{1}$$

The 3[rd] and 4[th] kinds of harmonics diverge at the origin (at $r = 0$) but vanish at infinity (at $r = \infty$), satisfying the radiation condition. The harmonics of the 1[st] kind $\vec{\mathrm{E}}_N(\vec{r}) = \mathrm{Re}\vec{E}_N(\vec{r})$, $\vec{\mathrm{H}}_N(\vec{r}) = \mathrm{Re}\vec{H}_N(\vec{r})$ are real functions and finite at the origin. They are used in the reconstruction of the field of source $\vec{I}_2$ (located outside the sphere S_0) in the inner part of the sphere S_0, not containing the charges and currents:

$$\vec{E}(\vec{r}) = \sum_N c_N \vec{\mathrm{E}}_N(\vec{r}),\ \vec{H}(\vec{r}) = \sum_N c_N \vec{\mathrm{H}}_N(\vec{r}). \tag{2}$$

In (1) and (2) N is a generalized summation index: $N = \{n,m,i\}$; $n = 1,2,3,\ldots, m = 0,1,2,\ldots n$, $i = 1,2,3,\ldots$. Radius-vector $\vec{r}$, characterizing the observation point, proceeds from the center of the sphere S_0 and is determined by the radial r, polar θ and azimuthal φ coordinates of a spherical coordinate system associated with the center of the sphere S_0.

3. Vector spherical harmonics. Explicit expressions

Tangential components of the electric $\vec{E}_N(\vec{r}), \mathrm{\vec{E}}_N(\vec{r})$ and magnetic $\vec{H}_N(\vec{r}), \mathrm{\vec{H}}_N(\vec{r})$ vector spherical harmonics of the third and first kind can be represented as the product of scalar radial $Z_{n,i}(r), \tilde{Z}_{n,i}(r)$ (electric and magnetic) and vector angular $\vec{Y}_N(\vartheta,\varphi), \tilde{\vec{Y}}_N(\vartheta,\varphi)$ (electric and magnetic) functions:

$$\vec{E}_{N_t}(\vec{r}) = Z_{n,i}(r)\vec{Y}_{N_t}(\vartheta,\varphi), \quad \vec{H}_N(\vec{r}) = -j\tilde{Z}_{n,i}(r)\tilde{\vec{Y}}_{N_t}(\vartheta,\varphi), \tag{3}$$

$$\mathrm{\vec{E}}_{N_t}(\vec{r}) = J_{n,i}(r)\vec{Y}_{N_t}(\vartheta,\varphi), \quad \mathrm{\vec{H}}_N(\vec{r}) = -j\tilde{J}_{n,i}(r)\tilde{\vec{Y}}_{N_t}(\vartheta,\varphi),$$

$$Z_{n,1}(r) = Z_{n,2}(r) = \tilde{Z}_{n,3}(r) = \tilde{Z}_{n,4}(r) = h_n(kr)/kr,$$

$$Z_{n,3}(r) = Z_{n,4}(r) = \tilde{Z}_{n,1}(r) = \tilde{Z}_{n,2}(r) = h_n'(kr)/kr,$$

$$J_{n,i}(r) = 2\,\mathrm{Re}(Z_{n,4}(r)), \quad \tilde{J}_{n,i}(r) = 2\,\mathrm{Re}(\tilde{Z}_{n,4}(r)).$$

Here k the wave number, $h_n(x) = \sqrt{\pi x/2}H_{n+1/2}(x)$ the spherical Bessel functions [4] of the third kind associated with the cylindrical Hankel function of the first kind and half-integer order. Tangential components of the angular functions are expressed through the associated Legendre functions $P_n^m(\cos\vartheta)$ [4] and trigonometric functions:

$$\vec{Y}_{nm,1(2)_t} = \tilde{\vec{Y}}_{nm,3(4)_t} = \vec{M}_{1,(2)}, \quad \vec{Y}_{nm,3(4)} = \tilde{\vec{Y}}_{nm1(2)} = \vec{N}_{1,(2)}, \tag{4}$$

$$\vec{N}_{1,(2)} = r\vec{\nabla}P_n^m(\cos\vartheta)\cos m\varphi(\sin m\varphi), \quad \vec{M}_l = \vec{N}_l \times \vec{e}_r, \quad \vec{e}_r = \vec{r}/r, \quad l = 1,2. \tag{5}$$

4. Vector spherical harmonics. Conditions of orthogonality

We introduce the notation:

$$W(r,\vec{A},\vec{B}) = \int_{S_r}[\vec{A}\times\vec{B}]d\vec{S}_r. \tag{6}$$

The integration in (6) is over the surface of a sphere S_r with radius r, concentric to sphere S_0; $\vec{A}$, $\vec{B}$ arbitrary vector functions. Using (6) we can write the orthogonality relations for vector spherical harmonics:

$$W(r,\vec{E}_N,\mathrm{\vec{H}}_M) = -j\pi Z_{n,i}\tilde{J}_{n,i}k_{nm}^{-1}\delta_{N,M}l_i, \quad W(r,\mathrm{\vec{E}}_N,\mathrm{\vec{H}}_M) = -j\pi J_{n,i}\tilde{J}_{n,i}k_{nm}^{-1}\delta_{N,M}l_i, \tag{7a}$$

$$W(r,\vec{E}_N,\mathrm{\vec{H}}_M) + W(r,\vec{H}_N,\mathrm{\vec{E}}_M) = 2\pi k^{-2}k_{nm}^{-1}\delta_{N,M}, \tag{7b}$$

$$W(r,\mathrm{\vec{E}}_N,\vec{H}_{N'}) + W(r,\mathrm{\vec{H}}_N,\vec{E}_{N'}) = 2\pi k^{-2}k_{nm}^{-1}\delta_{N,N'}, \tag{7c}$$

$$l_1 = l_2 = -l_3 = -l_4 = 1, \ \delta_{N,N} = 1; \quad \delta_{N,M} = 0,\ N \neq M; \ k_{nm} = (2n+1)(n-m)!/n(n+1)(n+m)!.$$

5. Determination of the weighting coefficients

The expansion coefficients d_N in (1) for the fields outside of the scanning sphere S_0 can be defined in two different ways: on the basis of the tangential electric components of the antenna radiation field (8) and on the basis of tangential electric and magnetic component of the radiation field of the antenna (9):

$$d_N = W(r_0,\vec{E},\mathrm{\vec{H}}_N)/W(r_0,\vec{E}_N,\mathrm{\vec{H}}_N), \tag{8}$$

$$d_N = \left(W(r_0,\vec{E},\mathrm{\vec{H}}_N) + W(r_0,\vec{H},\mathrm{\vec{E}}_N)\right)/\left(W(r_0,\vec{E}_N,\mathrm{\vec{H}}_N) + W(r_0,\vec{H}_N,\mathrm{\vec{E}}_N)\right). \tag{9}$$

In the absence of radiation sources outside of the scanning sphere S_0 algorithms (8) and (9) are equivalent. Equality of expansion coefficients (8) and (9) one can show, based on the Gauss theorem, on the well-known identity of vector analysis (10) [5] and from the homogeneous Maxwell equations (11):

$$div[\vec{A}\times\vec{B}] = \vec{B}rot\vec{A} - \vec{A}rot\vec{B}, \tag{10}$$

$$rot\vec{E} = jk\vec{H}, \ rot\vec{H} = -jk\vec{E}, \ rot\mathrm{\vec{H}}_N = -jk\mathrm{\vec{E}}_N, \ rot\mathrm{\vec{E}}_N = jk\mathrm{\vec{H}}_N. \tag{11}$$

Omitting the intermediate calculations, we obtain identical expressions for the algorithms (8) and (9):

$$d_N = W(r_0,\vec{E},\mathrm{\vec{H}}_N)/W(r_0,\vec{E}_N,\mathrm{\vec{H}}_N) = \int_{V_0}\{\mathrm{\vec{H}}_N\vec{H} + \vec{E}\mathrm{\vec{E}}_N\}dV \Big/ \int_{V_0}\{\mathrm{\vec{H}}_N\vec{H}_N + \vec{E}_N\vec{E}_N\}dV \tag{12}$$

The integration in (12) is produced over the infinite volume, external to the sphere S_0.

The field of source $\vec{I}_2$ in the inner region of the sphere S_0 can also be restored in two different ways: using only the electrical components (13) and by using both the electric and magnetic components (14):

$$c_N = W(r_0,\vec{E},\vec{H}_N)/W(r_0,\mathrm{\vec{E}}_N,\vec{H}_N), \tag{13}$$

$$c_N = \left(W\left(r_0,\vec{E},\vec{H}_N\right)+W\left(r_0,\vec{H},\vec{E}_N\right)\right)/\left(W\left(r_0,\mathrm{E}_N,\vec{H}_N\right)+W\left(r_0,\mathrm{H}_N,\mathrm{E}_N\right)\right). \tag{14}$$

The algorithm (8) is commonly used. The algorithm (9) has the property of automatically exclude of external (relative to the scanning sphere S_0) impact on the measuring probe [6]. To use it, however, there is a need to harmonize the calibrations of electric and magnetic probes and doubling the number of measurements. Proposed in [3] approximate method used Huygens element as a probe, equally responsive to electric and magnetic fields, imposes a lower limit on the radius of the scanning sphere, based on the requirements of the locally plane nature of the wave arriving at the opening of the probe. Meanwhile, as will be shown below, it is possible to exclude the distorting effects on the final results of the mathematical processing of the measured data, to use only measured electric field. For this purpose we represent the total field of the sources $\vec{I}_1$ and $\vec{I}_2$ in the form of an expansion in vector spherical harmonics.

6. The total field of the antenna and an external radiation source

The total field of source $\vec{I}_1$ and external radiation source $\vec{I}_2$ in the part of space, limited by two spherical surfaces, concentric to the sphere of measurements, immediately adjacent to the sources of radiation, may be represented in form of superposition of expansions in spherical harmonics of each of two sources:

$$\vec{E}(\vec{r})=\sum_N\left(d'_N\vec{E}_N(\vec{r})+c'_N\mathrm{E}_N(\vec{r})\right),\quad \vec{H}(\vec{r})=\sum_N\left(d'_N\vec{H}_N(\vec{r})+c'_N\mathrm{H}_N(\vec{r})\right). \tag{15}$$

The spherical scanning surface is between of these two surfaces: $r_1<r_0<r_2$, (r_1, r_2 are the radii of the spherical surfaces S_1 and S_2). The weighting factors d'_N, c'_N are determined by algorithms (7b) and (7c):

$$d'_N=\frac{W\left(r_1,\vec{E}^{(1)},\mathrm{H}_N\right)+W\left(r_1,\vec{H}^{(1)},\mathrm{E}_N\right)}{W\left(r_1,\vec{E}_N,\mathrm{H}_N\right)+W\left(r_1,\vec{H}_N,\mathrm{E}_N\right)},\quad c'_N=\frac{W\left(r_2,\vec{E}^{(2)},\vec{H}_N\right)+W\left(r_2,\vec{H}^{(2)},\vec{E}_N\right)}{W\left(r_2,\mathrm{E}_N,\vec{H}_N\right)+W\left(r_2,\mathrm{H}_N,\vec{E}_N\right)}, \tag{16}$$

where $\vec{E}^{(1)},\vec{H}^{(1)}$ and $\vec{E}^{(2)},\vec{H}^{(2)}$ are the field of sources $\vec{I}_1$ and $\vec{I}_2$ on surfaces S_1 and S_2 respectively.

Substituting (15) into (9) based on the orthogonality relations (7), gives: $d_N=d'_N$. Thus, in accordance with [6] the effect of impact of external radiation sources on the final result is eliminated.

If we use the algorithm (8), then in obtained weight coefficients (17) and in restored fields (18) contain an additional term, showing the distorting effect of external radiation:

$$d_N=d'_N+c'_N\,J_{n,i}(r_0)/Z_{n,i}(r_0), \tag{17}$$

$$\vec{E}(\vec{r})=\sum_N\left(d'_N+c'_N\,J_{n,i}(r_0)/Z_{n,i}(r_0)\right)\vec{E}_N(\vec{r}),\quad H(\vec{r})=\sum_N\left(d'_N+c'_N\,J_{n,i}(r_0)/Z_{n,i}(r_0)\right)\vec{H}_N(\vec{r}). \tag{18}$$

At $r>r_0$ expression (18) coincides with (15) only when $\gamma_N=0$, i.e. in the absence of an external source $\vec{I}_2$. However, when $r=r_0$, there is a coincidence for the arbitrary value of γ_N:

$$\begin{aligned}\vec{E}_t(\vec{r}_0)&=\sum_N\left\{d'_N\vec{E}_{N_t}(\vec{r}_0)+c'_NJ_{n,i}(r_0)\vec{Y}_{N_t}(\vartheta,\varphi)\right\}=\sum_N\left\{d'_N\vec{E}_{N_t}(\vec{r}_0)+c'_N\mathrm{E}_{N_t}(r_0)\right\}\\ \vec{H}_t(\vec{r}_0)&=\sum_N\left\{d'_N\vec{H}_{N_t}(\vec{r}_0)+c'_N\tilde{J}_{n,i}(r_0)\overline{\overline{Y}}_{N_t}(\vartheta,\varphi)\right\}=\sum_N\left\{d'_N\vec{H}_{N_t}(\vec{r}_0)+c'_N\mathrm{H}_{N_t}(r_0)\right\}.\end{aligned} \tag{19}$$

Thus, the correct restoration of the magnetic field, even in the presence of an external source $\vec{I}_2$, can be achieved on the scanning surface S_0, based on the measured on the same surface electric field components. The resulting information is sufficient for the application of algorithm (9), which is properly recover the antenna radiation field outside of S_0. The impact of external radiation to the final result is excluded.

The similar result is obtained by applying (14) to distribution (19) for recovering the field of source $\vec{I}_2$ in the inner region of the sphere S_0. The impact on the probe and on the final results from the source $\vec{I}_1$ is eliminated. Proved assertions are illustrated by the examples.

7 Examples

7.1. Example 1. Electrical dipoles

Consider the simplest radiating systems: two point electrical dipoles, placed at the points $\vec{r}_{1,2}$ $(r_2>r_1)$. Their tangential electric and magnetic field components in the observation point $\vec{r}$ may be presented as [7]:

$$\vec{E}^{S_{1,2}}_{1,2}(\vec{r},\vec{r}_{1,2})=\frac{1}{4\pi j}\sum_N k_{nm}\begin{cases}\mathrm{E}_{N_{S1,2}}(\vec{r}_{1,2})\vec{E}_N(\vec{r}) & r>r_{1,2}\\ E_{N_{S1,2}}(\vec{r}_{1,2})\mathrm{E}_N(\vec{r}) & r<r_{1,2}\end{cases},\quad \vec{H}^{S_{1,2}}_{1,2}(\vec{r},\vec{r}_{1,2})=\frac{1}{4\pi j}\sum_N k_{nm}\begin{cases}\mathrm{E}_{N_{S1,2}}(\vec{r}_{1,2})\vec{H}_N(\vec{r}) & r>r_{1,2}\\ E_{N_{S1,2}}(\vec{r}_{1,2})\mathrm{H}_N(\vec{r}) & r<r_{1,2}\end{cases}. \tag{20}$$

Symbol $s_{1,2}$ takes the values $r_{1,2}, \vartheta_{1,2}, \varphi_{1,2}$ and indicates the orientation of dipole $\vec{p}$ $(|\vec{p}|=1)$ along the direction of the unit v ector $\vec{e}_{r_{1,2}}, \vec{e}_{\vartheta_{1,2}}, \vec{e}_{\varphi_{1,2}}$ of the spherical coordinate s ystem at the point of di poles location $\vec{r}_{1,2}$. Measured on S_0 electric components and recovered on the same surface magnetic one are equal t

$$\{E_{\vartheta,\varphi}(\vec{r}_0), H_{\vartheta,\varphi}(\vec{r}_0)\} = \frac{1}{4\pi j}\sum_N k_{nm} \begin{cases} \mathrm{E}_{N_{S1}}(\vec{r}_1)\{E_{N\theta,\varphi}(\vec{r}_0), H_{N\theta,\varphi}(\vec{r}_0)\} + E_{N_{S1}}(\vec{r}_2)\{\mathrm{E}_{N\theta,\varphi}(\vec{r}_0), \mathrm{H}_{N\theta,\varphi}(\vec{r}_0)\} & for \quad r_1 < r < r_2 \\ \mathrm{E}_{N_{S1}}(\vec{r}_1)\{E_{N\theta,\varphi}(\vec{r}_0), H_{N\theta,\varphi}(\vec{r}_0)\} + \mathrm{E}_{N_{S1}}(\vec{r}_2)\{E_{N\theta,\varphi}(\vec{r}_0), H_{N\theta,\varphi}(\vec{r}_0)\} & for \quad r > r_2 \end{cases}. \quad (21)$$

Using (8) for electrical field distributions (21), one obtains for electrical and magnetic fields for $r > r_0$:

$$\{E_{\vartheta,\varphi}(\vec{r}), H_{\vartheta,\varphi}(\vec{r})\} = \frac{1}{4\pi j}\sum_N k_{nm} \begin{cases} \left(\mathrm{E}_{N_{S1}}(\vec{r}_1) + E_{N_{S2}}(\vec{r}_2) J_{n,i}(r_0)/Z_{n,i}(r_0)\right)\{E_{N\theta,\varphi}(\vec{r}), H_{N\theta,\varphi}(\vec{r})\} & for \quad r_1 < r_0 < r_2 \\ \mathrm{E}_{N_{S1}}(\vec{r}_1)\{E_{N\theta,\varphi}(\vec{r}), H_{N\theta,\varphi}(\vec{r})\} + \mathrm{E}_{N_{S2}}(\vec{r}_2)\{E_{N\theta,\varphi}(\vec{r}), H_{N\theta,\varphi}(\vec{r})\} & for \quad r_0 > r_2 \end{cases}. \quad (22)$$

At $r = r_0$ expressions (22) are identical to expressions (21). Application of the algorithm (9) to the mea sured electric and recovered magnetic components of (22) gives for $r > r_0$:

$$\vec{E}(\vec{r}_0) = \begin{cases} \vec{E}^{S1}(\vec{r}, \vec{r}_1) + \vec{E},^2(\vec{r}, \vec{r}_2) & for \quad r_0 > r_2 \\ \vec{E}^{S1}(\vec{r}, \vec{r}_1) & for \quad r_1 < r_0 > r_2 \end{cases}, \qquad \vec{H}(\vec{r}_0) = \begin{cases} \vec{H}^{S1}(\vec{r}, \vec{r}_1) + \vec{H},^2(\vec{r}, \vec{r}_2) & for \quad r_0 > r_2 \\ \vec{H}^{S1}(\vec{r}, \vec{r}_1) & for \quad r_1 < r_0 > r_2 \end{cases}. \quad (23)$$

Thus, if spherical surf ace S_0 includes both the source s $(r_0 > r_2)$, the result is the recovered total field. If on e of sources is outside of a scanning surface $(r_1 < r_0 < r_2)$, its effect vanishes.

7.2. Example 2. Dipole-sphere system

This example is related to stimulated emission: point electric dipole (20) irradiates ideally conducting sphere of radius a. The electric field of the system is represented by the vector spherical harmonics in the form of a superposition of a dipole (placed at $\vec{r}_1$) field (20), and induced field of a sphere (centered at $r = 0$) [7]:

$$\vec{E}'^s(\vec{r}_1, \vec{r}) = \vec{E}^s(\vec{r}_1, \vec{r}) - (4\pi j)^{-1}\sum_N k_{nm}\chi_n^i E_{N_s}(\vec{r}_1)\vec{E}_N(\vec{r}), \quad \chi_n^i = J_{n,i}(a)/Z_{n,i}(a). \quad (24)$$

Applying algorithm (8) to the (24) yields at $r = r_0$ the following expressions for the coefficients (25) and for distribution of the tangential component of the magnetic field on the surface S_0 (26):

$$d_N = \frac{k_{nm}}{4\pi j}\begin{cases} \mathrm{E}_{N_S}(\vec{r}_1) - \chi_n^i E_{N_S}(\vec{r}_1), & r_0 > r_1 \\ E_{N_S}(\vec{r}_1) J_{n,i}(r_0)/Z_{n,i}(r_0) - \chi_n^i E_{N_S}(\vec{r}_1), & r_0 < r_1 \end{cases}, \quad (25)$$

$$\vec{H}_t(\vec{r}_1, \vec{r}_0) = (4\pi j)^{-1}\sum_N k_{nm}\begin{cases} \mathrm{E}_{N_S}(\vec{r}_1)\vec{H}_{N_t}(\vec{r}_0) - \chi_n^i E_{N_S}(\vec{r}_1)\vec{H}_{N_t}(\vec{r}_0) & r_0 > r_1 \\ E_{N_S}(\vec{r}_1)\vec{\mathrm{H}}_{N_t}(\vec{r}_0) - \chi_n^i E_{N_S}(\vec{r}_1)\vec{H}_{N_t}(\vec{r}_0) & r_0 < r_1 \end{cases}. \quad (26)$$

Coefficients (9) obtained by the help of expansions (24) and (26) can be written as follows:

$$d_N = (4\pi j)^{-1} k_{nm}\{\mathrm{E}_{N_S}(\vec{r}_1) - \chi_n^i E_{N_S}(\vec{r}_1)\}, \quad r_0 > r_1; \; d_N = -(4\pi j)^{-1} k_{nm}\chi_n^i E_{N_S}(\vec{r}_1), \quad r_0 < r_1 \quad (27)$$

In the first ca se $(r_0 > r_1)$, when the scanning surface covers the whole sy stem, expansion for the fields of the system obtained by (27) and (9) describes a full field of the sy stem. In the second case $(r_0 < r_1)$ the dipole is outside of the scanning sphere and the expansion describes only the stimulated emission from the sphere.

8. Conclusion

The paper shows the possibility of r ecovery of t he antenna field by near-fieldmethod of spherical harmonics in the presence of external radiation by measuring the t angential electric field components of the antenna. The proposed method does not affect the measurement process: the result is achieved by converting the measurement data processing algorithm.

9. **References**

[1] J.A. Stratton, Electromagnetic Theory (McGraw Hill, NY, 1941).
[2] A.C. Ludwig, IEEE Trans. AP, 19 (1971) 214.
[3] P.J. Wood, The Marconi Review, 34 (1971), 149.
[4] M. Abramovitz, I. A. Stegun, Handbook of Mathematical Functions (Dover Publications, NY, 1972).
[5] A. Korn, T.M. Korn, Mathematical Handbook (McGraw Hill, NY, 1961).
[6] E.D. Gazazian, M.I. Ivanian, Izv. VUZ-ov, Radiofizika, 30 (1987) 1221.
[7] L.B. Felsen, N. Marcuvitz, Radiation and Scattering of Waves (Prentice-Hall, Englewood-Cliffs, 1973).

Possible regimes of plane electromagnetic wave self-action in ionizable medium: phase-plane analysis by the method of single expression

A.V. Daryan[1], H.V. Baghdasaryan[2], T.M. Knyazyan[2]

[1]A.Alikhanyan National Laboratory, Cosmic Ray Division,
2 Alikhanyan brothers str., Yerevan 0036, Armenia
[2]Fiber Optics Communication Laboratory, State Engineering
University of Armenia,105 Terian str., Yerevan 0009, Armenia

In this paper self-action of plane electromagnetic wave in nonlinear medium is analysed. Consideration is performed on the model of ionizable type cubic nonlinearity without specification of physical mechanism of nonlinearity. The analysis is carried out by the phase plane method, which permits to describe qualitatively all possible solutions of Helmholtz's nonlinear differential equation without performing numerical integration. Phenomenon of self-limitation of transmitted wave power in the medium is shown related to the fact that at the growth of field amplitude permittivity of a medium changes its sign from positive to negative.

1. Introduction

High intensity electromagnetic (EM) wave changes electromagnetic parameters of any material. This nonlinear phenomenon is referred to as wave self-action when no new frequencies are created at strong field-matter interaction. One of physical mechanisms of self-action is the ionization of a gas under high power EM wave radiation. At high enough intensities of incident wave a gas having initially positive permittivity changes the sign of permittivity to negative one. The last is a clear indication on free charges (electrons and positive ions) generation in the material that is called ionization. Sign change of permittivity means a strong nonlinear process which needs specific approach for correct electromagnetic description of EM wave interaction with matter. In the following, the relevant method of analysis is presented.

An important example of high intensity EM wave interaction with gases is an electromagnetic discharge. Gas discharge devices are used in communications equipment to protect from high power disruptive electromagnetic pulses. Gas discharge (low temperature plasma) operates as a limiter in the waveguide transmission lines. Once the high power microwave reaches the plasma limiter, a discharge occurs and the incident microwave radiation is reflected [1-3]. Special interest is directed to enhancement of EM power penetration in an ionizable medium [4]. Another nonlinear problem concerns to the ionization of air under high intensity EM wave beam which influences on radio communication systems [5,6].

For correct analysis of above listed strong nonlinear problems of high power electromagnetic wave interaction with ionizable medium well known traditional approach of Helmholtz's equation solution presentation as a sum of counter-propagating waves is useless. Superposition principle is not valid for strong nonlinear problems solution. To overcome this problem it was suggested to use specific expression describing electromagnetic wave behaviour in intensity-dependent nonlinear medium [7-9]. Based on this expression, method of single expression has been developed and many linear and non-linear problems have been solved [10-15].

2. Method of single expression

Plane wave propagation in a medium of permittivity ε in a frequency-domain is described by Helmholtz's equation, which in 1D case is:

$$\frac{d^2\dot{E}_x(z)}{dz^2}+k_0^2\varepsilon\dot{E}_x(z)=0 \quad , \tag{1}$$

where $k_0=\omega/c$ is free space wave number, complex value $\dot{E}_x(z)$ is a component of electric field propagating along z axis, ε is a permittivity of material. At wave self-action the permittivity of material is a function of field's intensity as $\varepsilon=\varepsilon(|\dot{E}_x|^2)$. In this case, widely accepted general solution of Helmholtz's equation in the form of counter-propagating waves is no longer valid approach, as the superposition principle failed in a strong non-linear medium. As an alternative approach for solution presentation, the method of single expression (MSE) is proposed, where general solution of equation (1) is presented in the following form:

$$\dot{E}_x(z) = U(z)\exp[-iS(z)]. \tag{2}$$

This expression describing amplitude $U(z)$ and phase $S(z)$ of wave in a medium satisfies Helmholtz's equation [10-15]. Substitution (2) into (1) brings to the system of differential equations equivalent to Helmholtz's equation:

$$\begin{cases} \dfrac{dU(z)}{dk_0 z} = Y(z) \\ \dfrac{dY(z)}{dk_0 z} = \dfrac{P^2 - \varepsilon(U^2)\cdot U(z)^4}{U(z)^3} \end{cases}, \tag{3}$$

Where $P = U(z)^2 \dfrac{dS(z)}{dk_0 z}$ is the value proportional to the power flow density in a medium [7,8].

This set of equations describes electric field distribution in a lossless medium i.e. when power flow density $P = const$. The system (3) gives opportunity to observe wave's amplitude behaviour in a medium by using phase-plane analysis avoiding integration procedure [16-23].

To obtain phase trajectories ($Y(U)$), it is necessary to get rid of explicit dependence on the z coordinate. Dividing the second equation of the system by the first one gives the following expression:

$$\frac{dY}{dU} = \frac{P^2 - \varepsilon(U^2)\cdot U^4}{U^3 \cdot Y}. \tag{4}$$

The expression (4) represents the equation of isoclines [24] and defines the direction of tangents to the phase trajectories in the plane UY. Integration of the equation (4) by taking into account the non-linearity of permittivity as $\varepsilon = \varepsilon_{lin} + \varepsilon_{nl} \cdot U^2$ gives the following equation for phase trajectories:

$$Y^2 + \frac{P^2}{U^2} + \varepsilon_{lin} \cdot U^2 + \varepsilon_{nl} \frac{U^4}{2} = C. \tag{5}$$

Here ε_{lin} is an initial value of permittivity, ε_{nl} is a non-linearity coefficient, that is negative for ionizable medium, C is an integration constant that is proportional to the average energy density of electromagnetic wave in a medium (in the case of $\varepsilon > 0$) [19].

To get the spatial distribution of field amplitude in a medium, the first equation of the system (3) should be integrated along the phase trajectory (5). In this case, an implicit dependence of the amplitude U on the coordinate z is presented as:

$$(z - z_0)k_0 = \int_{U_0}^{U(z)} \frac{dU}{Y(U)}. \tag{6}$$

As phase trajectories $Y(U)$ are determined by (5), the complexity of further analytical investigation is evident. There are specific singular points, where the direction of isoclines becomes indefinite [24]. The coordinates of specific points are defined from (4) as:

$$\begin{cases} P^2 - \varepsilon_{lin} \cdot U_s^4 - \varepsilon_{nl} \cdot U^6 = 0, \\ Y_s = 0. \end{cases} \tag{7}$$

Positions and type of singular points for ionizable medium at $\varepsilon_{lin} > 0$ and $\varepsilon_{nl} < 0$, at different values of power flow P are presented in **Table 1**, where $\alpha = \sqrt{-\varepsilon_{lin}/\varepsilon_{nl}}$, $\beta = \sqrt{-2\varepsilon_{lin}/3\varepsilon_{nl}}$, $\gamma = \sqrt{\varepsilon_{lin}^3/3\varepsilon_{nl}^2}$, A and B are positive solutions of equation (7). At the fixed power flow density P the values U_s and Y_s correspond to the wave of constant amplitude at any z coordinate, thus they describe travelling plane wave in a medium.

Table 1.

№	Power flow	Singular points			$\varepsilon(U_S)$
		coordinates num	ber	type	
1	$P=0$	$U_S=0 \quad Y_S=0$ $U_S=\pm\alpha \quad Y_S=0$	1 2	*centre* *saddle*	$\varepsilon=\varepsilon_{lin}$ $\varepsilon=0$
2	$P<\gamma$	$U_S=\pm A \quad Y_S=0$ $U_S=\pm B \quad Y_S=0$	2	*centre* *saddle*	$0<\varepsilon<\varepsilon_{lin}$ $0<\varepsilon<\varepsilon_{lin}$
3	$P=\gamma$	$U_S=\pm\beta \quad Y_S=0$	2	*cusp*	$\varepsilon=\varepsilon_{lin}/3$
4	$P>\gamma$	-------- -------- 0		--------	--------

Expressions (5) and (7) give the complete analytic description of phase trajectories of the considered problem. Singular points and various phase trajectories (at different values of C) describe the behaviour of electric field amplitude in a medium at the given power flow density P. Definite type of phase portraits obtained from (5) corresponds to each case indicated in **Table 1**. The phase portraits for different values of power flow P are presented in Figure 1 and Figures 2a,b,c.

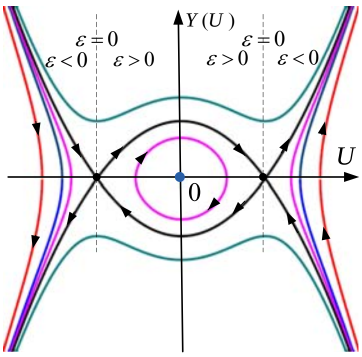

Figure 1. Phase portrait at $P=0$

At $P=0$ phase trajectories correspond to standing waves. Circles, at small amplitudes of wave, are similar to those of the linear case. The phase trajectories' interpretation in the case of linear medium has been presented previously in [16,19,22,23] . Separatrices enclose the circles and meet each others in "saddle" points. Any part of "separatrix", including singular point, is relevant to synchronous vibration of wave amplitude in space with finite amplitude of wave on infinity (at $z \to \pm\infty$).

At modest values of power flow ($0<P<\gamma$) there are either periodical distributions of field amplitude in space or non-periodic amplitude distributions (Fig.2a). The periodical distributions (circles) correspond to partially standing waves and can be realised in all space. Non-periodic trajectories can be realised only on part of space except for parts of "separatrix". Trajectories including singular point of "saddle" type are relevant to infinite distance in a space. The singular point of "centre" type corresponds to a plane travelling wave. The "saddle" type singular point corresponds to an asymptotical travelling wave of finite amplitude on infinity.

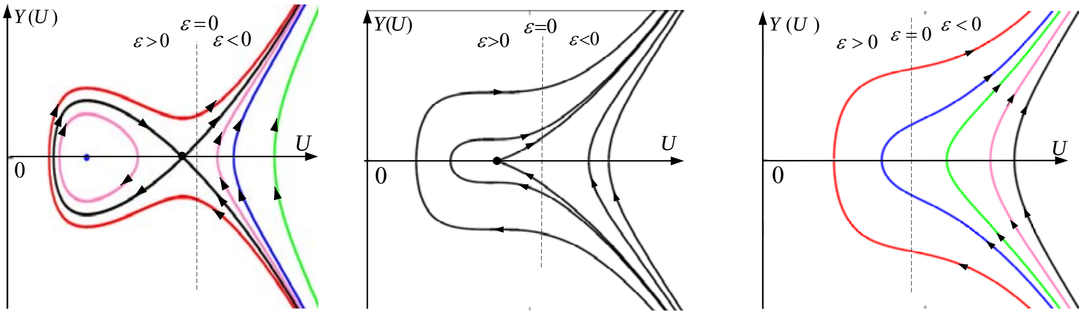

a) b) c)

Figure 2. Phase portraits at: a) at $0 < P < \gamma$, b) at $P = \gamma$, c) at $P > \gamma$

At $P = \gamma$ there are aperiodic field amplitude distributions (Fig.2b), and only one singular point of "cusp" type is observed. All trajectories can be realised only on part of space except for parts of "separatrix" including singular point of "cusp" type that is relevant to infinite distance in a space. This value of flux $P = \gamma$ in singular point is maximal for realization of plane wave penetrating in a non-linear medium of ionizable type.

At $P > \gamma$ there are no singular points (Fig. 2c) what is indication, that there are no phase trajectories which can be realised in infinite space.

The result is: at the incidence of plane wave on ionizable medium self-limitation of wave takes place in a medium with maximal value of transmitted power flow is $P = \gamma$. This phenomenon has been analysed also by direct integration of the system of differential equations (3) and agreement with qualitative analysis is obtained [17].

In conclusion, the phase-plane analysis indicated its usefulness for observation and interpretation of all possible plane electromagnetic wave propagation modes in a nonlinear (wave's intensity dependent) media.

3. Acknowledgements

This work was supported by State Committee Science MES RA, in the frame of the research project № SCS 13-2J204. H.V. Baghdasaryan and T.M. Knyazyan are thankful to COST TU1208 members for fruitful discussions.

4. References

[1] E. Nasser. Fundamentals of Gaseous Ionization and Plasma Electronics (Wiley Interscience, New York, 1961).

[2] G. Yang, J.Tan, D. Sheng, Yu.Yang, "Plasma limiter for protecting against high power microwave", *Journal of Scientific and Industrial Research*, **67 (**2008) 685.

[3] H. Goldie, S. Patel, "An RF-Primed All-Halogen Gas Plasma Microwave High-Power Receiver Protector", *IEEE Trans. Microw. Theory and Techniques*, **MTT-30** (1982) 2177.

[4] A.V. Kochetov, S.O. Dementyeva, "On Increasing the Efficiency of Penetration of an Electromagnetic Wave into a Dense plasma Layer", *Radiophysics and Quantum Electronics,* **56 (**2013) 433. (Russian Original Vol. 56, No. 7, July, 2013).

[5] V. L. Ginzburg. The Propagation of Electromagnetic Waves in Plasmas (Pergammon Press, 1964).

[6] M. S. Sodha, S. K. Mishra, S. K. Agarwal, "Nonlinear Propagation, Self-Modulation, and Faraday Rotation of Electromagnetic Beams in the Ionosphere", IEEE Trans. on Plasma Science, **37(**2009) 375.

[7] Басс Ф.Г., Вербицкий И.Л., Гуревич Ю.Г. К теории распространения электромагнитных волн в нелинейных средах. // Изв. Вузов. Радиофизика. -1968. Т. 11, №10. – с. 1480- 1489./ F.G. Bass, I.L. Verbitskii, Yu.G. Gurevich, "Theory of propagation of electromagnetic waves in nonlinear medium", *Radiophysics and Quantum Electronics*, **11(**1968) 834. (Translation from Russian).

[8] Силин В.П. Нелинейная теория проникновения высокочастотного поля в проводник // ЖЭТФ.- 1967.- Т. Вып.5(11). -С.1662-1677. V.P. Silin, "Nonlinear theory of penetration of a high frequency field into a conductor", *Soviet Physics JETP*, **26** (1968) 955. (Translation from Russian).

[9] R.L. Fante, "Propagation of electromagnetic waves in a simplified nonlinear gas", *Journ. Appl. Phys.*, **42** (1971) 4202.

[10] H. V. Baghdasaryan, A.V. Daryan, T.M. Knyazyan, Nikolaos K. Uzunoglu, "Modelling of nonlinear enhanced performance Fabry-Perot interferometer filter", *Microwave and Optical Technology Letters*, **14** (1997) 105.

[11] H.V. Baghdasaryan. "Method of backward calculation", in the book: Photonic Devices for Telecommunications: how to model and measure/ Edit. G.Guekos, (Springer 1999), 56-65.

[12] H.V. Baghdasaryan, T.M. Knyazyan, "Problem of plane EM wave self-action in multilayer structure: an exact solution", *Optical and Quantum Electronics*, **31** (1999) 1059.

[13] H.V. Baghdasaryan and T.M. Knyazyan, "Modelling of strongly nonlinear sinusoidal Bragg gratings by the Method of Single Expression", *Optical and Quantum Electronics*, **32** (2000) 869.

[14] H.V. Baghdasaryan, T.M. Knyazyan, T.H. Baghdasaryan, B. Witzigmann, and F. Roemer, "Absorption loss influence on optical characteristics of multilayer distributed Bragg reflector: wavelength-scale analysis by the method of single expression", *Opto−Electronics Review* **18** (2010) 438.

[15] H.V. Baghdasaryan, Basics of the Method of Single Expression: New Approach for Solving Boundary Problems in Classical Electrodynamics. Monograph. (Chartaraget, Yerevan, 2013).

[16] H.V. Bagdasaryan, V.A. Permyakov, "Qualitative analysis of H- wave propagation in a medium of ionizable nonlinearity", *Tr. Mosk. Energ. Inst.* No. 301 (1976) 72. (In Russian).

[17] O.V. Bagdasaryan, V.A. Permyakov, "Branching of conditions and effect of energy flux limitation of TE mode in a medium with ionization nonlinearity", *Radiophysics and Quantum Electronics*, **21** (1978) 940. (Translation from Russian).

[18] O.V. Bagdasaryan, A.M. Lebedev, V.A. Permyakov, "Properties of the passage of a plane H- wave through a dielectric layer with negative nonlinearity", Collection of papers Research Institute of Condensed Physics at Yerevan State University, Nonlinear optical interactions, Yerevan (1987) 169. (In Russian).

[19] O.V. Bagdasaryan, A.V. Dar'yan, "Phase – plane method in the theory of electromagnetic wave propagation", Interuniversity thematic collection of scientific works on radiotechnique, Electromagnetic wave radiation and propagation, Yerevan (1988) 64. (In Russian).

[20] O.V. Bagdasaryan, A.M. Lebedev, V.A. Permyakov, "Electromagnetic waves in media of negative nonlinearity", Collection of scientific works of Moscow Power Energy Institute No. 182, Utmost possibilities and optimization of radioelectronic equipments and systems, Moscow (1988) 120. (In Russian).

[21] O.V. Bagdasaryan, A.V. Dar'yan, V.A. Permyakov, "Numerical analysis of plane electromagnetic wave self-action in layer of a positive nonlinearity", Interuniversity thematic collection of scientific works of Yerevan Politekhnik Institute, Technical means and mathematical support of electronic computers and systems, Yerevan (1991) 14. (In Russian).

[22] H.V. Baghdasaryan, T.M. Knyazyan, A.A. Mankulov, "Electric Field Distribution in 1D Layered Media: Qualitative Analysis in the Method of Single Expression", ICTON 2004 Conference Proceedings, Poland (2004) 319.

[23] A.A. Mankulov, H.V. Baghdasaryan, T.M. Knyazyan, "Qualitative analysis of plane electromagnetic wave amplitude behaviour in confined media", Izvestiya NAN RA and SEUA, ser. TN, **57** (2004) 107. (In Russian).

[24] A.A. Andronov, A.A. Vitt, S.E. Khaykin, Theory of oscillators (Dover, Inc., N.-Y.,1987).

Alamouti STBC behavior in pseudo-coherent MIMO systems

G. Mardoyan[1]

[1] *State Engineering University of Armenia, 105 Teryan str, 0009 Yerevan, Armenia*

This paper presents the performance of 2x2 Alamouti Space-Time Block Code (STBC) [1] in multiple-input multiple-output (MIMO) systems, in which the individual channels of transmitter/receiver are not phase coherent but phase locked to the same reference signal, or pseudo-coherent. A simple mathematical model for pseudo-coherent Alamouti transceiver is derived, that represents phase noise as the main distortion contributor in pseudo-coherent MIMO systems. Next, the impact of phase noise on the immunity of Alamouti coded signal is presented. It is shown, that MIMO signal immunity depends not only on the intensity of phase noise, but also on the duration of the data frames. Finally the lower limit of the phase noise is defined, over which the pseudo-coherent MIMO system behaves like a coherent one.

Key words: pseudo-coherent, MIMO, Alamouti, phase noise, BER vs Eb/N0, burst duration, MIMO-SDR.

Introduction. Software Defined Radio (SDR) systems are widely used in prototyping, test and benchmark of wireless standards IEEE 802.11 a/b/g, 3GPP LTE, LTE Advanced. Now, they gain popularity in next generation cellular (5G) and WLAN standards. Therefore, as the next generation wireless communication tends to use MIMO technology, MIMO-SDR systems started to gain high demand. Moreover, as MIMO communication systems have many advantages over conventional Single-Input Single-Output (SISO) systems, in terms of spectrum efficiency and data redundancy, it has become reasonable to use MIMO-SDR systems in development of wireless communication systems.

The most of nowadays RF transceivers, that can be used in MIMO-SDR communication systems can be divided into two groups. The first ones are the high-end devices for high accuracy measurements, that are perfectly calibrated for their entire frequency range, and, as a matter of fact, are large in size. This devices have ability to share a single Local Oscillator (LO) and Sample Clock among many units. That ensures the coherency among all the transmit/receive channels. The transceivers of the second group, correspondingly, are middle price range and middle accuracy devices with smaller footprint [2] [3]. Those devices don't have the ability to share LO and Sample clock among many units and may only share the external Reference Clock, which is then used in PLL circuits of LO and Sample Clock (Fig. 1 and Fig. 2). In this case, transmit/receive channels are not coherent, but phase locked. The MIMO systems based on the second group of transceivers will be called pseudo-coherent further in this paper.

Though in the wireless research area it might be reasonable to use high accuracy, large footprint and expensive RF transceivers, that can ensure true coherency, for wireless research area those are just not acceptable, as a communication unit should be small, portable and affordable. Moreover, as the MIMO systems require multiple channels both for transmit and receive, the overall system cost and size dramatically increases with the count of channels.

In this paper we analyze the difference between coherent and pseudo-coherent systems in terms of performance of MIMO communication, and define the limits, over which the pseudo-coherent systems may be used without significant impact on wireless communication immunity compared to the coherent systems.

MIMO pseudo-coherency impact on Alamouti coded signal. Let's consider the MIMO system, that has two transmitter channels and two receiver channels, and both transmitter and receiver are pseudo-coherent (Fig. 1 and Fig. 2). The difference of instantaneous frequencies of the signals, generated by two independent oscillators, that are locked to the same reference source can be expressed as:

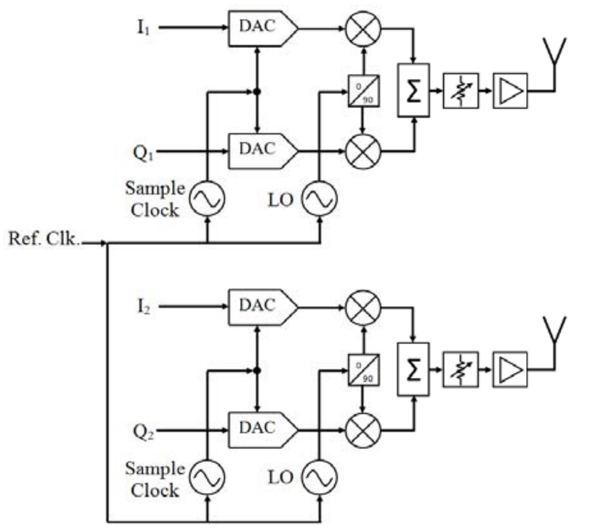

Fig. 1. Pseudo-coherent MIMO transmitter architecture

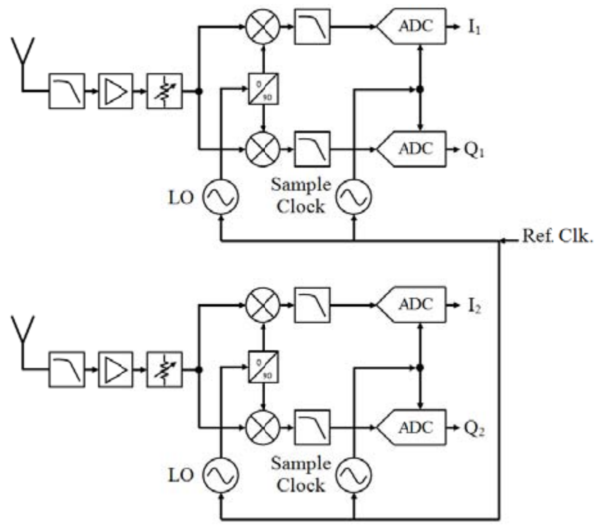

Fig. 2. Pseudo-coherent MIMO receiver architecture

$$\Delta f(t) = \frac{d}{dt}\frac{(\varphi_1(t) - \varphi_2(t))}{2\pi}. \tag{1}$$

where $\varphi_1(t)$ and $\varphi_2(t)$ are the phase noises of two oscillators [4], that can be modeled according to [5] and [6].

Let's see how the phase noises of Local Oscillators affect the immunity of 2x2 Alamouti coded signals. For that purpose let's mathematically model Alamouti coding, upconversion, downconversion and Alamouti decoding (Fig. 3).

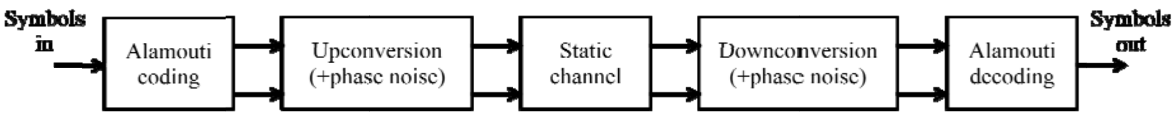

Fig. 3. Simple mathematical model data-flow

Firstly, let's assume that c_1 and c_2 are the complex symbols that need to be transmitted. Therefore, Alamouti coded signal will be expressed as follows [1]:

$$C = \begin{pmatrix} c_1 & c_2 \\ -c_2^* & c_1^* \end{pmatrix} \tag{2}$$

The Local Oscillators, used for signal upconversion can be expressed as:

$$LO_{Tm} = \cos\big(\omega_0 t + \varphi_m(t)\big), \tag{3}$$

and the upconverted signal can be expressed as:

$$s_{nm} = Re(C_{nm})\cos\big(\omega_0(t + (n-1)\Delta t) + \varphi_{Tm}(t + (n-1)\Delta t)\big) - Im(C_{nm})\sin\,(\omega_0(t + (n-1)\Delta t), \tag{4}$$

where, n is the integer, that expresses the time, when the symbol got transmitted, m is the number of antenna that was used for transmission, Δt is the symbol duration.

Using matrix form of expression for upconverted signal, we can express received signal as:

$$Y_n = H \cdot \begin{pmatrix} s_{n1} \\ s_{n2} \end{pmatrix} = \begin{pmatrix} h_{11} & h_{12} \\ h_{21} & h_{22} \end{pmatrix}\begin{pmatrix} s_{n1} \\ s_{n2} \end{pmatrix}. \tag{5}$$

Assuming that the wireless channel is static and is equal to $H = \begin{pmatrix} 1+0i & 1+0i \\ 1+0i & 1+0i \end{pmatrix}$, and the received signals is being downconverted with Local Oscillators

$$LO_{Rk} = \cos\big(\omega_0 t + \varphi_k(t)\big), \tag{6}$$

where k is the number of antenna in the receiver, than the decoded symbols can be expressed as follows:

$$\begin{aligned}\hat{c}_1 = &\frac{1}{2}(\mathrm{Re}(c_1)[\cos(\Delta\varphi_{13}(t))+\cos(\Delta\varphi_{14}(t))+\cos(\Delta\varphi_{23}(t))+\cos(\Delta\varphi_{24}(t))]+\\ &+j\,\mathrm{Im}(c_1)[\cos(\Delta\varphi_{13}(t))+\cos(\Delta\varphi_{14}(t))+\cos(\Delta\varphi_{23}(t))+\cos(\Delta\varphi_{24}(t))])+\\ &+\frac{1}{2}(\mathrm{Re}(c_2)[-\cos(\Delta\varphi_{13}(t))-\cos(\Delta\varphi_{14}(t))+\cos(\Delta\varphi_{23}(t))+\cos(\Delta\varphi_{24}(t))]+\\ &+j\,\mathrm{Im}(c_2)[-\cos(\Delta\varphi_{13}(t))-\cos(\Delta\varphi_{14}(t))+\cos(\Delta\varphi_{23}(t))+\cos(\Delta\varphi_{24}(t))])+\\ &+\frac{1}{2}(\mathrm{Im}(c_1)[\sin(\Delta\varphi_{13}(t))+\sin(\Delta\varphi_{14}(t))-\sin(\Delta\varphi_{23}(t))-\sin(\Delta\varphi_{24}(t))]+\\ &+j\,\mathrm{Re}(c_1)[-\sin(\Delta\varphi_{13}(t))-\sin(\Delta\varphi_{14}(t))+\sin(\Delta\varphi_{23}(t))+\sin(\Delta\varphi_{24}(t))])+\\ &+\frac{1}{2}(\mathrm{Im}(c_2)[\sin(\Delta\varphi_{13}(t))+\sin(\Delta\varphi_{14}(t))+\sin(\Delta\varphi_{23}(t))+\sin(\Delta\varphi_{24}(t))]+\\ &+j\,\mathrm{Re}(c_2)[-\sin(\Delta\varphi_{13}(t))-\sin(\Delta\varphi_{14}(t))-\sin(\Delta\varphi_{23}(t))-\sin(\Delta\varphi_{24}(t))])\end{aligned} \tag{7}$$

$$\begin{aligned}\hat{c}_2 = &\frac{1}{2}(\mathrm{Re}(c_2)[\cos(\Delta\varphi_{13}(t))+\cos(\Delta\varphi_{14}(t))+\cos(\Delta\varphi_{23}(t))+\cos(\Delta\varphi_{24}(t))]+\\ &+j\,\mathrm{Im}(c_2)[\cos(\Delta\varphi_{13}(t))+\cos(\Delta\varphi_{14}(t))+\cos(\Delta\varphi_{23}(t))+\cos(\Delta\varphi_{24}(t))])+\\ &+\frac{1}{2}(\mathrm{Re}(c_1)[\cos(\Delta\varphi_{13}(t))+\cos(\Delta\varphi_{14}(t))-\cos(\Delta\varphi_{23}(t))-\cos(\Delta\varphi_{24}(t))]+\\ &+j\,\mathrm{Im}(c_1)[\cos(\Delta\varphi_{13}(t))+\cos(\Delta\varphi_{14}(t))-\cos(\Delta\varphi_{23}(t))-\cos(\Delta\varphi_{24}(t))])+\\ &+\frac{1}{2}(\mathrm{Im}(c_2)[-\sin(\Delta\varphi_{13}(t))-\sin(\Delta\varphi_{14}(t))+\sin(\Delta\varphi_{23}(t))+\sin(\Delta\varphi_{24}(t))]+\\ &+j\,\mathrm{Re}(c_2)[\sin(\Delta\varphi_{13}(t))+\sin(\Delta\varphi_{14}(t))-\sin(\Delta\varphi_{23}(t))-\sin(\Delta\varphi_{24}(t))])+\\ &+\frac{1}{2}(\mathrm{Im}(c_1)[\sin(\Delta\varphi_{13}(t))+\sin(\Delta\varphi_{14}(t))+\sin(\Delta\varphi_{23}(t))+\sin(\Delta\varphi_{24}(t))]+\\ &+j\,\mathrm{Re}(c_1)[-\sin(\Delta\varphi_{13}(t))-\sin(\Delta\varphi_{14}(t))-\sin(\Delta\varphi_{23}(t))-\sin(\Delta\varphi_{24}(t))])+\end{aligned} \tag{8}$$

where $\Delta\varphi_{mk}(t)$ is the difference of phase noises between m-th transmitter and k-th receiver LOs.

In case there is no phase noise, and the phase differences in the above expressions are equal to zero, the decoded symbols will be equal to the sent ones. In case of coherent transmission and coherent reception, all the phase differences will be equal, therefore the symbol error will be less.

The symbol error can be estimated by Error Vector Magnitude (EVM) calculation using the following equation:

$$EVM = \sqrt{\frac{(Re(\hat{c}_n) - Re(c_n))^2 + (Im(\hat{c}_n) - Im(c_n))^2}{(Re(c_n))^2 + (Im(c_n))^2}} \tag{9}$$

Simulation results and conclusion. Let's validate QPSK modulated signal immunity in pseudo-coherent MIMO communication system using equations 8 and 9. Fig. 4 and Fig. 5 show the dependency of bit error rate (BER) of the received signal from Eb/N0 (energy per bit to noise power spectral density ratio). The simulation curves has been calculated for three different frame sizes: one thousand symbols per frame, hundred thousand symbols per frame and two hundred thousand symbols per frame.

The Fig. 4 shows BER vs. Eb/N0 curves when the phase noise of all the oscillators is -120 dBc at 100 kHz offset and the Flicker noise PSD incline (α) is equal to 2. As we can see there is a slight difference between the curves. The more symbols are transmitted in a frame the worse is the BER on a particular signal to noise ratio.

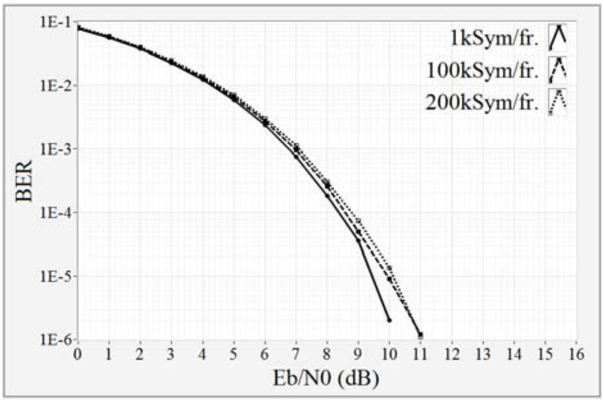

Fig. 4. BER vs. Eb/N0 graph when phase noise is -120 dBc@100kHz (α=2)

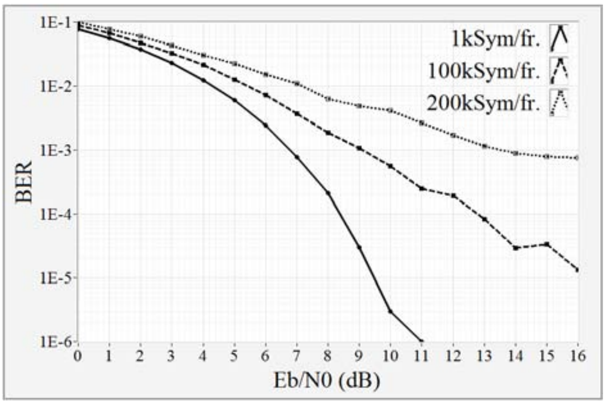

Fig. 5. BER vs. Eb/N0 graph when phase noise is -110 dBc@100kHz (α=2)

The Fig. 5 shows the same BER vs. Eb/N0 relationship when the phase noise is equal to -110 dBc. In this case we see, that the curves are much worse than in the previous one.

In both Fig. 4 and Fig. 5 the performance of Alamouti codes when the frame size is 1 kSym/fr. is the same. For low frame lengths phase noise impact is negligible and the overall system performance of pseudo-coherent system is close to the performance in coherent ones. On the other hand, this relationship shows that for larger frame sizes, there is a phase noise limit, below which its impact can also be negligible. For 100kSyb/fr. and 200kSym/fr. frame sizes that limit is equal to -120 dBc/Hz@100kHz, as to get 10^-6 BER the Eb/N0 values difference is less than 1 dB.

This relationship shows that in the pseudo-coherent systems that use reference clocks precise enough to provide Local Oscillators with phase noise close to -110 dBc@100kHz than their performance will be close to the performance of coherent system for broad range of frame sizes.

Understanding of how pseudo-coherency affects the MIMO communication performance is essential in order to choose the best system architecture in terms of both hardware and software. From hardware perspective it will help to chose RF transceiver and the reference clock source to provide MIMO-SDR system with the best combination of accuracy, price and size. From the software perspective, it will help to choose the modulation type and the frame length to get the best data rate and signal immunity that the chosen hardware can provide.

References

1. S. Alamouti, "A simple transmit diversity technique for wireless communications," *Selected Areas in Communications*, vol. 16, no. 8, pp. 1451 - 1458, 2002.
2. "bladeRF," Nuand, [Online]. Available: http://nuand.com.
3. "NI USRP," National Instruments, [Online]. Available: http://www.ni.com/usrp.
4. P. Almers, "Effect of random walk phase noise on MIMO measurements," in *Vehicular Technology Conference, 2005. VTC 2005-Spring. 2005 IEEE 61st (Volume:1)*, 2005.
5. S. Yousefi, "Phase Noise in Communication: Modeling, Simulation and Estimation," Microwave Electronics Laboratoy Department of MC2 Chalmers University of Technology, Goteborg, 2009.
6. N. Kasdin, "Discrete simulation of colored noise and stochastic processes and 1/fα power law noise generation," in *Proceedings of the IEEE (Volume:83 , Issue: 5)*, 2002.

Simple formula for Kirchhoff current on the main reflector of the generalized dual-reflector axisimmetric antenna in the transmit mode

N. R. Khachatryan[1], R.V. Ter-Antonyan[1]

[1]*National Institute of Metrology, Komitas Ave., 49/3, 0015 Yerevan, Armenia*

In [1] there is suggested a generalized dual-reflector axisimmetric antenna and simple formulae for designing and calculation of concrete antennas, in particular, a formula for amplitude distribution of the field in the antenna aperture in transmit mode which makes easier calculation of the pattern. In the present article there is suggested a simple formula for Kirchhoff current distribution on the main reflector of the mentioned generalized antenna in the transmit mode which makes easier analysis of cross-polarization component of a field of radiation of concrete antennas.

1. In [1] the concept of the generalized dual-reflector axisimmetric antenna based on idea of the generalized main reflector(GMR) set by the polar equation generatrix is suggested. By a choice of a polar corner(ψ) generatrix as the running parameter and introduction of two operated constants (f,n) of the optical scheme securing focusing, the system of simple formulas of universal character significantly simplifying radio physical design of concrete antennas is received.

Fig.1 makes clear the use of the symbols given below.

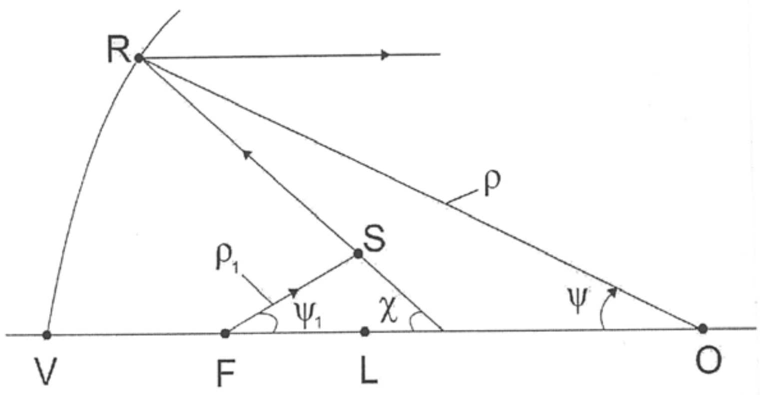

Fig.1

R – a running point of generatrix GMR, V – an apex of GMR at the symmetry axis OV, S – a running point of generatrix subreflector(SR), F – an antenna focus(OF=f), L– an initial point(ψ=0) of a curve of generatrixs subreflectors(OL=n), FSRA – is beam path in the transmit mode and all lengths normalized on OV($\rho(\psi=0)$).

The system of the formulas given in [1], includes in it self, in particular, the polar parametrical equations of the generatrixs subreflectors in shape

$$\rho_1 = \rho_1(\psi, \rho(\psi), \chi, f, n)\,, \qquad (1)$$
$$\psi_1 = \psi_1(\psi, \rho(\psi), \chi, f, n), \qquad (2)$$

formula for a corner χ,

$$\chi = 2\,\psi - 2\mathrm{arctg}(\rho'/\,\rho)\,, \qquad (3)$$

where the sign $'$ means a derivative on ψ,

formula for a transfer-function q which by multiplication by the scalar pattern a of the feed, transfers it to amplitude distribution of a field in an antenna aperture,

$$q(\psi)= \{(\psi_1' \sin \psi_1)/(rr')\}^{1/2}, \tag{4}$$

where $r=\rho(\psi)\sin\psi$.

The formula (4) allows by simple integration to count in aperture approach the main and cross-polarizing patterns of concrete antennas and results of such calculations are given in [1].
Meanwhile, the designer of reflector antennas is interested ways suppression of cross-polarization that demands a simple formula for the Kirchhoff current density ($2\vec{n} \times \vec{H}^{inc}$) on GMR in the transmit mode at rather general task of a field of radiation of the feed, and calculation of cross-polarization in current approach.
This formula is given below and the way which allowed to receive it is specified.

2. We will connect with focus F the right Cartesian rectangular system coordinates (x,y,z), as shown in Fig.2

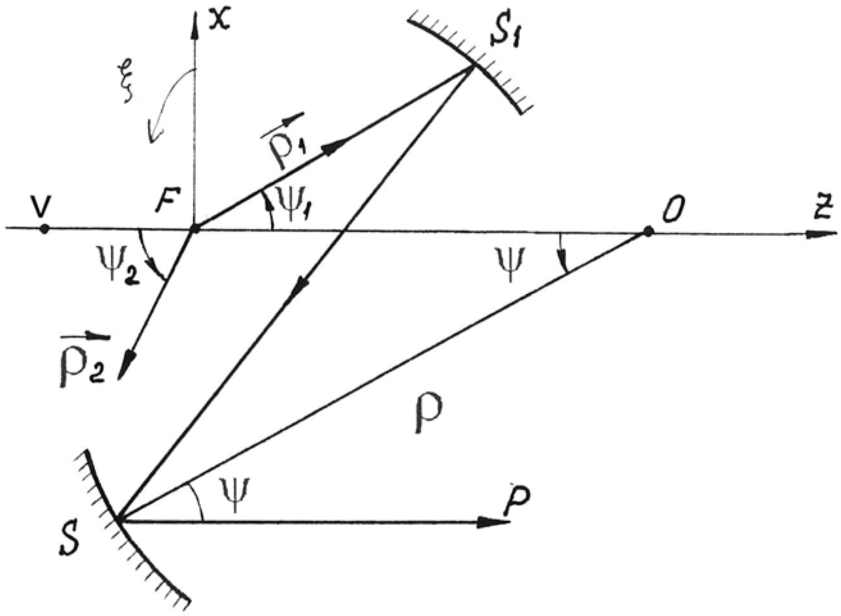

Fig.2

In spherical system of coordinates, a usual image connected with Cartesian, a running point of a subreflector (S_1) is defined by radius-vector $\vec{\rho}_1(\rho_1(\psi), \psi_1(\psi), \xi)$, and a running point (S) GMR – the radius-vector $\vec{\rho}_2(\rho_2(\psi_m), \psi_1(\psi_m), \xi_m)$, where the corner ψ_m is counted as well as a corner ψ, and a meridional corner ξ_m – the same as a meridional corner ξ.
Simple ratios

$$\psi = \psi_m\ , \quad \xi_m - \xi = 0, \pi, \tag{5}$$

where the choise of one of two values of meridional corner depends on subreflector type (Cassegren, Gregory), define a running stationary point S_1 of phase function

$$\Phi(\vec{\rho}_1 , \vec{\rho}_2) = \rho_1(\psi) + |\vec{\rho}_2 - \vec{\rho}_1|, \tag{6}$$

for a running point S of supervision on GMR. Thereby possibility to receive by stationary phaze method expression for magnetic component ($\vec{H}^{inc}$) of field near S, free from integrals, which is created by Kirchhoff current on a subreflector in transmit mode, with the subsequent allocation tangential component $\vec{H}^{inc}$, collinear to current $\vec{J}$ в S.
We will present final for Kirchhoff density of currents on GMR in the transmit mode in the form

$$\vec{J} \sim q(\psi)\, \vec{\Pi}(\psi, \xi), \tag{7}$$

where

$$\vec{\Pi}(\psi, \xi) = \vec{x}\{-[\, h_1(\psi_1, \xi)\sin \xi_m + h_2(\psi_1, \xi)\cos \xi_m \,] \cos(\chi/2) \} \\ + \vec{y}\, \{ [h_1(\psi_1, \xi)\cos \xi_m - h_2(\psi_1, \xi)\sin \xi_m] \cos(\chi/2) \} \\ \mp \vec{z}\, \{ h_{2mely}(\psi_1, \xi) \sin(\chi/2) \}, \tag{8}$$

$\vec{x}$, $\vec{y}$, $\vec{z}$ – unit vectors of rectangular system of coordinates, in a double sign –top for Cassegrain type, lower for Gregory type, by functions h_1 and h_2 set angular part magnetic component ($\vec{H}_f$) a field of radation of th e feed, namely,

$$\vec{H}_f(\psi_1, \xi) = \vec{\psi}_1 h_1(\psi_1, \xi) + \vec{\xi}\, h_2(\psi_1, \xi), \tag{9}$$

where $\vec{\psi}_1$, $\vec{\xi}$ –unit vectors of spherical system of coordinates.

For the practiced feeds of functions h_1 and h_2, as a rule, allow model representation

$$h_1 = - L_1(\psi_1, \xi)\sin\xi\,, \qquad h_2 = -L_2(\psi_1, \xi)\cos\xi\,, \tag{10}$$

at which (8) it is led to a characteristic form [2]

$$\vec{\Pi}(\psi, \xi) = \vec{x}\{ A\, (\psi, \xi_m) + B(\psi, \xi_m) \cos 2\xi_m \} + \vec{y}\, \{ B(\psi, \xi_m) \sin 2\xi_m \} \\ \pm \vec{z}\, \{ D(\psi, \xi_m) \cos \xi_m \}\,, \tag{11}$$

where

$$A\, (\psi, \xi_m) = 0{,}5\{L_1 + L_2\} \cos(\chi/2)\,, \quad B(\psi, \xi_m) = 0{,}5\{ L_2 - L_1\} \cos(\chi/2)\,, \tag{12}$$

$$D(\psi, \xi_m) = L_2 \sin(\chi/2)\,.$$

We will note that for linary polarized feed from (7) with evidence follow conditions on h_1 and h_2, at whom currents on GMR parallel to this or that coordinate plane.

References

[1] N. R. Khachatryan, R.V. Ter-Antonyan, IEEE Antennas and Propagation Magazin, **54**, (2012), 162.
[2] B.E. Kinber, V.A. Tishenko, The Radiotekhnic and Electronics (SU), **17**, (1972), 815.

The Modeling of the Detection of Electromagnetic Radiation in Ferromagnet

Yu.H. Avetisyan[1], H.G. Julfayan[2], A.H. Makaryan[1], Farokh Nazari[1], V.R. Tadevosyan[1]

[1] *Microwave Radiophysics and Telecommunications Dept.,Yerevan State University, Alex Manoogian 1, 0025, Yerevan, Armenia,*

[2] *Institute of Radiophysics and Electronics, Alikhanian Brothers str. 1, 0203 Ashtarak, Armenia*

Computer modeling of the detection of amplitude-modulated laser radiation in a ferromagnetic crystal YIG, based on the nonlinearity of the magnetization curve of a ferromagnetic medium was performed. Simulation was shown that detected signal absent when the ferromagnetic material is not magnetized, has maxima at certain values of the external magnetic field and changes sign when magnetic field is reversed.

The simulation results are in good agreement with experimental data. This suggests that the mechanism of the nonlinear interaction of electromagnetic radiation with a transparent ferromagnet well describes the process of optical detection.

1. Introduction

Ferromagnets are widely used in different areas of science and technology such as signal detection, amplification, frequency conversion, etc. [1-3]. They are one of the basic materials for recording and storing of the information. However in the last years, the traditional methods of the information recording and transformation don't satisfy growing requirements of the information speed. It is necessary to look for other methods to control of the magnetization of magnetic materials, advantageously differs from traditional.

The control of magnetization of the medium by laser radiation is one of the promising method for solution of this problem [4]. Under the impact of the changing magnetic field in the magnetized ferromagnet, a changing of the magnetic moment can occur, which generally has a nonlinear dependence from the magnetic field. Thus the ferromagnet behaves as a nonlinear medium, whereby the composition of the frequency spectrum of the magnetic moment, except components with the frequency of the alternating magnetic field, may also be present DC component and harmonics of the magnetic field [5-6].

In low frequency, RF and microwave bands such interactions are well known and studied. The possibility of generation, detection, frequency conversion and amplification of microwave radiation it was shown [2-3]. However, in studies of the microwave domain, represented in compilations [2-3], the nonlinear interactions have resonance character, and practically are not manifested in the infrared and visible bands. For this reason the nonlinearity of the ferromagnets in the listed regions (infrared and visible) has not been actively investigated. It is considered that in these regions magnetic permeability equals to one [7], and therefore the magnetic nonlinearity can't be manifested.

However, there are many works devoted to the interaction of optical radiation with a ferromagnetic medium, whereby a rotation of the plane of polarization of the radiation occurs, and electromagnetic radiation with circular polarization can cause the appearance of the magnetic field (direct and inverse Faraday effect), the scattering of light, and so on [8-14]. About of reorientation of the magnetic moment in ferromagnetic materials when exposed to optical radiation [4], and about obtaining of optical rectification as a result of the nonlinear interaction of laser radiation with the transparent ferromagnet it was also reported [5]. The experimental results of this interaction occurs is quite effective, even in a low power. Consequently, these interactions cannot be explained by a resonance mechanism, because in this case will require enormous, practically inaccessible magnetic fields.

In all experiments, the manifestation of nonlinearity in the ferromagnet essentially depends on the relative orientation of the magnetic field of the laser radiation and an external magnetic field. Therefore, we can assumed, that the appearance of the optical nonlinearity is due to the nonlinearity of the magnetic susceptibility (magnetization curve) of the ferromagnet.

In [5] the detection of plane-polarized amplitude-modulated infrared laser radiation in a transparent yttrium–iron garnet (YIG) ferromagnet at room temperature is performed experimentally. It is shown that the magnitude and sign of the detected signal depend significantly on the magnetizing external magnetic field. A mechanism of the nonlinear interaction of electromagnetic radiation with the ferromagnet is suggested.

For verification of the suggested mechanism, the modeling of the detection of amplitude-modulated electromagnetic radiation in a magnetized ferromagnetic medium was done in present work.

2. Modeling of the detection of amplitude-modulated electromagnetic radiation

The modeling was based on the nonlinearity of magnetization curve of the ferromagnet, presented in the work [5], and was made according to the experimental data of this work.

The orientation of the magnetic field $H_{\sim}$ of modulated laser radiation relatively to the ferromagnetic crystal in external magnetic field H_0 is shown in Fig. 1.

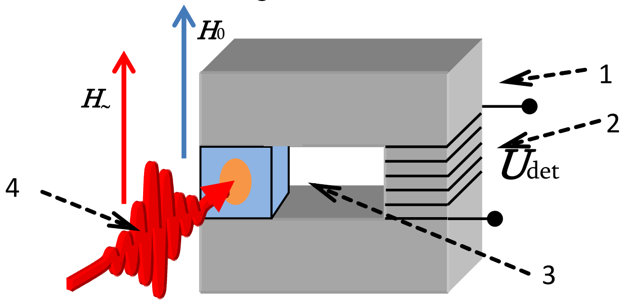

Fig. 1. The orientation of the magnetic field $H_{\sim}$ of modulated laser beam relatively to the magnetization of the ferromagnet (H_0-external magnetic field).

Magnetic sensor, representing a horseshoe ferrite body 1 with a coil inductor 2 coiled around it, was used to record changes in the average magnetic moment of the magnetized YIG sample 3. The sensor was attached to the sample as shown in Fig. 1. A change in the magnetic moment of the YIG crystal caused by the laser radiation 4 leads to a change in the magnetic flux in the magnetic sensor, and this induces a voltage in the inductor coil. The voltage across the inductor, which represents the detected signal U_{det}, was recorded by an oscilloscope.

Computer modeling of the detection process of the amplitude-modulated electromagnetic radiation was done thanks to Simulink (MatLab) program, when applied external magnetic field H_0 is a slowly varying linearly signal.

The block-diagram of Simulink model of ferromagnetic detector is shown in Fig. 2.

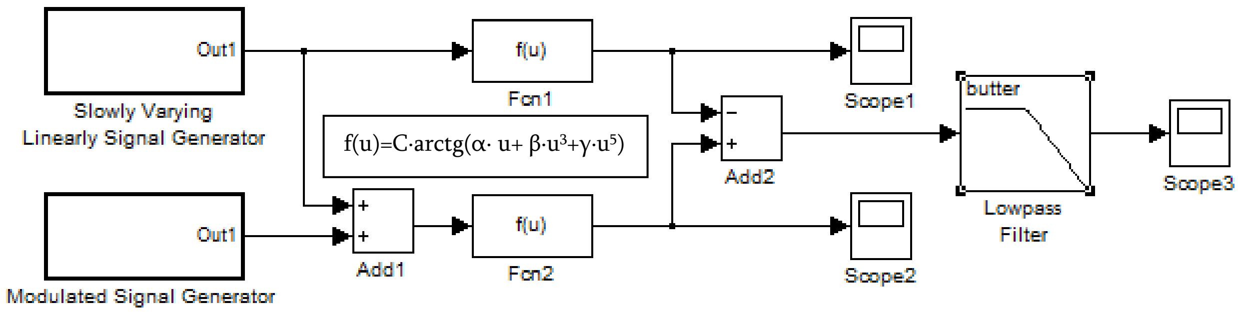

Fig. 2. Block-diagram of Simulink model of ferromagnetic detector.

The magnetization curve of YIG ferromagnet crystal, experimentally determined in [5], is shown in Fig. 3a. In modeling the magnetization curve was approximated by function

$$f(u)=C\cdot \mathrm{atan}\,(\alpha\cdot u+\beta\cdot u^3+\gamma\cdot u^5),$$

or

$$4\pi M(H) = 4\pi M_0\cdot(2/\pi)\cdot \mathrm{atan}\,(\alpha_1\cdot H+\beta_1\cdot H^3+\gamma_1\cdot H^5),$$

where $u = \eta\cdot H$, $\eta = 1\ \mathrm{Oe}^{-1}$, $C = 4\pi M_0\cdot(2/\pi)$, $4\pi M_0 \approx 1750$ Gs - is the saturation magnetization of YIG, α, β, γ - are constant coefficients ($\alpha = 0.02$, $\beta = 2.64\cdot10^{-3}$, $\gamma = 3.2\cdot10^{-9}$, $\alpha_1 = \eta\cdot\alpha$, $\beta_1 = \eta\cdot\beta$, $\gamma_1 = \eta\cdot\gamma$), and $H = H_0 + H_{\sim}$.

To obtain the magnetization curve shape by Simulink model,) to entrance of the unit Fcn1 was given the slowly varying linearly signal (magnetic field) (see Fig. 2). The unit Fcn1 in the modeling corresponds to ferromagnetic detector (YIG ferromagnet). The unit Fcn2 is absolutely identical to the Fcn1.

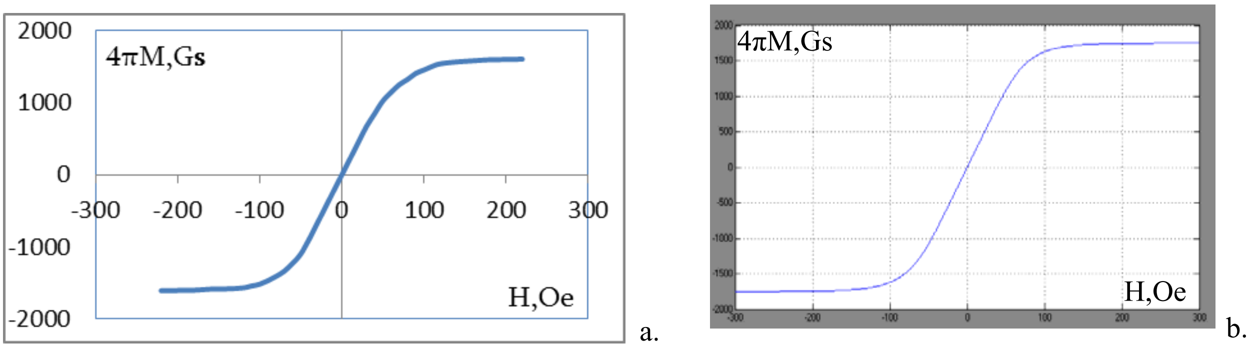

Fig. 3. a. Magnetization curve shape of YIG ferromagnet crystal, experimentally determined in [5],
b. Magnetization curve shape by Simulink model.

The output signal of the unit Fcn1 corresponds to magnetization curve, which is reflected in the Scope1 screen (Fig. 3b). The comparison shows that simulated curve coincides with the experimental curve with the ~10% accuracy.

Simulation of the detection process is performed as follows: to the input of the block Fcn1 the signal from the modulated signal generator was filed simultaneously with slowly varying linearly signal (bias magnetic field). The change of DC component of the magnetization under the influence of an alternating magnetic field of modulated signal is the detected signal.

The modeling result of the dependence of detected signal on the external magnetic field recorded on the oscilloscope Scope3 is shown in Fig. 4a. These dependence was obtained by subtraction of output signal of the detector Fcn2 slowly changing part of magnetization (output Fcn1) and filtration of the resulting signal by a lowpass filter (See Fig. 2). On Fig. 4b the dependence of the detected signal from the external magnetic field, obtained experimentally in [2] is shown to compare with the simulation results.

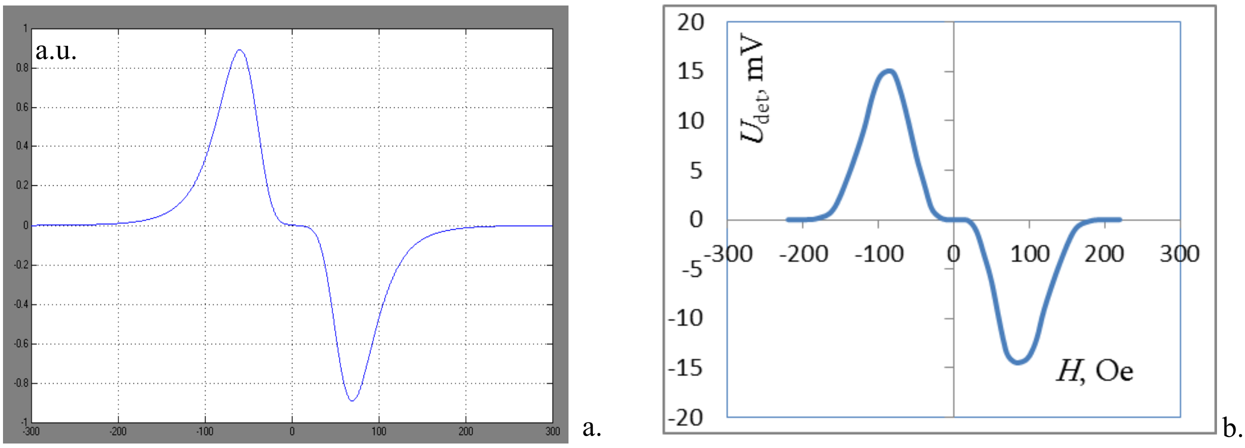

Fig. 4. Dependence of the detected signal from the external magnetic field a. modeling result, b. measured result by [5].

3. Discussion of results and conclusions

We performed computer simulations of the detection of amplitude-modulated laser radiation in a ferromagnetic crystal YIG based on the nonlinearity of the magnetization curve of a ferromagnetic medium. Comparison of experimental and simulation results show that they are in good agreement: the change of the magnetic moment occurs under the influence of an alternating magnetic field of the laser radiation, and the proposed model qualitatively explains the interaction mechanism.

The dependence of the changes of detected signal, its sign on the external magnetic field and the presence of its maximum values (see Fig. 4) well agreed with the YIG crystal magnetic curve (Fig. 3).

The maximum detected signal is recorded near the saturation threshold of the magnetization, but at deep saturation the probability of the magnetic moment reorientation decreases, which leads to a decrease of the amplitude of the detected signal. When the ferro magnetic material is not magnetized, the average value of the magnetic moment does not change by influence of laser radiation, because the reorientation occurs equally (symmetrically) in both directions.

Finally it should be noted that the nonlinear interactions between laser radiation and ferro magnetic material can have diverse practical applications for laser radiation frequency conversion, information recording, storing, etc.

4. References

[1] Yu.M. Yakovlev, S.Sh. Gendelev, Ferrite monocrystals in Electronics (Moscow, Sov. Radio, 1975), (in russian).

[2] Ferrites in nonlinear microwave devices, Collection of articles. Ed. by A.G. Gurevich (Moscow, Foreign Literature Publishing House, 1961), (in russian).

[3] Nonlinear properties of ferrites in microwave fields, Collection of articles, Ed. by A. L. Mikaelian (Moscow, Foreign Literature Publishing House, 1963), (in russian).

[4] A.V. Kimel, A. Kirilyuk, F. Hansteen, R.V. Pisarev, and Th. Rasing, J. Phys.: Condens. Matter 19, (2007) 043201.

[5] R.M. Martirosian, A.H. Makaryan, V.M. Mekhitarian, V.R. Tadevosyan, " Optical Detection in a Ferromagnet ", JETP Letters, Vol. 99, No. 8, (2014), pp. 435-440.

[6] Kang-Jeon Han, Ji-Hee Kim, Ki-Ju Yee, X. Liu, J. K. Furdyna and F. Hache, J. Appl. Phys. **101**, (2007) 063519.

[7] L.D. Landau and E. M. Lifshitz, Course of Theoretical Physics, Vol. 8: Electrodynamics of Continuous Media (Fizmatlit, Moscow, 2005; Pergamon, New York, 1984).

[8] J. Hohlfeld, Th. Gerrits, M. Bilderbeek, Th. Rasing, H. Awano, and N. Ohta, Phys. Rev., B 65, (2001), 012413.

[9] B. Koopmans, M. van Kampen, J. T. Kohlheppand, and W. J. M. de Jonge, Phys. Rev. Lett. **85**, (2000) 844.

[10] A.V. Kimel, F. Bentivegna, V. N. Gridnev, V. V. Pavlov, R. V. Pisarev, and Th. Rasing, Phys. Rev. B 63, (2001) 123520.

[11] W. A. Challener, T. W. McDaniel, C. D. Mihalcea, K. R. Mountfield, I. K. Pelhos and Sendur,Jpn. J. Appl. Phys., 42, (2003), 981.

[12] A.V. Kimel, A. Kirilyuk, P. A. Usachev, R. V. Pisarev, A. M. Balbashov, and Th. Rasing, Nature, 435, (2005), 655.

[13] F. Hansteen, A. V. Kimel, A. Kirilyuk, and Th. Rasing, Phys. Rev. B 73, (2006) 014421.

[14] Kirilyuk, J. Sci. Arts 3, (2011) 353.

The Evaluation of Measurement Errors of Radiation Pattern and Gain of the Near-surface Phased-array Antenna by On-site Measurement Method

A.A. Sargsyan

Russian – Armenian (Slavonic) University, 123 Hovsep Emin str., Yerevan, 0051 Armenia

In article the proposed new on-site measurement method of radiation pattern and gain of the VHF big near-surface phased-array antenna with the help of helicopter is described briefly. As radiating measurement antenna the half-wave vibrator was mounted on the helicopter which coordinates during the flight was fixed by GPS navigator. The evaluations of measurement errors of phased array radiation pattern and array gain depending on the following factors are discussed:

- error in the determination of the altitude of measuring half-wave vibrator;
- error in the determination of the horizontal coordinate of half-wave vibrator during the flight;
- extremity of distance between half-wave vibrator and VHF antenna under test (AUT);
- error in the azimuth angle of targeting of half-wave vibrator on the AUT;

As It known, to determine the parameters of antenna array (AA), the on-site method is frequently used when the aircraft performs flying around AA. But this method is a rather long and expensive process. An on-site method for measuring AA, is proposed in the mentioned work, where the aircraft is a helicopter, and the radiating antenna is a half-wave vibrator, mounted underneath the helicopter. The measurements are performed in two stages. The first is the measurement of AA vertical radiation pattern (RP) in the most important sector of angles up to 25^0 in a plane perpendicular to the canvas of A A.(Fig. 1). This is produced in vertical descent of the helicopter at a distance R_{fz}. The registration of the signal at the output of the receiver AA carried continuously during the vertical descent of the helicopter and synchronized in time with the GPS navigator. Taking full vertical RP in the upper half is performed by the horizontal flights of helicopter on several levels of the flight.(Fig. 2). [1,2]

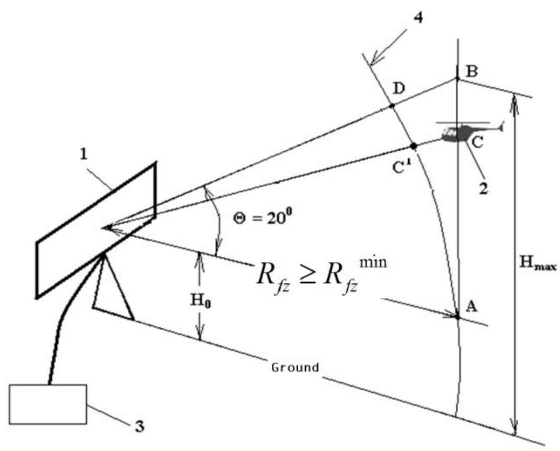

Fig. 1

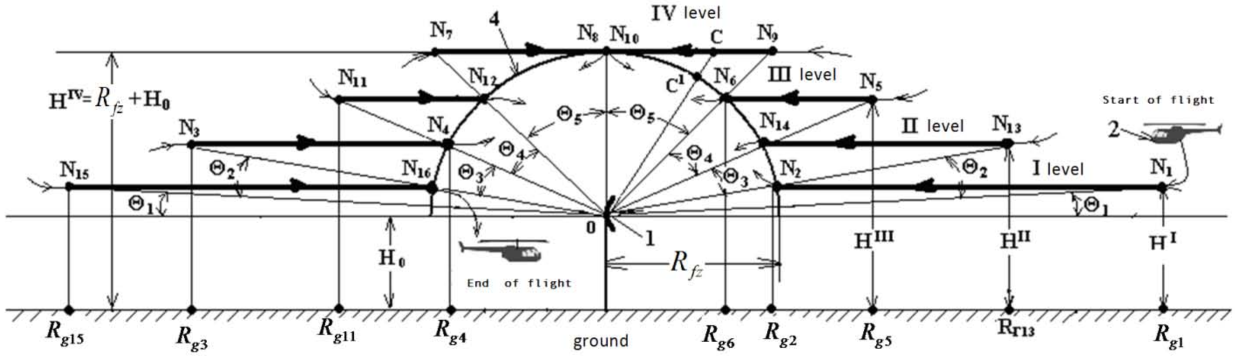

Fig. 2

The following notations are used in the figures: 1 – the antenna under test (AUT) in the receiving mode; 2 –the helicopter; 3 – the receiver AUT; 4 - a circle with a radius R_{fz} centered at the location AUT; H_0 AUT height above the ground; $H^I..H^{IV}$ heights of the levels of horizontal flights; $R_{fz}^{\min}$ minimal distance of AUT far zone; R_{fz} selected distance of the far zone of AUT during the measurements; $H_{\max}$ the maximum height of the helicopter; C - the current point of finding the helicopter; C' - a corresponding point on the circle along the direction OC; $N_1, N_3, N_5, N_7, N_9, N_{11}, N_{13}, N_{15}$ points with odd indices, indicated the start of the horizontal segments of the flights; $N_2, N_4, N_6, N_8, N_{10}, N_{12}, N_{14}, N_{16}$ points with even indices, denoting the end of the horizontal segments of flights; θ_0 the sector of angles DP from the horizon to 10 , which does not overlap with measurements of horizontal flight; $\theta_1, \theta_2, ..\theta_4$ the sector of angles, which overlap with measurements of horizontal flight; $R_{g1}...R_{g16}$ projections of inclined distances of points $N_1...N_{16}$.

The determination of the vertical DP is carried with the later recalculation of data array of received power levels as a result of the movement of the helicopter on the horizontal levels on the corresponding point on the circle with radius R_{fz} selected distance of the AA far zone . The recalculation is performed by the simple relation $P_{C'} = P_C k$ where $P_{C'}$ and P_C is the power at points C' and C, and k is the attenuation coefficient of the signal propagating in free space over a distance segment CC'. The described method can also duplicate measurements made with vertical descent.

After determining the angles of the vertical DP maximal petals, azimuthal DP in the direction of maximum of concrete petal is carried out by hanging helicopter at a height of the mentioned maximum. Whereas AA is rotated on 360^0 around its vertical axis.

The values of the angular sectors $\theta_0, \theta_1, ..\theta_4$ at the horizontal flight are determined by following way. Based on the minimum distance of the far zone $R_{fz}^{\min}$ of the antenna under test (AUT) the removal $R_{g1} \succ R_{fz} \ge R_{fz}^{\min}$ of point N_1 start of the horizontal flights is chosen, so that the correlation would be satisfied at $H^I \approx (25 \div 30)m$

$$\theta_0 = \arg tg\left\{\frac{H^I - H_0}{R_{g1}}\right\} \le 1^0 \quad (1)$$

The Angular sector θ_1 is

$$\theta_1 = \arcsin\frac{H^I - H_0}{R_{fz}} - \theta_0 \quad (2)$$

Subsequent sectors θ_M at $2 \le M \prec M_{\max}$ of vertical DP are

$$\theta_M = \arcsin\frac{H^M - H_0}{R_{fz}} - \sum_{j=0}^{M-1}\theta_j \quad 1 \quad (3)$$

The va lues define d angular sectors, starting from the sector θ_2 must als o satis fy the follow ing condition. For each vertical half-plane, the projection of the inclined distance of the helicopter at the starting point of the ho rizontal flight on a particular lev el should be less than th e projection of th e inclined distance of the helicopter at the starting point of th e horizontal flight of th e previous level. Concretely for the right half-plane Fig.2 we have $R_{g10} = R_{g8} = 0 \prec R_{g9} \prec R_{g5} \prec R_{g13} \prec R_{g1}$ and for the left half-plane - $R_{g10} = R_{g8} = 0 \prec R_{g7} \prec R_{g11} \prec R_{g3} \prec R_{g15}$.

The Evaluation of Measurement Errors of Radiation Pattern and Gain

Error $\delta\gamma_{\max}$ in the determ ination the a ngle γ h aving th e erro r δH i n the hi gh(the erro r in determination of the altitude of half-wave vibrator by navigator GPS)

$$\delta\gamma_{\max} = \frac{OD}{r_0} = \frac{\delta H}{r_0}\cos\gamma \quad (4)$$

At $\gamma \to 90^0$ $\delta\gamma \to 0$ and $\delta\gamma$ will be maximum $\gamma = 0$

$$(\delta\gamma_{\max})^0 = (\frac{\delta H}{r_0})57.3^0 \quad (5)$$

At $\delta H = 5m$ $r_0 = 500m$ $(\delta\gamma_{\max})^0 = (\frac{5}{300})57.3 = 0{,}57^0$

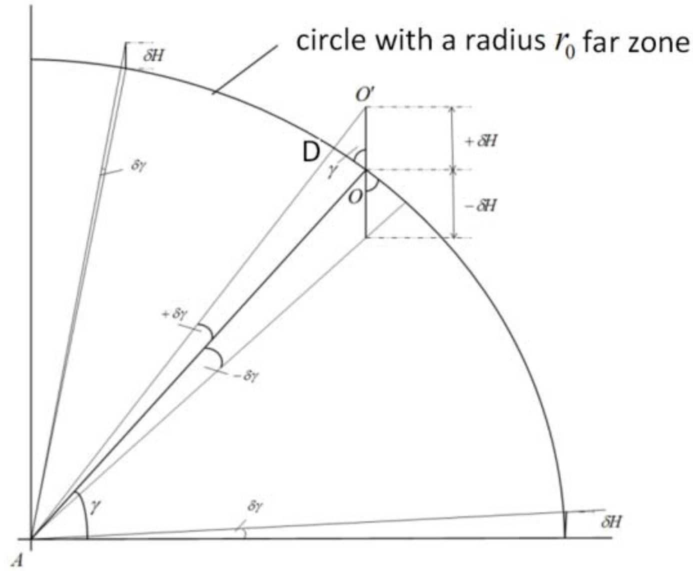

Fig.3

1. Error $\delta\gamma_{\max}$ in the determination the angle γ having the error in the horizontal coordinate δR_g of the helicopter

$\delta\gamma$ maximum at $\gamma = 90$

$$\delta\gamma_{\max} = \frac{O'D}{r_0} = \frac{\pm\delta R\sin\gamma}{r_0 \pm \delta R\cos\gamma} \approx \frac{\delta R}{r_0}\sin\gamma \qquad (6)$$

At $\gamma \to 0^0$ $\delta\gamma \to 0$

At $\delta R_\Gamma \approx 5m$ and $r_0 = 500м$ $\delta\gamma_{\max} = 0.57^0$

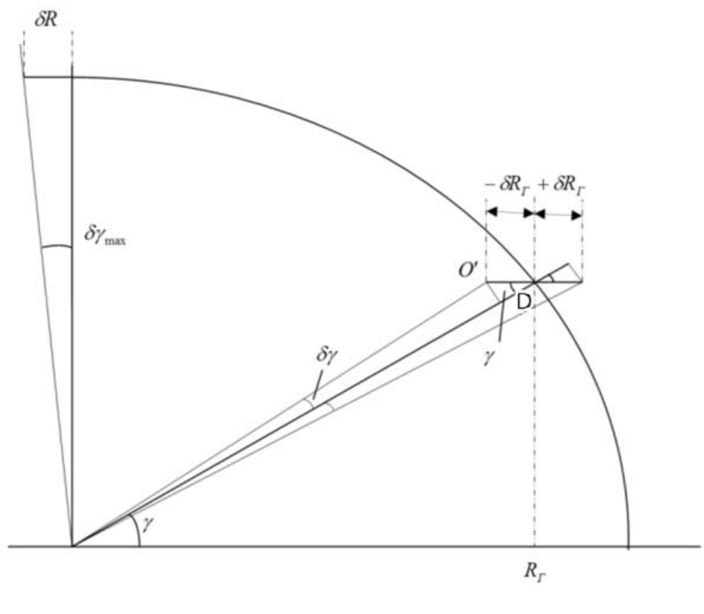

Fig.4

2. Error δL in the determination of the level DP of AUT depending from the error in distance ΔR ,due to attenuation in free space.

At $\Delta R = 25m = 0.025\,km \quad R_{ДЗ} = 0.5km$

$$\delta L(\partial Б) = 20\lg 0.525 - 20\lg 0.5 \approx 0.42\partial Б \tag{7}$$

3. Errors $\delta\gamma_i = \left|\gamma_{i\min} - \gamma_{i\min}'\right| \quad \delta\gamma_i = \left|\gamma_{i\max} - \gamma_{i\max}'\right|$ in the determination of the angular directions of min. and max. DP at infinite and finite far zones.

At $f = 160MHz, \quad \lambda = 1.875m$

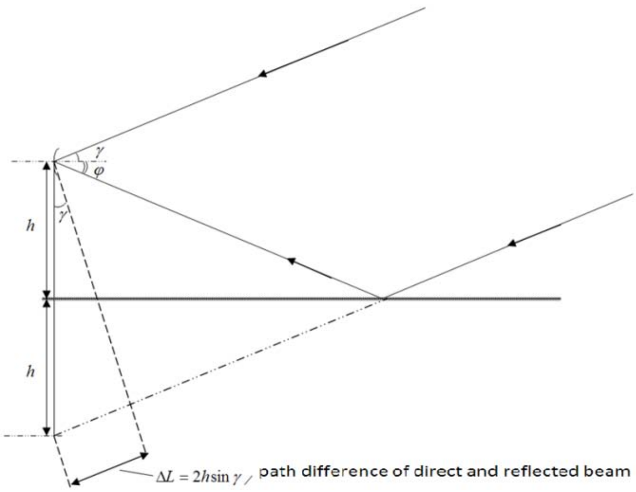

Fig.5

From the conditions of min. and max.

$$\begin{aligned} &2h\sin\gamma_{\min} = n\lambda, \quad where\ n = 0,1,2.. \\ &\gamma_{\min} = \arcsin\frac{n\lambda}{2h} \\ &2h\sin\gamma_{\max} = n\lambda + \frac{\lambda}{2} \\ &\gamma_{\max} = \arcsin\frac{(2n+1)\lambda}{4h} \end{aligned} \tag{8}$$

$\gamma_{1\min} = 0^0$; $\gamma_{2\min} = 7.697^0$; $\gamma_{3\min} = 15.537^0$; $\gamma_{4\min} = 23.689^0$; $\gamma_{5\min} = 32.39^0$;

$\gamma_{1\max} = 3.839^0$; $\gamma_{2\max} = 11.589^0$; $\gamma_{3\max} = 19.561^0$; $\gamma_{4\max} = 27.95^0$; $\gamma_{5\max} = 37.06^0$;

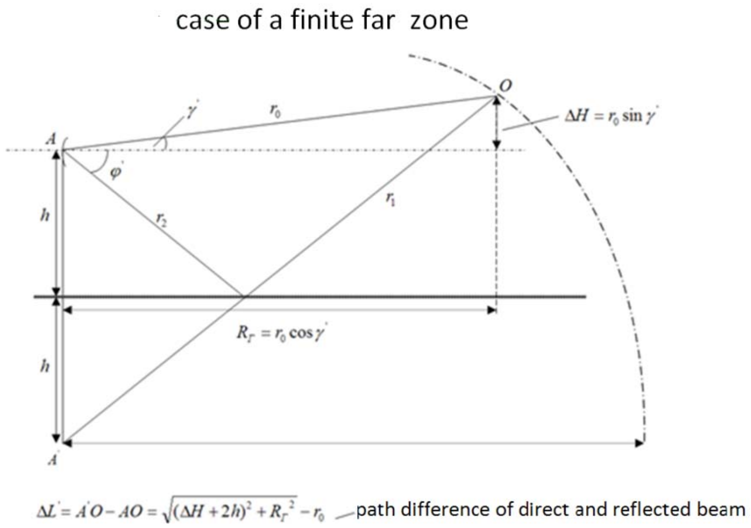

Fig. 6

From the conditions of min. and max. we get

$$\gamma_{\min}' = \arcsin\frac{(n\lambda - \frac{2h^2}{r_0})}{2h}$$
$$\gamma_{\max}' = \arcsin\frac{\frac{2n+1}{2}\lambda - \frac{2h^2}{r_0}}{2h} \tag{9}$$

$\gamma_{1\min}' = 0.8^0$; $\gamma_{2\min}' = 6.887^0$; $\gamma_{3\min}' = 14.708^0$; $\gamma_{4\min}' = 22.817^0$; $\gamma_{5\min}' = 31.45^0$;

$\gamma_{1\max}' = 3.04^0$; $\gamma_{2\max}' = 10.77^0$; $\gamma_{3\max}' = 18.71^0$; $\gamma_{4\max}' = 27.05^0$; $\gamma_{5\max} = 36.06^0$;

Errors in the determination of the angular directions of min. and max. DP at infinite and finite far zones are the following:

$\delta\gamma_{1\min} = 0.8^0$, $\delta\gamma_{2\min} = 0.81^0$, $\delta\gamma_{3\min} = 0.829^0$, $\delta\gamma_{4\min} = 0.872^0$, $\delta\gamma_{5\min} = 0.94^0$
$\delta\gamma_{1\max} = 0.799^0$, $\delta\gamma_{2\max} = 0.819^0$, $\delta\gamma_{3\max} = 0.851^0$, $\delta\gamma_{4\max} = 0.9^0$, $\delta\gamma_{5\max} = 1^0$

4. Error in determining the gain according to the error in the angle of targeting of half-wave vibrator on the AUT

From the theory of AA for half-wave vibrator DP by power we have $F(\theta)=\dfrac{\cos^2(\frac{\pi}{2}\sin\theta)}{\cos^2\theta}$,at

$$\theta=\pm 7^0 \qquad \delta F(DБ)\le |0.1DB|$$
$$\theta=\pm 10^0 \qquad \delta\, F(DБ)\le |0.2DB| \tag{10}$$
$$\theta=\pm 14^0 \qquad \delta F(DБ)\le |0.4DB|$$

5. Error in the determination of the gain depending on the instability of the generator power is equal to a long-term instability in power of the generator

$\Delta P_0 \approx 0.5DB$

References

[1]Արտոնագիր № 2803A, ՀՀ: Շրջաթիռ եղանակով վերգետնյա անտենայի պարամետրերի չափման սարք:/Մ. Մարկոսյան, Վ. Ավետիսյան, Ա. Հովհաննիսյան, Ա. Աիարոնյան, Ա. Սարգսյան: Առաջնության թվ. 23.05.2013: Հրապարակման թվ. 29.01.2014:

[2]Արտոնագիր № 2814A, ՀՀ: Ուղղաթիռի միջոցով վերգետնյա անտենայի ուղղորդվածության դիագրամի չափման եղանակ /Վ. Ավետիսյան, Մ. Մարկոսյան, Ա. Նիկողոսյան,Ա. Սարգսյան: Առաջնության թվ. 23.05.2013: Հրապարակման թվ. 25.02.2014:

Investigation of the antenna array's structure for organization of beam handling in system of target detection

M.V. Markosyan, **A.K. Aharonyan,** A.I. Petrosyan, G.Z. Sughyan

Yerevan Telecommunication Research Institute (YeTRI), Dzorap str. 26, (37410) 56 60 61 Yerevan, Armenia
mark@yetri.am, aharonaharonyan@yahoo.com

The problem of synthesis of an antenna phased array(PhA), forming the directional pattern (DP) by single beam in transmission mode and directional pattern consisting four beams along the line in receive mode is investigated in the given work. In case of different angles by synchronous scanning of beams the numerical simulation was carried out by MATLAB program to determine DP array, number of its m×n elements and necessary distribution of amplitude and phase by the array curtain. Several variants of array elements grouping by amplitude have been considered for the purpose of its simplifying in RF path.

Introduction

In the radiolocation the directional pattern (DP) in the aperture changes by individual radiating elements parameters management. This is achieved by electronic scanning.Within the aperture of PhA there are many radiating elements (antennas), which are excited by separate signals with controlled amplitude and phase. In phased array, beam handling is carried out in two planes with slope angles α and β in the spherical coordinate system, where α is the angle of displacement from the normal Yk plane of array and βis the angle displacement from the X axis in the array plane (Fig. 1).

During simulation of the array elements are arranged in form multiple of m × n matrix (where m and n are equal to 1,2,3, ...). In this case, using the direction cosine can determine the phase of each element during the displacement of the beam, and expression will be:

$$\Psi_{mn}=mT_{xs} + nT_{ys,}$$

where $T_{xs} = (2\pi/\lambda)d_x\cos\alpha_{xs}$ -phase shift between elements by x axis, $T_{ys} = (2\pi/\lambda)d_y\cos\alpha_{ys}$- phase shift between elements by y axis,and d_xиd_y- stepsbetween matrix elements by x and y axis accordingly[1,2].

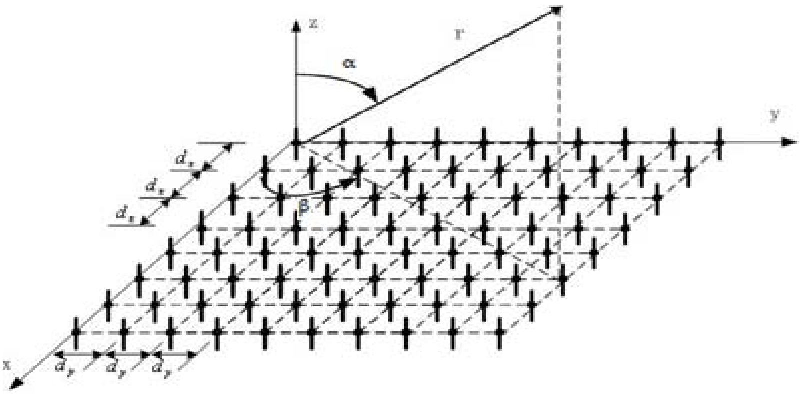

Fig.1. Geometrical view of radiation elements arrangement in the array

The factor of two-dimensional array can be calculated by summing of vector components of the signals from the elements of the array in each point of space. For an array consisting of m × n radiating elements and scans in the direction defined by $\cos\alpha_{xs}$and $\cos\alpha_{ys}$, the array factor is given by

$$E(\cos_{\alpha x}, \cos_{\alpha x}) = \sum_{m=0}^{M-1}\sum_{n=0}^{N-1}|A_{mn}|e^{j[m(T_x - T_{xs}) + n(T_y - T_{ys})]},$$

whereA_{mn}- signal's amplitude in $m\times n$ element, and$T_x = (2\pi/\lambda)d_x\cos\alpha_x$, $T_y=(2\pi/\lambda)d_y\cos\alpha_y$, accordingly [1,2].

Numerical simulation of phased array (PhA) with controllable beams[3].

The formed DP-s was determined in transmitting and receiving mode for multi-beam phased array by numerical simulation.In other words, the task is to form a DP, which would reduce the scanning time by elevation. It can be achieved by organizing beams management so as to obtain a wide transmitting beam and 4 receiving beam at the angles α and β changing in the receiving mode and by reducing the area of radiation (number of elements) in the transmission mode (Fig. 2a, b).

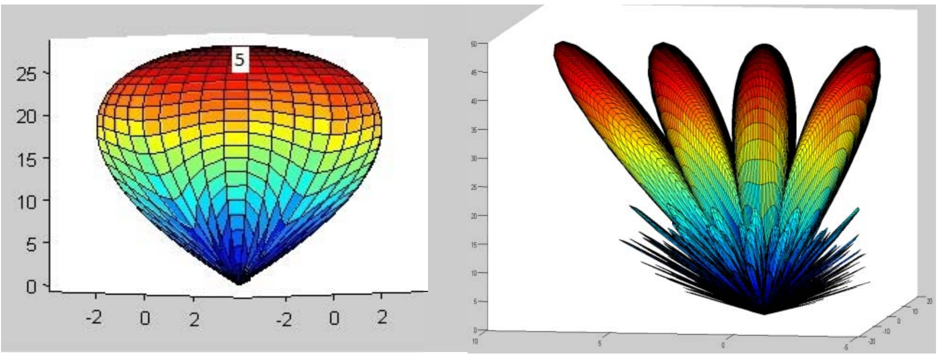

a) *b)*

Fig.2.DP of array without displacement from normal to array plane
a) transmission mode; b) receiving mode

For receiving of 4-beams it is necessary to have separate, independently amplitude and phase distributions. The displacement of these beams by changing the angle α has been considered by modeling. The case when the 4 beams are displaced, for example on 10 °, 20 ° from the normal to the array plane have been discussedas well (Fig. 3).

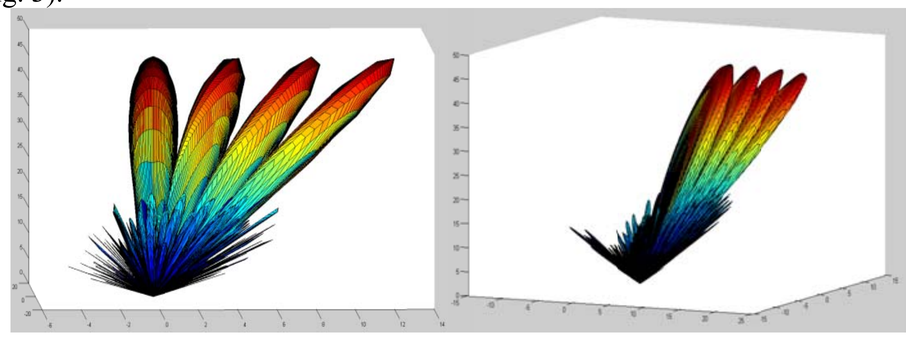

a)b)

Fig.3. DP of array consisting from m×nиradiating elements; a) with 10^0displacementfrom normal to the array plane;b) with 20^0displacement from normal to the array plane

In the simulation results the given PhA shows that in the case where the angle α is more than 27-30°, the diffraction effects occurs. In this case, the DP of array is divided, as shown in Fig. 4 (the angle displacement α is 35 °).

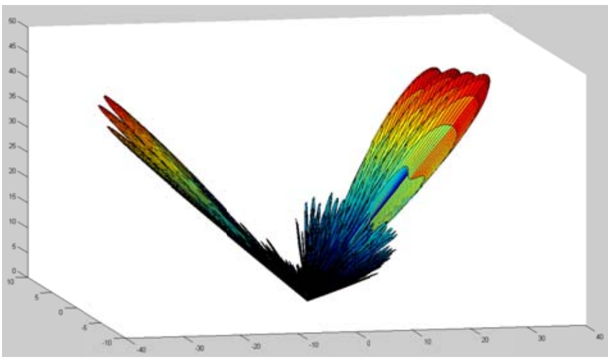

Fig.4. DP of array at displacement 35°from array plane

The amplitude distribution determination for multi PhA. In the PhA simulation in MATLAB, theTaylor amplitude distribution was used and several optionswere considered for grouping array elements by amplitude for making the RF path of the array more economical and simple. There 2 solutions were considered. Grouped elements by steps of 1,3, are show on fig Figure. 5 and 6 accordingly.

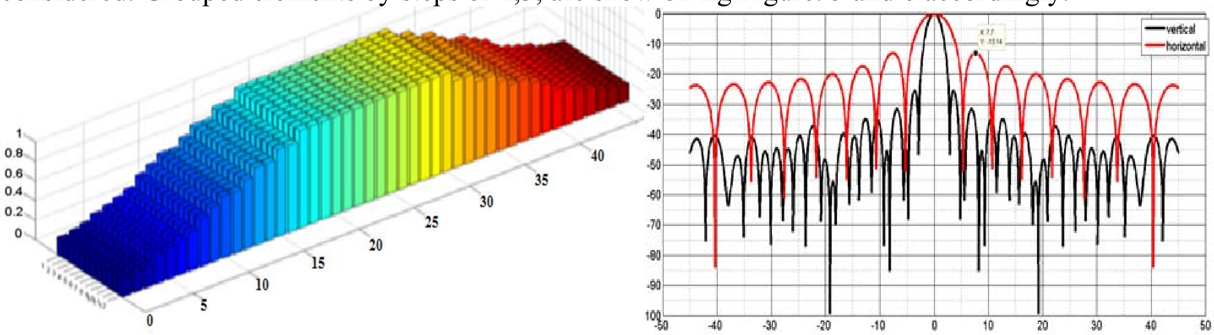

a) b)

Fig.5. Grouping of array elements by step1 : a) amplitude distribution in 3D, b)array directional pattern in two planes

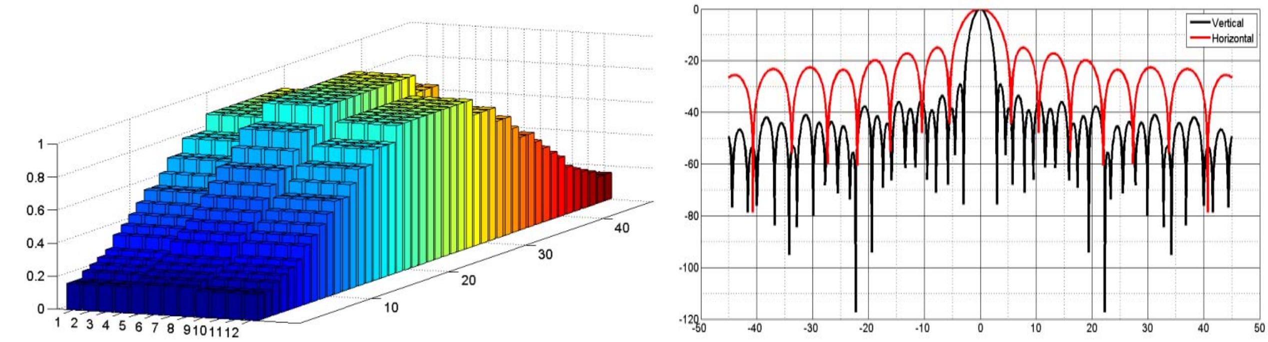

a) b)

Fig.6. Grouping of array elements by step3 : a) amplitude distribution in 3D, b)array directional pattern in two planes

Thus, according to research results we can conclude:

The beam in the direction of coinciding with the middle of the 2nd and 3rd beams is formed in the array at the transmission mode.

The width of the transmission beam must be equal to 4 * (reception beam width). In this case, the transmission of one probing signal is carried out reception by 4th channels. This allows almost 4 times reducing the scan time, hence, increases the possibility of coherent accumulation. Increasing of the receiving channels give more reserve time, but will lead to rising cost of the system connected with the need of additional phase shifters.

References

[1].**M.I.Skolnik**Radar handbook, second edition, San Francisco, California, 1990

[2].**О.Г. Вендик, М.Д.Парнес** Антенны с электрическим сканированием, 2001.

[3]. http://www.tutorialspoint.com/matlab/

Algorithm of Calculation of Interfering Sources Influence at Semi Open and Closed Tracks for Electromagnetic Compatibility Estimation

V.V. Grigoryan

Russian – Armenian (Slavonic) University, 123 Hovsep Emin str., Yerevan, 0051 Armenia

In current work, at estimation of electromagnetic compatibility (EMC) of radio relay communication line, the calculation of interaction between the recipient and the interference sources in case of semi open and closed tracks is discussed. A developed algorithm for calculation of that interaction type and following estimation of EMC is described. Unlike the established principal of merging of obstacles at estimation of EMC for these cases, the process of accounting of contributions from sequential obstacles on each of interfering station track is offered. For the purpose of optimization of the calculation amount in such process, the calculation algorithm consists of inserted criteria for reasonable cutoff in process of obstacle accounting in each track.

The estimation of EMC is one of key tasks in projecting of new radio electronic equipments (REE) or info communication systems and their implementation in already existing electromagnetic environment (EME). The estimation gives opportunity for new systems to operate in already existing EME with given quality without making unintended interference to other REE. For estimation of EMC International Telecommunication Union (ITU) has developed different recommendations depending on REE assignment, on frequency coverage, on type of wave propagation track. Based on ITU recommendations for different purpose REE and for different frequency coverage there are developed methods for calculation of EMC [1].

In current work the estimation of EMC for radio-relay communications line (RRL) case is considered. Here taking into consideration previous works dedicated to estimation of EMC of RRL [2]-[4], the calculation of interaction between recipient and sources of interference for closed and semi open tracks is discussed. Algorithm for calculation of precisely this type of interaction and its following estimation of EMC is developed. Realization of the algorithm imply for satisfying following criteria.

Satisfaction of wanted signal to fade margin

$$P_{want} \succ P_{thresh} * F , \tag{1}$$

P_{want} -is the power of wanted signal, P_{thresh} -is threshold sensitivity which is conditioned to reduce intrinsic noise on input of receiver, it is defined from product of Boltzmann coefficient K_B, antenna noise temperature T_n and frequency band of receiver B_n in which noise power is measured.

$$P_{thresh} = P_{n.own} = K_B \cdot T_n \cdot B_n , \tag{2}$$

where F- is a fade margin table1.

Table1. Dependency of fade margin from bandwidth [1]

Bandwidth, GHz	5.670-8.400	10.7-15.35	17.3-19.7
F, dB	37	40	25

Satisfaction to protection ratio to relation of wanted signal power to total power of interfering REE with open tracks

$$\frac{P_{wnat}}{\sum_{i=1}^{k} P_{i\ \mathrm{int}.open}} \succ A_0\,, \qquad (3)$$

$\sum_{i=1}^{k} P_{i\ \mathrm{int}.open}$ -is the total power of interfering REE with open tracks. A_0 -is protection ratio that is minimal admissible power ratio of wanted signal to power of interfering signal on receiver's input which permits in its output given quality of replayed signal.

$$A_0 = \left(\frac{P_{want}}{P_{\mathrm{int}.}} \right)_{out.}, \qquad (4)$$

Satisfaction to protection ratio to relation of wanted signal power to total power of interfering REE with open and semi open tracks.

$$\frac{P_{want}}{\sum_{i=1}^{k} P_{i\ \mathrm{int}.open} + \sum_{j=1}^{n} P_{j\ \mathrm{int}.semi\ open}} \succ A_0\,, \qquad (5)$$

$\sum_{j=1}^{n} P_{j\ \mathrm{int}.semi\ open}$ -is the total power of interfering REE with semi open tracks.

The developed algorithm is final for EMC calculation. It takes into account capability of modern computational tools and unlike the accepted principle of association of obstacles in EMC estimation in case of closed tracks it is proposed to calculate contribution of each successive obstacle. The algorithm consists of eight parts with following functionality.

First block supposes to define the type of obstacle for interfering REE with closed tracks (shading or semi shading obstacle) and approximation of obtained obstacle type (wedged, cylindrical, in the form of spheres).

Second block supposes the power calculation of each interacting REE from set of interfering stations with closed tracks. In every following cycle, the contribution from subsequent obstacle (if any) is taken into account.

Third block supposes the power summation of interfering REE for closed tracks.

Forth block supposes EMC check, taking into account total power from interfering REE with open and semi open and closed tracks.

In case of satisfaction to protection ratio to relation of power of wanted signal to total power of interfering REE with open, semi open and closed tracks is realizing fifth block otherwise sixth block.

$$\frac{P_{want}}{\sum_{i=1}^{k} P_{i\ \mathrm{int}.\ open} + \sum_{j=1}^{n} P_{j\ \mathrm{int}.\ semi\ open} + \sum_{e=1}^{m} P_{e\ \mathrm{int}.\ closed}} \succ A_0\,, \qquad (6)$$

$\sum_{j=1}^{n} P_{j\ \mathrm{int}.\ closed}$ -is total power of interfering REE with closed tracks, taking into account the subsequent obstacle of the track.

Fifth block supposes the end of EMC calculation establishing that viewed REE are electromagnetic compatible in given EME.

Sixth block supposes ejection from calculation of those REE with closed tracks that are satisfying reasonable cutoff criteria. Reasonable cutoff is determined by following formula

$$\frac{\frac{P_{want}}{A_0} - \sum_{i=1}^{k} P_{i\ \text{int.open}} - \sum_{j=1}^{n} P_{j\ \text{int.semi open}}}{m} \geq P_{e\ \text{int.closed}}\ , \tag{7}$$

m -is num ber of in terfering REE with closed track. $P_{e\ \text{int.closed}}$ -is power of interfering signal from e-one REE with closed track taking into account contribution from subsequent obstacle.

Seventh bloc k supposes checking the rest of th e tracks with closed drift for presence of subsequent o bstacle. If none of the tra cks have sub sequent obstacle block eig ht is realized, otherwise block two is realized.

Eighth block supposes the end of calculation for EMC esti mation establishing that viewed REE are electromagnetic not compatible in given EME.

Block scheme of the algorithm is shown bellow (see Fig. 1)

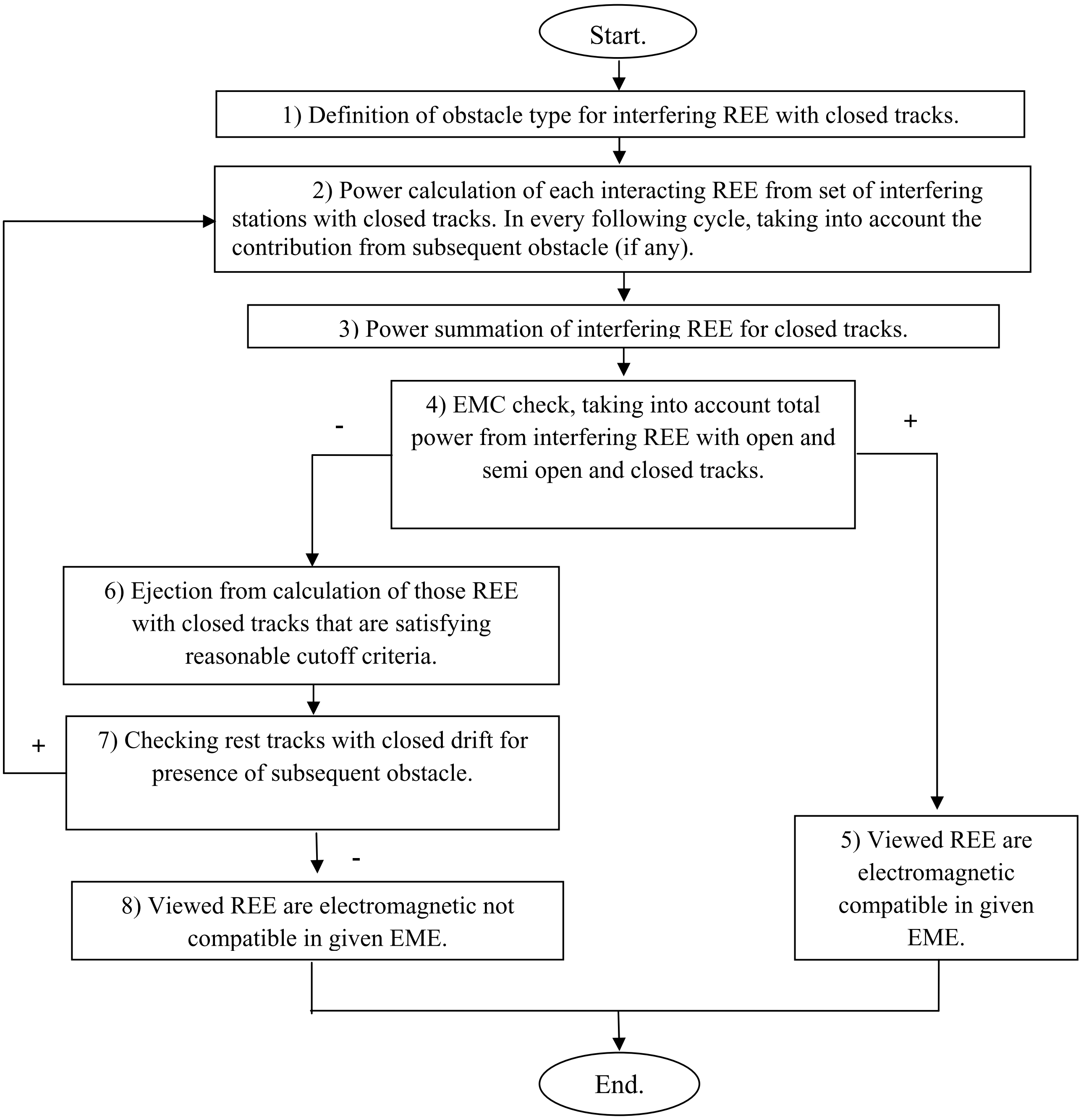

Fig.1 Final algorithm for EMC calculation

Thus the realization of this algorithm solves the question of detection of EMC fact for viewed pair of RRL REE in given EME. For optimization of computation process in final algorithm for EMC calculation contains inserted criteria for reasonable cutoff in process of accounting obstacles in interfering REE with closed tracks.

References

[1] Методика расчета электромагнитной совместимости земных станций фиксированной спутниковой службы гражданского назначения в полосах частот совместного использования от 1Ггц до 40Ггц. // Ленинградский отраслевой Научно-Исследовательский Институт Радиосвязи - Российская Федерация.

[2] V.H. Avetisyan, A. H. Nikoghosyan, V.V Grigoryan. The problem of automation of electromagnetic compatibility calculations for microwave-link equipment // International Conference on “Microwave and THz Technologies and Wireless Communications” 2012 Yerevan, Armenia.

[3] В.Г. Аветисян, В.В. Григорян. Расчет электромагнитной совместимости радиоэлектронных средств с привлечением программы Google Earth // Труды 5-ой годичной конференции РАУ / Ереван, декабрь 6-10, 2010.

[4] В.Г. Аветисян, В.В. Григорян. Метод автоматизированного определения профиля трассы между РРЛ станциями и расчета сигналов при открытой трассе // Труды 7-ой годичной конференции РАУ / Ереван, 3-7 декабря 2012 г.

Noninvasive monitoring of animals-blood glycemia with a microwave biosensor

K. Lee[1], S. Kim[1], J. Kim[1], Ogsen Galstyan[1], A. BabajanyanP[2], Gerard Berthiau[3], B. Friedman[4]

[1] Department of Physics & Basic Science Institute for Cell Damage Control, Sogang University, Seoul 121-742, Korea
[2] Department of Radiophysics, Yerevan State University, A. Manoogian 1, Yerevan 0025, Armenia
[3] IREENA, 37 Boulevard de L'iniversite, BP-406, 44602 Saint-Nazaire Cedex, France
[4] Department of Physics, Sam Houston State University, Huntsville, Texas 77341, USA

Noninvasive diagnosis and monitoring of blood glycemia in particular is individual and economic importance because of the large population of diabetics who require regular and accurate information regarding their blood glucose concentration. Microwave instruments have been used to analyze the dielectric property variations and have the ability to make nondestructive measurement of parameters inside a volume where direct contact with the sample cannot be achieved. This ability of microwave biosensors (MBS) provides the prospect for suitable noninvasive measurements of biological samples. The aim of this study is to outline the design of various MBS that could be applied for noninvasive detection and in vitro or in vivo monitoring of glycemia in animals, such as pig, goat, and mouse. The results show the sensitivity and the usefulness of MBS for sensing and monitoring of glycemia in animals. It can be useful for the real-time measurements of glucose concentration, and potentially it is an interesting approach for in vivo measurement of human glycemia.

1. Introduction

Diabetes affects about 6% of the adult population in the world [1]. It is an autoimmune disease or metabolic disorder, which results from the body's improper regulation of insulin. Insulin is secreted into the blood stream to manage the blood concentration of glucose, also called blood sugar or glycemia. Recently, a few research groups have focused on the quantitative monitoring of glycemia [2-4]. There are several types of blood glucose monitoring sensors, based on invasive [5], less-invasive [6], and non-invasive measurements [7]. The first two types of sensors have appeared in the commercial market for glycemia measurement. They have to use a small amount of blood directly pricked from the finger, so it is a painful and expensive method because invasive glucometers have to use an electrochemical strip to analyze the blood. Noninvasive glucose sensors are not commercially available but research indicates promising approach. The operational principles of the developed noninvasive glucose biosensors are based on near-infrared spectroscopy, Raman spectroscopy, photo-acoustic spectroscopy, scattering changes, polarization changes, and mid-infrared spectroscopy [8-10]. These methods for noninvasive monitoring are still being developed but there are limitations that exist for each of these methods. Another approach is to use techniques of impedance spectroscopy and electromagnetic coupling, which are based on impedance measurement of the dielectric parameters of blood [11]. Hayashi et al suggest that cell membrane capacitance of erythrocytes change as the glucose concentration in the blood changes [12]. In this proposed model, variations of glucose concentration and movement of glucose through the cell membrane of erythrocytes lead to a change in the electrolyte concentrations and hence to an alternation in the interfacial polarization of the cell membrane causing complex permittivity variations. These effects cause changes in the electromagnetic properties of the human skin and underlying tissue. The permittivity and conductivity decrease as the frequency grows. The study of glucose-induced variations of blood dielectric properties is a possible way for bloodless monitoring of blood glycemia. The real-time detection and monitoring of glycemia with high precision, sensitivity, selectivity, and speed is required for biomedical applications and clinical monitoring.

Microwave biosensors (MBS) are promising approach for the analysis of the glucose-induced dielectric property variations by using electromagnetic sensors thus avoiding any direct contact with the medium to be investigated. The aim of this study is to outline the MBS that could be applied for noninvasive detection of glycemia and can be used for real-time monitoring. Using microwave signal analysis, it is possible to detect the glucose concentration in blood in vitro and in vivo due to indirect measurement of the dielectric permittivity or direct measurement of the microwave reflection coefficient S_{11}. The estimated parameter is the complex dielectric permittivity ε, which is one of the main material characteristics of the medium.

2. Materials and methods

2.1. In vitro measurement of glucose in pig-blood and goat-blood by microwave cavity sensor

The microwave cavity sensor (MCS) was used to determine the glycemia in pig blood. The measured quantities are the microwave reflection coefficient S_{11} and the change at the resonant frequency. The resonant frequency f_0 and reflection coefficient, S_{11} of the microwave cavity sensor shifted due to substitution of the sample as a load.

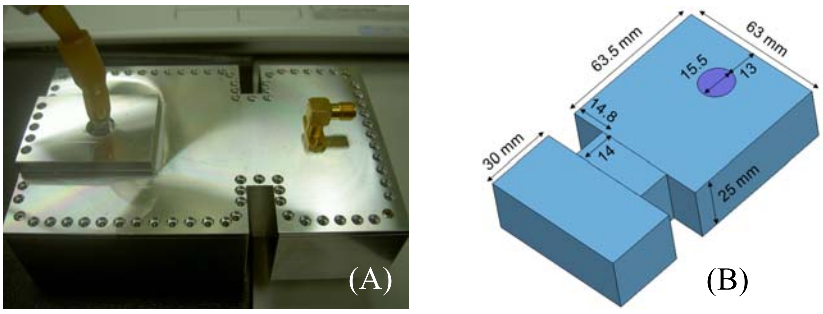

Fig. 1. The (A) photo and (B) schematic view of the MCS.

We fabricated the MCS based on the design of a waveguide cavity resonator (Fig. 1). The sample was placed in the cavity of sensor. The entire system was on a mechanical vibration isolation table and measurements were performed inside an electromagnetically shielded environment with automated temperature and humidity control. To determine the glucose concentration changes, we measured the reflection coefficient S_{11} of the microwave resonator. Subsequent changes in electromagnetic coupling between the probe and the sample cause changes in the magnitude of S_{11}, and this forms the basis for sample characterization. At resonance, the mode we used was TE_{011}, which is the dominant mode, and the sensitivity of the device is highest with operating this mode. The unloaded resonance frequency and microwave reflection coefficient minima were $f = 4.75$ GHz and $S_{11} = -9.175$ dB, respectively.

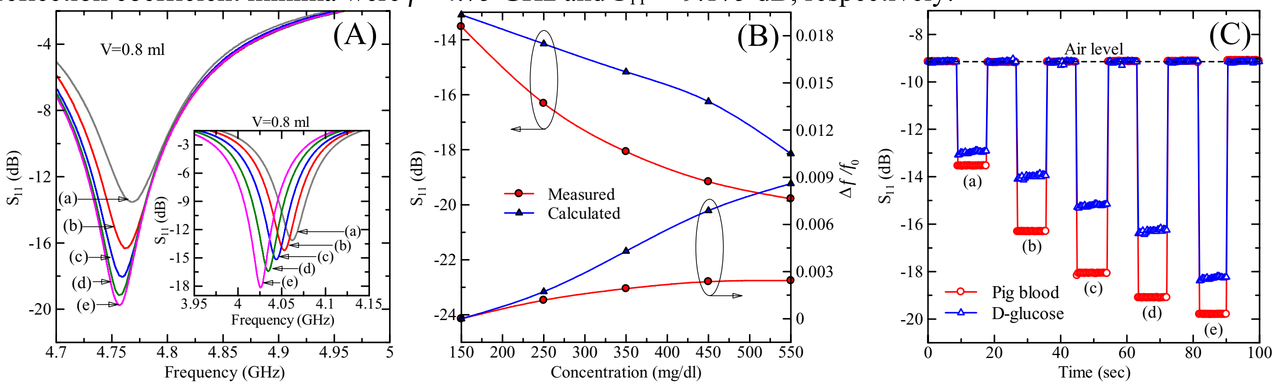

Fig. 2. (A) Measured microwave reflection coefficient S_{11} profile for pig blood samples. The inset shows the calculated microwave reflection coefficient S_{11} profile of the D-glucose aqueous solution for the same concentrations. The volume of the samples was taken to be 0.8 ml for both cases. (B) (a) Measured (circle) and calculated (triangles) microwave reflection coefficient S_{11} (left axis) and relative resonant frequency shift $\Delta f / f_0$ (right axis) vs. glucose concentration. (C) The real-time diagram of the microwave reflection coefficient for pig blood sample (circles) and for D-glucose aqueous solution (triangles) with two signal levels: for air (about -9 dB, i.e. empty tube) and for filled samples (pig blood or D-glucose) at an operating frequency of about 4.75 GHz.

The initial test samples based on pig blood have the glycemia of 150 mg/dl in the blood of the animal. By adding D-glucose to the initial sample, 5 samples were prepared with glycemia of 150 mg/dl, 250 mg/dl, 350 mg/dl, 450 mg/dl, and 550 mg/dl. The pig blood was mixed with sodium citrate ($C_6H_5Na_3O_7$) to avoid fast coagulation and then stored in a refrigerator with storage limitation of about 3 days. All samples were analyzed by the veterinary services.

Figure 2 (A) shows measured microwave reflection coefficient S_{11} profiles for pig blood samples with glycemia of (a) 150 mg/dl, (b) 250 mg/dl, (c) 350 mg/dl, (d) 450 mg/dl, and (e) 550 mg/dl. The inset shows calculated microwave reflection coefficient S_{11} profiles for D-glucose aqueous solution samples with glucose concentration of (a) 150 mg/dl, (b) 250 mg/dl, (c) 350 mg/dl, (d) 450 mg/dl, and (e) 550 mg/dl. The change of the S_{11} minimum and the frequency shift of the 150 mg/dl to 550 mg/dl pig blood samples were 6.26 dB and 11.25 MHz respectively, while the calculated changes for D-glucose aqueous solution were 5.05 dB and 35 MHz. Both measured and calculated results were obtained for the same sample volume (0.8 ml). Figure 2 (B) shows measured (circles) and simulated (triangles) microwave reflection coefficient S_{11} (left axis) and relative frequency shift $\Delta f / f_0$ (right axis) dependence on D-glucose concentration at the resonant frequency. It was found that the S_{11} decreased and $\Delta f / f_0$ increased as the glucose concentration increased. The S_{11} trend in the linear approximation varies with slope of $\Delta S_{11}/\Delta c$ = -0.0154 dB/(mg/dl) for blood samples, while the calculated data after linear approximation shows $\Delta S_{11}/\Delta c$ = -0.0122 dB/(mg/dl).

For an analogue of blood circulation in a vein we used a blood filled silicon tube inserted into the cavity circulating with a speed of 150 mm/sec. Figure 2 (C) shows the real-time diagram of the microwave reflection coefficient for the pig blood sample (circles) and for D-glucose aqueous solution (triangles) with two signal levels: for air (about -9 dB), that is the empty tube inserted in the cavity and for samples (the tube filled with pig blood or D-glucose aqueous solution) with D-glucose concentration of (a) 150 mg/dl, (b) 250 mg/dl, (c) 350 mg/dl, (d) 450 mg/dl, and (e) 550 mg/dl at an operating frequency of about 4.75 GHz. The real-time changes of the microwave signal during monitoring were clearly observed.

The initial test samples based on goat blood have the glycemia of 140 mg/dl, 92 mg/dl, and 110 mg/dl in the blood for the three different animals. These samples will be defined as samples group A, samples group B, and samples group C, respectively. By adding D-glucose to the initial samples, 5 samples were prepared with 100 mg/dl glycemia difference for each case. The goat blood was mixed with sodium citrate ($C_6H_5Na_3O_7$) to avoid fast coagulation and then stored in a refrigerator with storage limitation of 3 days.

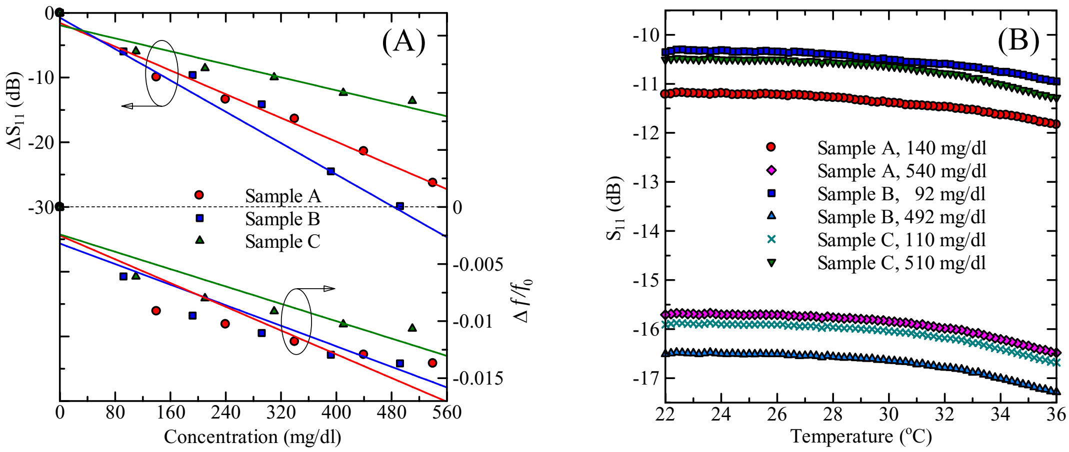

Fig. 3. (A) Measured microwave reflection coefficient minima S_{11} (left axis) and resonant frequency shift $\Delta f / f_0$ (right axis) dependence on glucose concentration for goat blood samples. (B) Measured microwave reflection coefficient S_{11} plotted as a function of the sample temperature for goat blood samples at the resonant frequency of about 4.76 GHz.

As the D-glucose concentration increased, the dielectric permittivity of sample increased and both the reflection coefficient S_{11} (left axis) and the resonant frequency shift $\Delta f/f_0$ (right axis) decreased as shown in Fig. 3 (A). Note that the microwave reflection coefficient S_{11} (and the resonant frequency shift $\Delta f/f_0$ also) is directly related to the sample electromagnetic parameters (dielectric permittivity, electric conductivity, magnetic permeability, etc.). Here, this relation thus the electric and magnetic field distribution behaviour shows the reverse dependence on glucose concentration due to the "two chambers" construction and mode structure of the resonant cavity. From the linear relationship as a function of glucose concentration, $\Delta S_{11}/\Delta c$ = 0.44 dB/(mg/dl) or $\Delta S_{11}/\Delta c$ = 0.13 1/(mg/dl) (0.0013 1/(mg/ml)) in the linear scale. The measured signal-to-noise (*SNR*) was about 42 dB. The smallest detectable change in concentration based on a criterion of *SNR* of 42 dB was about 10 mg/dl.

Figure 3 (B) shows the measured microwave reflection coefficient minima S_{11} plotted as a function of the goat blood temperatures with biggest difference of the glycemia concentrations for (a) group A, (b) group B, and (c) group C at the resonant frequency near 4.76 GHz. The temperature influence of S_{11} of the microwave cavity sensor is stronger in goat blood sample with low glycemia (140 mg/dl, 92 mg/dl, and 110 mg/dl); while for the high glycemia sample (540 mg/dl, 492 mg/dl, and 510 mg/dl) S_{11} is almost stable at temperatures bigger than 26 °C. This effect can be caused by the viscosity of the liquid, i.e. for the higher viscosity material (like a solid) the fluctuations of electromagnetic parameters due to temperature variations is smaller. On other hands, the temperature effect were weaker for samples with low glycemia (-0.046 dB/^{o}C) compared to samples with high glycemia (-0.052 dB/^{o}C). Note again that both temperature and humidity had significant effects on the reliability of blood glucose monitoring. The effect of temperature was greater than the effect of humidity.

2.2. In vitro and in vivo sensing of glucose in pig-blood and mouse-blood by spiral sensor

The microwave spiral sensor (MSS) was fabricated by preparing a microstrip board as shown in Fig. 4. The sensor is etched into double-sided gold-clad project board with a Teflon substrate. Teflon has a relative dielectric constant of approximately 2.2 and loss tangent of 0.0009 in the microwave frequency range. The center conductor is soldered to the stripline and the outer conductor is soldered to the ground plane. We placed the samples with various electromagnetic characteristics on the MSS and the response was measured. The MSS is connected through the 2 ports of the vector network analyzer (VNA, Agilent E5071B) for fully analyzing transmission and reflection. The resonator was calibrated with de-ionized (DI) water (for the 1st group of samples) giving an S_{11} minimum of -41.5 dB and with 100 mg/dl glycemia in blood (for the 2nd group of samples) giving an S_{11} minimum of -18 dB which were the reference levels for our experiments. Note that the reference level of blood was higher than the reference level of DI water (-18 dB > -41.5 dB) due to the highly conducting properties of blood (it contains minerals, hemoglobin, sodium chloride etc).

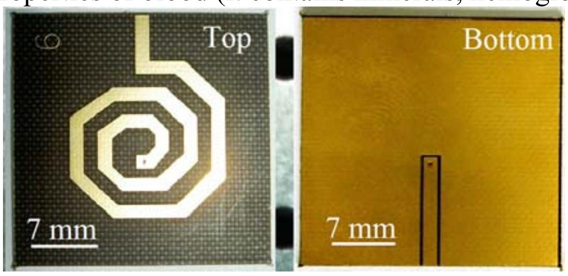

Fig. 4. The top and bottom view of MSS.

The 2nd group of samples, based on pig's blood concentration of natural glucose in the blood of the animal, is 72 mg/dl (concentration without addition of D-glucose). The pig blood glucose was balanced to 100 mg/dl for the reference level of the 2nd group of the samples and then by adding D-glucose in the blood, samples of glucose in the range 100 mg/dl to 600 mg/dl were prepared. Before making samples, the fresh blood was mixed with sodium citrate ($C_6H_5Na_3O_7$) in order to avoid fast coagulation (0.4%) The blood was then stored in refrigerator and the storage was limited to 3 days.

The data acquisition time for glucose real-time monitoring was 0.5 second and the ambient temperature was 25 ^{o}C. After each test, the Petri dish was washed and dried for the next measurement. The Petri dish diameter was chosen to be 8 mm for full interaction of the MSS with the sample.

The effect of the sample is observed by measuring S_{11} in the plane where the microwaves are input. The operational principle of MSS is based on the shift in the microwave reflection coefficient, S_{11} and resonant frequency shift, $\Delta f/f_0$ due to changes of the electromagnetic characteristics of the sample that vary with frequency. The resonant frequency f_0 and reflection coefficient, S_{11} of the MSS shifted due to substitution of the sample as a load. Note that, these shifts are the result of standing waves that form between the spiral input and output. These parameters are mainly defined by the three components of blood: H_2O, NaCl, and D-glucose due to its relatively high concentration in blood (NaCl and D-glucose have about 0.9 % and 1-1.4 % concentration, respectively). The concentration of NaCl in blood is very stable and even small variation of NaCl concentration is quite dangerous for organism while the variation of glucose concentration is in the range 0.4÷3.5 % and controllable. Thus, we monitored the changes in glucose concentration despite the fact that pig blood contains other components (NaCl, vitamins, proteins etc. in pig blood).

Figure 5 (A) shows the microwave reflection coefficient S_{11} profile for (a) DI water (i.e. no glucose) and for D-glucose aqueous solution with glucose concentration of (b) 50 mg/dl, (c) 100 mg/dl, (d) 150 mg/dl, (e) 200 mg/dl, (f) 250 mg/dl, (g) 300 mg/dl, (h) 400 mg/dl, (i) 500 mg/dl, and (j) 600 mg/dl at 7.65 GHz. Figure 5 (B) shows the microwave reflection coefficient S_{11} profile for blood samples with glycemia of (a) 100 mg/dl, (b) 200 mg/dl, (c) 300 mg/dl, (d) 400 mg/dl, (e) 500 mg/dl, and (f) 600 mg/dl at 7.77 GHz. It was found that the S_{11} decreased and $\Delta f/f_0$ increased as the glucose concentration increased as shown in the insets of Fig. 5.

The S_{11} minimum variation trend with glucose concentration was linear with slope of $\Delta S_{11}/\Delta c$ = -0.022 dB/(mg/dl), while the frequency shift $\Delta f/f_0$ has saturation behaviour with slopes of $(\Delta f/f_0)/\Delta c = 0.653\times10^{-4}$ $(mg/dl)^{-1}$ and $(\Delta f/f_0)/\Delta c = 0.0094\times10^{-4}$ $(mg/dl)^{-1}$ in the low (0 ÷400 mg/dl) and in the high (400 ÷600 mg/dl) concentration ranges, for the 1st group samples. The S_{11} trend varies with slope of $\Delta S_{11}/\Delta c$ = -0.0121 dB/(mg/dl), while the frequency shift varies with slopes of $(\Delta f/f_0)/\Delta c = 0.0112\times10^{-4}$ $(mg/dl)^{-1}$ and $(\Delta f/f_0)/\Delta c = 0.0005\times10^{-4}$ $(mg/dl)^{-1}$ in the low (100÷300 mg/dl) and in the high (300÷600 mg/dl) concentration ranges, for the 2nd group samples. The relationship of S_{11} as a function of glucose concentration is 2×10^{-4} $(mg/dl)^{-1}$ in the linear scale. The measured *SNR* was about 34 dB. The smallest detectable change in concentration based on a criterion of *SNR* = 34 dB was about 5 mg/dl.

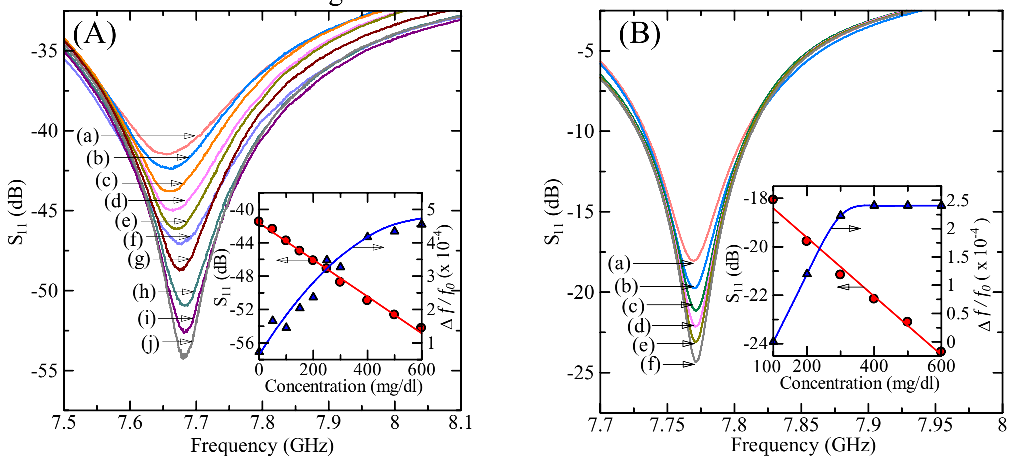

Fig. 5. (A) The microwave reflection coefficient S_{11} profile for DI water and for D-glucose aqueous solution at about 7.65 GHz. The inset shows (left axis) the microwave reflection coefficient S_{11} and (right axis) the relative frequency shift $\Delta f/f_0$ dependence on glucose concentration at the resonant frequency. (B) The microwave reflection coefficient S_{11} profile for pig blood samples at about 7.77 GHz. The inset shows (left axis) the microwave reflection coefficient S_{11} and (right axis) the relative frequency shift $\Delta f/f_0$ dependence on glucose concentration at the resonant frequency.

The experimental subjects were 8 alive mice with normal glycemia level. These animal patients were divided in 4 groups with 2 animals in each group: group A (mice with numbers 6 and 7) was the control group without any further intervention; group B (mice with numbers 1 and 8) where 0.2 ml DI water was orally injected into the mice; group C (mice with numbers 2 and 3) where the 0.2 ml 3% D-glucose solution was orally injected into the mice, and group D (mice with numbers 4 and 5) where the 0.2 ml 6% D-glucose solution was orally injected into the mice. The initial and finally test results of glucose level measured by glucometer Accuk Check One Touch Ultra. Both MSS and glucometer measurements were made before (initial) and 20 min after (final) intervention. The glycemia level almost linearly the increased with increase of injected glucose concentration.

Figure 6 shows measured microwave reflection coefficient S_{11} profiles for 8 animals at the resonant frequency of about (A) 4.14 GHz and (B) 4.89 GHz. The matched resonance curve for the DI water has a minimum level of -47.43 dB at 4.14 GHz and -12.79 at 4.89 GHz which are the reference levels for the microwave reflection coefficient S_{11} in our measurements in the low and high frequency range, respectively. As the injected glucose concentration increased, the dielectric permittivity of the sample increased and both the reflection coefficient S_{11} (left axis) and the resonant frequency shift $\Delta f/f_0$ (right axis) decreased for the low frequency resonance (4.14 GHz) as shown in the inset of Fig. 6 (A). On the other hand, with increase of injected glucose concentration, both the reflection coefficient S_{11} (left axis) and the resonant frequency shift $\Delta f/f_0$ (right axis) increased for the high frequency resonance (4.89 GHz) as shown in the inset of Fig. 6 (B). It is also notable that the behaviours of S_{11} and $\Delta f/f_0$ (i.e. measurements sensitivity) were different for different animals even for the similar glycemia level. We think that this effect (i.e. sensitivity of measurements) may be caused by the Cholesterol, Phosphorus, and urea Nitrogen level in blood. We suppose that the change in Nitrogen concentration (due to its high intrinsic conductance) is the main reason for the variation of the measured microwave slopes. The problem is the structure (i.e. other components) of blood for different animals. It is simpler to make a calibration for any animal before starting the glycemia measurement.

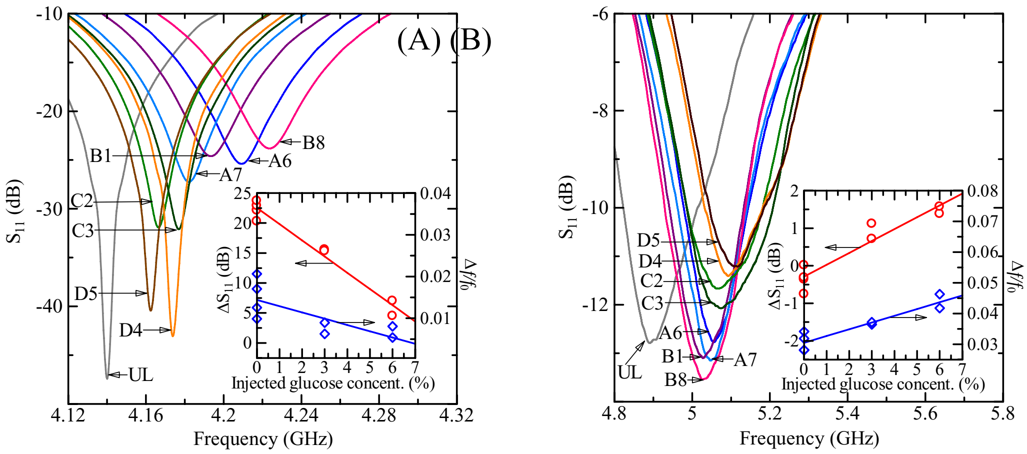

Fig. 6. (A) The microwave reflection coefficient S_{11} profiles for UL resonance and 8 mice at about 4.14 GHz. The inset shows (left axis) the microwave reflection coefficient S_{11} and (right axis) the relative frequency shift $\Delta f/f_0$ dependence on injected glucose concentration at the resonant frequency. (B) The microwave reflection coefficient S_{11} profiles for UL resonance and 8 mice at about 4.89 GHz. The inset shows (left axis) the microwave reflection coefficient S_{11} and (right axis) the relative frequency shift $\Delta f/f_0$ dependence on injected glucose concentration at the resonant frequency.

From the linear relationship as a function of glucose concentration, $\Delta S_{11}/\Delta c \cong$ -0.11 dB/(mg/dl) at 4.14 GHz (0.01 dB/(mg/dl) at 4.89 GHz) or $\Delta S_{11}/\Delta c \cong -3\times10^{-4}$ at 4.14 GHz (3×10^{-4} at 4.89 GHz) in the linear scale. The root-mean-square statistical noise in reflection coefficient S_{11} was about 10^{-5} in the linear scale. The measured *SNR* was 30 dB. The smallest detectable change in concentration based on a criterion of *SNR* of 30 dB was about 10 mg/dl.

3. Conclusions

Microwave biosensors have been developed for noninvasive determination of glycemia in animals-blood in vitro and in vivo. The MBS is a novel noninvasive glucometers with a minimum 10 mg/dl detectable change in blood. The results show the sensitivity and the usefulness of the MBS for in vitro and also in vivo sensing and monitoring of glycemia in animals. It can be useful for the real-time measurements of glucose concentration, and potentially it is an interesting approach for in vivo measurement of human glycemia.

Acknowledgements

This work was supported by a Sogang University Special Research Grant 2009 (201314002), Basic Science Research Program through the National Research Foundation of Korea (2009-0093822 & 2014R1A1A2A16055772), and Parts & Materials International Collaborative R&D Program funded by the Ministry of Knowledge Economy of Korea (MKE: N0000481).

References

1. IDF, *Diabetes atlas*, 4th ed. (2010).
2. C. Geddes, J. Lakowicz (eds.) *Topics in fluorescence spectroscopy: Glucose sensing*, Springer New York (2006).
3. O. Khalil, Diabetes Technol. Ther. 6 (2004) 660-697.
4. G. Wilson, R. Gifford, Biosens. Bioelectron. 20 (2005) 2388-2403.
5. J. Armour, J. Lucisano, B. McKean, D. Gough, Diabetes 39 (1990) 1519-1526.
6. M. Albers, J. Lekkala, L. Jeuken, G. Canters, A. Turner, Bioelectrochem. Bioeng. 42 (1997) 25-33.
7. J. Newman, A. Turner, Biosens. Bioelectron. 20 (2005) 2435-2453.
8. A. Tura, A. Maran, G. Pacini, Diabetes Res. Clin. Pract. 77 (2007) 16-40.
9. M. Ibbini, M. Masadeh, J. Med. Eng. Technol. 29 (2005) 64-69.
10. A. Rouane, Sens. Trans. J. 93 (2008) 69-81.
11. T. Tatara, K. Tsuzaki, Med. Biol. Eng. Comput. 38 (2000) 377-383.
12. Y. Hayashi, L. Livshits, A. Caduff, Y. Feldman, J. Phys. D 36 (2003) 369-374.

S-Band 1000 Watt Gallium Nitride Based Pallet Amplifier for Air Traffic Control Radars with Gate Pulsing and Bias Sequencing Circuitry

Apet Barsegyan[1], Daniel Koyama[1], Vinodh Thangam[1]

[1] *Integra Technologies, Inc., 321 Coral Circle, El Segundo, CA, 90245, USA*

Abstract — This article presents 1000 Watt Gallium Nitride (GaN) based pallet power amplifier operating in 2.7-2.9GHz frequency band with Class AB bias. The RF performance of the amplifier under pulse conditions with 300us pulse width and 10% duty cycle is characterized. The amplifier is designed for S-band Air Traffic Control Radar applications and can operate both under short pulse/low duty cycle and medium pulse/duty cycle conditions. The amplifier is based on 500 Watt, internally pre-matched, GaN high electron mobility transistor (HEMT). The pallet operates from +50V power supply, contains bias sequencing and RF-activated gate biasing circuitry to reduce output noise and simplify system integration.

Index Terms—Power amplifier, GaN, power transistors, power gain.

1. Introduction

As always, demand for high power S-band amplifiers for radar applications, such as Air Traffic Control, is strong and high power output and high efficiency are key requirements for these amplifiers. GaN transistors provide excellent power density and efficiency and as such are excellent choice for S-band high power applications. High efficient power amplifiers (PA) make the system level thermal aspects more manageable, reduce operational cost, and provide an opportunity to reduce the overall transmitter size by reducing the cooling element size.

A high power S-band Class AB power amplifier (PA) is designed, implemented and characterized based on 500 Watt, Gallium Nitride (GaN) high electron-mobility transistor (HEMT). A power gain of 11.5dB and drain efficiency of 51% was achieved at 1000 Watt power output level across the operating 2.7-2.9GHz band.

2-way high power Gysel combiner [1] is developed for up to 1.8 kilowatt power combining. Integra Technologies IGN2729M500 [2] transistor is used for amplifier design. Figure 1 below shows a picture of the amplifier. Rogers RO4350 circuit board material with a dielectric constant of 3.48 is utilized in order to minimize the size and loss from the transmission line matching networks while providing sufficient power handling capability for 1000 Watt operation.

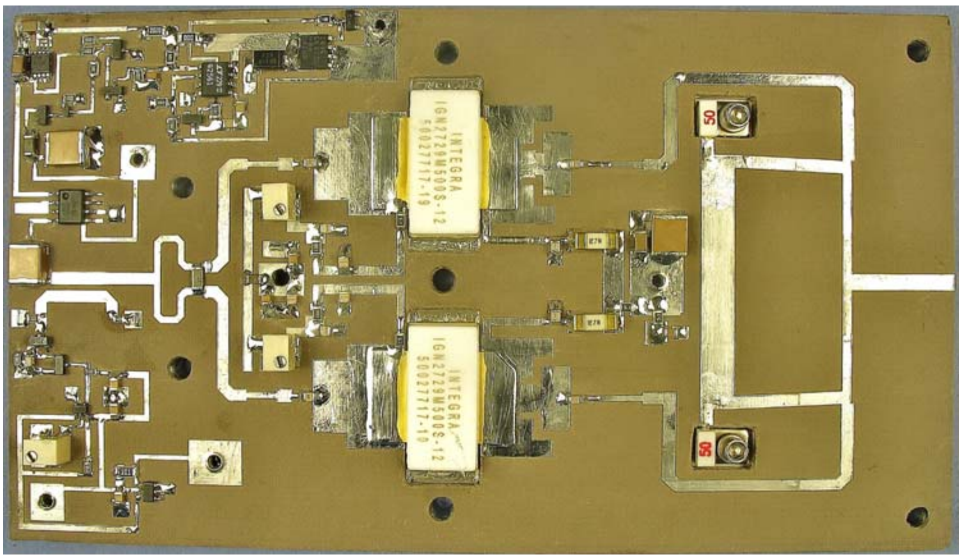

Figure 1. 2.7-2.9GHz, 1000 Watt pallet photo. Dimensions: 72.1mm x 69.6mm

To the best of our knowledge this is the highest power pallet amplifier based on two single ended transistors operating in the specified frequency range.

2. Pallet Amplifier Design

2.1. IGN2729M500 transistor

IGN2729M500 is an internally pre-matched, GaN HEMT. It is designed for S-band radar applications operating over 2.7-2.9GHz instantaneous frequency band. Under 300us pulse width and 10% duty cycle conditions it supplies a minimum of 500 Watts of peak output power with 11.4dB of minimum gain. Transistor operates with 50V drain bias with 100mA bias current. It is specified for Class AB operation. Rated minimum drain efficiency is 55%, which is calculated as

$$N_d = P_{out} / (V_D \times I_{D\,pk})$$

where N_d is drain efficiency , P_{out} is peak output power, V_D is drain bias voltage and $I_{D\,pk}$ is peak drain current.
Thermal impedance is rated at 0.15ºC/W at P_{out}=500W and Tcase=30ºC.
Device input and output impedances are given in the table below:

Table 1. IGN2729M500 IMPEDANCE CHARACTERISTICS

Frequency (GHz)	Z_{IF} (Ω)	Z_{OF} (Ω)
2.70	2.5 – j1.8	2.5 – 2.0
2.80	2.5 – j1.7	2.4 – j1.8
2.90	2.4 – j1.8	2.5 – j1.7
Impedance Definition	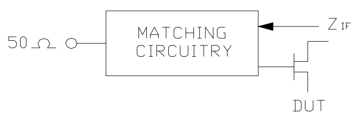	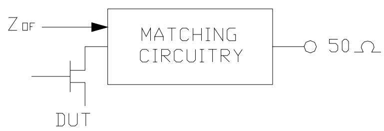

2.2. 2-way Gysel High Power Combiner

One of the major advantages of the Gysel power combiner is its ability to handle high power efficiently . It provides low loss combining, good isolation between the ports and good phase and amplitude balancing. Our Gysel combiner designed for this application, has been successfully tested for power handling capability for up to 1.8kW level.

Table 2 below summarizes measured S-parameters for power combiner, including port to port isolation:

Table 2. S-parameters for 2-Way Power Combiner

	F (GHz)	S11(dB)	S12(dB)	S13(dB)	S23(dB)
Power Combiner	**2.70**	-28.68	-3.26	-3.29	-34.50
	2.80	-29.90	-3.23	-3.28	-25.36
	2.90	-22.26	-3.25	-3.30	-20.88

2.3. 1000 Watt Amplifier

Two IGN2729M500 transistors were com bined in parallel to achieve 1000 Watt operating power across the 2.7-2.9GHz operating frequency range. Wilkinson power divider was employed for input power split and Gysel power combiner for output power combining. Amplifier is specified with 74 Watt input drive level and minimum gain of 11.3dB [3]. Recorded worst case efficiency was 51.0% and power gain was 11.50dB. Pulse droop, which was m easured from 30us to 270us interval was -0.17dB recorded at 2.9GHz frequency. Recorded worst case Return Loss was 14.0dB across the band. Overall, am plifier dem onstrates excellent stability against the load mismatch and is rugged to 5:1VSWR. Amplifier's power transfer curves are given in the figure below.

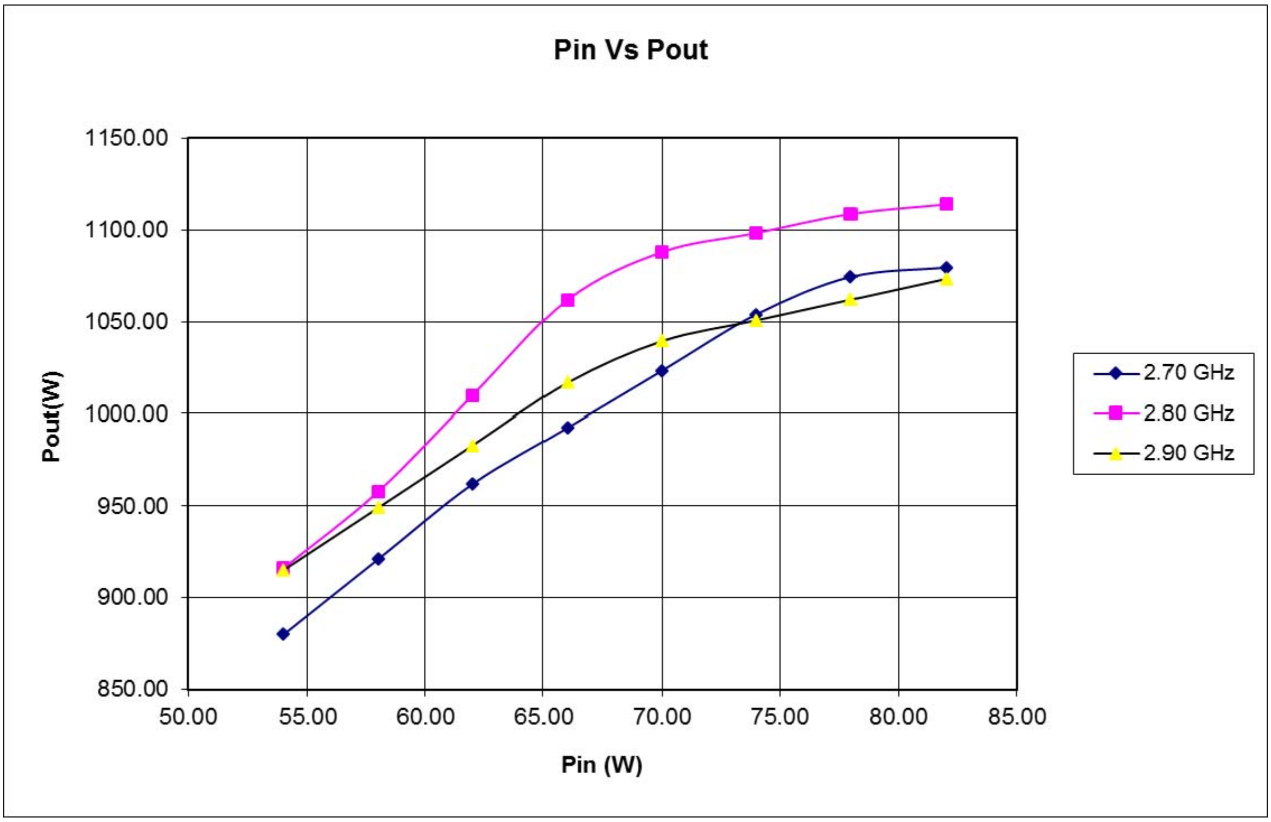

Fig.2: Measured Power Output vs. Power Input Characteristics

As can be seen from the graphs, at 74 Watt input drive level am plifier produces m ore than 1050 Watt output power across the operating 2.7- 2.9GHz frequency range.

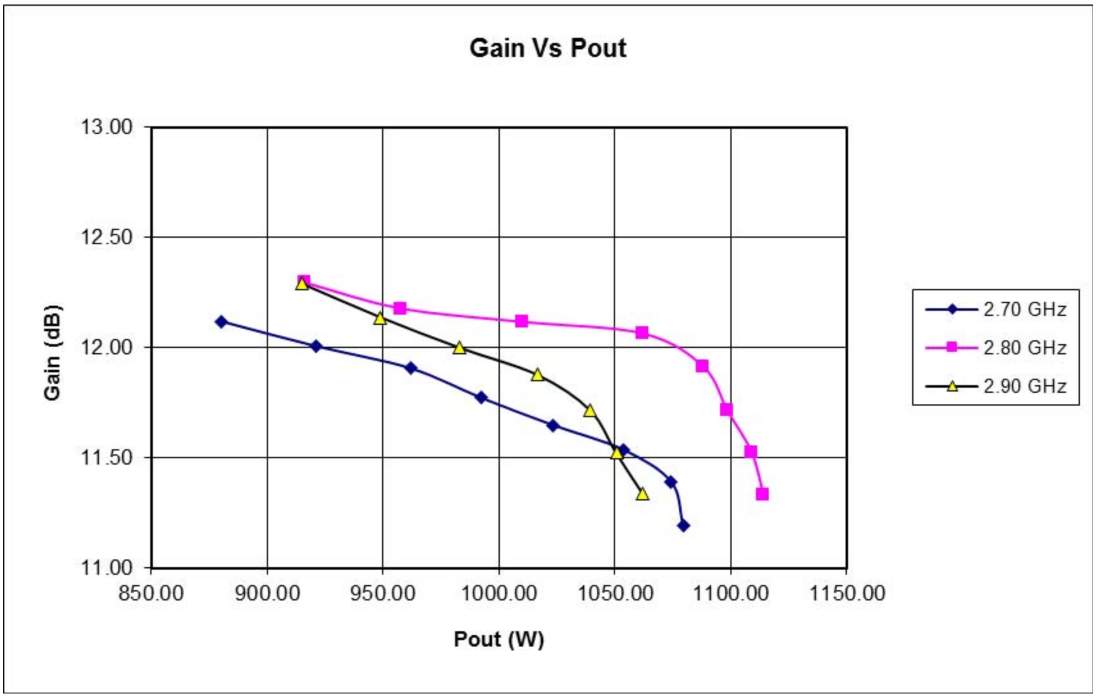

Fig.3: Power Gain vs. Power Output

Figure 3 above shows amplifier gain performance versus output power.

Figure 4 below shows power gain versus frequency at Pin=74 Watt. As can be seen from the graph, gain flatness is better than 0.75dB in 2.7-2.9GHz range.

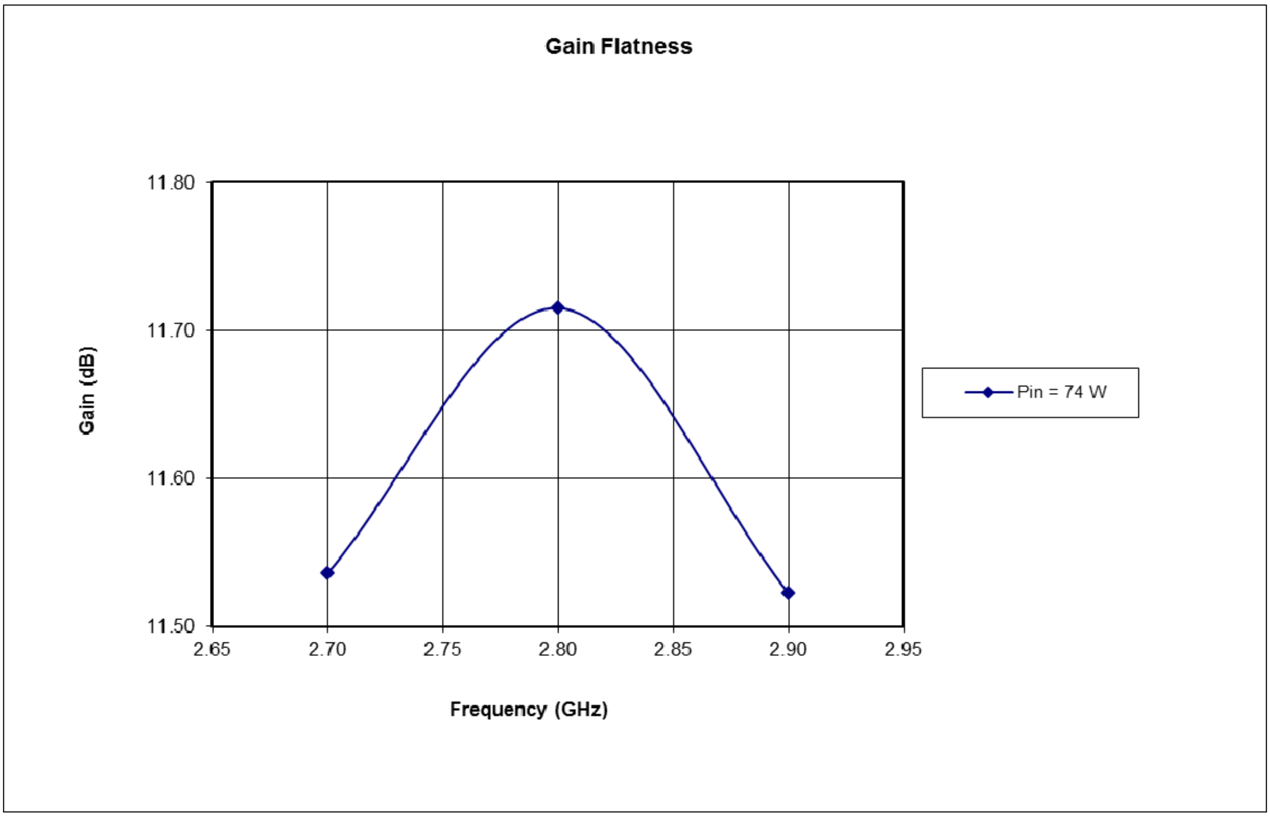

Fig.4: Power Gain vs. Operating Frequency at Pin=74 Watt

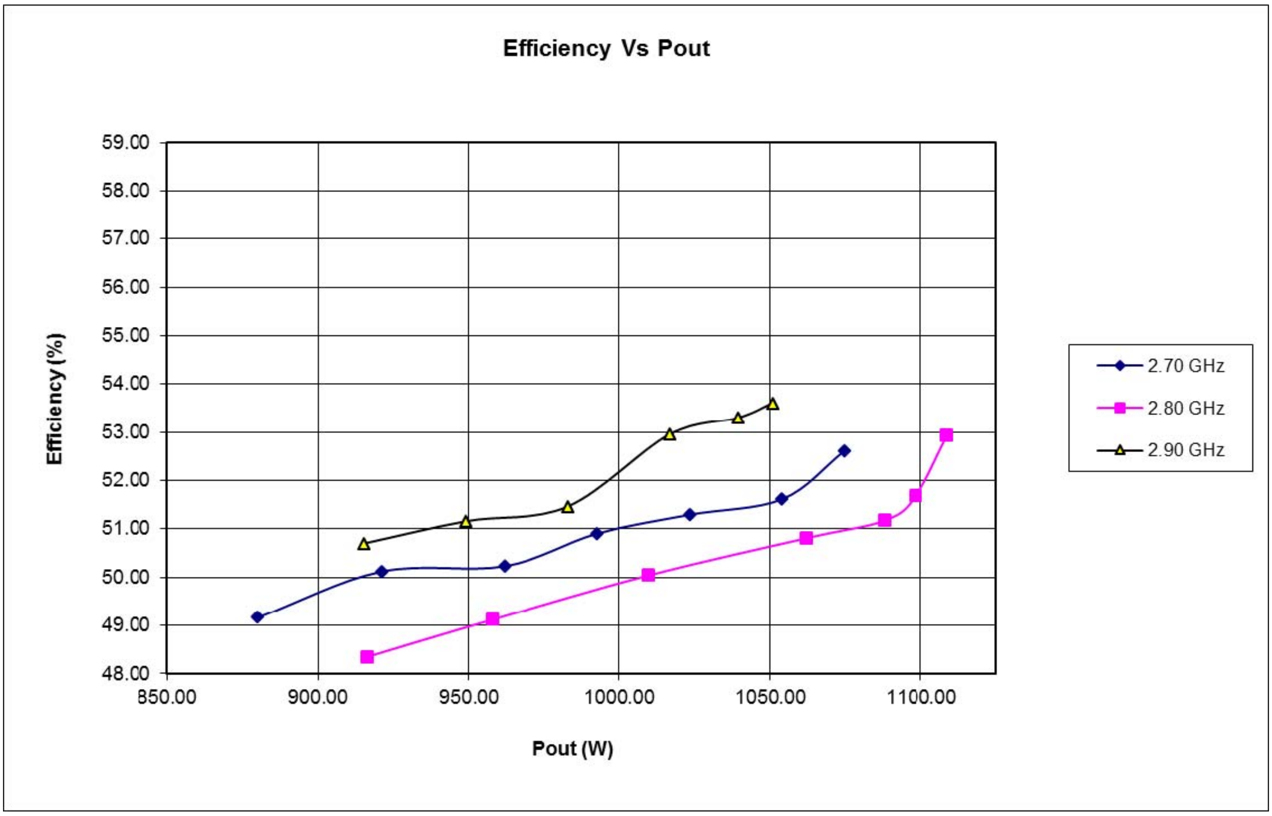

Fig.5: Drain Efficiency vs. Power Output

Figure 5 above shows amplifier drain efficiency versus Power Output and as expected it reaches maximum efficiency at saturated power levels. About 51% minimum drain efficiency was recorded across the entire frequency band.

Conclusions

S-band GaN-based 1000 Watt pallet amplifier was designed and implemented. Amplifier operates from single +50Volt power supply and contains RF-activated gate biasing circuitry to reduce output noise and bias sequencing to simplify system integration. Minimum of 1000 Watt operating power was obtained with 11.5dB power gain and 51% drain efficiency. Recorded worst case pulse droop was -0.2dB at 2.9GHz at power output level of 1059 Watt.

3. References

[1] Tri T. Ha, Solid State Microwave Amplifier Design, John Wiley & Sons
[2] Datasheet IGN2729M500 www.integratech.com
[3] Datasheet IGNP2729M1KW-GPS www.integratech.com

2D Imaging System for Alternating Magnetic Field Flux

A.A. Aghajanyan, A.A. Hakhoumian, H.K. Melikyan, N.G. Poghosyan, T.V. Zakaryan

Institute of Radiophysics and Electronics, National Academy of Sciences
Alikhanian brs. str. 1, Ashtarak, 0203, Armenia

The aim of this work is to develop and investigate the system for two-dimensional monitoring the RMS value of the alternating magnetic field in the horizontal plane of plasma processing chamber. To increase the measurement speed parallel method is implemented. All designed sensors are unique and have sensitivity approx. $1.8 \cdot 10^{-8}T$. Measurements in the etching chamber allow to monitor the uniformity of the electromagnetic field and allow to adjust it by changing the characteristics of RF transmitter.
Keywords: plasma processing of materials, the magnetic induction

1. Introduction

Plasma processing of semiconductor materials is relatively new technique used for etching and deposition of various materials on a substrate, as well as cleaning and modifying their surface. Plasma processing is used for manufacturing of microelectronic devices, MEMS devices, and for other applications in nanotechnology [1]. Plasma etching has several advantages over other methods of etching (e.g., photolithography). However, in practice, this technique can't be used in all cases. Plasma and phenomena associated with it have greatly complicated nature and are not fully explained yet in terms of existing models.

To generate a plasma for processing the semiconductor products it is required to apply an RF signal to plasma processing chamber filled with an inert gas. The frequencies of required RF signals are ranging from several to tens of MHz. There are two major methods for plasma generation: inductive and capacitive. Two basic problems are necessary to solve while developing plasma processing systems, i.e. RF generator and plasma chamber impedance matching to ensure maximum energy transfer from the generator to plasma chamber, and, the generation of uniform magnetic field in the plasma processing chamber. In order to create a most homogeneous magnetic field in the plasma processing chambers, variety of excitation systems are applied.

The aim of this work is to develop and investigate the system for two-dimensional monitoring the RMS value of the alternating magnetic field in the horizontal plane of plasma processing chamber.

2. Measurement method

To measure the magnetic flux of AC magnetic field in the whole plane of plasma processing chamber it is required to measure magnetic flux in various points of plane under test. It is possible to measure magnetic flux in appropriate points in the plate by applying only a single sensor. The sensor can be fixed to the movable mechanism allowing to move the sensor in the plane. Measuring the magnetic flux in all appropriate points and then applying specific digital processing tools, the whole picture of magnetic field flux distribution is constructed. It is obvious that there is a possibility to increase the magnetic field flux distribution measurement resolution by decreasing the step size of the movable mechanism. Therefore measuring systems based on this method doesn't offer high performance in terms of measurement speed.
To increase the measurement speed parallel method can be used [2,3]. The spatial resolution of such system depends on the number of sensors fixed in appropriate positions in the plane under test. Then sensors array is connected to the multichannel DAQ system, and finally, DAQ system collects data on each clock cycle from all sensors allocated in the plate.

3. System Description

Considering the features, advantages and disadvantages of methods for monitoring the alternating magnetic field in the plasma processing chamber, parallel measurement method is implemented in the developed system. The system consists of magnetic field sensors array, DAQ system and unit for control, processing and visualization. Fig.1 demonstrates the structure of the designed system.

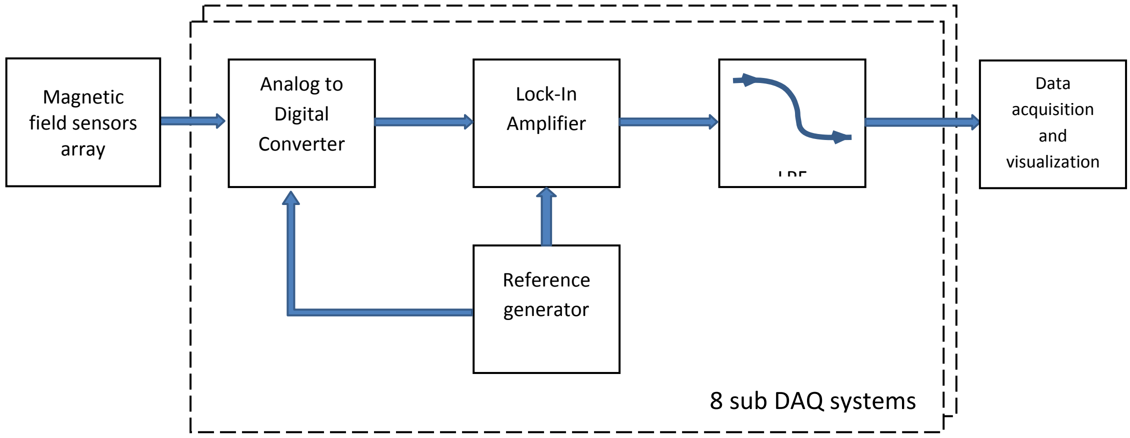

Fig. 1.Block diagram of 2D monitoring system

4. Magnetic field sensors array

To use plasma processing technique in various applications (for example in semiconductor production) it is important to develop tools for investigation of plasma parameters. The most valuable parameters for such systems are temperature, pressure and the uniformity of magnetic field distribution. There are different AC magnetic field measurement methods. One of the most simple and efficient methods uses single loop coil as an AC magnetic field sensor. The principle of operation is based on Faraday's law, stating that the induced electromotive force (EMF) in any closed circuit is proportional to the time derivative of the magnetic flow, limiting by that circuit,

$$V = -N\frac{d\Phi_B}{dt}, \quad (1)$$

where Φ_B is the magnetic flow through the circuit, and N is the number of coils.

The magnetic field sensors array is implemented on a platform of a round shape with 500 mm in a diameter. The sensors array is realized on a 4-layer PCB and consists of 64 single coils. The structure and location of the sensors is shown on Fig. 2. The identity of sensors, the uniformity of the insulator and the PCB zero inclined plane contours relative to the plane of the PCB ensures that measurements are identical for all sensors. The accuracy of performance of the PCB is about few micrometers.

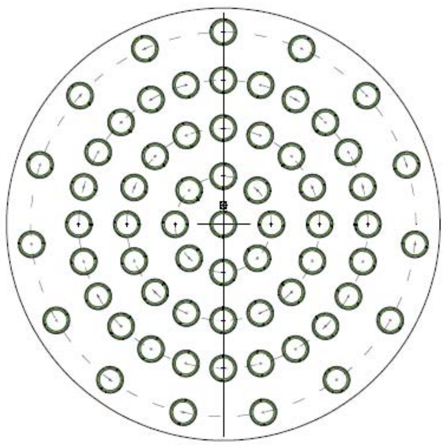
Fig. 2.The structure of magnetic sensors array

5. Data acquisition

Detected signals are transmitted to the data acquisition unit by low loss cables. Data acquisition system consists of 8 data acquisition sub units. One of them is master unit, which provides the whole system with reference signal. Other seven units are slave ones. Each channel has eight analog inputs. The numbers of units is limited only by load capacity of the reference generator. It is possible to connect in parallel additional data acquisition blocks increasing this way the number of sensors. Each subsystem admits up to eight point sensors connection (see Fig.1). Data acquisition unit consists of analog-to-digital converter, reference clock, and microprocessor which implements simultaneous amplification and low pass filtering algorithm.

6. Data processing and visualization

Signals from all data acquisition units flow to processing and visualization software. The number of sensors on plane under test is 64. Under such conditions it is possible to get information only on appropriate points, where coil sensors are placed. It is possible to increase the virtual resolution of the system by special mathematical approximation algorithms in similar systems, e.g. cubic interpolation method. Software performs statistical processing of measured data for estimating the homogeneity of a magnetic field (Fig. 3).

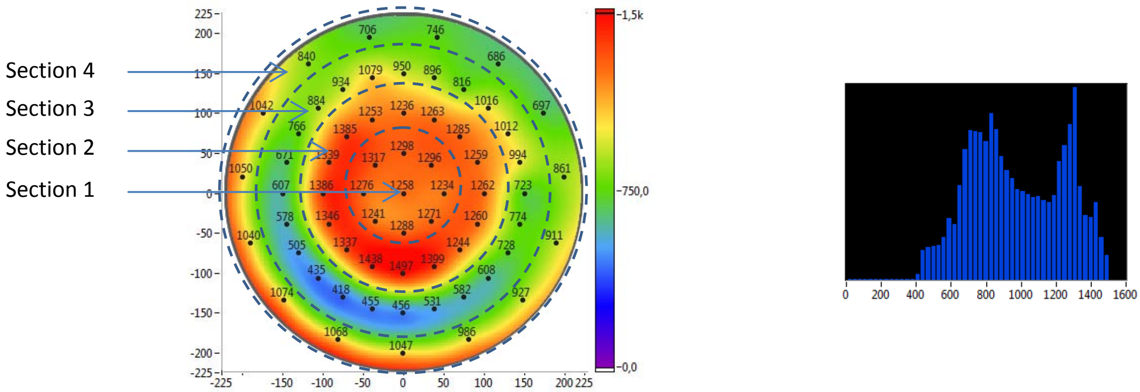

Fig. 3.Locations of sections on the plane under test and normalized histogram of the measurement data

Designed software generates cross-section for any arbitrary angle. Fig.4 demonstrates such cross-sections for 0, 90 and 180 degrees respectively.

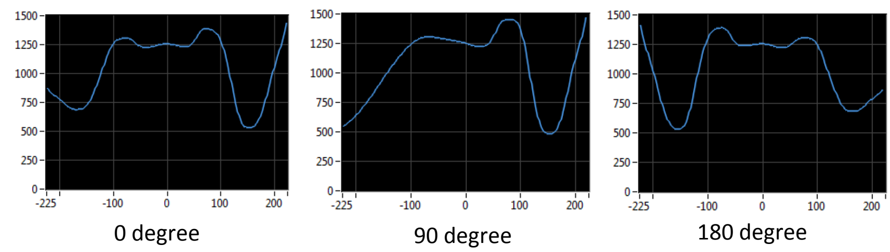

Fig. 4.Cross-sections for different angels

And finally, exponential averaging is performed before visualization.

7. Evaluation of sensitivity of the sensors and the measurement results.

As already noted, sensor array consists of 64 single-sensors, realized on a multilayer PCB using a photolithography technology that provides the identity of all sensors. According to (1), the alternating magnetic fields inducts an EMF at the free ends of each sensor equal to

$$\varepsilon = -N\frac{d\Phi_B}{dt}, \tag{2}$$

where Φ_B is the magnetic flow, through the circuit, and N is the number of coils.
The magnetic field flow through the sensors contour is equal to

$$\Phi_B(t) = BA\cos\omega t \tag{3}$$

where B is the magnetic induction, A is the area of the sensor, and ω is the angular frequency.
Output signal of each sensor is applied to the respective detector and is proportional to RMS value of the input signal

$$\varepsilon_{\mathrm{RMS}} = \frac{1}{\sqrt{2}}BA\omega. \tag{4}$$

Then the signal is applied to analog-to-digital converter with 12 bit resolution having dynamic range of

$$\varepsilon_{RMS_{max}} = FSR_{ADC} = 3V, \quad (5)$$

where FSR_{ADC} is the full scale range of analog-to-digital converter

$$B_{RMS_{max}} = \frac{\varepsilon_{RMS_{max}}}{2\pi Af}, \quad (6)$$

where f is the frequency of RF generator.

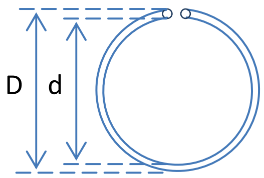

Fig. 5.Geometry of the magnetic field single sensor

$$A \approx 4.7 \cdot 10^{-4} m^2$$

The sensitivity of the measuring channel to RMS value of the magnetic field for 12 bit analog-to-digital converter is equal to

$$B_{RMS_0} = \frac{B_{RMS_{max}}}{2^{12} - 1} \approx 1.8 \cdot 10^{-8} T$$

The RF signal feds the transmitter antenna located in plasma processing chamber. Antenna consists of two antennas fed through a power splitter, the division factor (C.R.) varies from 0.3 to 3. Typical results of measurements at different current ratio of antennas are shown in Fig. 6. This way it is possible to achieve maximum uniformity of the electromagnetic field in the plasma processing chamber by geometric displacement of transducer, and changing its shapes.

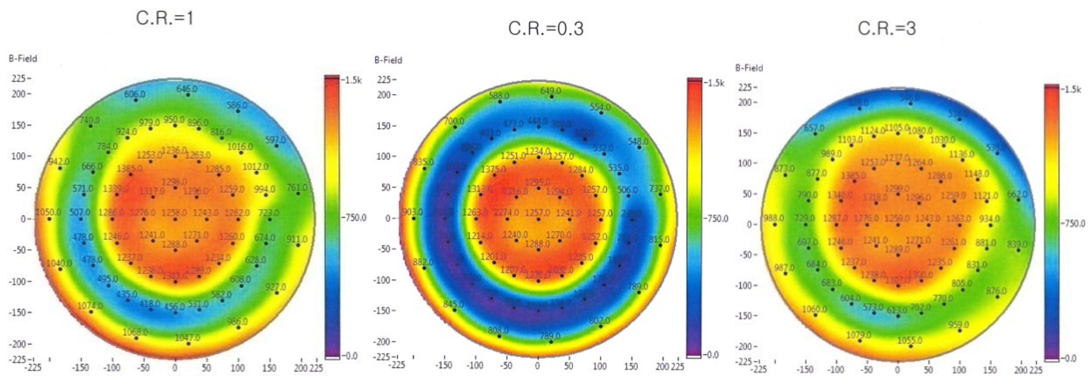

Fig. 6.Typical measurement results at different current ratios.

8. References

[1] Kakiuchi, Hiroaki - Atmospheric-pressure low-temperature plasma processes for thin film deposition,Journal of Vacuum Science & Technology A: Vacuum, Surfaces, and Films, 32, no.3 (2013), pp. 030801 - 030801-16

[2] Black, D.C., Mayo, R.M.– High sensitivity, inductively coupled miniature magnetic probe array for detailed measurement of time varying magnetic field profiles in plasma flows, Review of Scientific Instruments, 67, no.4 (1996), pp.1508-1516

[3] Kanamaru, Yuki - Magnetic probe array with high sensitivity for fluctuating field, Review of Scientific Instruments, 78, no.3 (2007), p. 036105

Preparation of Bi-YIG thin films by the MOD method for magneto-optical applications

O. Galstyan[1], Y. Park[1], J. Park[1], S. Kim[1], J. Kim[1],K. Lee[1],
A. Babajanyan[2], G. Berthiau[3],B. Friedman[4]

[1]*Department of Physics & Basic Science Institute for Cell Damage Control, Sogang University, Seoul 121-742, Korea*
[2]*Department of Radiophysics, Yerevan State University, A. Manoogian 1, Yerevan 0025, Armenia*
[3] *IREENA, 37 Boulevard de L'iniversite, BP-406, 44602 Saint-Nazaire Cedex, France*
[4]*Department of Physics, Sam Houston State University, Huntsville, Texas 77341, USA*

$Bi_xY_{1-x}Fe_5O_{12}$, (x=2) thin films with a thickness of about 0.8 μm were prepared on glass and garnet substrates by using a metal-organic decomposition method (MOD).The magnetization data indicate that the films have in plane easy axis. Films were used as indicators in the magneto-optical visualization system.We imaged the magnetic domains of magnetic materials and magnetic fields created by electromagnet.

1. Introduction

Bismuth substituted yttrium iron garnet ($Bi_xY_{1-x}Fe_5O_{12}$) is a material of choice for the magneto-optical and microwave applications because of its high Faraday rotation angle,high transmittance in the visible and infrared light regions, smallest ferromagnetic resonanceline width and controllable magnetic properties[1].

One of the main applications of garnet materials is in magneto-optical imaging system. By using Faraday rotation phenomena garnet materials for example imaging of magnetic vortex in semiconductor materials and magnetic domains of general magnetic cards become possible[2, 3].

To use $Bi_xY_{3-x}Fe_5O_{12}$materials in magneto-optical imaging system as indicators one need to deposit them on substrates to prepare garnet thin films.Finally we deposited Al mirrors on garnet layer[3].

There are several preparation techniques of garnet thin films, such as liquid phase epitaxy (LPE) [4], radio-frequency magnetron sputtering method [5], pulsed laser deposition (PLD) [6], the sol-gel method [7], and the metal-organic decomposition method (MOD) [8]. For the preparation of garnet films we used the MOD method because it is inexpensive, simple, and allows precise control of the composition of the MOD solution and the formation over the large area. Furthermore, in comparison with the melting point of Bi-YIG the MOD method requires relatively low temperature, so this property gives us the possibility to make thick and multilayer structures on a glass substrate [9].

In this paper we present the details of preparation of ($Bi_xY_{3-x}Fe_5O_{12}$)films by the MOD method on glass and garnet substrates. Samples used as indicator films for the magneto-optical imaging system. We discuss the magnetic, optical and magneto-optical properties of the samples.

2. Experiment

Figure 1 (a) shows the schematic of the MOD process. All thermal treatments were done in air. We prepared garnet films by spin coating of a metal-organic solution which chemical composition is $Bi_2Y_1Fe_5O_{12}$ on a Corning XG glass (Bi-YIG/GLASS) and on Gadolinium Gallium Garnet (Bi-YIG/GGG) substrate at 3000 rpm for 30 seconds. The deposited solution was dried at 70 °C for 30 minutes. After drying, we pre-annealed the samples at 450 °C for 30 minutes in order to decompose carboxylates into metal oxides and bring them to the amorphous phase. These processes have been repeated 20 times to achieve the thicker films with thicknesses of 0.8 μm. Finally, samples prepared on glass substrate were post-annealed in a furnace at 620 °C for 3 hours for the final crystallization process. Samples prepared on GGG substrate were post-annealedat 750 °C for 3 hours[8, 10].

Figure 2 shows schematic diagram of magneto-optical imaging setup. As a light source we used LED which has a dominant wavelength of 530 nm. Light passes through the polarizer, beam splitter and indicator film. Film is placed in front of the surface of a magnetic field source. Because of the parallel magnetic field along the light propagation direction in garnet medium, rotation of the plane of polarization: Faraday rotation occurs [11].

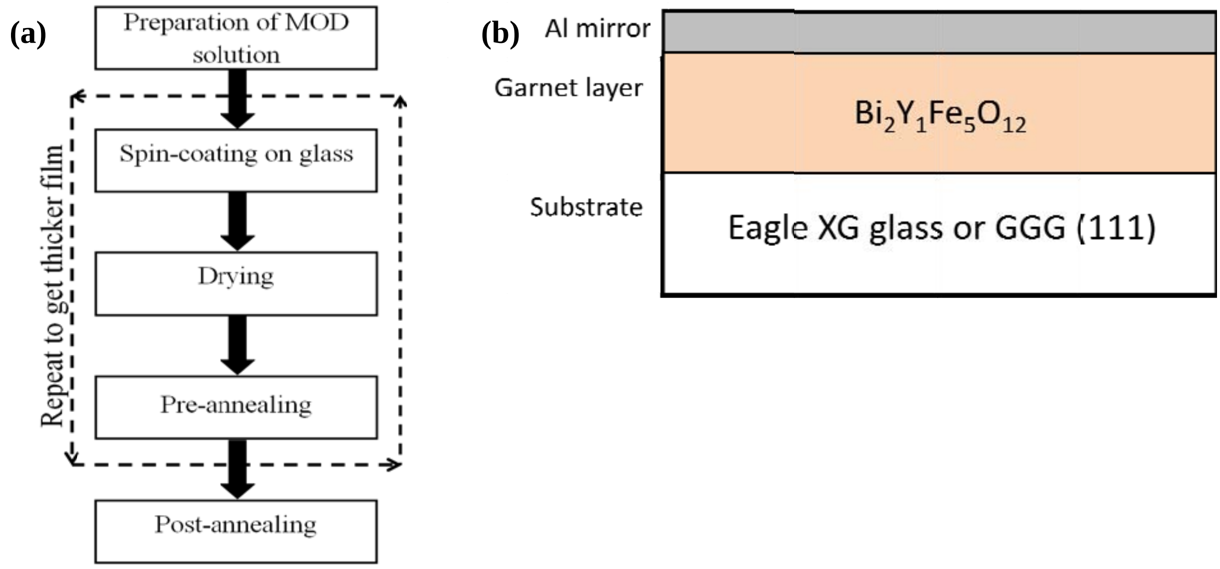

Fig. 1.(a) The schematic of the MOD procedureand (b) prepared indicator film.

After reflection from Al mirror light beam crosses garnetlayer one more time doubling the rotation angle in this way. The Faraday rotation angle depends on the magnetic field strength. Reflected light received by the CCD camera through the beam splitter and analyzer. Polarizer and analyzer are set in crossed position. If the analyzer will be rotated at an (π/2–θ) compared to the polarizer the measured light intensity will be given by the following equation:

$$I = I_0 sin^2(\theta - \theta_F) \approx I_0(\theta - \theta_F)^2, \quad (1)$$

where$I$ is the detected light intensity, $I_0$is the initial light intensity, and θ_F is Faraday rotation angle. We need to take into account that light passes film for two times. Then light intensity is transformed by CCD matrix into an electric signal which is digitized and displayed on the monitor.

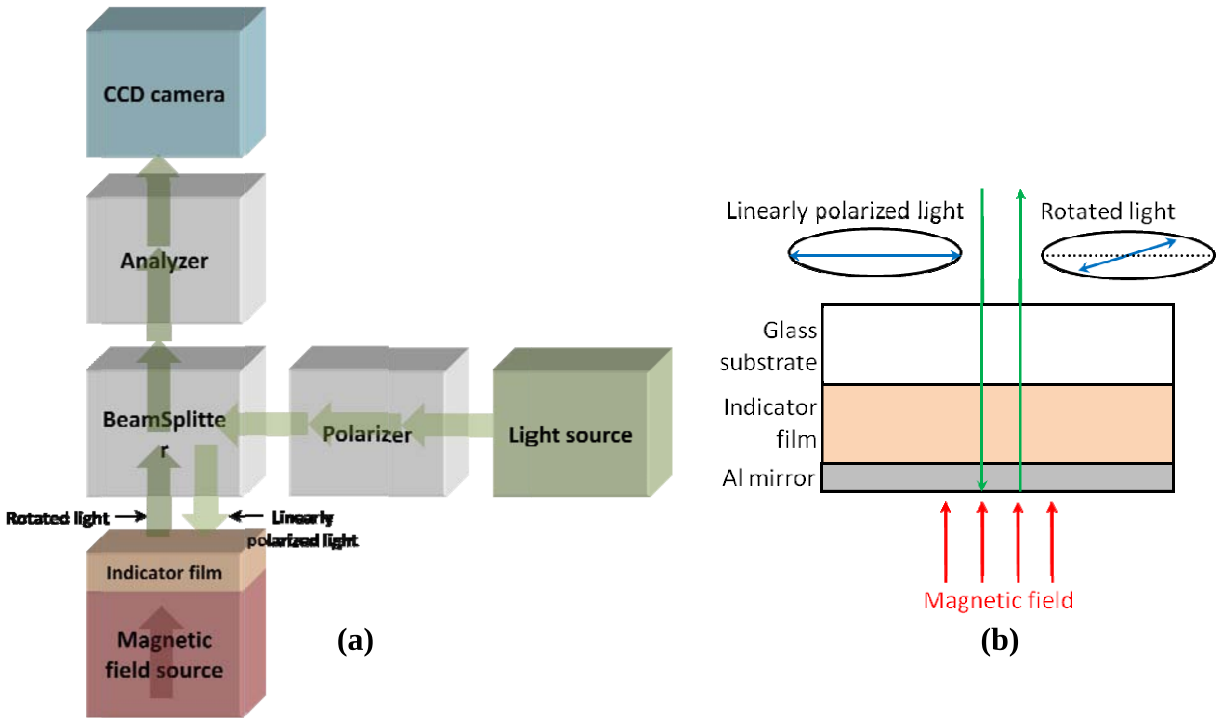

Fig. 2.(a) Schematic diagram of the magneto-optical imaging system and (b) the indicator film.

The magnetic and optical properties of Bi-YIG films were investigated by vibrating sample magnetometer (VSM) and by a UV-vis spectrometer. Magneto-optical images of magnetic field created by electromagnet and magnetic domains of general magnetic card have been detected using indicator thin films.

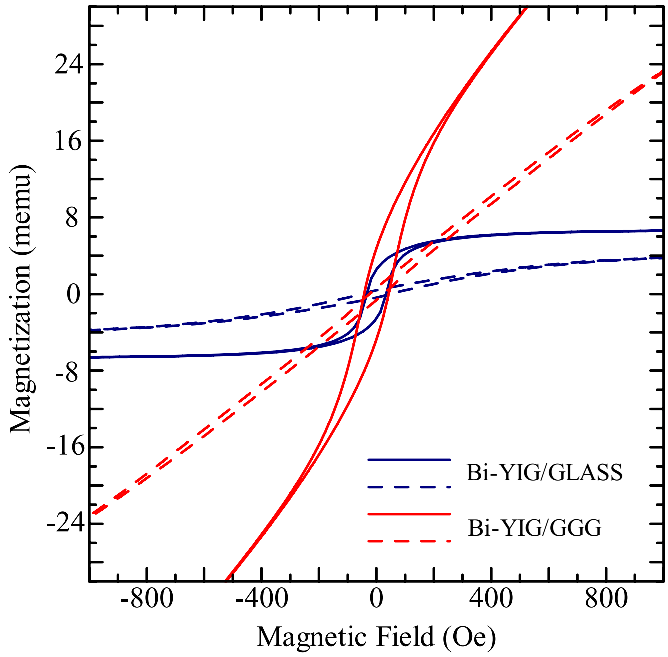

Fig. 3.Magnetization loops for the prepared films under in-plane (solid lines) and out-of-plane (dashed lines) magnetic fields.

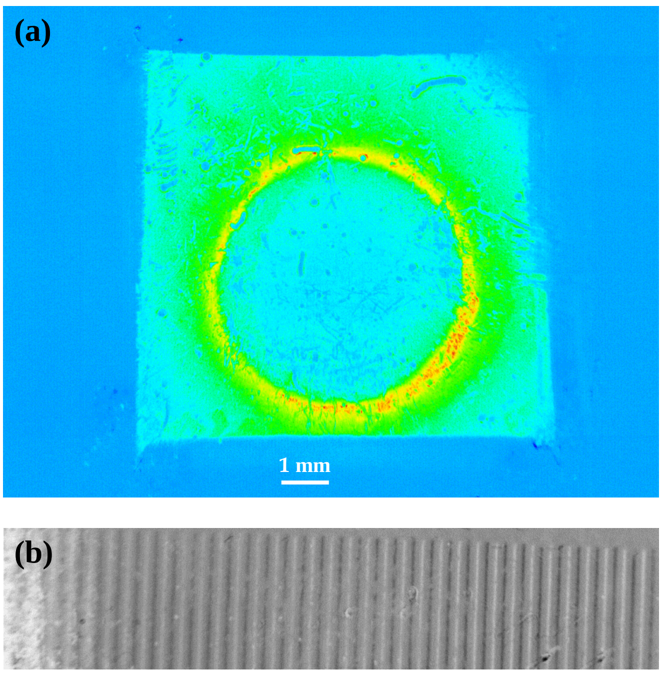

Fig. 4.Magneto-optical images of magnetic field distribution created (a) by electromagnet and (b) the recordingpatterns on credit card.

3. Results and discussion

Figure 3 shows magnetic loops of prepared samples which were measured under in- plane and out-of-plane magnetic field. Results indicate that garnet thin films prepared by MOD method on glass and garnet substrate have in-plane magnetic anisotropy. We came to this conclusion because films saturated at weaker magnetic fields when it applied parallel to the surface of the film [12]. Due to the substrate sample prepared on garnet substrate has paramagnetic component.

Samples prepared on garnet substrate have higher optical absorption comparing to samples prepared on glass substrate. We assigned these results to the preparation conditions of the films. There is a need of further research to find appropriate heat treatment schedule of MOD process for Bi-YIG/GGG samples. After the measurement of Faraday rotation angles of the samples we observed that sample Bi-YIG/GLASS has higher magneto-optical figure of merit comparing to the sampleBi-YIG/GGG. That's why we used sample Bi-YIG/GLASS for magneto-optical imaging experiments. Faraday rotation angle measurements have done using method discussed in ref. 13.

Figure 4(a) shows magneto-optical images of magnetic field distribution created by electromagnet. We used magnetic field source which has circular shape. It can be noticed in images detected by CCD camera. Presented image is the result of averaged 1000 images with 1024x768 resolutions. Fig. 4 (b) shows magnetic domains of general magnetic card. The detailed explanation of the imaging of magnetic domains is presented in Ref [3].

4. Conclusion

We succeed in preparation of garnet thin films by the MOD method for magneto-optical applications. Heat treatment schedule and preparation conditions have been discussed. Magnetic properties of the films indicate that all samples have in-plane magnetic anisotropy. Detection of magnetic fields and magnetic domains become possible using prepared garnet films as indicators in magneto-optical imaging system.

Acknowledgements

This work was supported by a Sogang University Special Research Grant 2009 (201314002), Basic Science Research Program through the National Research Foundation of Korea(2009-00 93822 & 2014R1A1A2A16055772), and Parts & Materials International Collaborative R&D Program funded by the Ministry of Knowledge Economy of Korea (MKE: N0000481).

References

1. T. Aichele, A. Lorenz, R. Hergt, P. Görnert, Cryst. Res. Technol. 38 (2003)575.
2. M. R.Koblischkat, R. J.Wijngaarden, Supercond. Sci. Technol. 8 (1995) 199.
3. H. Lee, T. Kim, S. Kim, Y. Yoon, S. Kim, A. Babajanyan, T. Ishibashi, B. Friedman, K. Lee, J. Magn. Magn. Mater. 322(2010) 2722.
4. P. Görnert, T. Aichele, A. Lorenz, R. Hergt, J. Taubert, Phys. Stat. Sol. A 201(2004) 1398
5. Q. Yang, Z. Huaiwu, L. Yingli, W. Qiye, IEEE Trans. Magn. 43(2007) 3652.
6. H. Hayashi, S. Iwasa, N. J. Vasa, T. Yoshitake, K. Ueda, S. Yokoyama, S. Higuchi, H. Takeshita, M. Nakahara, Appl. Surf. Sci. 197(2002) 463.
7. J. L. Rehspringer, J. Bursik, D. Niznansky, and A. Klarikova, J. Magn. Magn. Mater. 211 (2000) 291
8. H. Lee, Y. Yoon, S. Kim, H. K. Yoo, H. Melikyan, E. Danielyan, A. Babajanyan, T. Ishibashi, B. Friedman, K. Lee, J. Cryst. Growth 329(2011) 27.
9. T. Ishibashi, T. Yoshida, T. Kobayashi, S. Ikehara, T. Nishi, J. Appl. Phys. 113 (2013)17A926.
10. T. Ishibashi, A. Mizusawa, N. Togashi, T. Mogi, M. Houchido, K. Sato, J. Cryst. Growth 275 (2005) 2427.
11. M. V. Valeiko, P. M. Vetoshko, R. I. Kononov, A. Ya. Perlov, M. Yu. Sharonov, A. Yu. Toporov, , IEEE Trans. Magn. 31,(1995) 4293.
12. R.M. Grechishkin, M.Yu. Goosev, S.E. Ilyashenko, N.S. Neustroev, J. Magn. Magn. Mater. 157, (1996) 305.
13. O. Galstyan, H. Lee, S. Lee, N. Yoo, J. Park, A. Babajanyan, B. Friedman, K. Lee, J. Magn. Magn. Mater. 366 (2014) 21.

Parametric investigation of low-frequency noise in networks of carbon nanotubes

V. Avetisyan[1],T. Makaryan[2,3],and A. Makaryan[2]

[1]*Physics Department, Yerevan State University, 0005 Yerevan, Armenia*
[2]*Radiophysics Department, Yerevan State University, 0005 Yerevan, Armenia*
[3]*Instutute of Radiophysics and Electronics,0203 Ashtarak, Armenia*

Efficient exploitation of carbon nanotubes in the electronics requires knowledge of their noise parameters. We studied the dependence of these parameters for single walled carbon nanotube (SWNT) thin film in the range of 0-130V and 0-160kHz. We distinct two 1/f and shot type noise characters in the low-frequency up to 20 kHz and in the frequency range up to 160 kHz, respectively. Based on noise dispersion dependence on the applied voltage we attribute its origin to the charge carrier tunneling through the tube-tube contacts. The results can be useful for the applications of thin film nanotubes with disordered networks in sensorics and communication systems.

1. Introduction

SWNTshold potential for applications in electronics and photonics. Some of the most promising ones are chemical[1] and biological[2] sensors , transparent electrodes[3,4], ultrafast transistors[5], opto-electronic devices[6], connectors[7]. Nanotubes can be applied also for the generation[8,9] and detection[10] of THz radiation thanks to nonlinear current-voltage characteristics. Various manifestations of electronic noise can however significantly impede the development of practical applications of SWNTs. Alongside with the ubiquitous thermal and shot noises, the flicker (or 1/f) noise has also a large impact in nano tubes especially in the low-frequency range.[11-13] This noise is observed in other C-based systems including grapheme[14]. By getting use of stochastic resonance, it is possible to achieve noise-enhanced signal detection in the subthreshold region in single[15] and multiple nanotubes[16] as well as bi-layer grapheme[17]. This task is however more challenging in disordered SWNT thin films be cause of the lack of system symmetry. Moreover, the order of 1/f noise can be especially higher in SWNT networks due to the charge tunneling between the chaotically distributed nanotubes.[18]It is nevertheless desirable to achieve low-noise devices based on SWNT disordered films owing to their relatively easy synthesis possibility directly on transparent dielectric substrates.

The dependency of the1/f noise and resistivity of SWNT thin films on temperature is correlated with the fluctuation-induced tunneling.[19]Furthermore, the amplitude of the noise is scaled with the geometry/thickness of the film and device. [20,21]For the efficient application of SWNT thin films in ultrafast electronics it is necessary to understand the combination of I-V, temperature and noise characteristics.

In this contribution, the current-voltage and noise characteristics of a SWNT thin film was investigated. The heat-induced effect on nonlinearity of I-V characteristics was revealed. The dependence of noise dispersion on applied voltage is obtained. The 1/f noise arises in a wide bandwidth (up to 20 kHz) due to the two-dimensional nature and complex mechanism of conductivity. The knowledge of these characteristics is essential for the efficient application of SWNT thin films in fast electronics.

2. Experimental Methods

A 95.9% transparent SWNT film is grown on 1 cm^2 quartz substrate via catalytic chemical vapor deposition method using iron nano particles as a catalyst. Fig. 1 illustrates the scheme of the experimental set-up used for measurements of the SWNT thin film current-voltage characteristics and noise, in time- and frequency-domains.

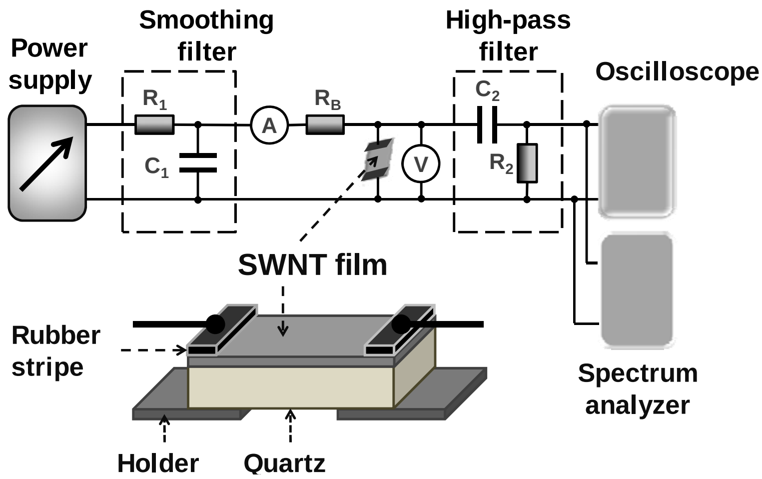

Fig. 1. Schematic cartoon of the designed system for noise/current measurements. In the inset the sample is depicted schematically.

To minimize the impact of external noise on the measurement results, the voltage of the DC power supply to the sample is fed through the smoothing filter R_1C_1(Fig. 1). Ballast resistor R_B acts as a load of noise voltage which arose in the nano tubes. The sample is connected by conducting rubber stripes attached onto the surface of SWNT film by conductive glue (inset of Fig. 1). The noise voltage after filtering of the DC component by the high-pass filter $C_2R_2$is fed to an oscilloscope and a spectrum analyzer. The entire system is electromagnetically screened in order to avoid the influence of external noise.

3. Results and Discussion

The results of the measurements on the SWNT film are summarized in Fig. 2. For I-V characteristics determination, we carry out measurements (Fig. 2a) in two ways: fast (triangles) and slow (diamonds). In the fast case, we avoid giving enough time for the SWNT film to warm up considerably by the heat induced by the external voltage. In contrary, sample resistance starts to increase during the slow measurements initially due to the increase in temperature. After some time (~1 min.), the temperature of the sample begins to stabilize. At complete temperature stabilization the sample resistance seizes fluctuating. The fast and slow measurements (Fig. 2a) appear to be considerably different in the 20-120 V range. Hence, the temperature effect in this range plays an important role. In contrary, the induced temperature is not high enough to be critical in the ≤ 20 V range, where the induced-heat effect causes only ~2 % current variation. The differential resistances of the sample calculated for fast (slow) measurements at lowest and highest voltages are ~27 (20) and ~9 (18) kΩ, respectively. Thus, the initial and final resistances differ only by ~10 % in slow measurements case, whereas this difference reaches 3 times for fast ones. Hence, the increased temperature hinders the nonlinearity of the I-V characteristics of the SWNT film. This effect could be applied for THz generation from such a SWNT thin film by optical rectification with ultra-short laser pulse pumping.[22,23]

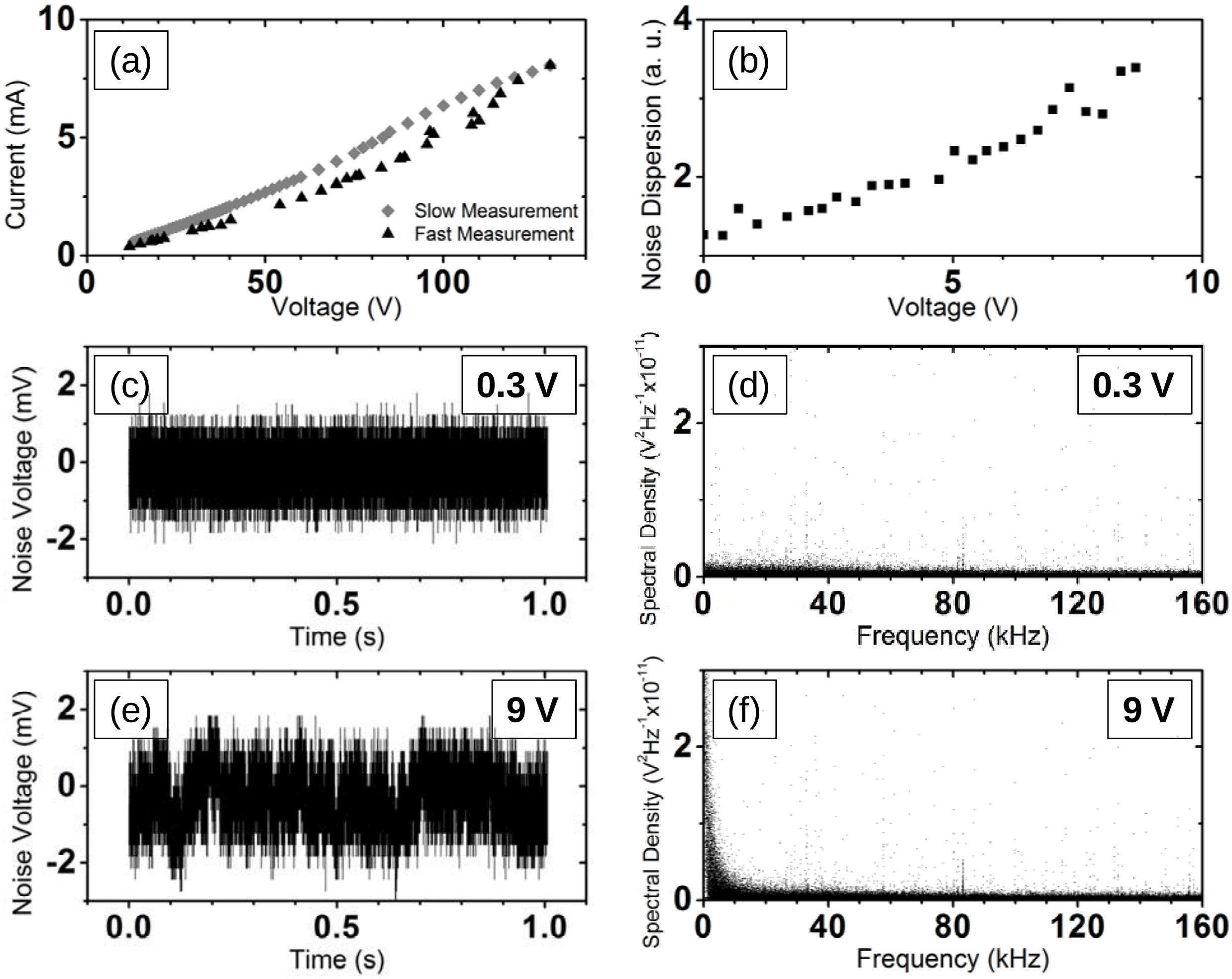

Fig. 2. (a) Current-voltage dependence of 95.9% transparent SWNT thin film on quartz substrate measured (slow measurements as triangles, and fast measurements as diamonds) by the set-up described in Fig. 1. (b) Noise dispersion dependence on voltage in the range up to 9 V. Noise amplitude in time-domain collected for 1 s at 0.3 (c) and 9 (e) V applied bias voltage, and their corresponding power spectra (d and f) collected in the frequency range up to 160 kHz.

To assess the dependence of the SWNT thin film noise characteristics on the applied bias voltage (Fig. 1), for each value of the bias voltage the temporal behavior and noise spectrum are simultaneously recorded by an oscilloscope and a spectrum analyzer (Fig. 1). Then, based on these data we calculate the corresponding variance of the noise (Fig. 2b). The analysis of Fig. 2a and b reveals that the dispersion is proportional to the current in the low voltage regime (≤ 10 V), which indicates its shot character.

Variation of noise in time at the bias voltages 0.3 and 9 V are presented in Fig. 2c and e, respectively, with their corresponding spectra in Fig. 2d and f. The emergence of low-frequency noise component at a bias voltage of 9 V is clearly seen in Fig. 2e. This additional noise, whose power is increased by increasing the bias voltage, has 1 / f character in the low frequency range (20 kHz), as evident in Fig. 2f. The increasing of the bias voltage does not alter the high-frequency part (20-160 kHz) of the noise spectrum.

4. Conclusion

It was determined that if bias voltage is applied, there is considerable noise that has 1/f characteristics up to the 20 kHz range in a carbon nano tube horizontal thin films deposited on quartz substrate. In low voltage regime the dispersion of noise is proportional to the current, which indicates its shot character.

It was also experimentally investigated the current-voltage dependence of this SWNT film in the range of 0 to 120 V. The nonlinear nature of I-V characteristics was demonstrated. We argue that this nonlinearity could be due to the tunneling of charge carriers between neighboring nano tubes. The film shows increase of non-linear characteristics during instantaneous measurement which suggests its possible application for puls-pumped THz generation, frequency conversion, etc. These findings can be useful for controlling the noise for the efficient vertical downscaling of the conventional electronics systems.

5. Acknowledgements

The authors thank A. Harutyunyan and G. Chen from Honda Research Institute USA Inc. for SWNT and its characterization support and for valuable discussions.

6. References

[1]E. S. Snow, F. K. Perkins, E. J. Houser, S. C. Badescu, and T. L. Reinecke, Science **307,** 1942 (2005).
[2]M. Bhattacharya, S. Hong, D. Lee, T. Cui, and S. M. Goyal, Sensors and Actuators B: Chemical **155,** 67 (2011).
[3]C. Wang, J.-C. Chien, K. Takei, T. Takahashi, J. Nah, A. M. Niknejad, and A. Javey, Nano Letters **12,** 1527 (2012).
[4]J. van de Lagemaat, T. M. Barnes, G. Rumbles, S. E. Shaheen, T. J. Coutts, C. Weeks, I. Levitsky, J. Peltola, and P. Glatkowski, Applied Physics Letters **88** (2006).
[5]S. Kivistö, T. Hakulinen, A. Kaskela, B. Aitchison, D. P. Brown, A. G. Nasibulin, E. I. Kauppinen, A. Härkönen, and O. G. Okhotnikov, Optics Express **17,** 2358 (2009).
[6]J. Kyoung, E. Y. Jang, M. D. Lima, H.-R. Park, R. O. Robles, X. Lepró, Y. H. Kim, R. H. Baughman, and D.-S. Kim, Nano Letters **11,** 4227 (2011).
[7]P. Jarosz, C. Schauerman, J. Alvarenga, B. Moses, T. Mastrangelo, R. Raffaelle, R. Ridgley, and B. Landi, Nanoscale **3,** 4542 (2011).
[8]O. V. Kibis, M. Rosenau da Costa, and M. E. Portnoi, Nano Letters **7,** 3414 (2007).
[9]Z. Zhong, N. M. Gabor, J. E. Sharping, A. L. Gaeta, and P. L. McEuen, Nat Nano **3,** 201 (2008).
[10]X. He, N. Fujimura, J. M. Lloyd, K. J. Erickson, A. A. Talin, Q. Zhang, W. Gao, Q. Jiang, Y. Kawano, R. H. Hauge, F. Léonard, and J. Kono, Nano Letters **14,** 3953 (2014).
[11]Y. An, H. Rao, G. Bosman, and A. Ural, Applied Physics Letters **100** (2012).
[12]R. A. Sayer, J. D. Engerer, N. S. Vidhyadhiraja, and T. S. Fisher, Journal of Applied Physics **113** (2013).
[13]R. Lu, R. Kamal, and J. Z. Wu, Nanotechnology **22,** 265503 (2011).
[14]A. A. Balandin, Nat Nano **8,** 549 (2013).
[15]I. Lee, X. Liu, Z. Chongwu, and B. Kosko, Nanotechnology, IEEE Transactions on **5,** 613 (2006).
[16]Y. Hakamata, Y. Ohno, K. Maehashi, S. Kasai, K. Inoue, and K. Matsumoto, Journal of Applied Physics **108** (2010).
[17]M. Kocaoglu, B. Gulbahar, and O. B. Akan, Nanotechnology, IEEE Transactions on **PP,** 1 (2014).
[18]H. Ouacha, M. Willander, H. Y. Yu, Y. W. Park, M. S. Kabir, S. H. M. Persson, L. B. Kish, and A. Ouacha, Applied Physics Letters **80,** 1055 (2002).
[19]A. Behnam, A. Biswas, G. Bosman, and A. Ural, Physical Review B **81,** 125407 (2010).
[20]V. K. Sangwan, A. Behnam, V. W. Ballarotto, M. S. Fuhrer, A. Ural, and E. D. Williams, Applied Physics Letters **97** (2010).
[21]S. Soliveres, J. Gyani, C. Delseny, A. Hoffmann, and F. Pascal, Applied Physics Letters **90** (2007).
[22]Z. Zhong, N. M. Gabor, J. E. Sharping, A. L. Gaeta, and P. L. McEuen, Nat Nano **3,** 201 (2008).
[23]G. M. Mikheev, R. G. Zonov, A. N. Obraztsov, and Y. P. Svirko, Journal of Experimental and Theoretical Physics **99,** 942 (2004).

One-step electrodeposition technology for fabrication of CuInSe films on molybdenum coated perlite substrates

L.A. Harutyunyan

Institute of Radiophysics and Electronics, NAS RA, Ashtarak, Armenia
e-mail: hlevon1989@gmail.com; tel: (+374) 55 466001;fax:(+374) 232 33770.

The technology of obtaining of CuInSe films on molybdenum coated perlite substrates by one-step electrodeposition from an aqueous acidic solution containing $CuCl_2$, $InCl_3$, H_2SeO_3 and Na-citrate (as complexing agent) is reported. Optical studies and energy-dispersive X-ray microanalysis were performed for as-deposited CuInSe layers.

Problem statement and current status

Despite the fact that the development of solar energy involves intensive study materials and technologies through which will be implemented effective demand for photovoltaic modules, at the present stage is attractive as portable application and integration of solar modules in the architecture of buildings. Using of thin-film technology and expediency for the manufacture of semiconductor solar cells is well-described in [1-3]. For example, thin-film silicon technology compares favorably to the classical silicon technology because amorphous hydrogenated silicon can be deposited on a glass substrate with large size and almost any form. This makes it possible to produce thin-film solar modules on glass panels used for the facing of buildings of various purposes. However in our view, as substrates for solving of many applications may be more appropriate glass ceramics. Modern types of ceramics (including glass ceramics) are sometimes divided into two groups - structural and functional. With respect to the glass perlite, which belongs to the structural group of ceramics, has certain advantages: allows the use of higher temperature for film deposition; perlite substrate thickness can be decreased to 300 microns, using standard silicon processing methods of grinding and polishing technology; integration in building elements (e.g. solar roof shingles).

Background and Experiment

Earlier we made solar cell on the perlite substrate by application of polycrystalline CIGS film with thickness of about 1.7 microns by using of vacuum co-evaporation of copper, gallium, indium and selenium [4, 5]. Solar cell efficiency was more than 10% with 48.4% fill factor and open circuit voltage 518 mV. This result can be considered as an important step towards the development of semiconductor solar cells, integrated into building elements. However, despite of the flexibility, vacuum technologies are costly. In this work for production of CIS absorber layer electrodeposition technology was used, which is the part of overall technological way of creation solar cells (see fig.1).

CIS samples were single bath electrodeposited using a Potentiostat/Galvanostat IPC system (see fig.2) in a simple two-electrode cell configuration with Mo coated perlite substrates as a working electrode (area 10 mm × 10 mm), and a palatine sheet as the counter electrode. Deposition was carried out at a room temperature, without stirring the solution in a galvanostat mode. For optical analyses, CIS samples were grown on transparent conducting fluorine tin oxide (FTO) substrates also. The deposition bath was acidic (pH ~ 2) chlorine-based solution containing 10 mM $CuCl_2$, 20 mM $InCl_3$, 20 mM H_2SeO_3 and Na-citrate as a supporting salt, dissolved in de-ionized water.

The thickness of deposited films was measured with profilometer AMBIOS XP-2.Independent measurements of transmittance (T) and reflection (R) of films were made at the room temperature by using a Filmetrics F20 spectrometer (spectral range 400-1000 nm) in the mode of normal incidence of light. Studies of elemental composition were performed with the scanning electron microscope VEGA TS 5130MM. Crystalline structure of films was studied by the high-energy electron diffraction method in a reflection regime (accelerating voltage 75 kV).

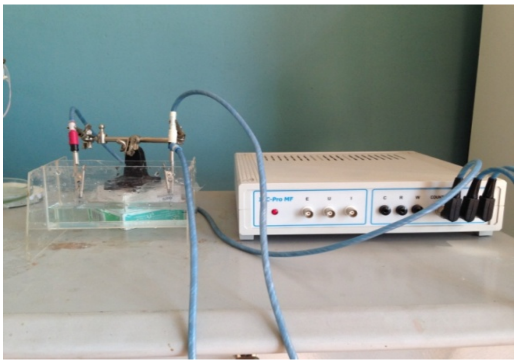

Fig.1

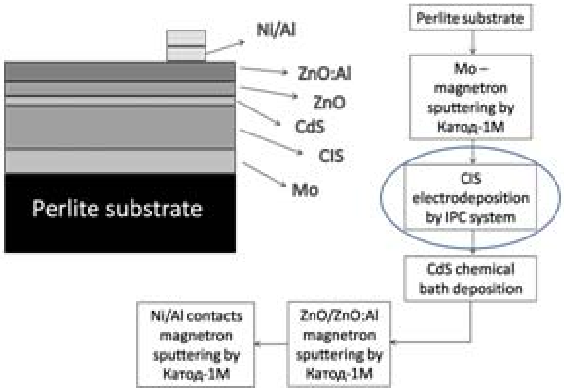

Fig.2

Results and Discussion

From measurements of thickness by profilometer it was found that the film growth rate is 3 nm/min. Nanoscale (<100nm) films of $CuInSe_2$ were investigated in this work. Electron-diffraction investigations shows that obtained films have a polycrystalline structure independent of their thickness. Energy-dispersive X-ray microanalysis of as-deposited films shows the presence of close to stoichiometric $CuInSe_2$ and non-stoichiometric $Cu_{2-x}Se$ phases (x~0.2). The obtained films have high-absorption in the investigated wavelength range (A/d ~ 2×10^{5} cm^{-1}). Fig. 3 shows the dependence of absorption A (A = 1-R-T) from energy of incident light (film thickness is 50 nm). Such absorption dependence in the range of 2.0-2.8 eV is associated with the presence of $Cu_{2-x}Se$ phases.

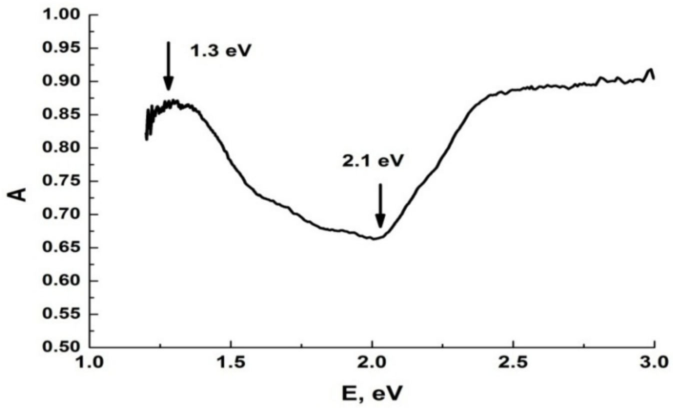

Fig.3

Conclusion

The result of research shows that for obtaining CIS absorption layer on Mo coated perlite substrate it is possible to substitute costly vacuum technologies by low-cost electrodeposition technique.

References

1. Yoshihiro Hamakawa. Thin-Film Solar Cells: Next Generation Photovoltaics and Its Applications. Springer, 2004.

2. Jef Poortmans, Vladimir Arkhipov. Thin Film Solar Cells: Fabrication, Characterization and Applications. John Wiley & Sons, 2006.

3. Гременок В.Ф., Тиванов М.С., Залесский В.Б. Солнечные элементы на основе полупроводниковых материалов. Минск: Изд. Центр БГУ, 2007.

4. В.Б.Залесский, В.М.Кравченко, Т.Р.Леонова, А.М.Поликанин, Е.П.Зарецкая, С.Г.Петросян, А.М.Кечиянц. CIGS-солнечные элементы с эффективностью 10,1% на перлитных стеклокерамических подложках. Проблемы физики, математики и техники, 2013.

5. S.G.Petrosyan, V.H.Babayan, A.S.Musayelyan, L.A.Harutyunyan, V.B.Zalesski, V.M.Kravchenko, T.R.Leonova, A.M.Polikanin, A.A.Khodin. Thin-film solar cells on perlite glass-ceramic substrates.The European Physical Journal Applied Physics, 2013.

Characterization of F16CuPc field-effect transistors fabricated at various heat-treatment conditions

A. Babajanyan[1], N. Yoo[2], S. Lee[2], O. Galstyan[2], J. Park[2],
Y. Lee[2], K. Lee[2], B. Friedman[3], G. Berthiau[4]

[1] *Department of Radiophysics, Yerevan State University, A. Manoogian 1, Yerevan 0025, Armenia*
[2] *Department of Physics & Basic Science Institute for Cell Damage Control, Sogang University, Seoul 121-742, Korea*
[3] *Department of Physics, Sam Houston State University, Huntsville, Texas 77341, USA*
[4] *IREENA, 37 Boulevard de L'iniversite, BP-406, 44602 Saint-Nazaire Cedex, France*

We analyzed the performance of $F_{16}CuPc$ field-effect transistor (FET) prepared at the different substrate heating temperatures where the active layer was grown by thermal evaporation method. A FET with $F_{16}CuPc$ active layer was fabricated at 25 °C (RT), 65 °C, 150 °C, and 200 °C in situ substrate temperatures. As the heating temperatures increased from RT to 200 °C, the FET electric properties were improved while the grain sizes, the traps and the lattice constants were decreased. In order to study the effect of substrate heating treatment on the crystal structure, we observed the fabricated $F_{16}CuPc$ thin films by field emission scanning electron microscope, atomic force microscope, and X-ray diffraction method.

1. Introduction

In the display industry, technologies with clear purposes and good functions can survive, but design of equipment has also become important. Not only the wide view and clear resolution, but design as well is required to fulfil customers' want. These days, we are paying our attention to organic light-emitting diode (OLED) and organic field-effect transistor (FET) because organic devices can be flexible and emit light by itself. They have a good luminescence properties and large view angle. It could work at low bias voltage and make it thin [1-3]. Most of all, it can deal with a design limit. Organic molecules are attached to each other by van der Waals bond (normally molecules have a covalent bond which is much stronger), and it is possible that polymer (a large molecule) can be printable or coated. This property makes the manufacturing process easier and has driving voltage. However, if the sample is left in the air or humidity, the connection that van der Waals makes in the sample will be broken and lose its property. The shorter life and less safety it has, the more expense will be needed for production. In addition, organic FET has poor parameters such as mobility and sub-threshold to be compared with low temperature poly-silicon and oxide FET which is used in the present industries [4,5].

To use organic materials in transistors, usage span quality and fundamental improvements in technologies is needed. Organic layer is easily changed by external condition such as temperature or thickness, because it weak to bond them together and low height growth varies the layer characteristics. The conditions during the deposition have caused the different surface of organic layer and it has the device (work in) with different properties. This characteristic is used for improving organic functions. Weak epitaxy growth (WEG) method is control the interaction force between molecular and substrate. Thus, it is effect on growing nucleation and layers.

In this paper, we study different temperature WEG effect on FET with *n*-type Copper hexadecafluorophthalocyanine ($F_{16}CuPc$). We observe the morphology and crystallinity of $F_{16}CuPc$ thin films fabricated at various substrate temperatures by field-emission scanning electron microscope (FE-SEM), atomic force microscope (AFM), and X-ray diffraction (XRD) method.

2. Experiment

Figure 1 (a) shows the structure of $F_{16}CuPc$ and Phthalocyanine. The bottom gate organization was used as the fundamental structure with Au drain and source electrodes (Fig. 1 (b)). The channel length and width of fabricated FET were 50 μm and 1 mm, respectively. The $F_{16}CuPc$ (purchased from Sigma-Aldrich) with 35 nm thickness was fabricated on 200 nm silicon dioxide substrate. It was cleaned by 5 processes (acetone-TFD-NEUT-IPA-DI-water) using SH-2100. The each layer made by thermal evaporator fewer than 10^6 Torr pressure and 0.1 ~0.2 Å/s fixed rate. The rate variation can change the properties of layers and even pressure can affect the sublimation point. Thus, except substrate temperature, it is the important to maintain the conditions. Before deposition, the substrate temperature was kept at 25 °C (RT), 65 °C, 150 °C, and 200 °C for 1 hour. After, $F_{16}CuPc$ active layer has been made.

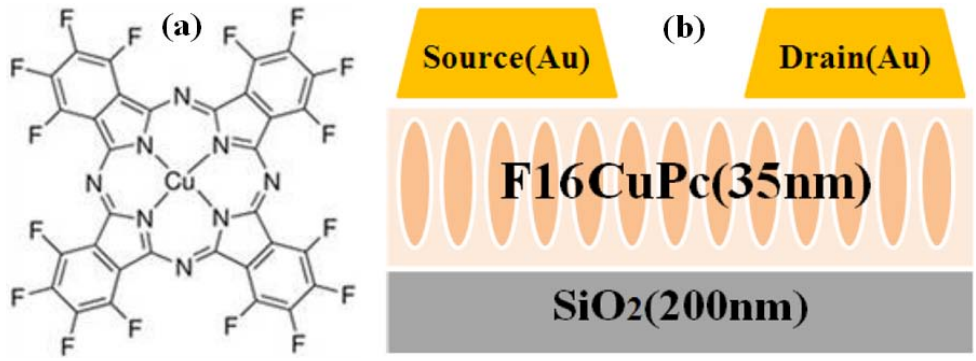

Fig. 1. (a) Molecular structure of $F_{16}CuPc$ and Phthalocyanine. (b) The structure of the top-bottom gate type FET with $F_{16}CuPc$ active layer.

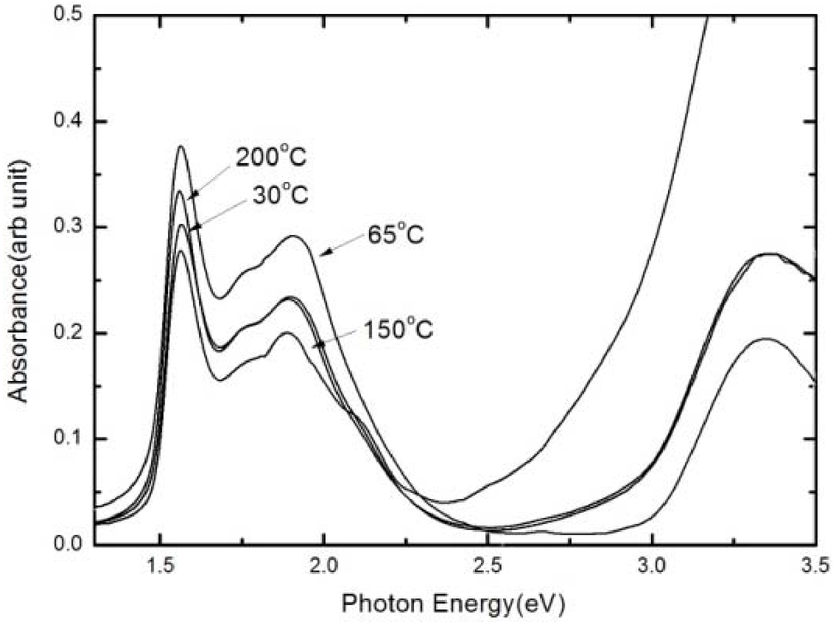

Fig. 2. Optical absorption of $F_{16}CuPc$ thin films grown at substrate heating temperatures of (a) RT, (b) 65 °C, (c) 150 °C, and (d) 200 °C for 1 hour.

3. Results and discussion

Figure 2 shows the optical absorption spectra of fabricated $F_{16}CuPc$ thin films obtained by UV-visible Spectrophotometer (S-3100). The calculated band-gap energy, E_g, is used to idealize the potential difference between the Fermi energy of the source and drain and the majority carrier reside of the band edge which is LUMO for *n*-type materials or HOMO for *p*-type materials. If the energy band structures of organic layer are mismatched in multilayers, they can cause resistant materials (barrier), which makes it important to know energy band structures. The three different maximum values from Fig. 2 represent the electrons transfer valence band to conduction band in π-π^* orbital. These values have two *Q*-bands in visible region and *B*-band in UV region. The E_g is arranged by using one electron theory as [4]

$$\alpha = \alpha_0 (h\upsilon - E_g)^n . \tag{1}$$

The mechanisms of electron's moving from valence band to conduction band n and thus, the optical absorption coefficient α has two values (2 or 1/2) [6,7]. If electron is direct allowed transitions n has value 1/2. For indirect allowed transitions of electron n has value 2. The values of band-gap energy obtained from experiments for the all fabricated $F_{16}CuPc$ thin films are summarized in Table 1.

Table 1. The band-gap energy of $F_{16}CuPc$ thin films grown at different substrate heating temperatures.

Substrate temperature (°C)	Band-gap energy (eV)		
	***n*=1/2**	***n*=2**	***n*=1/2**
RT 2.99		1.39	1.25
65 3.04		1.37	1.28
150 2.98		1.41	1.33
200 2.98		1.39	1.33

$F_{16}CuPc$ layers were deposited by Ostwald ripening growth [8]. The islands relatively bigger have been combined with the neighborhood islands. The m olecules accelerated by therm al energy are diffused in substrate to make the free energy low. Thus, the su rface condition is dependent of temperature and exposing time. The higher therm al energy was given, the bigger grain size which has a re-cry stallization to get lower surface energy we can get.

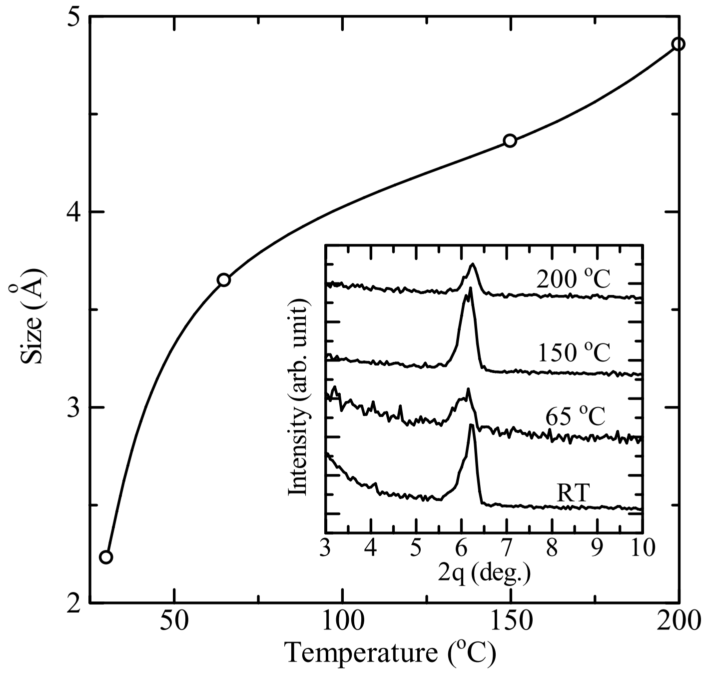

Fig. 3. (a) XRD pattern and (b) crystal size of $F_{16}CuPc$ thin films grown on substrate at different heating temperatures.

Figure 3 shows the cry stallinity of the $F_{16}CuPc$ gotten from Debye-Scherer equation. Both FWHM and Bragg angle increased with increasing of the substrate heating tem perature: 2.23 Å and 4.85 Å for 30 °C and 200 °C, respectively [5]. The XRD patterns with the di ffraction peak at (100) gives full width at half maximum (FWHM) and the Bragg angle as shown in inset of Fig. 3.

Table 2. Summary of performance parameters of $F_{16}CuPc$ FET.

Heating temp. (°C)	Mobility (cm^2/Vs)×10^{-4}	on/off ratio	Sub-threshold swing (V/°C)	Threshold voltage (V)
RT 5.61		22	39	-
65 6.14		104	26.4	-
150 11.3		153	15.3	4
200 20.6		791	14.6	17

We same results are confirmed by FE-SEM and AFM m easurements. Figure 4 and 5 shows the surface morphology and topology of $F_{16}CuPc$ layers fabricated at substrate heating temperatures at (a) RT, (b) 65 °C, (c) 150 °C, and (d) 200 °C for 1 hour. The different therm al energy effectiveness to the surface morphology is clearly visible in FE-SEM im ages. The sam ple growth at 65 °C (Fig. 5 (b)) has elongated hillock shape while the sample growth at 200 °C has enlarged grain size and agglomerated forms.

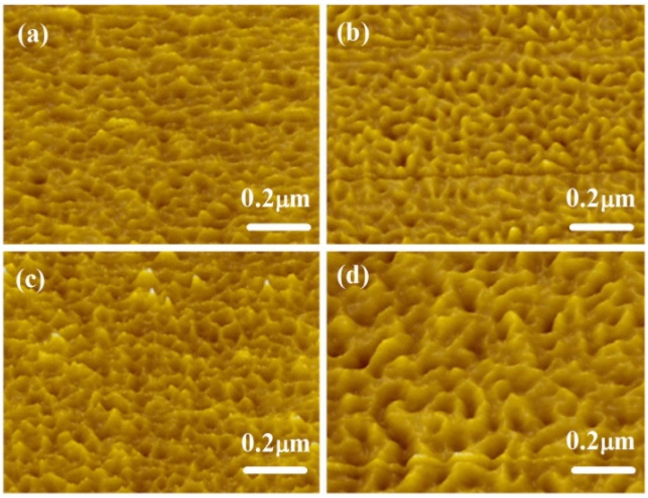

Fig. 4. FE-SEM micrographs for $F_{16}CuPc$ thin film grown at substrate heating temperature of (a) RT, (b) 65 °C, (c) 150 °C, (d) 200 °C for 1 h.

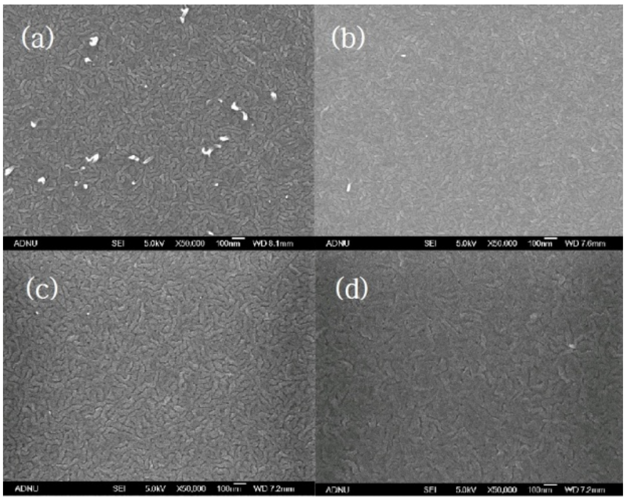

Fig. 5. AFM topographies for $F_{16}CuPc$ thin film grown at substrate heating temperature of (a) RT, (b) 65 °C, (c) 150 °C, (d) 200 °C for 1 h.

The molecules stocking structures are obtained by using the Bragg equation (with the XRD pattern) and shown in Fig. 6. The space value is 1.51 nm 1.46 nm, 1.44 nm , and 1.42 nm for the substrate heating temperatures of RT, 65 °C, 150 °C, and 200 °C, respectively. Through this result it is shown that the angle between F_{16} molecule and surface is shrieked with perpendicular height reduced as well and the distributions are more overlapped each other [9].

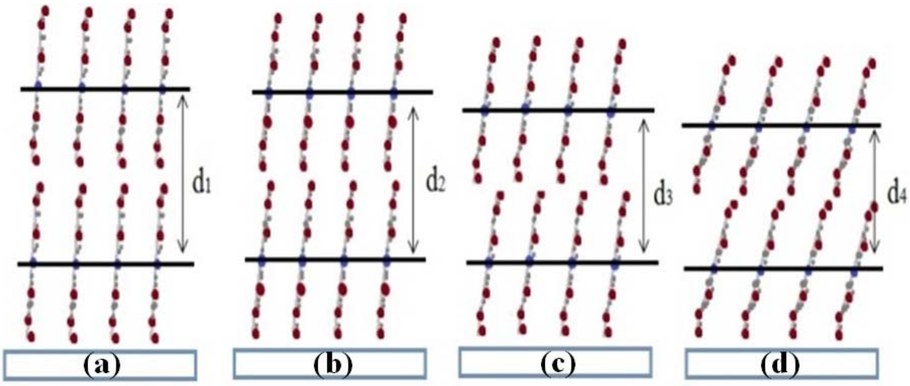

Fig. 6. Structures of $F_{16}CuPc$ molecular stacking grown at substrate heating temperatures of (a) RT, (b) 65 °C, (c) 150 °C, (d) 200 °C for 1 h.

The electronic properties of FET are mainly caused by organic layer and studied by *I-V* transfer characteristics. Figures 7 and 8 compare the transfer and *I-V* characteristics of $F_{16}CuPc$ FET with SiO_2 as a gate insulator with substrate heating temperature at (a) RT, (b) 65 °C, (c) 150 °C, and (d) 200 °C. The electronic properties such as mobility, threshold voltage, on/off ratio and inverse sub-threshold swing can be obtained from transfer characteristics graph and shown in Table 2. The FET fabricated at 200 °C has good capacities compared with other samples. The FET fabricated at 200 °C has good properties compared with other samples. An organic layer surface has low free energy that causes decreasing dangling bond effect. Dangling bond on the surfaces traps electron moving from drain into active layer and from active layer into source. Next, the number of molecules composed critical nucleus has been changed by external condition. The higher temperature, the bigger size grain is made. This means that many $F_{16}CuPc$ molecules are connected by π-π*. It causes mobility getting faster. Figure 7 gives us intuition of the relationship grain size with mobility. The resistors have less effect on moving electrons by hopping into another nucleus. Thus, the FET electric performance is better for the high substrate heating temperatures [10,11]. On the other hands, the FET with RT substrate heating temperature showed not fully saturated behavior (Fig. 8) that will cause in quality degradation.

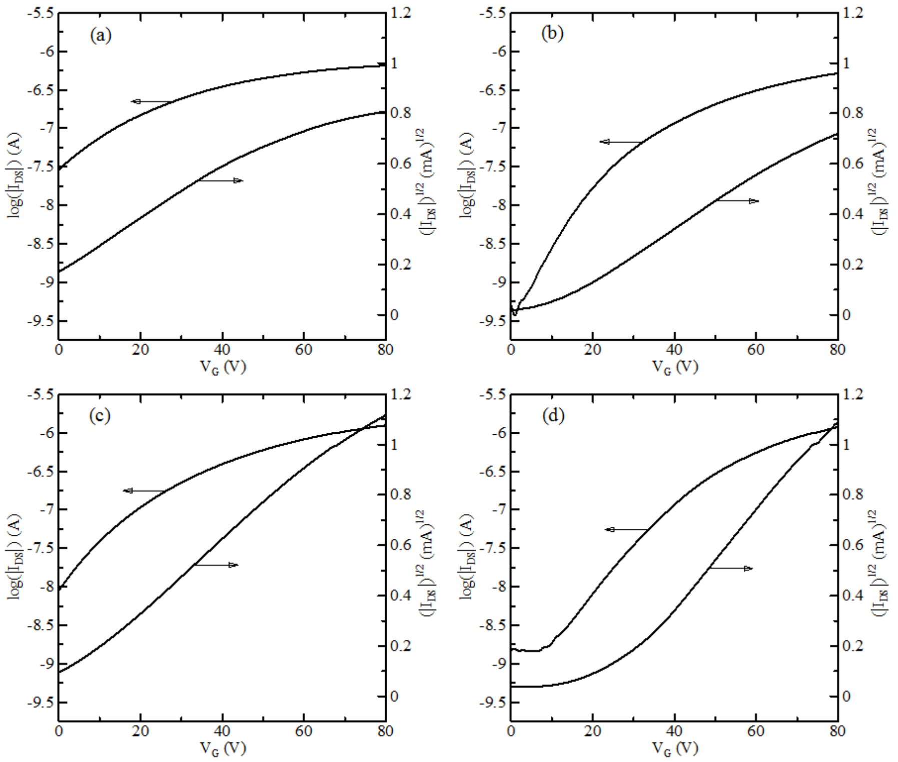

Fig. 7. Transfer characteristics of F $_{16}$CuPc FET fabricated at substrate h eating temperatures of (a) R T, (b) 65 °C, (c) 150 °C, (d) 200 °C for 1 h.

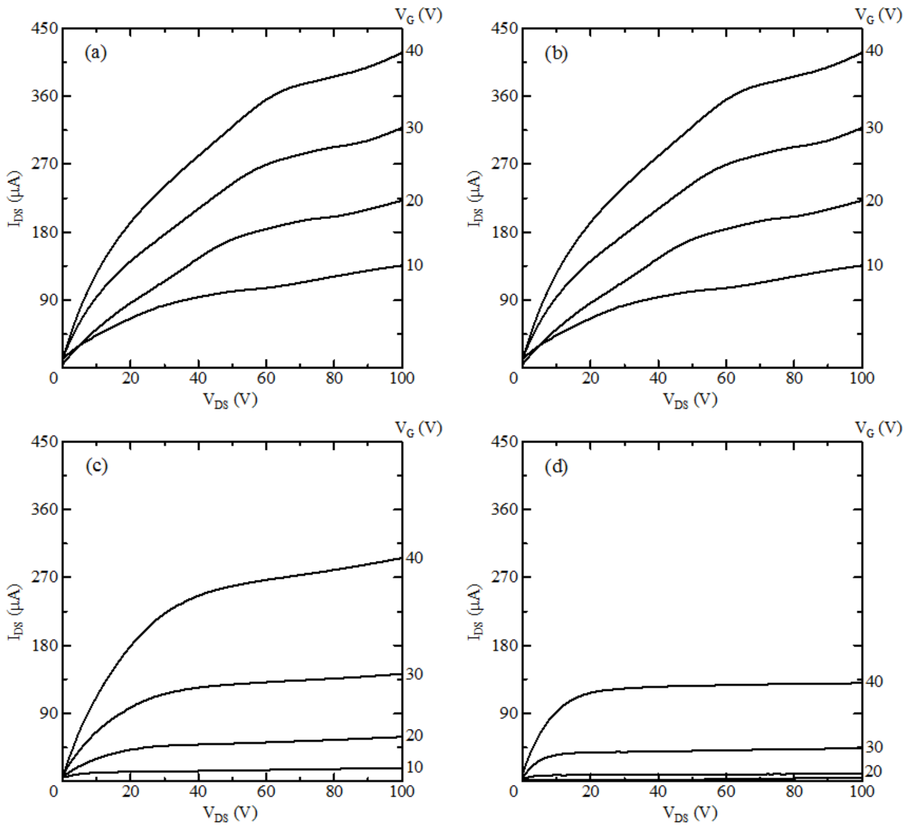

Fig. 8. *I-V* characteristics of F_{16}CuPc FET fabricated at substrate heating temperatures of (a) RT, (b) 65 °C, (c) 150 °C, (d) 200 °C for 1 h.

4. Conclusions

We analy zed the variation of the electrical characteristics of F $_{16}$CuPc FET due to different substrate heating tem peratures during fabrication process. The different heating tem peratures lead to changing molecular structure and surface roughness. When exposed with higher annealing temperature, the bigger grain size was formed and larger roughness coefficient. At the same time, the decreasing of lattice constant tells that molecular angle with surface decreased and the different phase of active layer was formed. This has less electrons trapped affect in boundary surface. By this alteration, mobility improves about 3.7 times and on/off ratio increased about 36 times. The additional substrate heating gives enhanced electric characteristics to $F_{16}CuPc$ FET related to device performance.

Acknowledgements

This work was supported by a Sogang University Special Research Grant 2009 (201314002), Basic Science Research Program through the National Research Foundation of Korea (2009-0093822 & 2014R1A1A2A16055772), and Parts & Materials International Collaborative R&D Program funded by the Ministry of Knowledge Economy of Korea (MKE: N0000481).

References

1. G. Gelinck, P. Heremans, K. Nomoto, T. Anthopoulos, Adv. Mater. 22 (2010) 3778.
2. F. Cicoira, C. Santato, Adv. Funct. Mater. 17 (2007) 3421.
3. A. Babajanyan, H. Melikyan, J. Kim, K. Lee, M. Iwamoto, B. Friedman, Org. Electron. 12 (2011) 263.
4. G. Horowitz, Adv. Mater. 10 (1998) 365.
5. N. Moriguchi, T. Nishikawa, T. Anezaki, A. Unno, M. Tachibana, K. Kojima, Physica B, 376-377 (2006) 276.
6. J. Singh, *Electronic and optoelectronic properties of semiconductor structure,* Cambridge Press, New York (2003).
7. R. Koshy, C. Menon, E J. Chem. 9 (2012) 294.
8. A. D. McNaught, A. Wilkinson (eds.), *Compendium of chemical terminology*, 2nd ed., IUPAC, Gold Book, (1997).
9. K. Sethuraman, P. Kumar, K. Santhakumar, Sh. Ochiai, .P. Shin, J. Kor. Phys. Soc. 61 (2012) 113.
10. D. de Oteyza, E. Barrena, S. Sellner, J. Osso, H. Dosch, J. Phys. Chem. B 110 (2006) 16618.
11. S. Yadav, P. Kumar, S. Ghosh, Appl. Phys. Lett. 101 (2012) 193307.

Pre-annealing effects on a pentacene organic field-effect transistor

T. Abrahamyan[1], A. Babajanyan[1], S. Choi[2], O. Galstyan[2],
J. Park[2], Y. Lee[2], B. Friedman[3], G. Berthiau[4], K. Lee[2]

[1] *Department of Radiophysics, Yerevan State University, A. Manoogian 1, Yerevan 0025, Armenia*
[2] *Department of Physics & Basic Science Institute for Cell Damage Control, Sogang University, Seoul 121-742, Korea*
[3] *Department of Physics, Sam Houston State University, Huntsville, Texas 77341, USA*
[4] *IREENA, 37 Boulevard de L'iniversite, BP-406, 44602 Saint-Nazaire Cedex, France*

A pentacene organic thin film transistor (OTFT) was fabricated at 25 °C (RT), 90 °C, 120 °C, and 150 °C in situ substrate temperatures [1]. In order to study the effect of pre-annealing treatment on the crystal structure, we observed the fabricated pentacene thin films by scanning electron microscope, atomic force microscope, and X-ray diffraction method. The pentacene film remains in the bulk phase and the carrier's mobility decreases only after 150 °C substrate temperature compared with RT preparation. A pentacene OTFT fabricated at 90 °C in situ substrate temperature exhibited enhanced electric characteristics, including hole mobility of 0.13 cm^2/Vs, current *on*/*off* ratio on order of 10^2, and a threshold voltage less than -4 V.

1. Introduction

Organic thin-film transistors (OTFT) have attracted much attention due to their attractive features such as low cost, low temperature processing, and mechanical flexibility [1,2]. Currently, because of these excellent properties there are many applications such as flexible organic light emitting diodes, radio frequency identification tags, smart cards, plastic logic circuits, etc. [3,4]. The three fundamental components of such devices are the contacts (source, drain, and gate), the semiconductor thin film, and the gate insulator layer. To improve the performance of organic transistors, the condition of the organic semiconductor/gate insulator layer interface is very important. Various materials with high dielectric constant have been investigated for gate insulator such as high-*k* inorganics, polymers, and self-assembled small molecules. Organic transistors with a polymer gate insulator layer exhibited OTFT performance comparable to inorganic dielectrics. Polymers such as poly (vinyl phenol), poly (styrene), poly(methyl methacrylate), and poly(vinyl alcohol) have been used as OTFT gate insulators [5,6].

Among the most popular organic semiconductors, pentacene is widely studied for p-channel organic transistors due both to its stability and its high field effect mobility [7]. Pentacene consists of a linear chain of five benzene rings. With X-ray diffraction techniques, the four different polymorphs can be classified according to their *d* (001) spacing perpendicular to the substrate surfaces: 14.1, 14.4, 15, and 15.4 Å. Two polymorphs of 14.4 and 15.4 Å have been found in the pentacene films grown on SiO_2 substrate; so called "thin film" and "bulk" phases [8-10]. The phase transition between the two polymorphs depends on the substrate deposition temperature and the film thickness. In organic semiconductors, molecular ordering has influence on the electrical performance of devices since charge transport is dominated by hopping [11,12]. Thus, the phase transition in pentacene induced by the post annealing process correlates with electric transport [13].

In this paper, we study the pre-annealing effect on the pentacene OTFT. First, we focus on the electrical characteristics of pentacene based OTFT fabricated at 25 °C (RT), 90 °C, 120 °C, and 150 °C in situ substrate temperatures. Second, we observe the morphology and crystallinity of pentacene thin films pre-annealed at various substrate temperatures by scanning electron microscope (SEM), atomic force microscope (AFM), and X-ray diffraction (XRD).

2. Experiment

The pentacene OTFT was fabricated on highly doped p-type silicon substrates. The pentacene thin films were deposited on the SiO_2 substrates at 25 °C (RT), 90 °C, 120 °C, and 150 °C by the thermal vacuum evaporation method. The resulting films were about 50 nm thick with deposition rate of approximately 0.1 Å/s and base pressure of about 5×10^{-6} Torr. After depositing the pentacene thin film, a 100 nm thick Au layer was deposited through a metal mask, using a thermal evaporator. The channel length and width of fabricated OTFT were 50 μm and 1.1 mm, respectively.

The electrical measurements of the device characteristics were performed using a Keithley 2400-SCS source-meter in the dark condition at RT. The structure, morphology, and crystallinity of pentacene thin films were investigated using SEM, AFM, and XRD.

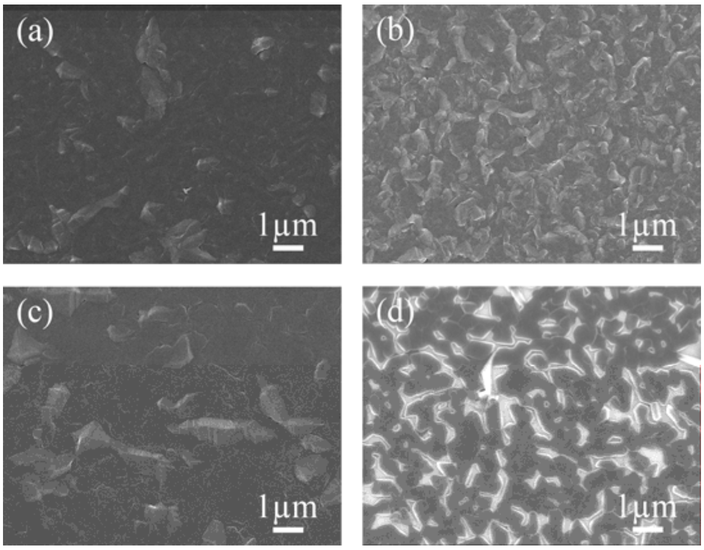

Fig. 1. (a) Molecular structure of $F_{16}CuPc$ and Phthalocyanine. (b) The structure of the top-bottom gate type FET with $F_{16}CuPc$ active lay SEM micrographs of pentacene thin films pre-annealed at (a) RT, (b) 90 °C, (c) 120 °C, and (d) 150 °C grown on SiO_2 substrate.

3. Results and discussion

In order to study pre-annealing on the morphology of pentacene thin films, we investigated its effect by using SEM and AFM. Figure 1 shows the SEM micrographs of pentacene thin films pre-annealed at (a) RT, (b) 90 °C, (c) 120 °C, and (d) 150 °C on SiO_2 substrate. The grain size of pentacene grown on the SiO_2 layer was 1-1.5 μm. Although the average grain size of the pentacene thin film pre-annealed at RT was bigger in compression to 90 °C, the average grain size of pentacen e thin film increased with further increase of the pre-annealing temperature. The pentacene thin film pre-annealed at 150 °C did not fully cover the SiO_2 surface due to re-evaporation of pentacene which has been previously observed for substrate temperature above 100 °C [14]. Since transport properties is depend on the molecular ordering of the pentacene film at the grain boundary, the larger grain size and better ordering of pentacene grown on the SiO_2 interface should improve the electrical properties of the pentacene OTFT [15].

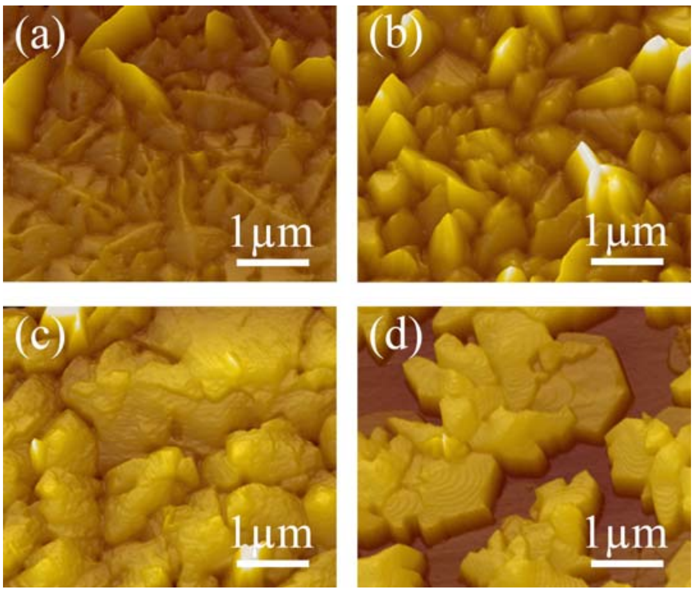

Fig. 2. AFM images obtained for pentacene thin films pre-annealed at (a) RT, (b) 90 °C, (c) 120 °C, and (d) 150 °C grown on SiO_2 substrate.

Figure 2 shows the AFM images of pentacene thin films pre-annealed at (a) RT, (b) 90 °C, (c) 120 °C, and (d) 150 °C on the SiO_2 substrate. The pentacene thin film before annealing (RT) and after pre-annealing at 90 °C shows typical dendritic grains with the average grain size of 1-1.5 μm. However, the surface of the pentacene thin film pre-annealed at 90 °C displays "inclined grains" which are similar but more asymmetric than the pyramidal grains [16]. It can be seen that the lamellar structure appears when the pre-annealing temperature is higher than 90 °C. Figure 5(d) shows a large lamellar grain structure with the average grain size of 2-2.5 μm and a terrace-like structure. The lamellar structure was also called the bulk phase [17]. Thus, the bright part observed in Fig. 2 (c) is probably a grain of the bulk phase pentacene.

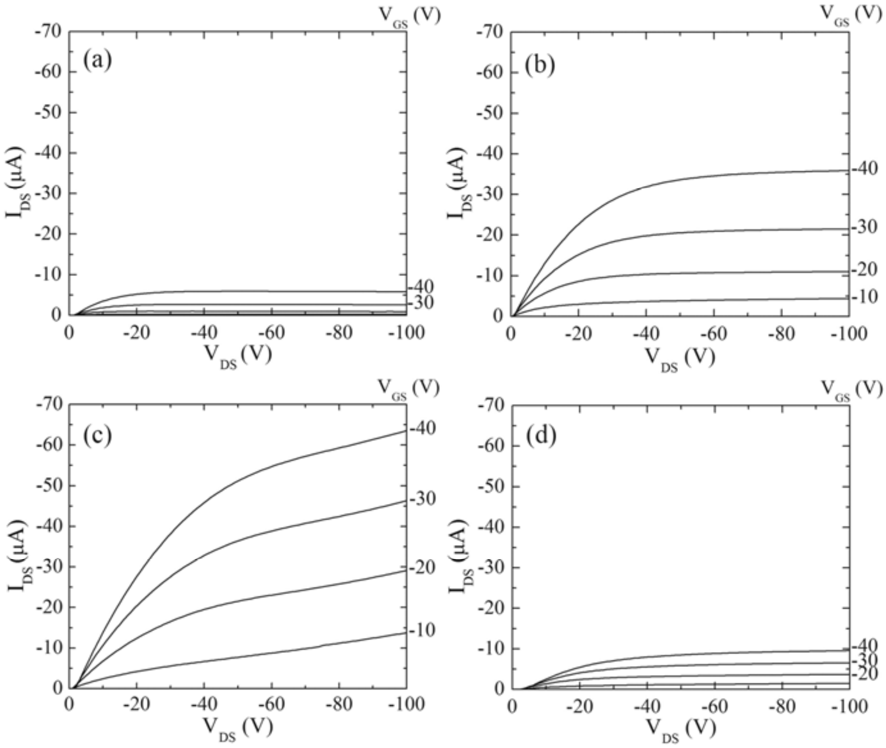

Fig. 3. *I-V* characteristics of pentacene OTFT with SiO_2 as a gate insulator layer pre-annealed at (a) RT, (b) 90 °C, (c) 120 °C, and (d) 150 °C.

Figures 3 and 4 compare the *I-V* and transfer characteristics of pentacene OTFTs with SiO_2 as a gate insulator layer pre-annealed at (a) RT, (b) 90 °C, (c) 120 °C, and (d) 150 °C. As the annealing temperature increases up to 120 °C, the magnitude of drain current I_{DS} gradually increases but decreases to a low value again at the annealing temperature 150 °C. We already observed that the pentacene grain size increases with the temperature (Fig. 5). The maximum drain current -62 μA was obtained for the OTFT with the pentacene layer pre-annealed at 120 °C. Note that the drain current is not saturated due to the channel length modulation effect [18]. A hole mobility $\mu = 0.1$ cm^2/Vs, a threshold voltage $V_T = -17$ V, and a current *on*/*off* ratio $\geq 10^3$ were obtained for the pentacene OTFT with SiO_2 as a gate insulator layer pre-annealed at RT. According to the measured data, the drain current increases but the carrier mobility and current *on*/*off* ratio decrease with increasing of annealing temperature up to 120 °C. In addition, pre-annealing reduces the threshold voltage; the V_T moved toward a positive bias with increasing annealing temperature. All performance parameters of the fabricated OTFTs are summarized in Table 1.

Table 1. Summary of performance parameters of pentacene OTFT.

Substrate pre-annealing temperature (^oC)	Mobility, μ_{sat} (cm^2/Vs)	Threshold voltage, V_T (V)	*On/off* ratio
25 0.1		-17	$\geq 10^3$
90 0.13		-4	$\geq 10^2$
120 0.06		-2	≥ 20
150 0.04		-2	$\geq 10^2$

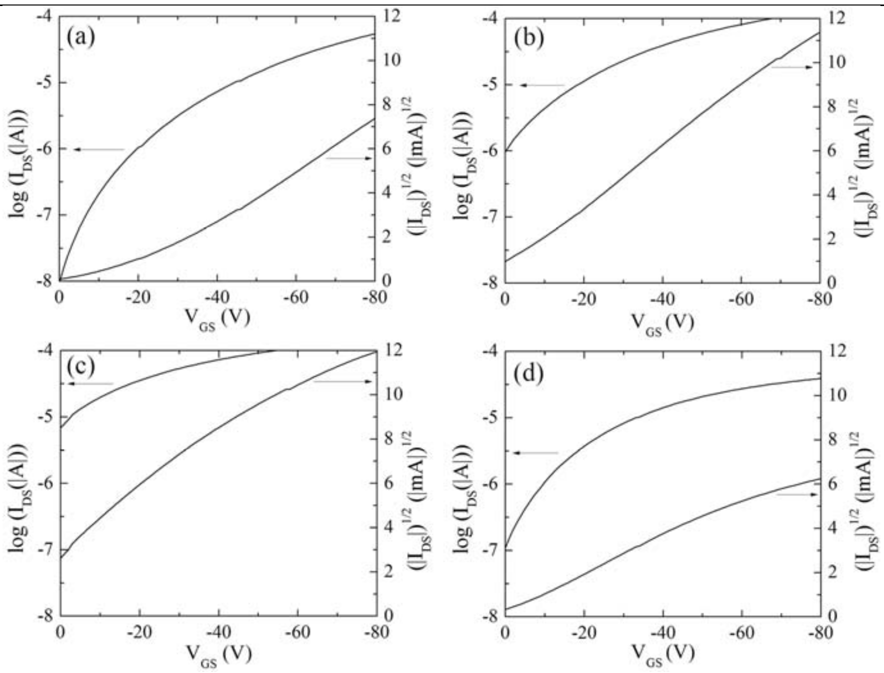

Fig. 4. Transfer characteristics of pentacene OTFT with SiO_2 as a gate insulator pre-annealed at (a) RT, (b) 90 °C, (c) 120 °C, and (d) 150 °C.

The cry stallinity of pentacene thin films deposited on SiO_2 substrate at various pre-annealing temperatures was examined with XRD and is shown in Fig. 5. The mobility seems inconsistent with the grain size and XRD intensity for pentacene thin films evaporated at pre-annealing temperature 90 °C. Various defects such as chemical impurities and dislocation may exist in the vacuum deposited films. D. Guo et al. reported that the number of defects such as dislocation and crystallite boundary inside the grains may be decreased and the degree of order and the grain size of the main charge transport layers near the interface may be increased, although annealing decreased the apparent grain size in the horizontal direction [19]. This occurs because of the high mobility and free energy of the defects, especially when a large number of defects and traps appear. The polymorph of the pentacene film deposited on the SiO_2 substrate (Fig. 5) transforms from the thin film phase to the bulk phase when the substrate temperature increased up to 150 °C. The pentacene growth mode transition occurs due to the interfacial surface energy mismatches, related to the difference between the pentacene surface energy and the bulk energies of the two different phases [20,21]. Therefore, pentacene grains on SiO_2 substrate pre-annealing at 90 °C is highly interconnected with one another which can lead to more efficient charge transport.

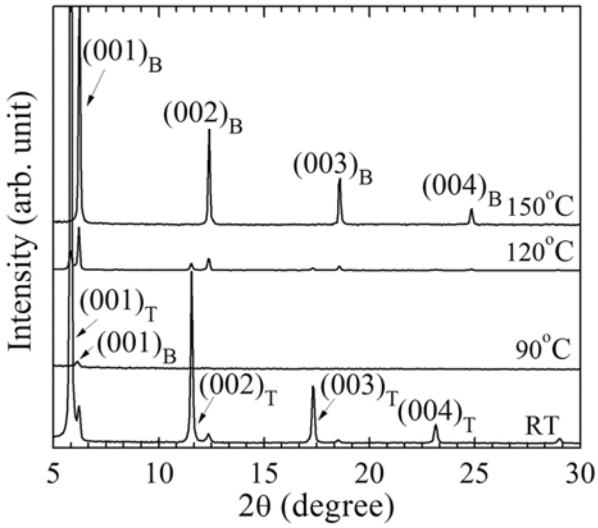

Fig. 5. XRD profiles of pentacene thin films pre-annealed at (a) RT, (b) 90 °C , (c) 120 °C, and (d) 150 °C grown on SiO_2 substrate.

4. Conclusions

We fabricated pentacene-based OTFTs on SiO_2 as an insulator layer using different pre-annealing temperature conditions. Pentacene OTFT with substrate pre-annealing temperature of 90 °C exhibited enhance electric properties; including hole mobility of 0.13 cm^2/Vs, current *on*/*off* ratio of >10^2, and the threshold voltage of less than -4 V. For pentacene thin films deposited on SiO_2 substrate polymorphism not observed and there was no phase transformation which from the thin film phase to the bulk phase. On the other hand, pentacene thin films deposited on SiO_2 substrate completely transforms to the bulk phase at pre-annealing temperature of 150 °C. The additional substrate pre-annealing gives enhanced electric characteristics to pentacene OTFT related to device performance.

Acknowledgements

This work was supported by a Sogang University Special Research Grant 2009 (201314002), Basic Science Research Program through the National Research Foundation of Korea (2009-0093822 & 2014R1A1A2A16055772), and Parts & Materials International Collaborative R&D Program funded by the Ministry of Knowledge Economy of Korea (MKE: N0000481).

References

1. J. Veres, S. Ogier, G. Lloyd, Chem. Mater. 16 (2004) 4543.
2. G. Horowitz, Adv. Mater. 10 (1998) 365.
3. C. D. Sheraw, L. Zhou, J. R. Huang, D. J. Gundlach, T. N. Jackson, M. G. Kane, I. Hill, Appl. Phys. Lett. 80 (2002) 1088.
4. C. D. Dimitrakopoulos, P. R. L. Malenfant, Adv. Mater. 14 (2002) 99.
5. A. Faccheti, T. J. Marks, M. -H. Yoon, Adv. Mater. 17 (2005) 1705.
6. X. Peng, G. Horowitz, D. Fichou, F. Garnier, Appl. Phys. Lett. 57 (1990) 2013.
7. C. D. Sheraw, L. Zhou, J. R. Huang, D. J. Gundlach, T. N. Jackson, M. G. Kane, I. G. Hill, M. S. Hammond, J. Campi, B. K. Greening, J. Franc, J. West, Appl. Phys. Lett. 80 (2002) 1088.
8. C. C. Mattheus, A. B. Dros, J. Baas, G. T. Oostergetel, A. Meetsma, J. L. de Boer, T. T. M. Palstra, Synth. Met. 138 (2003) 475.
9. C. C. Mattheus, G. A. de Wijs, R. A. de Groot, T. T. M. Palstra, J. Am. Chem. Soc. 125 (2003) 6323.
10. C. D. Dimitrakopoulos, A. R. Brown, A. Pomp, J. Appl. Phys. 80 (1996) 2501.
11. D. J. Gundlach, T. N. Jackson, D. G. Schlom, S. F. Nelson, Appl. Phys. Lett. 22 (1999) 3302.
12. D. Guo, S. Ikeda, K.Saiki, Condens. Matter. 22 (2010) 262001.
13. T. S. Ji, S.Y. Jung, V. K. Varaadan, Org. Electron. 9 (2008) 895.

14. M. Brinkmann, S. Graff, C. Straupe, J. C. Wittmann, J. Phys. Chem. B, 107 (2003) 10531.
15. D. J. Gundlach, Y. Y. Lin, T. N. Jackson, S. F.Nelson, D. G. Schlom , IEEE Electron Device Lett. 18 (1997) 87.
16. H. Yanagisawa, T. Tamaki, M. Nakamura, K. Kudo, Thin Solid Films 464-465 (2004) 398.
17. I. P. M. Bouchoms, W. A. Schoonveld, J. Vrijmoeth, T. M. Klapwijk, Synth. Met. 104 (1999) 175.
18. R. Jacob Baker, H. W. Li, D. E. Boyce, *CMOS Circuit Design Layout and Simulation* (John Wiley & Sons, New York, 1997).
19. D. Guo, S. Ikeda, K. Saiki, J. Appl. Phys. 99 (2006) 094502.
20. L. F. Drummy, D. C. Martin, Adv. Mater. 17 (2005) 903.
21. C. Kim, A. Facchetti, T. J. Marks, Adv. Mater. 19 (2007) 2561.

Circularly Distributed Multi Beam Patch Array Antenna

[1]A.Hakhoumian, [1]K.Dadalyan, [1]N.Poghosyan,[2]O.Mahmoodian

[1]Institute of Radiophysics and Electronics, NAS of Armenia

[2] PhD students, Iran Islamic Republic

Abstract – Circular distributed multi beam patch array antenna in order to use in X and K_a band has been proposed and realized. To illuminate the amount of losses we have used a reactive radial power divider combiner and also sixteen microstrip patch antennas have been designed and investigated.

Introduction

X and K_a bands frequencies as the segments of microwave radio region of electromagnetic spectrum are widely used in various applications such as cellular communication and radar,etc.In some radar and cellular communication systems the high gain omnidirectional antennas are needed. Various types of omnidirectional antennas exist and monopole antenna is one common and basic type of these antennas. Monopole antenna due to their simple structures and easy manufacture and also low cost and wide band properties are widely used in much application such as cell phone, Walkie- talkie and vehicles. The gain of a quarter wave monopole antenna is approximately 5.16 dbi and radiation resistance is about 36 ohms. Large magnitude of its input reactance and also reducing radiation efficiency of antenna because of introducing Ohmic loss into the antenna circuit are main disadvantages of monopole antennas. Another type of omnidirectional antenna is biconical broad-band antenna which made of two roughly conductive objects touching at their points.Biconical antennas have dipole characteristics with an enormous wideband compare to monopole antenna. The gain of Biconical antenna is about 6 db that is also better than monopole. The main disadvantage of this antenna to use in X and K_a band frequencies is various difficulties to design and making it and because of this problem it is not a good choice for these bands. In this paper we have tried to investigate circular multi beam distribute base on patch array antenna

1. Single patch antenna design

Microstrip patch antennas (MSA) as a common type of low profile and easy manufacturing antenna with ability to use in various application such as aircraft, military and satellite are widely used. Patch antennas because of high gain more than 6 db and its appropriate properties for both vertical and perpendicular polarization is a good choice to use in X-band region. In this project a circular array consist of sixteen rectangular microstrip patch antenna is design and tested. For a rectangular patch, the length L of patch is usually $0.3\ \lambda_o < L < .5\ \lambda_o$,where λ_o is free space wavelength. A practical width that leads to good radiation efficiencies is calculated by

$$W=c/2f_r[2/(\varepsilon_r+1)]^{1/2} \qquad (1)$$

where **c** is the free-space speed of light and $\mathbf{f_r}$ is resonance frequency.

Actual length of patch is presented by

$$L=1/[2f_r(\varepsilon_{reff})^{1/2}\cdot(\mu_0\varepsilon_0)^{1/2}]-2\Delta L \quad (2)$$

Where μ_0 and ε_0 are permeability and permittivity of free space and ε_{reff} is effective dielectric constant that is determined by

$$\varepsilon_{reff}=(\varepsilon_r+1)/2+(\varepsilon_r-1)/2\cdot\left[1+12\cdot h/w\right]^{-1/2} \quad (3)$$

The high of the substrate is usually .003< λo<*.05* λo[5,6].In the first step, sixteen rectangular patches of dimension W= 8 mm, L= 9.5 mm and H=0.15mm was designed and printed on dielectric surfaces with ε_r=2.2 dielectric constant which The length, height and width of dielectric surfaces are 23mm, 1.25mm and 15.5 mm respectively. These dielectrics are positioned as circular form on a sixteen port radial divider/combiner and sixteen thin metal surfaces fill the space between them. All patches were tested in 9.316MHz frequency and value of VSWR was about 1.22.the shape and radiation pattern of patch antenna are shown in figure (1).

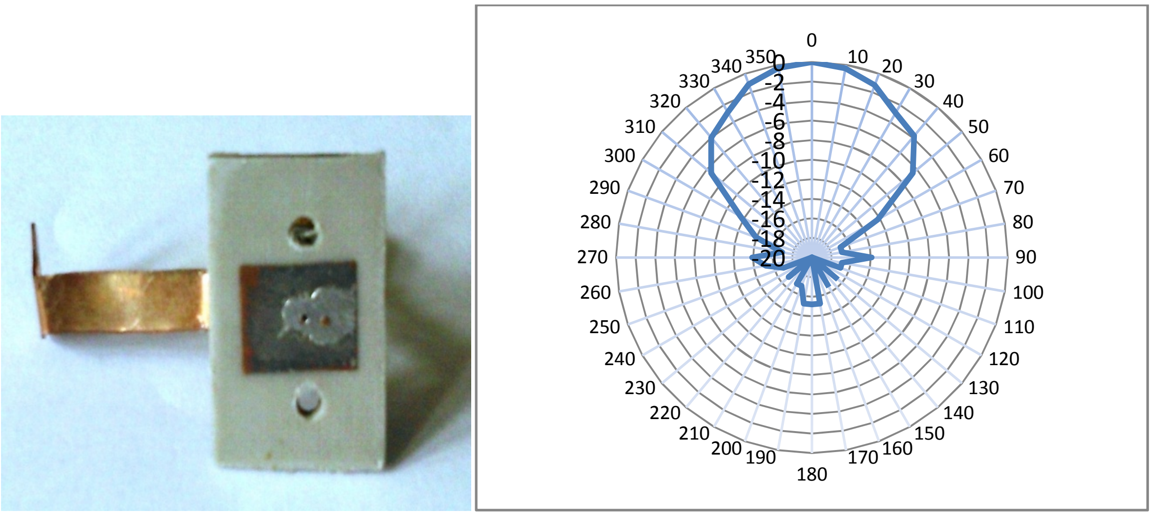

Fig1: single patch(left),patch radiation pattern(right)

2. RADIAL POWER/COMBINER STRUCTURE

In this study in order to split RF signal into sixteen ports with roughly same amplitude it was necessary to use a divider/combiner. Distributed system base on Wilkinson divider was common choice. Unfortunately if the number of ports increases the amount of losses also increase rapidly. In this study we have N=16 ports that means more losses. To solve this problem we used another type of divider called reactive divider/combiner that was suitable for this application. This power divider/combiner consist of 16 identical micro strip PA which via micro strip-to-coax 50Ω adapter directly connected to receiving coaxial line main port as a load fig 2.

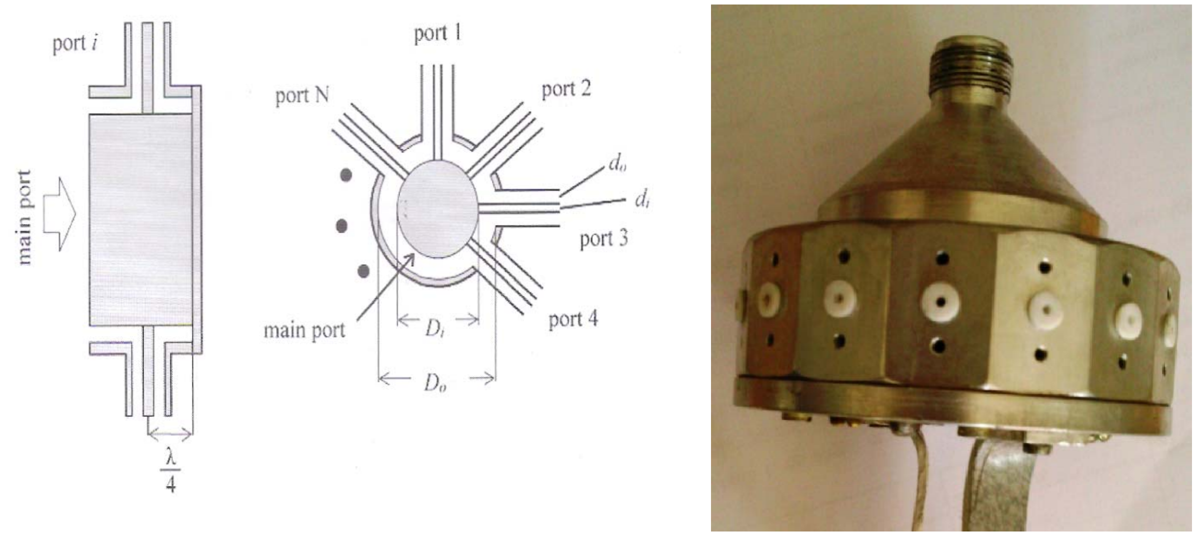

Fig2: divider/combiner structure

The corresponding impedances and dimensions of coaxial lines can be determined from[4],

$$Z_N=60\frac{1}{\sqrt{\varepsilon}}\ln\frac{d0}{di}\ ,\ Z_m=60\frac{1}{\sqrt{\varepsilon}}\ln\frac{D0}{Di}\ ,\ Z_M=\frac{Zn}{N} \tag{4}$$

$$D_0> \frac{1}{\pi}Nd_0\ ,\ D_i> \frac{1}{\pi}\ Nd_i \tag{5}$$

As it follow from equation, Z_M=3.1Ω and (Z_N=50 Ω, N=16) D_i,D_0≈Nd_0 therefore Combiner design meet the serious problem to match receiving coaxial line, having extra impedance and big inner and outer

diameters, with the Standard 50Ω output coaxial line (fig.3).in order to match circuits with high ratio of own impedance both conventional methods using $\lambda/2$ coaxial lines transformers and continuously changing inner and outer diameters of coaxial lines provide to unavailable lengths of matching . Matching can be done by connecting lines with appropriate impedance

(Z_1,Z_2……Z_n) and lengths(L_1,L_2……….L_n).length of matching lines are about $\lambda/12$).

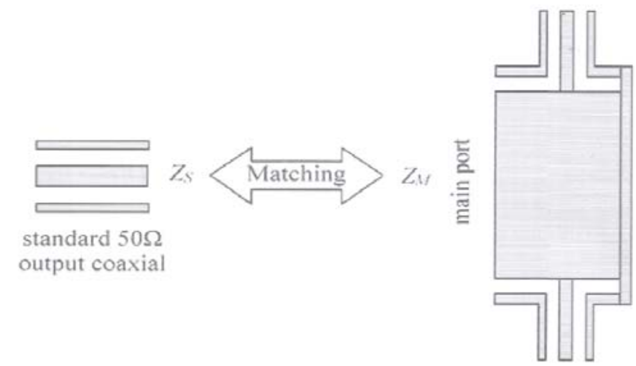

Fig:3

Discontinuity admittance Y_d can be calculated for a (Sudden Change in diameter of Inner Cylinder) and b (Sudden Change in diameter of Outer Cylinder) as follow:

$$Y_d=\frac{j2\pi\omega\varepsilon}{\ln r3/r2}\sum_N 2A0^2\ (K_n\ _,r_2)/K_n\ k_n\{[k_n r_3 A_1(K_n r_3)]^2-[k_n r_1 A_1(K_n r_1)]^2\} \quad (6)$$

$$Y_d=\frac{j2\pi\omega\varepsilon}{\ln r2/r1}\sum_N 2A0^2\ (K_n\ _,r_2)/K_n\ k_n\{[k_n r_3 A_1(K_n r_3)]^2-[k_n r_1 A_1(K_n r_1)]^2\} \quad (7)$$

The $A_0(K_n r)$ and $A_1(K_n r)$ $(r=r_1,r_2,r_3)$ can be calculated from

$$A_0(K_n r)=J_0(K_n r)+G_n N_0(k_N r)\ .A_1(K_n r)=J_1(K_n r)+G_n N_1(k_N R) \quad (8)$$

Where J_p and N_p are p-th order Bessel functions of the first and second kinds accordingly and

$$G_n= J_0(K_n r_1)/\ N_0(k_N r_1)=-\ J_0(K_n r_3)/\ N_0(k_n r_3) \quad (9)$$

Where number K_n calculated from transcendental equations

$$J_0(K_n r_1)\ N_0(k_N r_3)-\ J_0(K_n r_3)\ N_0(k_N r_1)=0 \quad (10)$$

And K_n from

$$K_n=\sqrt{1}-(\frac{2\pi}{\lambda k_n})^2 \quad (11)$$

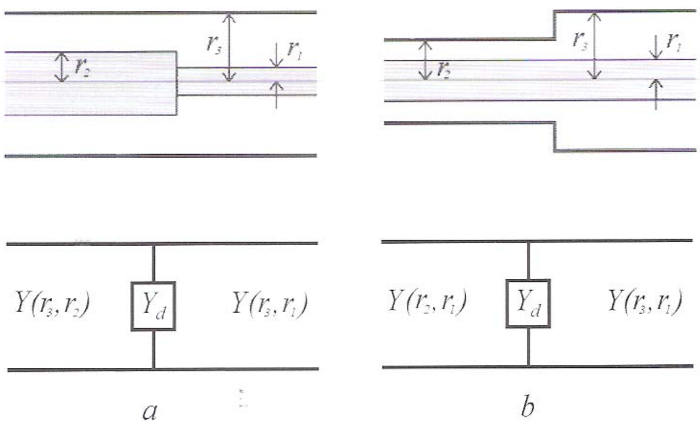

Fig 4: equivalent circuits of coaxial line discontinuity

step all sixteen patches were installed on radial power divider N=16 input ports. On base of coaxial combiner before the high power amplifier(HPA) with 140 W operating I frequency 8.5 – 9.5 GHz was used and the length of designed matching section is L=3 cm or $l=\lambda$ which three times smaller compared same condition conventional quarter waves transformer. Insertion loss of this combiner is less than 0.5 dB. The shape and radiation pattern of multi beam array patch antenna in four different frequencies is shown below in

fig (5). It was necessary to use power divider/combiner which presents Low loss, reasonable amplitude and phase balance. Also radial divider permits to place a large number of ports very close to central feed port.

3. Circularly distributed multi beam patch array antenna

In this section distributed multi beam patch array antenna is designed and investigated.this multi beam patch array consist of one radial divider with 16 ports which 16 identical microstrip patches via microstrip-to-coax 50Ω adapter directly connected to receiving coaxial line main port of radial power as it is shown below.

This antenna is designed to use in k_a band and because of that we have tested the multi beam patch array antenna in frequency 9.2 GHz .the radiation pattern and VSWR of antenna in four various frequencies is presented in figure (5).

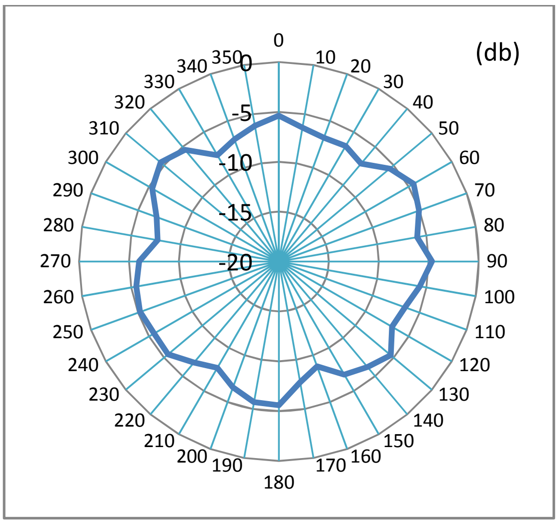

f=9.319GHz , vswr=1.22

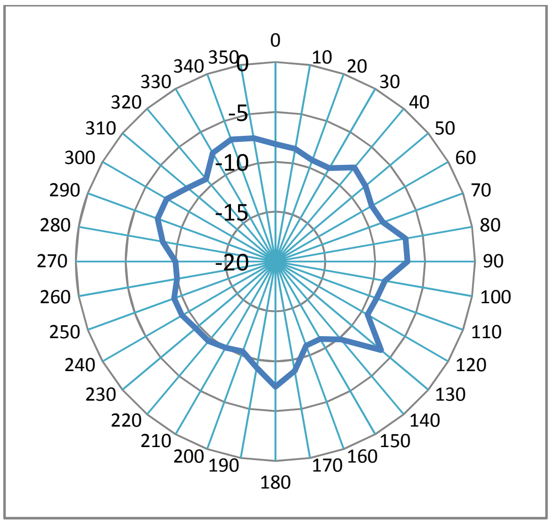

F=8.909 ,vswr=5.0

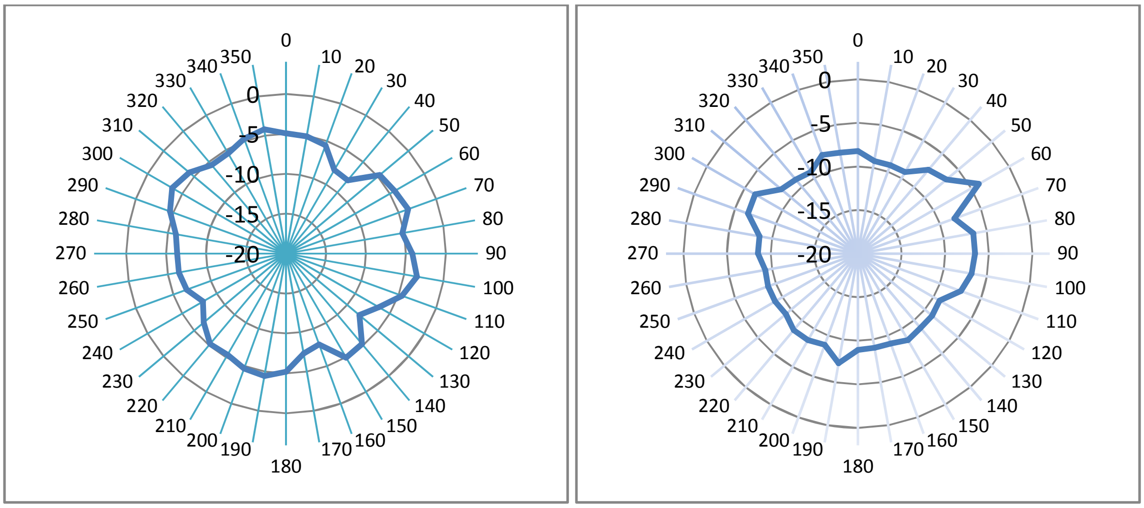

f-9.550GHz ,vswr=2.2

f= 9.760GHz , vswr=1.4

Fig5: The shape and radiation pattern of multi beam patch array antenna in various frequencies

.

4.Conclusion

An X-Band micro strip patch array antenna and radial type 16-way coaxial power divider/combiner has been investigated and realized. The antenna in different frequencies was tested and radiation pattern of single patch and array of circular patches was plotted. The length of the used matching section is three times smaller than those of conventional quarter wave transformers. Results from radiation pattern show good performance and efficient directivity in all direction compare to other common Biconical broad bandwidth antennas.

References

[1] P.Marchand, et al.Proceedings of EPAC (2004).

[2] P.C.Jia,L. –Y.Chan,and A.Alexanian,IEEE Trans Microwave Theory Tech,51,2469(2003).

[3] Winnery,J.R,Jamieson,H.W.Robbins,Proc.IRE,32,695(1944).

[4]D.M.Pozar.Microwave Engineering,New York,Wiley;2 edition (1997).

[5]V.Mohen kumar,N.Sujith,Enhancment of bandwidth and gain of rectangular patch antenna,Department of Electronics and Communication Engineering National Institute of TechnologyRourkela (2010).
[6]Constantine A.Balanis,Antenna theory,analysis and desigh,third edition 2005.

INSTITUTE OF RADIOPHYSICS
AND ELECTRONICS

National Academy of Sciences of Armenia

State Committee of Science of Armenia